Worcester Polytechnic Institute

Digital WPI

2008-04-16

Magnetic Resonance Imaging of the Rat Retina

Govind Bhagavatheeshwaran
Worcester Polytechnic Institute

Follow this and additional works at: https://digitalcommons.wpi.edu/etd-dissertations

MAGNETIC RESONANCE IMAGING
OF THE RAT RETINA

A Dissertation Presented

By

GOVIND BHAGAVATHEESHWARAN

Submitted to the Faculty of the

UNIVERSITY OF MASSACHUSETTS MEDICAL SCHOOL
And
WORCESTER POLYTECHNIC INSTITUTE

in partial fulfillment of the requirements for the degree of

DOCTOR OF PHILOSOPHY IN
BIOMEDICAL ENGINEERING AND MEDICAL PHYSICS
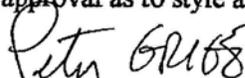
March 04, 2008

MAGNETIC RESONANCE IMAGING OF THE RAT RETINA

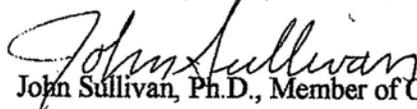A Dissertation Presented

By

Govind Bhagavatheeshwaran

The signatures of the Dissertation Defense Committee signifies

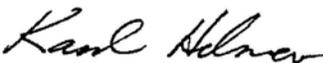completion and approval as to style and content of the Dissertation

Peter Grigg, Ph.D., Thesis Advisor

Glenn Gaudette, Ph.D., Member of Committee

John Sullivan, Ph.D., Member of Committee

Karl Helmer, Ph.D., Member of Committee

Peter Grigg, Ph.D., Member of Committee

The signature of the Chair of the Committee signifies that the written dissertation meets

the requirements of the Dissertation Committee

Christopher Sotak, Ph.D., Chair of Committee

The signature of the Dean of the Graduate School of Biomedical Sciences signifies

that the student has met all graduation requirements of the school.

Anthony Carruthers, Ph.D.,

Dean of the Graduate School of Biomedical Sciences

Program

Biomedical Engineering

March 04, 2008

To my wife.

And to the broad shoulders of giants…

Acknowledgement

I would like to thank Timothy Duong for giving me the opportunity to work on the retinal imaging project, for providing the financial support, and for his guidance on the thesis. I am extremely grateful to my colleagues Tsukasa Nagaoka and Yoji Tanaka for the various discussions and suggestions which proved invaluable in getting this thesis to a completion. I thank them for their assistance in various forms and patience during the course of the research. I would like to thank Haiying Cheng for her various suggestions and assistance in getting the project started. I thank my colleagues Qiang Shen, Xiaodong Zhang, Swati Rane, Yingxia Li and Robbie Champion for all their assistance and comments during the course of the research. I am especially thankful to Swati Rane, Nanna Sulai and Hanh Nguyen for keeping the group lively.

I thank Machelle Pardue of Atlanta VA Hospital for her valuable suggestions to improve the experimental design, expertise in the field of retina, and for providing Royal-College-of-Surgeon rats for our studies. I thank my colleagues Moon Kim, Amanda Faulkner and Tiffany Walker at Atlanta VA hospital, for their assistance in providing RCS rats, with ERG experiments, and with retinal histology. I am extremely grateful to Micheal J. Kuhar for teaching me the emulsion autoradiography technique, for his expertise which helped resolve technical issues, and for his buoyant spirit. I thank Li-Ling Shen for her help during emulsion autoradiography experiments. I also want to thank Darin Olson and Peter Thule of Atlanta VA hospital for their various suggestions and guidance.

This thesis could not have been completed without the help and guidance from Peter Grigg. I appreciate the time he took out of his busy schedule to make sure I was on

Preface

The dissertation describes high-resolution magnetic resonance imaging techniques developed for anatomical and functional imaging in the rat retina. The imaging techniques developed were then applied to detect layer-specific changes in a rat model of retinal degeneration. The work described in this dissertation was carried out between November 2005 and December 2007, primarily at the Yerkes Primate Research Center, Emory University, Atlanta, GA. This work was supported in part by the Whitaker Foundation (RG 02-0005) and the NIH/NEI (R01 EY014211) to Dr. Timothy Duong, and a contract between Emory University and University of Massachusetts Medical School.

Chapter 4 and first part of Chapter 7 of this dissertation includes results published in Cheng et al, PNAS (2006) 103:17525-17530. The data in those chapters were collected by me and Haiying Cheng. I have received a lot of assistance for retinal histology from Dr. Machelle Pardue's lab at the Atlanta VA hospital. Toluene-blue histology sections, as well as histological thickness measurements reported in this dissertation were done by me, Moon Kim or Amanda Faulkner at Dr. Pardue's lab. I want to thank Ryan Jesse and Meghna Bhatt, summer students at the Yerkes Imaging Center during 2007, for their assistance with intraparitoneal injections of $MnCl_2$ reported in first part of Chapter 5. Lastly, Mn^{54} autoradiography reported in Chapter 5 of this dissertation was done by me under the supervision of Prof. Michael J. Kuhar, Research Professor and Chief, Division of Neuroscience, Yerkes National Primate Research Center, Emory University, Atlanta, GA.

Abstract

The retina is a thin layer of tissue lining the back of the eye and is primarily responsible for sight in vertebrates. The neural retina has a distinct layered structure with three dense nuclear layers, separated by plexiform layers comprising of axons and dendrites, and a layer of photoreceptor segments. The retinal and choroidal vasculatures nourish the retina from either side, with an avascular layer comprised largely of photoreceptor cells. Diseases that directly affect the neural retina like retinal degeneration as well as those of vascular origin like diabetic retinopathy can lead to partial or total blindness. Early detection of these diseases can potentially pave the way for a timely intervention and improve patient prognosis. Current techniques of retinal imaging rely mainly on optical techniques, which have limited depth resolution and depend mainly on the clarity of visual pathway. Magnetic resonance imaging is a versatile tool that has long been used for anatomical and functional imaging in humans and animals, and can potentially be used for retinal imaging without the limitations of optical methods. The work reported in this thesis involves the development of high resolution magnetic resonance imaging techniques for anatomical and functional imaging of the retina in rats.

The rats were anesthetized using isoflurane, mechanically ventilated and paralyzed using pancuronium bromide to reduce eye motion during retinal MRI. The retina was imaged using a small, single-turn surface coil placed directly over the eye. The several physiological parameters, like rectal temperature, fraction of inspired oxygen, end-tidal CO_2, were continuously monitored in all rats. MRI parameters like T_1, T_2, and the apparent diffusion coefficient of water molecules were determined from the rat retina

at high spatial resolution and found to be similar to those obtained from the brain at the same field strength.

High-resolution MRI of the retina detected the three layers in wild-type rats, which were identified as the retinal vasculature, the avascular layer and the choroidal vasculature. Anatomical MRI performed 24 hours post intravitreal injection of $MnCl_2$, an MRI contrast agent, revealed seven distinct layers within the retina. These layers were identified as the various nuclear and plexiform layers, the photoreceptor segment layer and the choroidal vasculature using $Mn^{54}Cl_2$ emulsion autoradiography. Blood-oxygen-level dependent (BOLD) functional MRI (fMRI) revealed layer-specific vascular responses to hyperoxic and hypercapnic challenges. Relative blood volume of the retina calculated by using microcrystalline iron oxide nano-colloid, an intravascular contrast agent, revealed a superfluous choroidal vasculature. Fractional changes to blood volume during systemic challenges revealed a higher degree of autoregulation in the retinal vasculature compared to the choroidal vasculature, corroborating the BOLD fMRI data. Finally, the retinal MRI techniques developed were applied to detect structural and vascular changes in a rat model of retinal dystrophy.

We conclude that retinal MRI is a powerful investigative tool to resolve layer-specific structure and function in the retina and to probe for changes in retinal diseases. We expect the anatomical and functional retinal MRI techniques developed herein to contribute towards the early detection of diseases and longitudinal evaluation of treatment options without interference from overlying tissue or opacity of the visual pathway.

Table of contents

List of Figures

List of Tables

List of Commonly Used Abbreviations

ADC: Apparent diffusion coefficient

B_0:   External or main magnetic field of the system

B_1:   Magnetic field component of the radio frequency pulse

BBB: Blood-brain barrier

BOLD: blood-oxygen-level dependent

BRB: Blood-retinal barrier

CA: Contrast agent

CCD: Charge-coupled device

CNR: Contrast-to-noise ratio

CNS: Central nervous system

$\Delta R2^*$:   Change in transverse relaxivity (or change in $\frac{1}{T_2^*}$)

E: Energy level associated with a nucleus or electron

EMG: Electromyogram

EOG: Electrooculography

EPI: Echo-planar imaging

ERG: Electroretinography

EtCO2:   End-tidal carbon dioxide level

FA: Flip-angle of the radio frequency pulse

fMRI: Functional magnetic resonance imaging

FOV: Field of view

fps: frames per second

FWHM: Full-width-at-half-maximum

γ: Magnetogyric or Gyromagnetic ratio of a particle

GC: Ganglion cell layer

Gd-DTPA: Gadolinium diethylene triamine pentaacetic acid, a contrast agent

$\hbar$:   Dirac's constant

h: Hours

HDL: High-density lipoprotein

HFR: High frame-rate

i.v.:   intravenous (administration of drugs)

i.p.:   intraperitoneal (administration of drugs)

ICG: Indocyanine green (fluorescent dye for retinal angiography)

INL: Inner nuclear layer

IOP: Intraocular pressure

IPL: Inner plexiform layer

k: Boltzmann's constant

l: Spin angular momentum

LDL: Low density lipoprotein

LE: Long Evans

LFR: Low frame rate

MABP: Mean arterial blood pressure

MEMRI: Manganese-enhanced magnetic resonance imaging

m_I: Magnetic quantum number

μm: Micrometer or 10^{-6} meters

min :   Minute

MION: Microcrystaline iron oxide nanocolloids, a contrast agent

μL :   microliter or volume of 1×10^{-6} Liters

MRI: Magnetic resonance image or magnetic resonance imaging

OCT: Optical coherence tomography

ONL: Outer nuclear layer

OPL: Outer plexiformlayer

P: Postnatal age

p: p-value (in statistical hypothesis testing)

Pseg: Inner and outer photoreceptor segments

PVE: Partial volume error

rBV: Relative blood volume

RCS: Royal college of surgeons (rat strain, a model of retinal dystrophy)

RF: Radio frequency

RP: Retinitis pigmentosa

RPE: Retinal pigmented epithelium

SAR: Specific absorption rate of the radiofrequency pulse in the tissue

SD: Standard deviation

SLO: Scanning laser ophthalmoscopes

SNR: Signal-to-noise ratio

SPIO: Superparamagnetic iron oxide nanoparticle, a contrast agent

T: Tesla (unit of magnetic flux density)

T_1:   Longitudinal relaxation time constant

T_2:   Transverse relaxation time constant

T_2^*:   Transverse relaxation time constant T_2-star (including contributions from local magnetic-field inhomogeneities)

TE: Echo time in an MRI pulse sequence

TR: Repetition time in an MRI pulse sequence

Vit: Vitreous

χ: Susceptibility of tissue or sample

Chapter 1: Introduction

The retina is a thin layer of neural tissue in the back of the eye and has a distinct layered structure. The retina is supplied by two separate vasculatures, the retinal and the choroidal vasculature. The retinal layers that are made up of the photoreceptor cells are essentially avascular, despite their consistently high metabolic demand. Degenerative or vascular diseases that affect the retina, like retinitis pigmentosa or diabetic retinopathy often lead to severe loss of visual acuity if not detected early. However, current techniques in retinal imaging have limited depth resolution and contrast to detect changes in retinal anatomy or have limited vascular imaging capability.

Magnetic resonance imaging (MRI) has long been used for anatomical and functional imaging of the brain. This thesis reports high resolution techniques for anatomical and functional MRI of the rat retina. These techniques were then applied in rat models of retinal degeneration and diabetic retinopathy.

Part 1: Introduction to the Retina

The eye is the organ of sight in humans. The globe of the eye or eye ball rests in a protective bony socket. Six small but strong extraocular muscles attach to the globe which turns the eye about the three geometrical axes. Lacrimal glands behind the eye lid, secretes a mixture of water, lipids, electrolytes and antibodies (tears) which help to keep the external eye nourished and healthy.

The eye ball is divided into anterior and posterior segments at the boundary of the sclera and cornea also called the limbus (Fig. 1.1). The anterior segment therefore includes the cornea, anterior and posterior chamber, iris, ciliary body and the lens. The
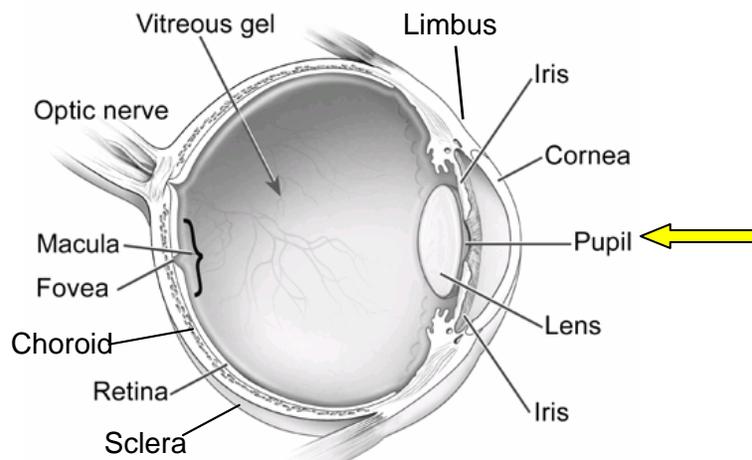
Fig. 1.1: A schematic diagram of the human eye showing the location of the retina, optic nerve, cornea and lens in relation to the other structures. Thick arrow depicts the direction of the incident light (Adapted from National Eye Institute catalog # NEA09).

posterior segment includes the optic nerve, sclera, choroid, retina and the vitreous body.

The cornea is transparent fibrous tissue in the anterior segment through which light enters the eye. Cornea provides most of the light focusing ability of the eye. The light then passes through the fluid-filled anterior chamber. The fluid, aqueous humor, is

continually produced by the ciliary body and drained at the junction of the iris and the cornea, called the angle. The aqueous humor provides nutrition and removes the breakdown products of the cornea, iris and lens. The iris is a thin opaque membrane made of elastin, attached to a circular muscle called the sphincter. The opening in the center of the sphincter, called the pupil, controls the amount of light that can pass through, thereby providing brightness control. The light is then focused onto the retina by a crystalline lens located directly behind the pupil. The lens has a soft core and is suspended by fibers called zonules. Zonules can contract or relax to change the curvature of the lens, thereby giving selective focusing ability to the eye [1-3].

The focused light then passes the vitreous humor, a clear fluid that fills the space between the lens and the retina. The vitreous is mostly composed of water, electrolytes and has phagocytes that remove debris from the path of the light. The light incident on the retina is then 'coded' as neuronal action potentials. The action potentials are sent to the visual cortex in the brain through the optic nerve fibers. Sclera is the tough, protective, layer of the eye, made up of bundles of collagen and elastin fibers. The sclera extends from the cornea to the optic nerve and provides firm attachment to the muscles that move the eye. As the sclera merges into the cornea in the anterior chamber, the fibers of the sclera become transparent [4, 5].

The retinal neurons originate from the developing brain, and are therefore considered a part of the central nervous system (CNS). The retinal neurons form networks of complex synapses and processes just as in the brain [6]. Neurotransmitters active in the brain, such as glutamate [7, 8], glycine [9], γ-aminobutyric acid (GABA) [10], acetylcholine [11], dopamine [12], and aspartate are also active in the retina [13].

Studies on the vertebrate retina have been historically important not only because it is the primary transducer in the process of vision, but also because it is a part of the CNS observable non-invasively.

1.1   The retina – structure and function

The retina is a highly stratified but thin layer of neural tissue at the back of the eye (Fig. 1.1) [14, 15]. It is primarily responsible for the transduction of light to neuronal action potential and the associated neuronal signal processing. In general, the retina is made up of neurons, their synapses, glial cells, epithelial cells, and photoreceptors [16]. The primate retina is nourished by the retinal and choroidal blood vessels.

The primate retina in itself has many regions with slightly different layered structure [17, 18]. The fovea-centralis is a very thin region of the central retina located directly across from lens. It is about 0.3 mm in diameter and is entirely composed of photoreceptor segments [19, 20]. Due to the high density of photoreceptor segments in this region, the fovea is primarily responsible for the best visual acuity in bright light. Just outside the foveal region in the central retina is the macula-lutea, with a diameter of about 1.5 mm. The thickness of the macula is highly variable. Medial to the macula, there is a 1-mm-diameter region devoid of any photoreceptor cells, called the optic disc or blind spot. The region of the retina outside these structures is called the peripheral retina, and it is essentially uniform.

1.1.1 Retinal structure

Different types of neurons in the vertebrate retina like bipolar, amacrine, horizontal and ganglion cells are arranged in layers. Each layer plays a specific function in transduction of light to action potential, processing of these action potentials or its transmission to the brain. These layers are arranged in an inverted fashion with the

Vitreous Body
Ganglion Cell Layer

Inner Plexiform Layer

Inner Nuclear Layer
Outer Plexiform Layer

Outer Nuclear Layer

Photoreceptor Segment Layer

Retinal Pigment Epithelium
Choroid Vasculature
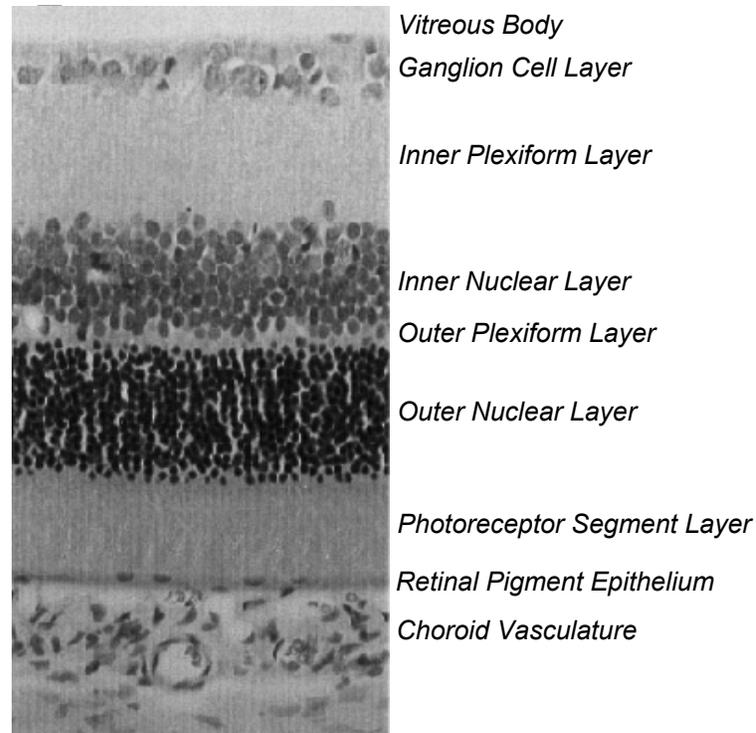
Fig. 1.2: Toluidine blue-stained section of the rat retina depicting its various layers. Arrow depicts the direction of incident light. (Adapted from Cringle and Yu, Comp Biochem Physiol A Mol Integr Physiol. 132(1):61-6)

photoreceptor cells on the outside and the ganglion cell axons that carry the action potential to the brain on the inside of the retina (Fig. 1.2).

Photoreceptor cells

The photoreceptors in the retina form three distinct layers, namely, the outer nuclear layer and the inner and outer segment layers (collectively called the photoreceptor segments in Fig. 1.2). The outer nuclear layer is made up of the soma of

these photoreceptor cells and its processes that connect to the segments. The inner segments contain mitochondria and ribosomes and are responsible for the assembly of membrane stacks that make up the outer segments. The membrane stacks in outer segments of the photoreceptors house a light-sensitive pigment called opsin. A photon-induced change in structure of opsin starts a signal cascade that leads to a decrease in the membrane potential of the photoreceptor cell and thus the frequency of action potential generated (discussed in more detail in section 1.1.2).

The retina contains two types of photoreceptor cells, the rods which are very sensitive to a broad spectrum of light frequencies, and the cones which have much narrower range of frequency response [21, 22]. In human retina, there are three types of cones: red cone (maximally responsive at 575 nm wavelength), green cone (maximally responsive at 535 nm wavelength) and blue cone (maximally responsive at 445 nm wavelength). The rod population exceeds the cone population by 20:1 over the entire retina; however, their relative populations across the retina are variable. The rods make up almost the entire peripheral retina, while they are essentially absent in the fovea.

Inner nuclear layer

Inner nuclear layer is made up of horizontal, bipolar, and amacrine neurons. The horizontal and bipolar cells synapse with the photoreceptor cells in the outer plexiform layer. The horizontal cells exclusively synapse with cones and have ionotropic glutamate receptors showing hyperpolarizing response to cone activation. This architecture of horizontal cells is thought to play a role in the center-surround inhibition, and it has been

shown that light-induced response of a cone can be reduced by illumination of the surrounding cones [23].

The bipolar cells synapse with the photoreceptor cells at the outer plexiform layer and with ganglion and amacrine cells at the inner plexiform layer [24, 25]. Bipolar cells can be broadly classified into two types depending on the type of receptors they express. The ON type bipolar cell express metabotropic receptor mGluR6, while the OFF type expresses AMPA or kainate glutamate receptor [26, 27]. The ON bipolar cell is excited and OFF bipolar cells inhibited when light is incident on the retina. Furthermore, some bipolar cells exclusively synapse with rods while others contact varying number of cones, depending upon their location in the retina. In the central retina, bipolar cells may contact one cone and one ganglion cell while at the periphery they can contact many cones, thus participating in signal integration [28].

Amacrine cells are interneurons situated in the inner plexiform layer and synapse with bipolar cells and ganglion cells in the inner plexiform layer [24]. These neurons maybe be either GABAergic or glycinergic, and make lateral connections like horizontal cells. However, the processing done by these cells are thought to be more specialized, for example, detecting motion.

Ganglion cell layer

Ganglion cells essentially carry the processed signal from the retina to the lateral genniculate nucleus via the optic nerve. The ganglion cell bodies make up the ganglion cell layer while their axons, running radially to the optic disc, make up the nerve fiber layer. There are many different types of ganglion cells identified in the primate retina [29,

30], but a majority of these are either parvocellular cells (80% of the population) or magnocellular cells (10% of the population). Another relevant cell type is the melanotropic ganglion cells which make up about 2% of the population, and are light sensitive.

In the central retina one ganglion cell carries the signal from one cone relayed through one bipolar cell, while in the peripheral retina, one ganglion cell may carry signal integrated from many bipolar cells, each of which integrates signal from many photoreceptor cells. This is one of the reasons for high visual acuity of the central retina compared to the peripheral retina [31].

The axons of the ganglion cells travel along the inner surface of the retina toward the optic nerve and make up the nerve fiber layer (not shown in Fig. 1.2). These axons exit the globe of the eye at the optic nerve head and become the optic nerve running towards the visual cortex.

Retinal Pigmented Epithelium

Retinal pigmented epithelium (RPE) is a single celled layer outside the photoreceptor layer. It is involved in recycling photosensitive molecules in the photoreceptor segments through the phagocytosis of the outer segments of the photoreceptors. The RPE also functions as a tight barrier regulating passage of substances between the choroid and the neural retina. RPE are therefore critical not only homeostasis of the retina but also in renewing the primary transducer molecules responsible for vision.

1.1.2 Blood supply to the retina

Nutrition and oxygen is supplied to the retina through two independently regulated vasculatures, namely the choroidal and retinal blood vessels. The choroidal vessels are situated in the outside of the neural retina sandwiched between the sclera and the RPE layers. The retinal vessels lie on the inner surface of the retina running radially from the optic nerve towards the periphery, with penetrating capillaries reaching as far as the outer boundary of the inner nuclear layer. The outer nuclear and photoreceptor segment layers of the retina are completely avascular, and receive most of their oxygen and nutrients from the choroidal vasculature through diffusion [32]. The retinal vessels are also absent in the foveal region of the primate eye, and the entire foveal retina is supplied by diffusion of nutrients from the choroidal circulation.

The choroidal layer comprises of dense vasculature, characterized by very high flow rate and low vascular resistance [33]. Figure 1.3 shows the corrosion cast of the choroidal vessels in Wistar rat, produced by the intra-arterial perfusion of Mercox CL-2B resin, and studied under a
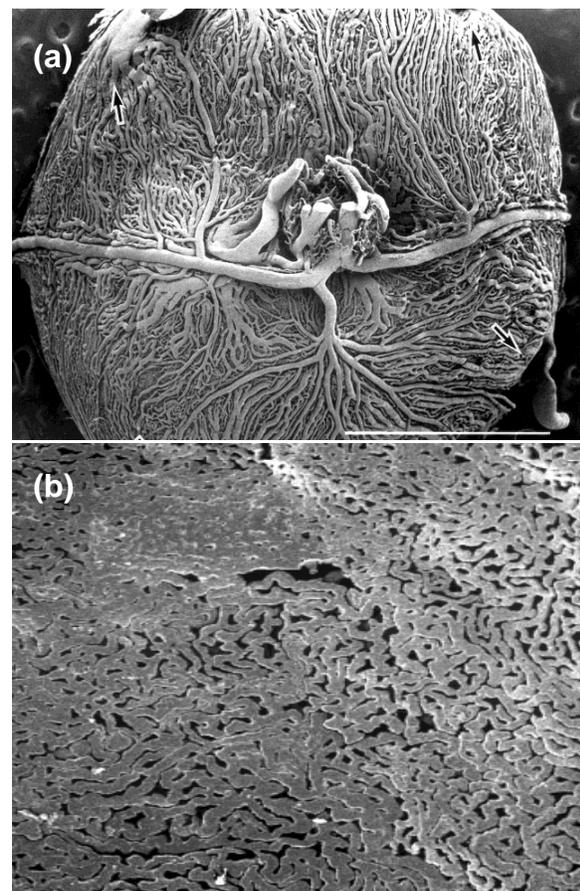
Fig. 1.3 (a) Posterior and (b) anterior view (with retinal vasculature removed) of the choroidal vasculature in Wistar rats obtained using corrosion cast and viewed with an electron microscope. Scale bar (a) 2mm. (Adapted from Bhutto and Amemia Anat Rec (2001) 264:63)

scanning electron microscope. These studies revealed large arteries and veins in the outer choroid and irregular mesh of capillaries in the inner choroid. The diameter of these choriocapillaris was determined to be in the range of ~15 μm, slightly larger than the capillaries in the brain, and suggesting a low resistance to blood flow.

Choroid vessels are supplied by the many medial and lateral posterior ciliary arteries, which arise from the ophthalmic artery [34]. The choroidal vessels are known to have dense sympathetic innervations, which upon stimulation causes vasoconstriction [35, 36]. The anterior choroids which essentially perfuse the ciliary bodies and anterior chamber also have abundant parasympathetic innervations which exhibit a vasodilatory response on stimulation [37].

The retinal vessels arise from the central retinal artery, another branch of the ophthalmic artery, and runs along the optic nerve before entering the eyeball. Once within the orbit, the artery symmetrically splits into many radial branches and runs towards the peripheral retina (Fig. 1.4). In the vicinity of the optic nerve head (4-5 mm), these major branches of the central retinal artery give rise to retinal peripapillary capillaries, and all the vasculature lies entirely in the optic nerve fiber layer [38]. Further from the

Fig. 1.4: Corrosion cast of retinal vasculature in Wistar rat, as seen with an SEM. Scale bar is 1mm. (Adapted from Bhutto and Amemia Acta Anat (1995) 153(4):290)

optic nerve head, two distinct beds of capillaries arise from these arterioles. The inner

capillaries lie in the ganglion cell layers under and parallel to these arterioles and the outer capillary network are denser and run from the inner plexiform layer to the outer plexiform layer thought the inner nuclear layer. The inner and the outer capillary networks have interconnections, vertical runs, and short vascular bridges. The retinal veins are more tortuous than the arteries and drain into the central retinal vein.

The retina has a tight blood retinal barrier formed by the endothelial cells of the retinal vasculature and the retinal pigmented epithelium. Choroidal capillaries have many fenestrations that are thought to be leaky to some proteins and vitamins required by the photoreceptors. The outer blood retinal barrier is therefore composed of structures outside the choroids like the retinal pigmented epithelium and limiting membrane. The RPE retains adherens junctions and develops a low permeability form of tight junction [39, 40]. Mostly all the nutrients are transferred into the retina by means of active transport or exchange pumps.

1.1.3 Mechanism of photo-transduction

As introduced in the previous section, the photoreceptor cell consists of an outer segment of membranous disks, an inner segment rich in mitochondria, the cell body in the outer nuclear layer and finally the axon terminals which synapse with horizontal and bipolar cells in the outer plexiform layer (Fig. 1.5). The disks in the outer segment are rich in light sensitive, G-protein
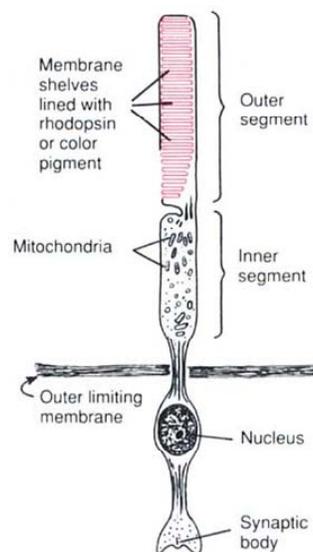
Fig. 1.5: Schematic diagram of a photoreceptor cell (rod). (Adapted from: upload.wikimedia.org)

coupled receptor, called opsin and a cyclic-Guanine monophosphate (cGMP) activated sodium channel. Opsin is covalently associated with a chromatophore, *11-cis retinal*.

As in neurons, the Na^+/K^+ pump in photoreceptor cells use the energy from ATP to maintain a concentration gradient of Na^+ and K^+ across its membrane at a resting potential of about -65 mV. In the dark, the outer segment is rich in cGMP, activating the Na^+ channels and causing it to be leaky to sodium ions. Since the concentration of Na^+ is higher in the extracellular space, it enters the photoreceptors, causing a net increase in the membrane potential from -65 mV to about -40 mV. At this membrane potential the photoreceptor cell is more likely to fire action potential and release neurotransmitters onto the synapse with bipolar or horizontal cells. Therefore, maintaining the resting membrane potential in the dark is an energy intensive process for the photoreceptor cell [41].

When a photon is incident on the chromatophore, it isomerizes from its *11-cis* form to *all-trans* form. This in turn causes a conformational change in the opsin itself and triggers a signal cascade through the associated G-protein called transducin. Activated transducin in turn activates phosphodiestrase (PDE) which catalyses the hydrolysis of cGMP. As the concentration of cGMP within the cell decreases, the cGMP-activated Na-channels close, decreasing the membrane potential and hyperpolarizing the cell. This causes a reduction in the action potentials generated by the photoreceptor, and the overall energy consumption of the photoreceptor is reduced. *All-trans* retinal is converted back to its *11-cis* form through a slower process mediated by enzymes and opsin returns to its original shape [42].

1.2   Diseases of the retina

Diseases of the retina often cause or contribute to vision deficits and many lead to total blindness. As with other organs, retinal diseases may originate in the retina or may be systemic diseases that affect the retina. Retinal diseases may be inherited or they may be adverse effects of the environment or drugs. Retinal diseases may be broadly classified into non-progressive diseases like night blindness or progressive diseases like diabetic retinopathy and retinitis pigmentosa.

Congenital diseases often compromise retinal function without appreciable retinal changes and with little or no changes to retinal function over time. A variety of functional tests may be required for their differential diagnosis for the more common progressive disorders. Progressive retinal diseases, on the other hand, are often further classified into stages depending upon the state of progress of the disease. For example, diabetic retinopathy, which is precipitated by the vascular complications arising from diabetes, is broadly classified into stages depending upon the severity of the vascular degeneration. Similarly, early or delayed onset retinitis pigmentosa, a genetic disorder that leads to rod-cone dystrophy, may show myriad symptoms at each stage of disease progression, like night-blindness followed by tunnel vision followed by complete vision loss.

A variety of techniques are currently used for the early detection, accurate diagnosis, staging and even the evaluation of therapeutic techniques.

1.3   Diagnosis of retinal diseases – current techniques

1.3.1   Test of visual acuity and field

The most basic and popular technique for the evaluation of retinal function is the visual acuity and field test. Loss of sharpness of vision can result from refractive problems of the lens, cornea or disorders that affect the retina. The visual acuity of each eye can be tested separately using the Snellen chart with letters or symbols. Peripheral vision can tested using a blinking light or moving object. These tests cannot directly diagnose retinal disorders. However, some retinal disorders like macular edema will show early signs of loss of visual acuity. To detect either structural or functional changes in the retina, a more specific test is often prescribed.

1.3.2 Ophthalmoscope

The retina can be directly visualized through the cornea, and most current techniques in retinal diagnosis depend on imaging the retina through the visual pathway. Optical imaging techniques for the retina have long been used to study the retinal morphology and more recently retinal function.

A direct ophthalmoscope is a handheld device that shines a light into the eye to enable a doctor to examine the cornea, lens, retina, vitreous humor, optic nerve head, and the major retinal vessels. Some of the diseases that can be detected with an ophthalmoscopic examination include cataract in the lens, retinal hemorrhage, macular edema, evidence of increased intraocular pressure, gross changes in the retina due to diabetes or macular degeneration, neovascularization and tumors. A direct ophthalmoscope gives a two-dimensional view of the retina greatly inhibiting the examiners ability to see structures clearly. An indirect ophthalmoscope [43] uses a binocular eyepiece for the examiner to visualize the retina with some depth perception. It

also enables the use of a brighter light source and observation of a wider field of view in the retina (routine: 30 degrees; wide angle 45-90 degrees).

Neither the direct nor the indirect ophthalmoscope has the ability to resolve the retinal layer structure. Generally, these techniques can be used only if the visual field is clear, which precludes conditions like vitreous hemorrhages and cataract. These techniques also lack the ability to evaluate functional capability of the retina. Physicians mark findings during an examination down on a retinal chart, which can then be used for longitudinal studies.

An indirect ophthalmoscope could be combined with a camera to get fundus photography. Digital or analog imaging of the fundus reduces physician errors, as retinal details may be more easily visualized and recorded. Photographic documentation helps keep track of disease progression. Advent of higher resolution digital photography has further helped the field of retinal diagnosis through digital image processing for better visualization, and even the ability to be sent across the internet for remote expert diagnosis. However, this technique suffers from most of the drawbacks of the ophthalmoscope.

Fig. 1.6: Retinal artery stenosis (arrowheads) as visualized by (a) fundus photography and (b) fluorescein angiography. (Adapted from: Papastathopoulos andJonas Br. J. Ophthalmol (1998) 82;48-50)

Monochromatic fundus photography may be used to isolate and imaging specific retinal layers [44, 45]. For example, arteries and veins are best differentiated from each other at a wavelength of

around 600-700 nm due to the differences in absorption spectra between oxy- and deoxy-hemoglobin. Retinal nerve fiber layers are best studied with a blue filter (~490 nm), red-free fundus photographs are taken with a green filter (540-570 nm) (Fig. 1.6a) and choroidal vessels best seen with a deep-penetrating red light source (650 nm). Hemorrhages and micro aneurysms are reported to be best seen with the 525–575 nm wavelengths. Degenerative changes in the retinal vessels [46] and human albinism [47] have also been studied using monochromatic light. Furthermore, the autoflorescence from lipofuscins, a toxic byproduct of polyunsaturated fatty acids and a sign of increased oxidative damage, has been used to detect regions of age-related macular degeneration [48, 49].

1.3.3 Retinal angiograms

Apart from direct examination of the retinal structures, ophthalmoscope can also be used to study the dynamics of blood flow in the retina. For this, an optical contrast agent is injected intravenously, and its circulation through the retinal vessels is recorded through a fundus camera. The pattern of dye circulation can be used to detect ischemia, aneurisms, hemorrhages and angiogenesis among other circulatory defects. Red-free fundus photography usually accompanies the angiographic images to help orient the physician.

Fluorescein and indocyanine green (ICG) are the most commonly used dyes for retinal angiography (Fig. 1.6b). Sodium fluorescein is a highly fluorescent molecule with high molecular weight of 332 daltons. When excited with blue light (wavelength of 490 nm), fluorescein emits yellow-green light at 520 nm. Fluorescein angiography is

performed by photographing this fluorescence with a high speed fundus camera and yellow-green filter under blue illumination after the intravenous injection of sodium fluorescein. The use of filters for both illumination and imaging allow interference free imaging of the fluorescence from the blood. Generally, aneurism, hemorrhages or other irregularities in the retinal vessels can be detected by this technique. Choroidal vessels are, however, only poorly visible in this technique due to the presence of the pigmented epithelial cells. Furthermore, fluorescein has been reported to leak from the choroids due to its low molecular size [50].

The molecular weight of ICG is 775 daltons, but it is known to aggressively bind with high density lipoprotein (HDL) and moderately to low density lipoprotein (LDL) in the blood plasma. ICG is known to have very low vascular permeability even in the choroidal vessels, which are otherwise known to be leaky to some proteins and vitamins. This is attributed to the large complexes ICG forms when bound to HDL (particle size of 8-11 nm and 22 nm for HDL and LDL respectively). When the bound form ICG is excited at ~805 nm, it is known to fluoresce maximally at 830 nm, which is in the near infrared region of the spectrum [51]. Infrared fluorescence has the distinct advantage of larger tissue penetration, making it possible to study choroidal vessels [52].
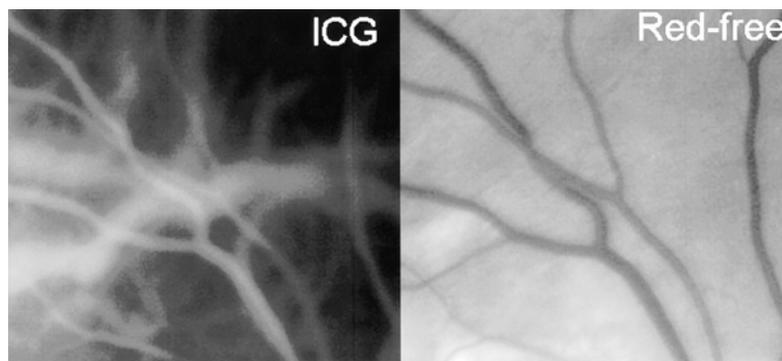
Fig. 1.7: Comparison of indocyanine green (ICG) angiography with fundus photograph (red-free) depicting the retinal vessels in a magnified portion of the retina. Choroidal vessels can be clearly seen in the ICG image, which cannot be picked up with fundus photography due to the presence of the retinal pigmented epithelium. (Adapted from: Desmettre et al Survey of Ophthalmology (2000) 45(1):15).

Therefore, the low vascular permeability and the high depth of penetration of the ICG fluorescence makes it an ideal technique to study choroidal circulation (Fig. 1.7).

Despite the advantages of ICG, conventional angiography is limited in its ability to differentiate between the retinal and choroidal vascular contributions of the signal (Fig. 1.7). Furthermore, large vessels in the retinal and choroidal vasculature fill rapidly with the dye, leaving little or no contrast from the dye in the capillaries. Studies performed under aphysiologic conditions, like elevated intraocular pressure or vascular occlusions, have provided useful information on retinal blood flow [53]. In the primate eye, detailed blood-flow studies from the choroid are possible at the macular region, without interference from the retinal vasculature. It is thought that the choroidal blood flow at the macula is about 10 times that in the peripheral regions and that these vessels fill first due to the shorter distance of feeding vessels [33, 54].

1.3.4 Scanning Laser Ophthalmoscope

While the fundus camera can obtain high resolution (~10 μm/pixel) pictures of the retina at extremely high frame rates of 100 frames per second (fps) if required, the intraocular scattering of light can cause a loss of contrast during retinal fluorescence angiography. Scanning laser ophthalmoscopes (SLO) uses a narrow beam of excitation (~20 μm light spot) light and scans the retina in a raster pattern, one pixel at a time to form the complete picture [55]. Since a very small region of the retina is illuminated at a time, the SLO can selectively use light reflected parallel to the incident beam to create the image, thereby reducing the effects of scattered light and increasing image contrast (Fig. 1.8).

The routine frame rates achievable by the SLO depend on the raster speed and area covered, which is usually in the range of 30 fps. SLO offers a better visualization
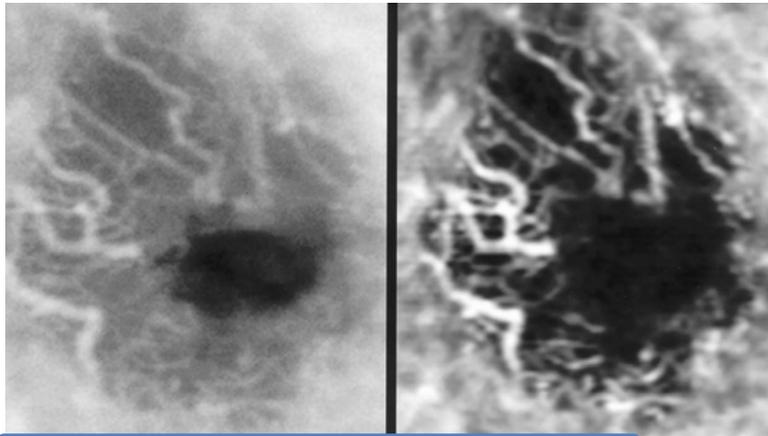
Fig. 1.8: A comparison of retinal angiographic images obtained by fundus camera (left) and scanning laser ophthalmoscope or SLO (right). The SLO images depict a much higher contrast between the vessels and background compared to the fundus camera due to the lower amount of intraocular scattering. (Adapted from: Lawrence et al American Journal of Ophthalmology (2004) 137(3): 511).

of the peripheral retina by increasing the field of view to about 200 degrees, albeit at a loss of temporal resolution. However, due to the limitation of the size of the scanning laser, the best resolution of the SLO is worse off than the best fundus photograph. Despite these disadvantages, SLOs are fast becoming a standard in fundus photography due to the far superior image contrast.

1.3.5 Retinal Ultrasonography

All the above techniques for retinal diagnosis depend on a clear optical pathway. Frequently though, the optical path is obstructed by cataract in the lens or by hemorrhages into the vitreous humor. In such cases, the visualization of the retina by optical methods is hampered and reliance on other techniques is needed. One of the earliest techniques used to overcome the opacity of the media was ultrasonography [56]. Ultrasound is transparent to most lesions in the eye; however, sometimes there can be an

increased absorbance to sound waves like in severe cataract. B-scan or two-dimensional ultrasonography (Fig. 1.9) is sometimes used even if the pathology is clearly visible in an ophthalmoscopic examination to differentiate, for example, between intraocular tumors, various choroidal and retinal detachments.

The ultrasound is generated from a hand-held probe held in contact with the eye. As the sound propagates through the various tissue layers of the anterior and posterior segment of the eye, some portion of the sound is reflected backwards, where it is then detected by the same probe. The time delay between transmission of the ultrasound pulse and reception of the echo is proportional to the distance of the interface from the probe. The amplitude of the reflected ultrasound or echo depends on the differences in impedances to sound propagation of the various tissue layers. For instance, while fluids may have low impedance to sound waves, bone has high impedance, and a strong echo is reflected from a tissue-bone interface. The way the reflected echo is displayed depends on the mode of operation of the machine. In A-mode scanners, the amplitude of the echo is displayed as a peak from a baseline and in B-mode scanners the amplitude information is displayed as the brightness of the pixel. Therefore, A-mode scanners are essentially one-dimensional, whereas B-mode scanners can display a two-dimensional image by changing the direction of the ultrasound.

As the insonation frequency of the ultrasound increases its tissue penetration decreases, but the resolution of the image that can be produced increases. The average diameter of the adult human eye is about 25 mm and therefore the retina can be imaged with relatively high frequencies compared to visceral organs. Ophthalmic ultrasonography uses sound waves in the frequency range of 5-50 MHz. A 50 MHz probe

can produce B-scan images with a resolution of 50 μm; however the penetration is limited to 5 mm. Therefore, such high resolution ultrasonography of the eye is limited to imaging the
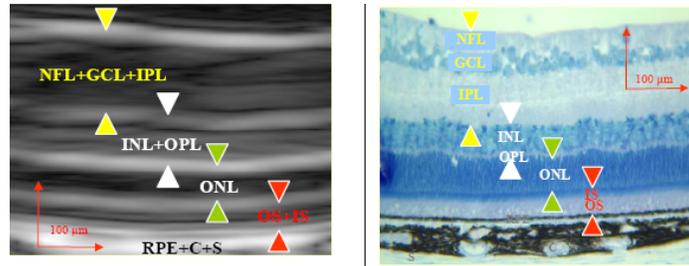
Fig. 1.9: B-scan ultrasonography of a rat retina obtained by using an 80 MHz probe, compared with the corresponding histological section. The ultrasonography image shows high reflectivity at the interface between the various layers. (Adapted from: C. Jolly et al. Experimental Eye Research 81 (2005) 592–601)

anterior segment and peripheral retina [57]. A better coverage of the entire retina can be achieved by using a lower frequency like 5-10 MHz, albeit at resolutions unusable for efficient structural imaging of the retina. Figure 1.9 shows comparison of retinal layer interfaces imaged using an 80MHz ultrasound at an in-plane resolution of 20 μm with histology in rats due to their small size of about 6 mm [58].

Doppler shifts in ultrasound echo frequencies when reflected of moving blood corpuscles has been used effectively to image blood velocities. In order to produce a Doppler shift, the cosine of angle of incidence of the ultrasound and direction of blood flow should be non-zero. In the eye, with the ultrasound probe placed on the cornea, the general angle of incidence is very close to, if not 90 degrees, giving rise to a very small Doppler shift and inefficient blood flow calculations. Furthermore, this technique also suffers from the resolution disadvantage at differentiating between the retinal and choroidal vessels. Doppler ultrasound has been effective in blood-flow calculations in the ophthalmic and central retinal vessels.

Recent advances in ultrasound contrast agents, and sub- and super-harmonic imaging could potentially provide ways for imaging the retinal and choroidal blood

vessels with high contrast as well as low background noise [59-61]. Ultrasound contrast agents are surfactant stabilized microbubbles which increase the reflectance of blood when injected into the blood stream; improving the signal-to-noise ratio. It has also been observed that due to the non-linear nature of reflectance of these microbubbles, the echo from them contain a higher proportion of harmonics of the insonation frequency. Therefore, imaging using these higher harmonics, one could potentially envision ways for imaging the retina at high resolution and signal-to-noise ratios.

1.3.6 Optical Coherence Tomography (OCT)

Light, just like ultrasound, penetrates into the tissue, and is reflected by boundaries between the layers of different refractive indices. The direct detection of individual echo and their timings in normal tissue is difficult due to the extremely high velocity of light compared to the detectors time resolution. However, interference of two beams of light can be used to detect the relative distance traveled by them, as the interference is maximal when the two beams have traveled roughly the same distance (coherence distance). The coherence distance is very small for a broad band source of light. Therefore, OCT uses the interference from two broad-band light beams, one reflected from different layers of the tissue to be imaged, and the other, a reference beam, reflected by a mirror, to obtain images at micrometer resolution (time-domain OCT). Strong interference can be obtained for every region in the tissue that reflects light by scanning the mirror back and forth. Therefore, the position of the mirror is indicative of the position of the interface reflecting the light [62]. A cross-sectional OCT can be obtained by performing a series of these time-domain OCTs (single-point scanning

system). Alternatively, the full field of view of the sample is illuminated by a light beam and interference pattern of individual pixels recorded on a CCD (parallel OCT).

Due to the ease of penetration of light in the retina (clear optical path), and the high resolutions that can be obtained by using a broad band light source, OCT is ideally suited for anatomical imaging of the retina (Fig. 1.10). The axial and lateral resolutions achievable by an OCT operating with a super luminescent diode at 840 nm are 10 and 70 μm respectively [63]. For these reasons, OCT has been used extensively in retinal-thickness measurements, as well as to detect gross anatomical abnormalities like age-related macular degeneration, macular holes, edema, cysts, retinal detachments, RPE tear and gross choroidal neovascularization.
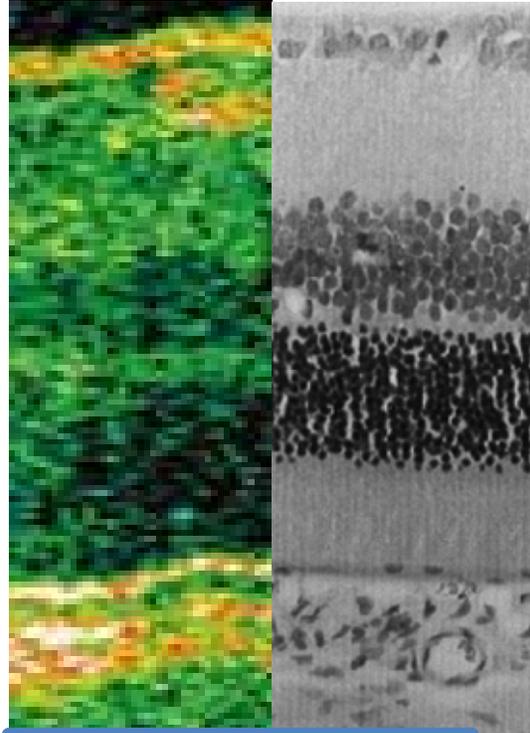
Fig. 1.10: A comparison of Optical Coherence Tomography (left) of the retina with histology (right). OCT depicts the boundaries of the tissue layers with high reflectivity (red, yellow and white colors). Scalebar is 50 μm. (Adapted from vitreous-retina-macula consultants of New York website, and Cringle and Yu, Comp Biochem Physiol A Mol Integr Physiol. 132:61-6)

The main disadvantage of the OCT is that the technique is limited by the transparency of the media. Presence of cataract hemorrhages and tumors preclude the use of OCT. Furthermore, most of the light is reflected back from the tissue interfaces and OCT mainly detects the most obvious tissue boundaries, and its diagnostic capabilities

are limited to changes to tissue boundaries. OCT to date is also not capable of detecting blood flow information, and lacks functional capabilities.

1.3.7 Electroretinography (ERG) and Electrooculography (EOG)

ERG is an electrophysiological test of the retina to measure its functional response as a whole or its parts. Action potentials generated from a stimulus travels through the retinal neurons to create an electric field that can be measured by electrodes placed on the cornea and the skin near the eyes. These electrical signals are then analyzed for their amplitude (usually in μV) and timings (in milliseconds after a stimulus) to detect the effects of various disease conditions like retinal tears and retinitis pigmentosa.

A white-light stimulation flash elicits response from both the rod and cone photoreceptor and is seen in the ERG as a large negative wave, called the a-wave [64]. The rod response can be separated if the flash used for stimulation is very dim, and sufficient time has been provided for dark adaptation. The a-wave lasts for approximately 10-12 ms, and soon becomes dominated by the high-amplitude b-wave. The b-wave is thought to reflect the health of the ON-bipolar cells and the Muller cells. Oscillatory potentials are often seen in the rising phase of the b-wave and are thought to reflect the amacrine cell activity.

A bright-flash stimulus to a non-adapted eye is sometimes used to detect response generated from the cones alone. In this case, the ERG recorded lasts for a much shorter time, with the amplitude response also reduced. Color filters can be used to separate the response of each type to cone. Sometimes a 10-30 Hz flicker is used instead of a single flash.

The ERG a provides unique opportunity for early diagnosis of diseases like retinitis pigmentosa before symptoms can be noticed through routine retinal examination. It can also help evaluate the extent of retinal damage in disease. However, it is estimated that over 20% of the retina has to be affected for the ERG to start showing abnormalities. To overcome this shortfall, multifocal ERG (mfERG) has been developed, where a focal stimulus is applied to different parts
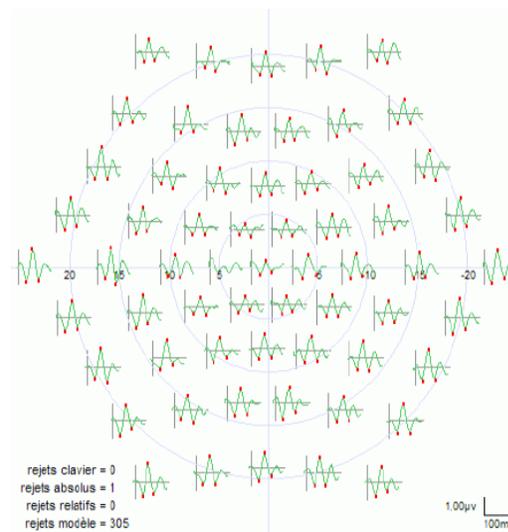
Fig. 1.11: Multifocal ERG represented on a diagrammatic representation of the retina with the macular region in the center. Concentric circles represent distance from the fovea in mm. (Adapted from www.metrovision.fr)

of the retina and ERGs recorded after each stimulus. This technique provides a two dimensional map of the retinal function, and detect small regions of retinal abnormalities as shown in Fig. 1.11.

EOG measures the standing potential between the cornea and the retina [65, 66]. In the inverted retina of vertebrates, the cornea is slightly positive with respect to the retina. This potential changes when the eye is exposed to normal light conditions as compared to dark adaptation, and is thought to be due to the hyperpolarization of the vast number of photoreceptor cells at the back of the eye. Although this standing potential difference between the front and back of the eye is distributed over many membranes of the retina, an intact RPE is most responsible for it [67, 68]. Therefore, the rise in EOG potential after illumination requires a normal RPE as well as normal mid-retinal function.

This standing potential acts like an electric dipole pointed roughly in the direction of the visual axis. The potential is then measured by placing electrodes on the nasal and temporal corners of the eyes, and recorded as the eye moves from side to side. These changes
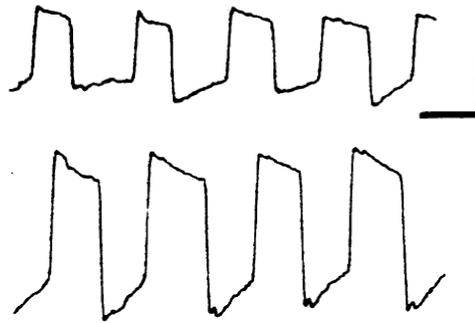
Fig. 1.12: Standing potential (EOG) measured from a normal eye as it moves between two fixed points after 12 mins of dark adaptation (top) and after 8 mins of re-illumination (bottom). Scale bar: 500 μV; 500 ms. (Adapted from Arden and Kelsey, J. Phyiol. (1962), 161, pp. 189-204)

in potential measured at the electrodes can reflect the standing potential of the eye if eye movements of constant amplitudes are made (Fig. 1.12). A normal eye has an EOG amplitude ratio between light and dark of about 2, and a ratio less than 1.7 is considered abnormal.

The entire study in this case takes about 20 minutes, and is affected adversely by any movement of the head, as the amplitude of the eye movement has to be kept constant throughout the study. Furthermore, most retinal disorders producing an abnormal EOG will usually produce an abnormal ERG, and ERG can provide better information from individual retinal layers. EOG is widely used to diagnose Best's vitelliform macular dystrophy and variants of this disease in which the ERG is normal but the EOG is abnormal. This is due to a mutation in the VMD2 gene that encodes a chloride channel in the RPE and causes the abnormal EOG, without affecting the retinal response to a stimulus.

As seen in this section, current techniques in retinal imaging and diagnosis rely heavily on the clarity of the optical pathway. Conditions such as cataract and hemorrhages preclude the use of commonly used diagnostic techniques. Furthermore, multiple techniques may be required for separate anatomical and functional diagnosis. Magnetic resonance Imaging (MRI), on the other hand, has long been used effectively for both anatomical and functional imaging of the brain, albeit at much lower resolution. Contrast agents used with MRI can improve the sensitivity and specificity of the images. We, therefore, sought to apply the principles of high resolution MRI to study the structure and function of the retina, in normal and diseased rats.

Part 2- Magnetic Resonance Imaging

1.4 MRI – Brief Introduction

MRI is based on the principles of nuclear precession and relaxation. MRI uses a powerful external magnetic field, smaller magnetic field gradients and radio frequency (RF) waves tuned to specific frequency to align and then selectively excite the nucleus of atoms in the region of interest. These excited nuclei then relax back to their equilibrium state, dissipating energy and inducing a signal, which is then detected, amplified and processed to obtain images. Routine MRI measures the relaxation properties associated with the proton in the hydrogen atom, because it is the most abundant element in the human body.

1.4.1 Quantum mechanical properties of particles

Subatomic particles like protons, neutrons and electrons have an intrinsic spin associated with them, which gives rise to spin angular momentum (*l*). Some of these particles, like protons and electrons, also have an associated charge. The spin of these charged particles gives rise to a magnetic moment, analogous to a moving charge giving rise to a magnetic field. The nuclear magnetic moment is pointed parallel to the direction of its angular momentum.

The magnetic moments of subatomic particles can interact with external magnetic fields. Stern and Gerlach in the early 1920s showed that a beam of electrons were deflected by a very specific amount in a non-uniform magnetic field. This uneven distribution of deflection could not be explained by classical physics, where the angular momentum, and hence the magnetic moment of the electron is expected to be random, and an evenly distributed deflection. Ronald Fraser, later, explained this observation by quantizing the values of the spin angular momentum of the particle.

In quantum mechanics, the spin quantum number of a particle is directly proportional to its spin angular momentum. The magnitude of the angular momentum is a vector quantity given by

$$\left|\overline{P}\right| = \hbar * \sqrt{l*(l+1)} \, , \tag{1.1}$$

where $\hbar$ is Plank's constant divided by 2π. The direction of the vector is also quantized and can orient in only $(2l+1)$ ways, such that its projection on any fixed axis can take on values between $-l$ and l with integer steps, i.e., $-l\hbar$, $(-l+1)\hbar$, … $l\hbar$. This component of angular momentum along a fixed axis is called the magnetic quantum number and denoted by m_I. Therefore, m_I can take the values

$$m_I = -l,(-l+1),...(l-1),l \tag{1.2}$$

For example, for a spin-½ particle like a proton or an electron, the magnetic quantum number m_I can have values of -½ or ½, i.e., it can have only two possible orientations in space.

In an atom, the spins from similar subatomic particles will pair up in nuclear energy levels in an anti-parallel fashion, with one spin-up particle canceling the effects of the spin-down particle. The net spin of a nucleus, therefore, is the sum of the unpaired proton and neutron in the nucleus. In the case of the electron, the net spin is the number of unpaired electrons in all the electronic orbitals. As with electrons, the nucleons occupy specific energy inside the nucleus which get filled in a specified order. Therefore, it is possible for nuclei of some elements to have a net spin which exceeds one, similar to the total electronic spin. For example, Na has a net nuclear spin of 3/2, while hydrogen with one proton has a net nuclear spin of ½.

The net magnetic moment of a particle is proportional to its angular momentum and given by

$$\mu = \gamma P,$$ (1.3)

where γ is a constant for each type of particle, called the magnetogyric ratio. As seen in the above equation, the magnetogyric ratio is proportional to the ratio of magnetic moment to the angular momentum. Since the magnetic moment is proportional to the charge of the particle and the angular momentum to the mass of the particle with all other conditions being constant, the magnetogyric ratio is proportional to the charge to mass ratio of the particle. Since electrons and protons have similar but opposite charge and the mass of the electron is much smaller than that of the proton, the magnetogyric ratio

(divided by 2π) of the electron is 176.1 GHz/T, and that of a proton is about 42.56 MHz/T.

1.4.2 Larmor frequency

When an ensemble of charged particles is placed inside an external magnetic (B_0) field oriented along, say, the z-axis of a Cartesian coordinate frame, the magnetic dipole of the particle aligns itself with respect to B_0. This results in a net magnetization of the ensemble of nuclei which can be given by

$$M = \chi B_0 ,$$
(1.4)

where χ is the susceptibility of the sample and M is the magnetization produced in the ensemble. For example, 1cc of water placed in a 1T magnetic field at room temperature produces a field of 34 nT in the sample. This field is very small to be measured directly. MRI, on the other hand, exploits the differences in energy levels between the spins aligned parallel and anti-parallel to the external field for image formation. This implies that MRI can detect signal from elements that have unpaired protons in their nucleus. This includes elements, for example, like hydrogen, deuterium, carbon-13, sodium-23, fluorine. However, since the human body is almost 80-90% water and fat, hydrogen is the most abundant element that can be measured by MRI.

When spin-½ nuclei align with the external magnetic field in parallel and anti-parallel fashion, each orientation is associated with a different energy level. This is called Zeeman splitting, and the energy of a particular level is

$$E = -\hbar \gamma m_I B_0 .$$
(1.5)

The energy states associated with spin-½ particles are $\dfrac{-\hbar\gamma B_0}{2}$ and $\dfrac{\hbar\gamma B_0}{2}$, with the lower energy being associated with particles aligned parallel to the external magnetic field. Furthermore, the energy difference between two states is directly proportional to the external magnetic field, and is given by

$$\Delta E = \hbar\gamma B_0. \tag{1.6}$$

The transition between high energy and low energy levels can be achieved by the absorption or dissipation of a photon of energy equal to the difference in energy. As the energy of a photon is given by E=$h\nu$, where ν is the frequency of the RF, then

$$h\nu = \hbar\gamma B_0. \tag{1.7}$$

Since, $\hbar = \dfrac{h}{2\pi}$, then

$$\nu = \frac{\gamma}{2\pi}B_0 \ \text{ or } \ \omega = \gamma B_0. \tag{1.8}$$

The frequency of the RF that matches the energy-level difference between the two states causes a transition between one state to the other.

1.4.3 Equilibrium magnetization and precession

The energy difference in the Zeeman splitting implies that there is a higher number of spins in the lower energy state, so as to minimize entropy. The relative population of the spins in each orientation is given by Boltzmann's distribution. If N_α and N_β are the number of nuclei in the lower and upper energy levels, respectively, then the population difference between the two energy states can be shown to be

$$\Delta n = \frac{N_T \Delta E}{2kT}, \qquad (1.9)$$

where N_T is the total number of spins in the sample ($N_\alpha + N_\beta$), ΔE is the difference in energy between the two states, k is Boltzmann's constant and T is the absolute temperature of the sample. Substituting the equation for ΔE gives

$$\Delta n = \frac{N_T \gamma \hbar B_0}{2kT}. \qquad (1.10)$$

The total magnetization (M) of the sample is

$$M = \Delta n \mu_z, \qquad (1.11)$$

where μ_z is the z-component of the magnetic moment of each spin in the lower energy state. For spin-½ nuclei, $\mu = \frac{1}{2}\gamma\hbar$ and

$$M = \frac{N_T \gamma^2 \hbar^2 B_0}{4kT}.$$

From a classical point of view, a particle of non-zero spin not only aligns itself with respect to the external magnetic field, but also precesses around it (Fig. 1.13). The external magnetic field excerts a torque on the magnetic dipole [69, 70] of the nucleus, given by

Fig. 1.13: Schematic diagram of single nuclear magnetic moment in an external magnetic field B_0.

$$T = [\vec{\mu} \times \vec{B}_0] = \frac{d\vec{P}}{dt}. \qquad (1.12)$$

Based on this definition, it is evident that the torque will act perpendicular to the plane containing both $\vec{\mu}$ and $\vec{B}_0$. Therefore, in the event that they are not aligned, the nuclear spin must precess about the external magnetic field (B_0) as shown in Fig. 1.13.

By definition, from Eq. 1.3,

$$\vec{\mu} = \gamma \vec{P}.$$

Therefore, $\dfrac{d\vec{\mu}}{dt} = \gamma[\vec{\mu} \times \vec{B}_0] = -\gamma \vec{B}_0 \times \vec{\mu} = -\gamma B_0 \mu \sin\theta$ \hspace{2cm} (1.13)

From the geometry shown in Fig. 1.13, $d\vec{\mu}$ can be defined as $\mu \sin\theta\, d\varphi$ where $d\varphi$ is the small distance traveled by the spin in small time dt. Or $d\varphi = \omega_0 dt$, where, ω_0 is the angular frequency of the presessing spin. Therefore, the two equations can be rewritten as

$$-\gamma B \mu \sin\theta\, dt = \mu \sin\theta\, \omega_0 dt$$

$$\text{or, } -\gamma B = \omega_0. \hspace{2cm} (1.14)$$

This is referred to as the Larmor equation and the expression is identical to that obtained by calculating the quantum energy required to induce a spin transition from the lower to the upper energy level. Therefore, the Larmor frequency is the frequency of precession of the spins about the external magnetic field. For an ensemble of spins, the relative positions of the precessing magnetic moments with
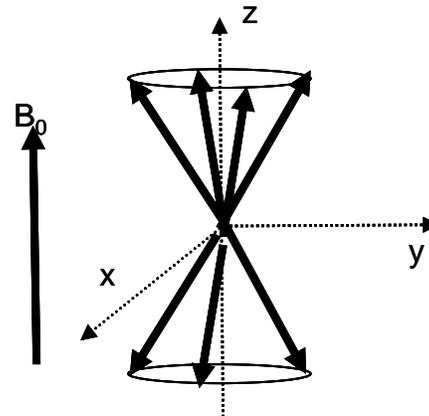
Fig. 1.14: Schematic diagram showing individual nuclear magnetic moments precessing about an external magnetic field B_0.

respect to each other is random, consequently there is no net magnetization in the x-y plane and the equilibrium net magnetization points in the z-direction (Fig. 1.14), due to the population difference between the two orientations.

1.4.4 Time-varying magnetic field

In addition to the constant magnetic field B_0, if a time-varying magnetic field B_1 is applied in a direction perpendicular to the z-axis, the magnetic field variations would be given by

$$B_1(t) = B_1 \cos \omega t \hat{i} - B_1 \sin \omega t \hat{j} . \qquad (1.15)$$

Each Cartesian component of the total B field is then given by

$$B_x(t) = B_1 \cos \omega t , \text{ and } B_y = -B_1 \sin \omega t \text{ and } B_z = B_0 . \qquad (1.15a)$$

Applying the equation for torque, $\dfrac{dM}{dt} = \gamma M \times B$

$$M \times B = (M_y B_z - B_y M_z)\hat{i} - (M_x B_z - B_x M_z)\hat{j} + (M_x B_y - B_x M_y)\hat{k} \qquad (1.16)$$

Therefore,

$$\frac{dM_x}{dt} = \gamma B_0 M_y + \gamma B_1 \sin \omega t M_z$$

$$\frac{dM_y}{dt} = -\gamma B_0 M_x + \gamma B_1 \cos \omega t M_z$$

$$\frac{dM_z}{dt} = -\gamma B_1 (\sin \omega t M_x + \cos \omega t M_y) \qquad (1.17a,b,c)$$

It can be seen that the change in M_x and M_y depends not only on the equilibrium state of magnetization B_0, but also the strength of the applied RF field and its frequency ω. The change in M_z though depends only on the applied RF amplitude and frequency. Furthermore, if we define the initial condition as the net magnetization of the sample pointing along the z-direction, i.e., $M(0) = M_0 \hat{k}$, then the solutions to the above differential equations become

$$M_x(t) = M_0 \sin \omega_1 t \sin \omega_0 t$$
$$M_y(t) = M_0 \sin \omega_1 t \cos \omega_0 t \qquad \text{(1.18a,b,c)}$$
$$M_z(t) = M_0 \cos \omega_1 t$$

To better understand the effect of the RF, it is assumed that there is a reference frame that is rotating about the z-axis or B_0 at an angular velocity of ω. For a particle in an external magnetic field B_0, the angular momentum becomes

$$\vec{M} = M_x \hat{i} + M_y \hat{j} + M_z \hat{k}.$$
$$\frac{d\vec{M}}{dt} = M_x \frac{\partial \hat{i}}{\partial t} + \hat{i} \frac{\partial M_x}{\partial t} + M_y \frac{\partial \hat{j}}{\partial t} + \hat{j} \frac{\partial M_y}{\partial t} + M_z \frac{\partial \hat{k}}{\partial t} + \hat{k} \frac{\partial M_z}{\partial t}, \qquad \text{(1.19a,b)}$$

where, i, j and k are unit vectors in the rotating frame of reference. Rearranging the terms,

$$\frac{d\vec{M}}{dt} = \left(\hat{i} \frac{\partial M_x}{\partial t} + \hat{j} \frac{\partial M_y}{\partial t} + \hat{k} \frac{\partial M_z}{\partial t} \right) + \left(M_x \frac{\partial \hat{i}}{\partial t} + M_y \frac{\partial \hat{j}}{\partial t} + M_z \frac{\partial \hat{k}}{\partial t} \right). \qquad \text{(1.20)}$$

The term in the first parenthesis is the rate of change of M in the rotating frame. The second term is the rate of change of the unit vectors and can be rewritten in terms of the angular velocity of the rotating frame ω. Therefore,

$$\left(\frac{dM}{dt} \right)_{lab} = \left(\frac{\partial M}{\partial t} \right)_{rot} + M_x \vec{\omega} \times \hat{i} + M_y \vec{\omega} \times \hat{j} + M_z \vec{\omega} \times \hat{k} \qquad \text{(1.21)}$$

$$\left(\frac{dM}{dt} \right)_{lab} = \left(\frac{\partial M}{\partial t} \right)_{rot} + \vec{\omega} \times \left(M_x \hat{i} + M_y \hat{j} + M_z \hat{k} \right) \qquad \text{(1.22)}$$

$$\left(\frac{dM}{dt} \right)_{lab} = \left(\frac{\partial M}{\partial t} \right)_{rot} + \vec{\omega} \times \vec{M}. \qquad \text{(1.23)}$$

Since $\dfrac{dM}{dt} = \gamma M \times B_0$, then

$$\gamma M \times B_0 = \left(\frac{\partial M}{\partial t} \right)_{rot} + \vec{\omega} \times \vec{M} \qquad \text{(1.24)}$$

$$\left(\frac{\partial M}{\partial t}\right)_{rot} = -\gamma \hat{M} \times B_0 + \vec{\omega} \times \vec{M} \qquad (1.25)$$

$$\left(\frac{\partial M}{\partial t}\right)_{rot} = \gamma \hat{M} \times \left(B_0 + \frac{\vec{\omega}}{\gamma}\right). \qquad (1.26)$$

Therefore, comparing with the equation in the laboratory frame, the effective magnetic field seen by the nuclei is

$$B_{eff} = B_0 + \frac{\vec{\omega}}{\gamma}. \qquad (1.27)$$

If the rotating frame of reference has an angular velocity equal to that of the Larmor frequency, then, as per the Larmor equation, $\frac{\omega_0}{\gamma} = -B_0$ or $B_{eff} = 0$. Under this condition, if the RF field B_1 is applied, the nuclei will see only the B_1 field [69, 71], i.e.,

$$\left(\frac{dM}{dt}\right)_{rot} = \gamma M \times B_1. \qquad (1.28)$$

If the B_1 is applied along the x- or y-axis, the net magnetic moment of the sample would tilt away from the z-axis and start precessing about B_1. The amount of rotation therefore can be controlled by changing the duration or the amplitude (B_1) of the RF pulse. If the RF pulse rotates M by 90 degrees into the x-y plane, then the pulse is referred to as a 90 degree RF pulse. If the RF pulse rotates the magnetization so that it is aligned with the –z axis then it is referred to as a 180 degree RF pulse and so on.

1.4.5 Relaxation and signal detection

When the magnetization vector M is deflected from the z-axis, and then the RF is turned off, the magnetization tends to return to its original state through a process called spin-lattice or T_1 relaxation. This process involves the exchange of energy between the

individual spins and their surroundings (the "lattice"), and hence the name. This is because an individual nucleus in a sample placed in B_0 also undergoes a myriad of rotational and vibrational thermal motions. Such movements of one nucleus affect the magnetic field seen by its nearby nuclei. Therefore, the field experienced by any nucleus will fluctuate over time. Of all the microscopic fluctuations in magnetic field seen by a nucleus, any fluctuations at or near the Larmor frequency will directly affect the nucleus by causing a change in its energy state. Therefore, this relaxation depends not only on the
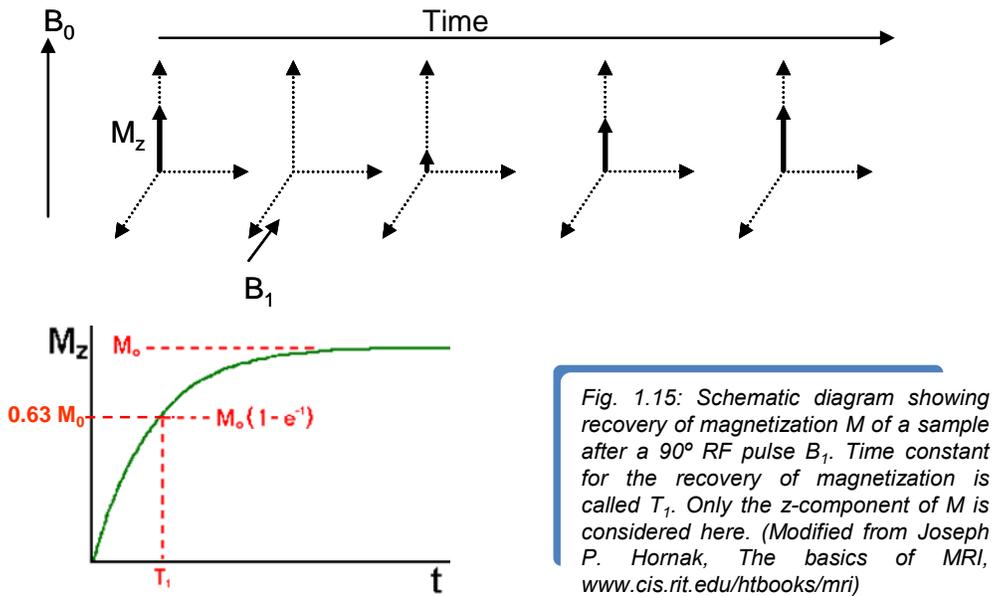
Fig. 1.15: Schematic diagram showing recovery of magnetization M of a sample after a 90° RF pulse B_1. Time constant for the recovery of magnetization is called T_1. Only the z-component of M is considered here. (Modified from Joseph P. Hornak, The basics of MRI, www.cis.rit.edu/htbooks/mri)

temperature and viscosity of the sample but also its Larmor frequency (which depends on the magnitude of the external magnetic field), as well as the size of the molecule that contains the nuclei. The T_1 relaxation rate is given by the equation

$$\frac{dM_z}{dt} = -\frac{(M_z - M_0)}{T_1},$$ (1.29)

Where, T_1 is the relaxation rate constant of the sample (Fig. 1.15).

The spins are not only affected by the energy variations in the lattice but also by local inhomogeneities in the B_0 field. Consider an ensemble of particles exposed to a 90

Fig. 1.16: Schematic diagram showing loss of transverse magnetization M_{xy} of a sample after a 90° RF pulse B_1. Time constant for the decay of the transverse magnetization is called T_2. Only the xy-component of M is considered here in a rotating frame of reference. (Modified from Joseph P. Hornak, The basics of MRI, www.cis.rit.edu/htbooks/mri)
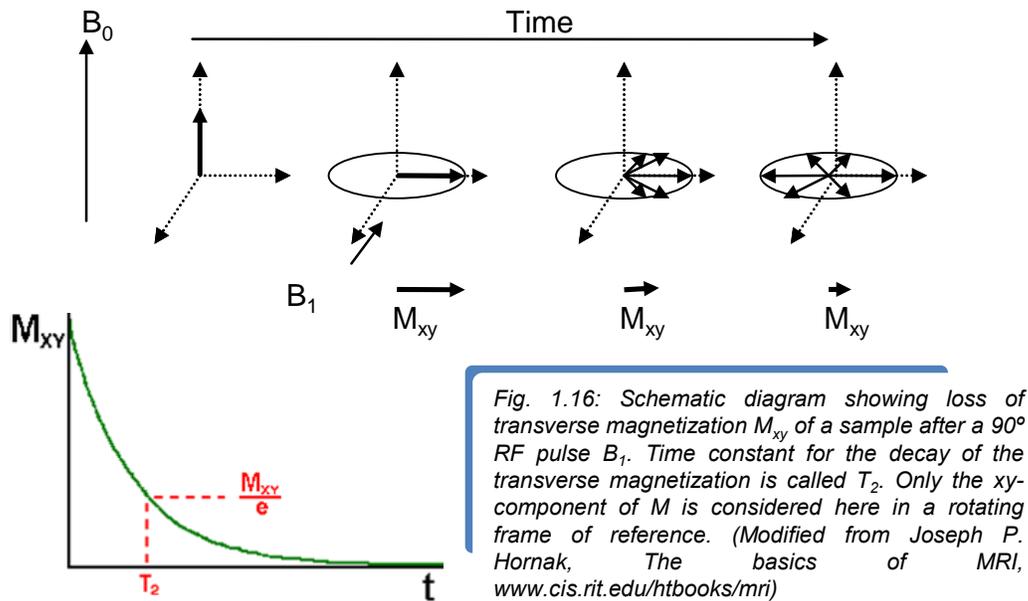
degree RF pulse. After the pulse, all the spins in the sample are in the x-y plane, are phase coherent, and precessing about the external magnetic field B_0. However, local magnetic field inhomogeneities, differences in tissue susceptibilities and magnetic field fluctuations due to the thermal motion of neighboring nuclei cause each nucleus to experience a slightly different magnetic field. These microscopic differences in magnetic field, as seen by the different nuclei in an ensemble, results in each nucleus having a slightly different Larmor frequency. Therefore, the various nuclei of the ensemble precess around B_0 at slightly different frequencies, causing a loss of phase coherence, and thus eventual loss of the total magnetization in the x-y plane (Fig. 1.16). This signal detected in the x-y plane is called the free induction decay (FID) and this type of relaxation is called the spin-spin or transverse relaxation (Fig. 1.17).
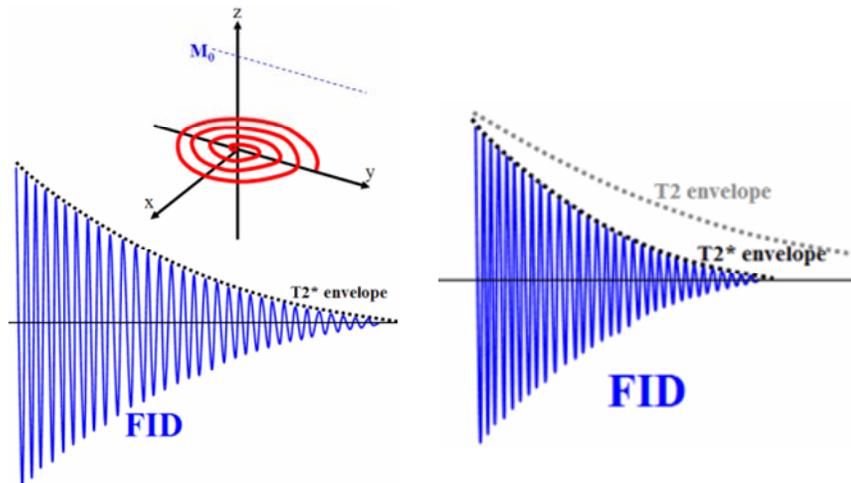
Fig. 1.17: Schematic diagram showing loss of transverse magnetization Mxy of a sample after an RF pulse. The Mxy magnetization induces a current in the coil placed perpendicular to B0. Local inhomogeneities in the B¬0 magnetic field cause a faster decay of the signal than if the sample and magnet were absolutely uniform

The effects of intrinsic tissue spin-spin relaxation and that due to external magnetic field inhomogeneities and tissue susceptibility can be analyzed separately. The time constant for the intrinsic transverse relaxation is denoted as T_2 and the combined effect of T_2 relaxation and that due to magnetic field inhomogeneities is called the T_2* relaxation time.

Therefore, the equation for the time rate of change of magnetization in the x- and y-axis can be rewritten as

$$\frac{dM_x}{dt} = -\frac{M_x}{T_2} \text{ and } \frac{dM_y}{dt} = -\frac{M_y}{T_2}. \qquad (1.30a,b)$$

The equations for magnetizations are modified by the relaxation terms as follows:

$$M_x(t) = M_0 \sin\theta \sin(\omega_0 t) e^{\frac{-t}{T_2}}$$

$$M_y(t) = M_0 \sin\theta \cos(\omega_0 t) e^{\frac{-t}{T_2}} \qquad (1.31a,b,c)$$

$$M_z(t) = M_0 \left[1 - (1 - \cos\theta) e^{\frac{-t}{T_1}} \right]$$

This magnetization signal can be detected by placing a RF coil in the x-y plane, sensitive to magnetization that is perpendicular to B_0. MRI exploits the differences in T_1 and T_2 relaxation times of different tissue to achieve image contrast [72].

1.4.6 Localization of signal in MRI and image formation

An MR image has been described to be the graphical representation of a two-dimensional slice through the sample [73]. However, in all the above illustrations, it has been assumed that the sample is placed in a uniform magnetic field, and that the applied RF field excites the entire sample uniformly. This would give rise to a uniform signal from the entire sample. In order to localize the signal from each point of the sample (also called voxel or volume element in the sample) MRI uses magnetic field gradients applied across the sample in addition to B_0 [73].

Consider a linear magnetic field gradient applied along the z-axis in addition to B_0. This would cause a linear variation in the Larmor frequency of the spins along z-axis. Under this condition, if an RF pulse of a specific bandwidth were applied, only selected spins at a particular section along the z-axis would be rotated, where the Larmor frequency equals the applied RF frequency. Therefore, any signal induced in the receiver coil would arise from this two-dimensional slice of spins. This gradient is called the slice-select gradient and the process is called slice selection.

Localization of spins within the slice is done by two additional gradients, in the x- and y-axis directions, which are switched on and off at specific times during the MRI pulse sequence. If the FID is acquired while playing out a gradient along the x-axis (say), then the spins along different points in the x-axis will have a different frequency. Calculating the signal magnitude at each frequency will therefore give the position and number of nuclei at each position along the x-axis. This gradient is called the readout gradient and the process encodes the position of the nuclei in the frequency of the signal.

Finally, to locate the signal strength along the y-axis, phase encoding is used. Another gradient applied along the y-axis is turned on for a short period of time after the RF pulse but before signal collection. This causes the spins along the y-axis to precess faster for the duration of the gradient. The rate of precession will depend upon the position of the nuclei along the phase-encoding axis. After the gradient is switched off, the spins along the y-axis will have accumulated a phase shift that is unique to the position of the spin along the phase-encoding axis. To detect this phase shift, multiple signal acquisitions are required, each time with a different amplitude of the gradient applied along the y-axis.

The signal acquired by the coil with a readout gradient and with different phase encode steps is digitized and arranged in a two-dimensional matrix referred to as the k-space [74]. The signal acquired can then be represented as

$$S(t_x, t_y) = \iint \rho(x, y) \exp\left[i\gamma(G_x x t_x + G_y y t_y)\right] \tag{1.32}$$

where $\rho_{x,y}$ is the spin density at (x,y), G_x is the gradient applied along x-direction for time t_x and G_y is the gradient applied along the y-direction for t_y. A two-dimensional inverse

Fourier transform will therefore recover the actual spatial distribution of spins within the two-dimensional slice through the sample, and thus form the image.

1.4.7 Pulse sequences

It is clear from the last section that multiple signal acquisitions are required for the formation of a complete two-dimensional image. Therefore, the sequence of events required for the simplest image would be: (1) a slice-selective RF pulse that tips the magnetization into x-y plane; (2) a phase encode gradient applied as soon as the RF is turned off; and (3) a readout gradient applied simultaneously with the acquisition of the signal. Such a sequence of events is called the pulse sequence.

In most biological tissues, the T_2^* decay of the signal is rapid, which implies the gradients need to be applied in rapid succession for the receiver to detect substantial
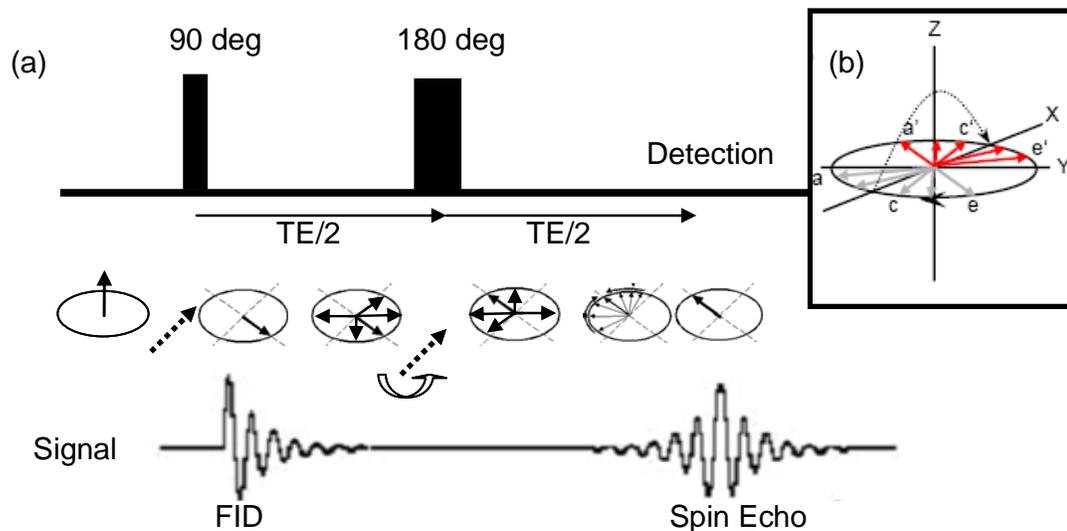
Fig. 1.18: (a) Schematic diagram of signal formation during a spin-echo pulse sequence. The magnetization is rotated around the x-axis using a 180° RF pulse causing the individual spins to rephrase forming an echo in time TE, as shown. (b) Inset shows a close up of the effect of a 180° pulse applied along the y-axis. The spins a, c and e have been flipped around the y-axis, the direction of B_1, to their new positions of a', c' and e', respectively, causing phase reversal. (Modified from Joseph P. Hornak, The basics of MRI, at www.cis.rit.edu/htbooks/mri)

amounts of signal. Furthermore, the application of the readout gradient creates its own magnetic field inhomogeneity, and causes extremely rapid decay of the signal. It is therefore desirable to design a pulse-sequence that allows acquisition of the entire signal in order to increase the amount of information acquired. This is routinely achieved in MRI pulse sequences by using a phenomenon called the echo [75].

In spin-echo and gradient-echo pulse sequences, an echo of the initial FID is produced by rephasing the transverse magnetization. In the spin-echo sequence, a 90 degree RF pulse is first applied, rotating the magnetization into the transverse plane. This magnetization soon dephases due to the T_2* of the tissue. After a specific amount of time, a 180 degree RF pulse is applied which reverses the phase of the nuclear magnetic moments, and causes them to rephrase and generate an echo (Fig. 1.18). The time elapsed between the 90 degree and the 180 degree RF pulse is equal to the time between the 180 degree RF pulse and the peak echo signal. The advantage of this technique is that the signals lost due to static magnetic field inhomogeneities are rephased and recovered. Therefore, the signal lost in time TE is due only to the intrinsic T_2 relaxation time of the tissue.

The spin-echo technique also allows ample time to play out the spatial-encoding gradient before the echo formation. Furthermore, a gradient can be played out in the readout and slice select axis, equal in amplitude and opposite in direction to the readout and slice select gradient, which will compensate the effects these gradients have on dephasing the signal (Fig. 1.19). Therefore, the signal received by the spin-echo technique will have a higher magnitude and is less affected by the local constant field inhomogeneities. A typical spin echo pulse sequence diagram is shown in Fig. 1.19. Note

that the gradient played in front of the 180 degree pulse has the effect of a negative gradient played after the 180° RF pulse. The main disadvantage of this sequence is that the echo time cannot be extremely short, as a 180° RF pulse has a finite duration.
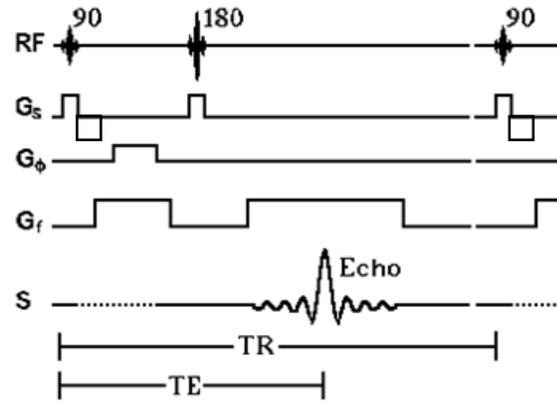
Fig. 1.19 Pulse sequence diagram for spin-echo sequence. (Modified from Joseph P. Hornak, The basics of MRI, at www.cis.rit.edu/htbooks/mri)

Another technique for echo formation is to simply reverse the sign of the readout gradient. This technique eliminates the need for a 180° RF pulse, and thus is capable of achieving extremely short TEs (Fig. 1.20). The echo formed in this technique does not involve phase reversal of the various magnetic moments, but just a reversal of dephasing caused by the readout gradient. This implies that the effects of magnetic inhomogeneities are not rephrased, but contribute to the final signal amplitude. Therefore, the image formed by this technique is T_2* weighted.

The RF pulse applied in a gradient echo sequence need not be a 90° RF pulse. This allows considerable shortening of the time required for TR as the spins experiencing a smaller flip angle will return to their equilibrium state sooner. The RF pulse is generally denoted as an α-degree pulse.
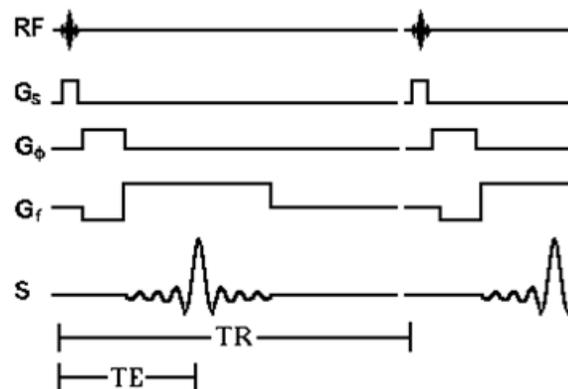
Fig. 1.20: Pulse sequence diagram for a gradient-echo sequence. (Modified from Joseph P. Hornak, The basics of MRI, at www.cis.rit.edu/htbooks/mri)

1.4.8 Image contrast

In tissue, the relaxation time T_1 is much longer than T_2. Therefore, the signal in the x-y plane will decay away much sooner than the recovery of T_1 to its equilibrium value. Furthermore, different tissues in the body have specific T_1 and T_2 relaxation rates at a particular magnetic field. A second 90º pulse applied at a time before the complete T_1 recovery of tissue will give a transverse magnetization which is less than the Boltzmann-equilibrium value M_0. Therefore, the signal is proportional to the T_1 relaxation rate and an image so formed is called a T_1-weighted image. Similarly, if equilibrium is established before the application of the next 90º RF pulse and the time period (TE) before the acquisition of the echo is relatively long, then the signal in the x-y plane will be proportional to the T_2 or T_2* relaxation time of the tissue. If the echo is acquired with long TR but short TE, so that the signal is neither weighted by T_1 or T_2, then the resultant echo strength simply varies according to the density of protons in tissue, and is called a spin-density image (Fig. 1.21).
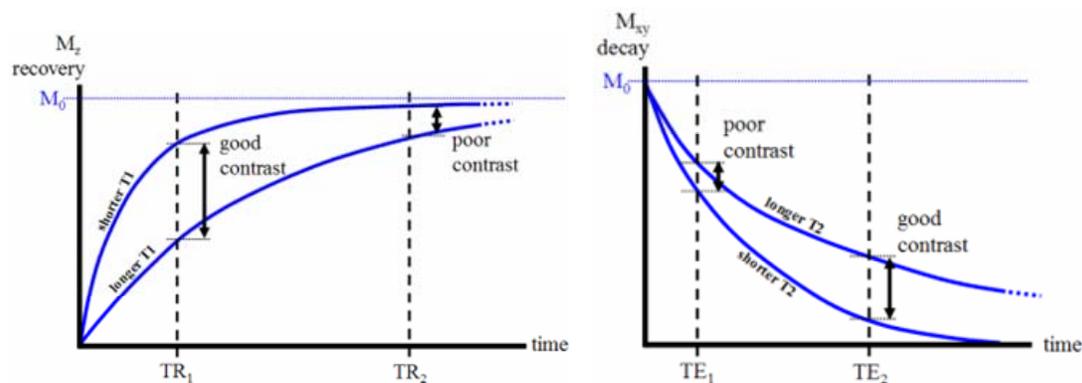
Fig. 1.21: Signal evolution of two hypothetical tissues with different T1 and T2 relaxation times. Signal acquired at time TR1 but with extremely short TE, will show good T1 contrast between the two tissues. Similarly, if TR is suitably long to allow both tissue magnetizations to return to equilibrium, a spin-echo acquired at TE2 will show good T2 contrast between the two tissues. An image taken at long TR and short TE will have signal-intensity proportional to the equilibrium magnetization of each tissue or in other words, the density of spins of each tissue. (Adapted from Joseph P. Hornak, The basics of MRI, at www.cis.rit.edu/htbooks/mri).

Different tissues in the body, depending upon their composition, have different T_1 and T_2 relaxation times. Furthermore, the T_1 and T_2 relaxation properties of tissue can change in disease state. These differences in relaxation times are routinely exploited in MRI to achieve image contrast and aid in diagnosis (Fig. 1.21). Apart from spin density, T_1, T_2 and contrast-enhanced imaging, MRI can also be made sensitive to blood flow (angiography), the diffusion coefficient of the spins in the tissue (diffusion-weighted imaging), concentration of metabolites (chemical-shift imaging) or the pH of the tissue.

1.4.9 MRI contrast agents

Contrast agents (CAs) are very commonly used with MRI systems to enhance or better visualize specific tissue types or compartments. Commonly used CAs include gadolinium (Gd^{3+}), manganese (Mn^{2+}), and iron (Fe^{3+}). Routine MRI generates contrast from differences in the T_1 and T_2 relaxation rates of protons in the various tissues of the body. MRI contrast agents act to shorten the T_1 and/or T_2 relaxation times of the solvent molecules in the tissue targeted by the CAs, thereby increasing the contrast and visibility.

MRI contrast agents are mostly paramagnetic particles (with unpaired outer-shell electrons), which exert a strong magnetic field on the solvent-water molecules in its immediate vicinity. Random diffusion of both the paramagnetic solute and the solvent, as well as specific interactions between the solute and solvent, are important in reducing the relaxation rates $\dfrac{1}{T_1}$ and $\dfrac{1}{T_2}$ of the solvent molecules. This change in longitudinal or transverse relaxation rate is given by

$$\frac{1}{T_{i,observed}} = \frac{1}{T_{i,solvent}} + \frac{1}{T_{i,contribution}} \quad ; i = 1,2 , \qquad (1.33)$$

where $T_{i,contribution}$ is the change in relaxation rate of the solvent due to contributions from the CA.

When the concentrations of the paramagnetic solute are relatively low, $\dfrac{1}{T_{i,contribution}}$ is directly proportional to the concentration of the paramagnetic particles. The proportionality constant between the CA concentration (M) and its contribution to the change in relaxation rate of the solvent is called its relaxivity (R) and has the units of mM^{-1} s^{-1}. Therefore, the equation for observed relaxation rate can be expressed as

$$\frac{1}{T_{i,observed}} = \frac{1}{T_{i,solvent}} + R_i[M] \; ; \; i = 1,2 \; . \hspace{2cm} (1.34)$$

Enhancement of Longitudinal Relaxation

Random tumbling of the paramagnetic ions cause the solvent to experience strong magnetic field fluctuations. Magnetic field fluctuations at the Larmor frequency directly affect the magnetization of the solvent, analogous to external RF energy, providing an additional pathway for relaxation of the solvent. This property is called dipolar relaxation. The increase in relaxation rate of the solvent is not only proportional to the concentration of the CA but also to the square of the total electron spin of the CA, its effective correlation time (τ_c), and inversely proportional to the sixth power of the distance between the solvent molecule and the CA particle (r) [76]. A good approximation of the interaction of these parameters is given by the equation

$$\frac{1}{T_1} \propto \frac{\gamma_I^2 \gamma_e^2}{r^6} J(\omega) \; ,$$

$$\text{where } J(\omega) = \frac{\tau_c}{(1+\omega^2\tau_c^2)} \text{ and } \frac{1}{\tau_c} = \frac{1}{\tau_s} + \frac{1}{\tau_m} + \frac{1}{\tau_r}, \qquad (1.35\text{a,b,c})$$

where τ_r is the rotational correlation time, τ_s the electron spin relaxation and τ_m the time of residence of the proton. As seen in the Eq. 1.35a, a larger rate of change is expected from the electron spin due to its higher magnetogyric ratio (γ_e).

The correlation time of a particle is a measure of its movement and defined as the time taken for a molecule to rotate one radian or move a distance of the order of its own dimension. As seen in the Eq. 1.35c, the correlation time is typically heavily influenced by the rotational motion τ_r as it is orders of magnitude smaller (few pico seconds) than either the electron spin relaxation τ_s or the time of residence of the proton τ_m (few to several nano seconds). Therefore, small CA molecules associated with small relative rotational correlation times have extremely small relaxivity [77]. Therefore, one strategy to increase the relaxivity of a paramagnetic ion is to increase its effective correlation time. To achieve this goal, paramagnetic metal ions are routinely chelated with large molecules to increase their effective mass or size and thereby increase their solvent relaxation efficiency.

The chelating molecule is generally chosen such that the solvent molecules can still access the paramagnetic ions. The sphere of influence of a single paramagnetic ion, and therefore the extent of the fluctuating magnetic field, is on the order of a few Angstroms and falls off rapidly with the sixth-power of distance [78]. Therefore, relaxation properties depend on the processes that bring solvent molecules within the sphere of influence of the CA. One form of interaction is the direct binding of the solvent molecule to the paramagnetic ion either through covalent or hydrogen bonding. Once

influenced by the paramagnetic ion, the bound molecules (or the protons from the bound molecule) can exchange with those in the bulk solvent, thereby affecting the solvent T_1. These kinds of interactions result in inner-sphere (covalent bond) and second-coordination-sphere (hydrogen bond) relaxation. Outer-sphere relaxation is when the solvent molecules passively diffuse past the paramagnetic particle. The net relaxivity of a paramagnetic ion is therefore the sum of relaxivity contributions due to the inner, secondary, and outer sphere relaxivity.

Finally, the relaxivity of the contrast agent is approximately proportional to the square of the total electron spin (S) in the outer orbitals. Transition and Lanthanide metal ions therefore make excellent CAs due to the presence of large number of unpaired electrons in their outer orbitals. Gadolinium (Gd^{3+}, S=7/2), manganese (Mn^{2+}, S=5/2) and iron (Fe^{3+}, S=5/2) are therefore some of the best candidates for exogenous MRI CAs. However, these metal ions are toxic at the concentrations required to enhance MRI contrast. Therefore, extremely stable and inert organic complexes of these compounds are generally used.

Enhancement of transverse relaxation

Paramagnetic agents shorten both T_1 and T_2 relaxation rates, however, most CAs shorten T_1 more than T_2. CAs that have larger T_2 enhancement than T_1 are characterized by having no inner coordination sphere relaxation. In these T_2 CAs, the relaxation occurs due to the outer-coordination-sphere alone. In addition, the T_2 contrast agents rely on the susceptibility effect to induce a larger sphere of field fluctuations in the solute.

Superparamagnetic iron oxide (SPIO) is one of the most commonly used transverse relaxation agents. SPIOs are stabilized crystals of Fe_2O_3 and Fe_3O_4. Typically, crystal domains of Fe_2O_3 and Fe_3O_4 align with an external magnetic field and they retain their magnetization even when removed from an external magnetic field (ferromagnetic property). However, SPIOs use a domain size smaller than the typical ferromagnetic domain, which allows the magnetization of individual crystals in SPIOs to return to zero when removed from an external magnetic field. Each nanoparticle then becomes a magnetic monodomain.

The final magnetization that can be induced (saturation magnetization) in the SPIO reduces with its size, thereby reducing its relaxivity. The magnetization induced in these nanoparticles saturates at fields of about 1T, compared to about 50T for paramagnetic particles. Superparamagnetic particles do not produce a large T_1 enhancement as the size of the field perturbation is very large [79]. However, some T_1 contrast, mainly from the outer-coordination spheres, has been extracted using appropriate imaging sequences [80]. Due to their relatively large size, most of nanoparticles remain intravascular when given intravenously. Therefore, the extravascular solvent molecules have limited access to their coordination spheres. Signal loss in T_2 relaxation occurs due to the frequency dispersion in spins within a voxel due to the induced magnetization in the CA. A typical SPIO particle has 10-20 times more T_2 relaxivity than T_1 relaxivity [81].

The SPIO particles used in routine imaging are classified based on their size; the ultra-small or USPIO particles with hydration spheres that are smaller than 50 nm and those that are larger. Several nanoparticles of both classes, stabilized against aggregation

by dextran or silicon coating, have been approved for human use; their main target being liver. These nanoparticles are extremely long-lasting in the blood pool and are cleared by macrophages through endocytosis.

Commonly used MRI contrast agents

Gadolinium-III

Gd^{3+} chelated with diethylene triamine pentaacetic acid (DTPA) has been used in humans since 1983 as an *in vivo* MRI CA. DTPA is an organic compound with five carboxymethyl groups having high affinity for metal cations. This complex of Gd-DTPA is extremely hydrophilic, and has been shown to interact with water molecules in both inner- and outer-coordination spheres [82]. The hydrophilic nature of this chelate prevents it from crossing the cell membrane, and this compound is generally used as an extracellular CA. The large size of Gd-DTPA makes it unable to cross blood-brain or blood-retinal barriers. Therefore, it can be used as a blood-pool contrast agent in the brain and retina post-intravenous administration.

Other chelate complexes of Gd^{3+} are also approved for human use. However, the existence of the inner-coordination sphere in DTPA chelates play an important role in the high relaxivity seen by Gd-DTPA (4.8 $mM^{-1}s^{-1}$ at 20MHz), compared to Gd-TETA (2.1 $mM^{-1}s^{-1}$ at 20 MHz) which lacks inner-coordination-sphere interactions [83]. Most of the Gd^{3+} chelates approved for human use have an inner sphere of relaxation, which contributes to approximately 50% of its relaxivity [84].

Manganese –II

Mn^{2+} has fewer unpaired electrons in its outer shell compared to Gd^{3+}, and thus a smaller relaxivity. However, unlike Gd^{3+}, Mn^{2+} is a biologically-active element with interesting properties that enhance specific anatomical and functional properties *in vivo*. Mn^{2+} has been used extensively to detect cytoarchitecture in the brain, as well as its distribution in the brain studied after acute or chronic systemic administration [85, 86]. Mn^{2+} has been shown to preferentially accumulate in active neurons in the brain, enhancing the active brain regions in a T_1-weighted image following functional activation [87]. It is thought that the main pathway for the entry of Mn^{2+} into the neuron is the L-type voltage-gated calcium channel, which opens in response to an action potential [88, 89]. Once inside the neuron, Mn^{2+} is transported anterograde [90], and even crosses synapses traveling from one neuron to the next. This property of Mn^{2+} has been exploited in neuronal tract-tracing using MRI. The fast transport of Mn^{2+} indicates that it may be adhering to intracellular proteins and gets transported in a microtubule dependent mechanism [90].

In order to exploit the biochemical property of Mn^{2+}, most manganese-enhanced MRI (MEMRI) uses $MnCl_2$ as the CA. Intracellular Mn^{2+} has been demonstrated to quickly bind to various proteins, increasing its correlation time, and thereby its relaxivity many fold. The relaxivity of Mn^{2+} chelated with EDTA or DTPA is in the range of 1.5 to 3.0 $mM^{-1}s^{-1}$ at 20 MHz, and increases to 50 and 275 $mM^{-1}s^{-1}$ when bound to proteins like carboxypeptidase and pyruvate kinase respectively [91].

Mn^{2+} is, however, a neurotoxic chemical, with most of its toxicity associated with the formation of free radicals [92, 93] and its interference with normal glial-cell processes [94]. Overexposure to Mn^{2+} is associated with idiopathic Parkinson's disease-like

syndrome, and $MnCl_2$ is therefore not approved for human use. Chelated forms of Mn^{2+} have, however, been approved as CAs in the liver.

Deoxy-hemoglobin

Every hemoglobin molecule is an assembly of four globular subunits, each subunit tightly binding a Fe^{2+} ion. The unpaired electrons in Fe^{2+} make the entire hemoglobin molecule paramagnetic, when not bound to oxygen. The hemoglobin molecule in the body acts to transport oxygen, with one molecule of O_2 binding to each of the four Fe^{2+} ions. Molecular oxygen is paramagnetic with two unpaired electrons in the antibonding orbital. However, binding of oxygen to hemoglobin converts the whole molecule to a diamagnetic form, since oxygen binds in its superoxide state (O2-); emporarily converting Fe^{2+} to Fe^{3+}, and the remaining two unpaired electrons aligning opposite to each other in antiferromagnetic manner [95]. Therefore, while oxy-hemoglobin is diamagnetic, deoxy-hemoglobin is paramagnetic.

This change in the magnetic property of hemoglobin has been used extensively to indirectly detect the functional activation of neurons. Neuronal activation leads to increased energy consumption and increased oxygen consumption. This increased demand for oxygen is thought to cause an increase in bood flow and vasodialation in neighboring blood vessels; although the exact mechanism of action is not fully understood. Increased blood flow in these vessels decreases the amount of deoxy-hemoglobin, thereby reducing the T_2^* and T_2 decay in the signal. Therefore, the MRI signal increases as a result of neuronal activation. This effect is called blood-oxygenation-level-dependent imaging (BOLD) [96, 97].

Microcrystalline iron oxide nanocolloids (MION)

MION is an USPIO class CA, with an average size of 17 nm [98, 99]; almost twice the size of high-density lipoproteins in blood plasma. MIONs contain a central Fe crystal of size 4-7 nm, surrounded by multiple dextran molecules, thereby increasing its size. The coating of dextran molecules prevents easy access of solvents to the Fe core, making MION an effective T_2* contrast agent. This large size makes MION a blood-pool contrast agent, with a half-life on the order of hours. When administered intravenously, MION is moderately cleared by the macrophages in the liver and spleen. Intravenous administration of MION has been used extensively in the next chapter to image retinal blood flow and volume.

MRI is therefore an extremely versatile modality for imaging, offering minimally invasive techniques for anatomical and functional imaging. These advantages have been exploited to develop retinal MRI techniques in rats using 4.7T and 7T MRI scanners made for research purposes.

1.5 Animal model for technique development

The rat was chosen as the animal model for these studies since homogenous genetic strains are easily available and because of the relatively low cost for procurement and maintenance. Retinal disease models have been developed in the rat and their retina has long been used for research into disease etiology and therapeutic techniques. Although sight is not the primary sense in rats, the layer structure and vasculature in the

rat retina is similar to the human peripheral retina. The rat retina is dominated by rods just like the peripheral retina in humans. Most of the neural connections and mechanisms are conserved between the rat and human peripheral retina.

The differences between the rat and human eye lie mainly in their sensitivity. The rats lack a fovea, and the retina is comparatively quite uniform across the entire eye, with only slight variations in thickness. Rats are unable to change the shape of their lens as the lens is very hard and the ciliary muscles are very weak, rendering rats nearsighted. The cornea and lens in the rat eye is transparent to UV-A light (longer wavelength UV light, having wavelengths of 320 to 400 nm) in addition to the visible spectrum of humans. The cones in rat retina are of only two types, the green and blue, with blue cones being sensitive to higher frequencies than in humans. Thus, rats can see some part of the near ultraviolet light. The photoreceptors in the rat retina are also arranged in a more coarse fashion, sacrificing visual acuity for higher sensitivity.

Therefore, the rat retina is not significantly different from the human retina, and is suitable for retinal-imaging technique development. Rats are also relatively small in size and thus can be accommodated in the small bore of high-field research MRI systems.

1.6 Outline of thesis

Chapter 2: Experimental setup

This chapter outlines the choice of anesthesia, MRI hardware as well as the data analysis techniques used in this thesis for anatomical and functional imaging of the rat retina.

Chapter 3: T_1, T_2, T_2* *and water apparent diffusion coefficient measurements of the rat retina*

This chapter details experiments performed in wild-type rats to determine T_1, T_2, T_2* and average water ADC in the rat retina and vitreous. The retinal T_1, T_2 and average water ADC values correlated well with known values in the brain at the same field strength.

Chapter 4: Structural and functional MRI reveals multiple retinal layers in the rat

High-resolution anatomical and functional imaging of the retina is detailed in this chapter. Layer-specific structural and functional response to systemic stimuli could be detected in the wild-type rat retina.

Chapter 5: High-resolution, manganese-enhanced imaging of retinal structure

This chapter details anatomical imaging of the retina at 25 μm in-plane resolution, with the help of manganese chloride as an intracellular contrast agent. Both intraperitoneal (i.p.) and intra-vitreal injection of $MnCl_2$ was explored for structural imaging of the retina. Seven distinct layers were seen in the retina following intravitreal injection, which were then assigned using emulsion autoradiography with Mn^{54}.

Chapter 6: Functional imaging of rat retinal blood-flow and blood-volume using MION

Relative blood volumes in retinal and choroidal vessels were assessed using MION as an intravascular contrast agent. Fractional changes in blood volume in the retinal and choroidal vessels, in response to systemic stimuli of hyperoxia or hypercapnia were also measured.

Chapter 7: Application of retinal MRI techniques to retinal dystrophy disease model

Retinal MRI techniques developed in the thesis were applied to detect anatomical and vascular changes in a rat model of retinal dystrophy. Changes in retinal structure and vasculature could be detected robustly using the MRI techniques developed herein.

Chapter 8: Conclusion

Chapter 2: Experimental Setup

This chapter discusses the effect of various anesthetics on eye movement, criteria for the choice of RF coils and other general experimental setups for MRI of the retina. The primary requirement for MRI is the immobilization of the sample or imaging area during the scan. Hence, removal of major eye movements is essential for retinal MRI. A CCD camera focused on the rat eye was used to record eye movements under various anesthetic conditions in a bench-top experiment. Supplementing the anesthesia with a muscle relaxant (pancuronium bromide 1ml/kg/hr i.v.; or 3ml/kg/hr i.p.) helped to abolish all significant eye movements in rats. Electroretinographic (ERG) functional response to a single scotopic stimulus revealed no significant changes due to pancuronium when used with isoflurane anesthesia. 1% isoflurane with pancuronium bromide was determined to be optimal for all our MRI studies.

Secondly, different RF-coil designs were evaluated. Careful attention was paid to the sensitivity of the coil and coverage of the entire retina. A 0.6-mm-radius, single-turn surface coil placed directly above the eye was chosen for retinal MRI as it gave relatively good SNR from the entire retina and coil the setup was not invasive.

Finally, other general-setup issues, like physiological monitoring, and imaging techniques like slice positioning and time-series acquisition, are discussed.

2.1 Choice of anesthesia

2.1.1 Introduction

One of the basic requirements for MRI is that the region being imaged does not move for the duration of the pulse sequence. MR image formation requires encoding of nuclear spins in two dimensions during signal acquisition. This is done by playing out RF and magnetic field gradient pulses. The spatially-encoded signals are then reconstructed into an image using two-dimensional Fourier transformation. Any movement of the sample during the pulse sequence will cause inaccurate spatial encoding, resulting in motion artifacts like blurring, ghosting, and the loss of image information.

One strategy to avoid motion artifacts would be to use a 'snapshot' acquisition with the help of an ultrafast acquisition technique such as echo-planar imaging (EPI). In an EPI pulse sequence, the readout gradient is rapidly reversed multiple times, within a single TR, to get multiple gradient-echoes. Each gradient-echo can be encoded with a different phase-encoding-gradient magnitude, which fills a different line in the k-space. When pushed to its limit, this technique is capable of acquiring an image in a single TR interval, potentially with a scan time of a few tens of milliseconds per slice. However, this technique suffers from the disadvantage of a relatively long TE. Since multiple reversals of the readout gradient are required to acquire the echo train, the TE for each echo becomes progressively longer. With a high number of points (for higher resolution), the TE is longer and the echo weaker due to T_2^* decay. A long TE for echoes that make up the central lines of k-space affect the signal-to-noise ratio (SNR) and contrast-to-noise ratio (CNR), while long TE values affecting the peripheral lines of k-space will cause loss of high frequency (high-spatial-resolution) information.

The TE in EPI scans can be shortened by (i) reducing the number of samples of the echo train, thereby reducing the resolution; and (ii) by acquiring the k-space lines in batches (multiple-segmentation) rather than a single shot. The second option is feasible for high resolution scans, but the scan time would increase substantially from tens of milliseconds to a few seconds, increasing the possibility of movement during image acquisition.

Non-EPI scans, on the other hand, acquire one echo at a time and have a total scan time of a few tens of seconds to a few minutes. While being extremely susceptible to movement artifacts, this technique can achieve very short and uniform TE for all lines of the k-space, thereby improving SNR and CNR.

Although, offline corrections using navigator echos [100-102] have been developed to help remove motion artifacts from segmented EPI and non-EPI scans, the ability to retrieve all encoded information depends on the pulse sequence and type of correction algorithm employed. Such corrections require acquisition of additional echo(s), which may increase the echo time (TE) and/or scan time by up to 100%. An increase in TE results in altered image contrast as well as a decrease of signal intensity due to T_2^* decay. It is therefore highly desirable to remove any motion at the time of image acquisition.

Animal MRI is usually conducted under general anesthesia to immobilize and prevent movement. The eye is highly susceptible to motion artifacts not only because of its freedom of movement but also because eye movements are in part involuntary. The rat eye moves freely in a bony socket called the orbit, with the help of six extraocular muscles. These muscles attach the eyeball to the back of the orbit and are responsible for

the eye movement in all three axes (medial-temporal, superior-inferior and even anteroposterior). Eye movements are generally classified as gaze stabilizing or gaze shifting mechanisms. Gaze stabilizing mechanisms, like the vestibule ocular reflex and optokinetic reflex, keep the object of interest in the field of vision when the head or the object is moving. Gaze stabilization mechanisms involve involuntary eye movements like saccades, pursuit and vergence [103]. Under light general anesthesia, the eye moves in slow oscillatory sweeps due to the incomplete recovery from saccades, which switches to microsaccadic motion under deep anesthesia [104, 105].

Movements of the eye can generally be reduced by increasing the depth of anesthesia; however, deep anesthesia also reduces functional and systemic responses to stimuli [106]. Common anesthetics used in animal MRI, for example, isoflurane, causes vasodilatation. Functional MRI (fMRI) techniques like BOLD depend solely on the vascular reactivity during stimulus, and any reduction of vascular reactivity compromises fMRI signal [107]. Furthermore, most anesthetics suppress sensory perception [108]. Anesthetics like alpha-chloralose have been shown to decrease the resting glucose consumption, indicating a change in neuronal activity [109]. It is therefore highly desirable, especially in functional MRI (fMRI), to keep the dosage of anesthesia to a minimum, while at the same time removing all motion of the sample. A combination of multiple anesthetics, like use of general anesthetic with an ophthalmic block for removing eye motion, was also avoided.

As a first step towards MRI of the retina, anesthetics approved for use in the laboratory were evaluated for their ability to stop eye motion. Three types of general anesthetic drugs were tested: inhalation, intravenous (i.v.) and intraperitoneal (i.p.). The

advantages of using an injectable muscle relaxant to supplement the general anesthesia were also evaluated to determine its effect on the amplitude and latency of its electrophysiological response to a functional stimulus. A final consideration for the choice of anesthetics was the ease of recovery after the study. Since some of these studies involve the use of costly disease models and longitudinal examinations, it is desirable that the rats completely recover from anesthesia. These experiments were not intended to be a comprehensive review of all anesthetics, but just those routinely used with MRI.

2.1.2 Materials and method

Rats were anesthetized with isoflurane and their trachea intubated with a 14-gauge catheter. Rats were maintained under controlled ventilation throughout the experiment. The femoral artery and vein were then catheterized under 2% isoflurane. The catheter from the femoral artery was connected to a pressure transducer and the blood pressure was continuously monitored (Harvard Instruments, Holliston, MA). After surgery the rats were transferred to a stereotaxic device to immobilize the head.

Eye movements under various anesthetics were monitored using a CCD camera (7.4 μm/pixel resolution) focused with two camera lenses mounted back-to-back [110]. Magnification of up to 4x could be achieved with this arrangement. A spot of black ink was placed on the cornea to make eye movements more visible on the black and white image as shown in Fig. 2.1. The movies were recorded at two different frame rates: 1 frame/s for 4 min (low frame rate or LFR) and 25 frames/s for 20 s (high frame rate or HFR). The resolution of the picture was determined by taking a photograph of a

millimeter scale under the same conditions, and the resolution was ~3 μm/pixel. The recordings were then analyzed using programs written in Matlab.

Various parameters were derived from the movies of eye movement and its analysis. The pixel co-ordinates of the center-of-mass of the black ink spot (*center co-ordinates*) were recorded from frame to frame and plotted on a chart (*movement pattern*). The distance between the center-of-mass coordinates in each frame and the center-of-mass coordinates of the first frame was plotted to view the amplitude and frequency of eye movement (*movement waveform*). The average displacement of the eye from frame to frame in an LFR movie was calculated (*motion index*, units of mm/s) as a measure of total eye movement. The movement waveform from the HFR movie was Fourier transformed to determine its frequency components.

Four commonly-used anesthetics were analyzed: isoflurane, urethane, ketamine/xylazine and propofol. Isoflurane (n=6; 1%, 1.5% and 2% in air), a volatile anesthetic, was delivered in breathing air through a ventilator, and its concentration was controlled by a vaporizer. While testing urethane (n=6; 1000 mg/kg, 30% solution in water, i.p. injection), ketamine/xylazine (n=6; 75 mg/kg and 10 mg/kg respectively, i.p. injection) or propofol (n=6; 45 mg/kg/hr continuous i.v. infusion), the anesthetic was switched from isoflurane after the surgery and the animal allowed to stabilize for one hour. After the experiments the animals were euthanized with a transcardial injection of urethane (1cc, 30% solution).

Finally, any effect of pancuronium on the electrophysiological response to a light stimulus was measured using ERG in separate groups of rats. Dark-adapted rats (overnight in dark room) were setup in a stereotaxic frame under isoflurane anesthesia

and the ERG response to a single flash of light recorded using a corneal electrode. Two groups were tested: one anesthetized with isoflurane (n=4) and second with isoflurane supplemented with pancuronium bromide (n=4, 3ml/kg/hr, i.p.).
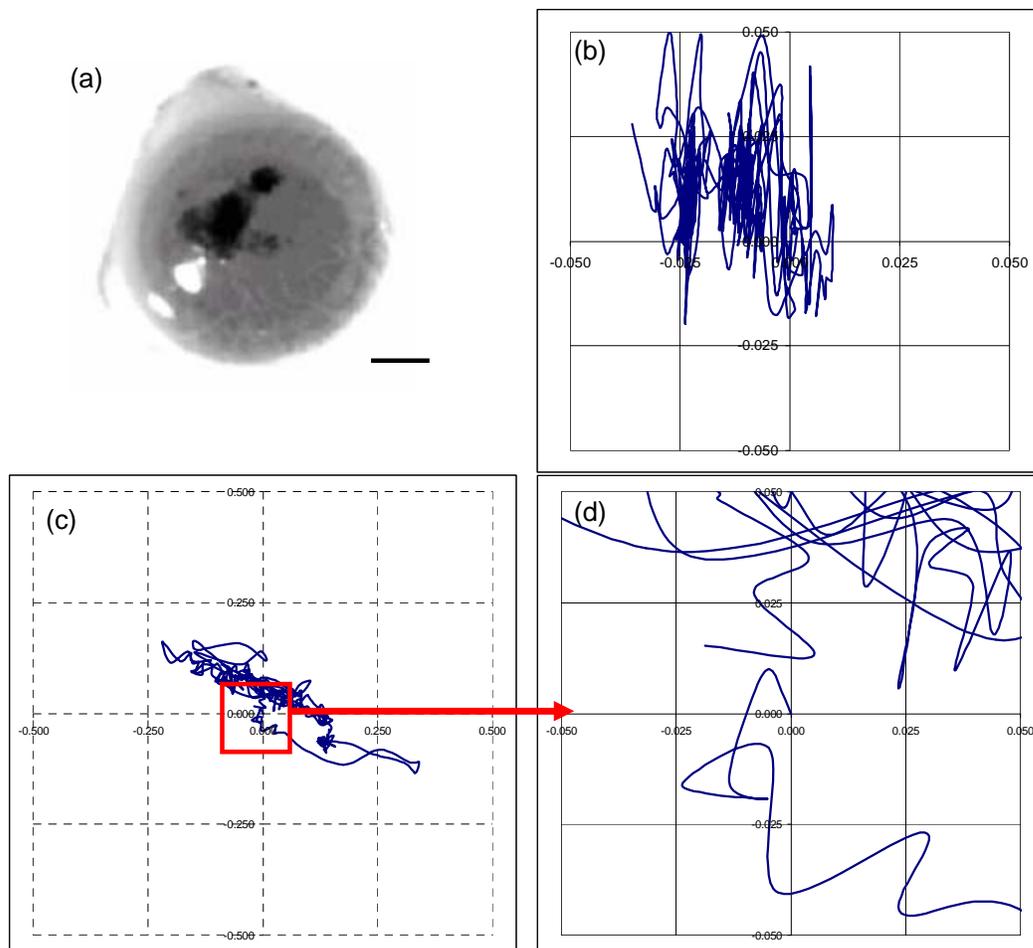
Fig. 2.1: Rat eye movement under isoflurane anesthesia. (a) Still frame from a movie of eye movement recorded under isoflurane anesthesia. Brightness of the image has been increased so as to be able to clearly see the iris and the spot of ink on the cornea. The resolution of this image is ~3 μm/pixel. Trace of eye movement (movement pattern) under (b) 1% isoflurane anesthesia and (c) 2% isoflurane anesthesia in a four-min recording in two different rats. **x- and y- axis are in mm.** Note that scale in (c) is 10 times the scale in (b). Movement pattern in (c) is zoomed in in (d) to give the same scale as (b). Care was _not_ taken to align the co-ordinate axis with the naso-temporal or superior-inferior anatomical direction, although the setup was done in a uniform way in all animals. Scale bar in (a) is 1mm.

2.1.3 Results and Discussion

Low frame-rate recordings

The iris and the black spot on the cornea were clearly visible in the CCD camera, making the detection of eye motion from one frame to the next possible (Fig. 2.1a). A typical pattern of motion recorded over 4 min in an animal anaesthetized with 1% isoflurane and 2% isoflurane anesthesia is shown in Fig. 2.1b and Fig. 2.1c. The eye was seen to move in a slow rolling fashion under isoflurane anesthesia, just as in Stage 1 or light sleep. These eye movements did not disappear with higher anesthetic level as seen on Figs. 2.1b and 2.1c [105], and the amplitude of these oscillatory eye movements became larger and the frequency reduced as the isoflurane level was increased to 2%. When anesthetized with propofol, ketamine/xylazine and urethane, the amplitudes of the eye movements were comparatively smaller
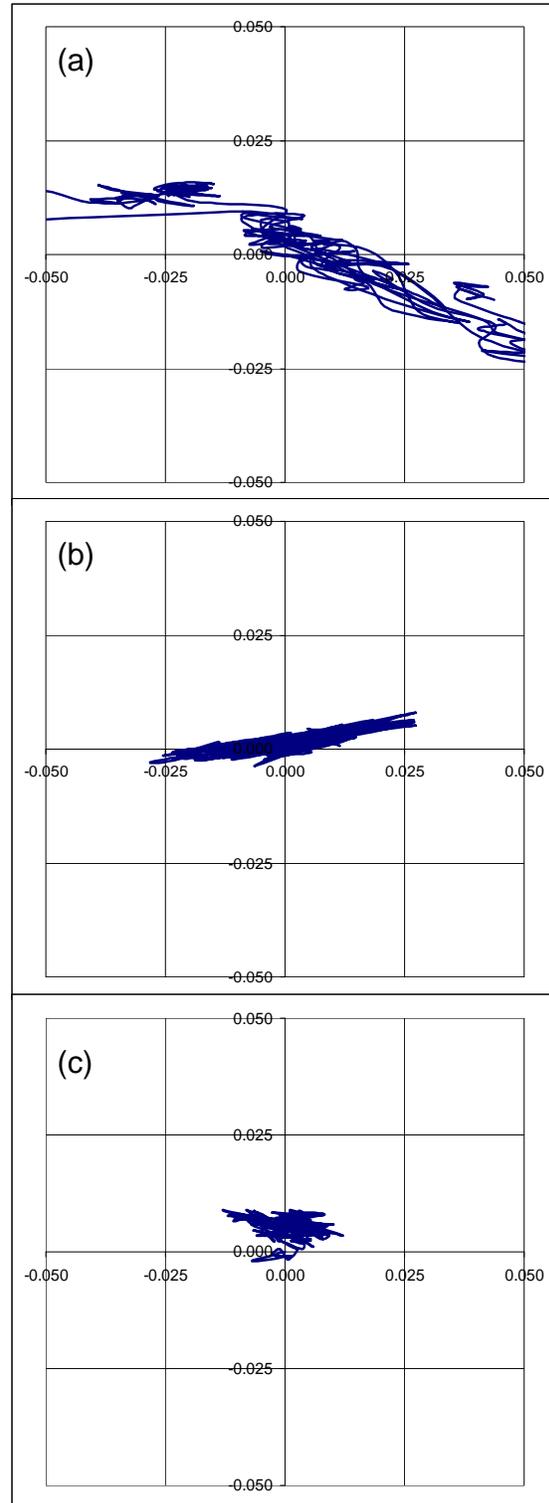
Fig. 2.2: Trace of eye movement (movement pattern) under (a) propofol (45 mg/kg/hr i.v.), (b) ketamine/xylazine (75 mg/kg and 10 mg/kg respectively, i.p.) and (c) urethane (1000 mg/kg,i.p.) anesthesia in a four-min recording in different rats. **x- and y- axis are in mm.**

and of higher frequency as seen in Fig. 2.2. The direction of eye movement could not be accurately assigned, as care was not taken to accurately align the naso-temporal or superior-inferior axis to the x- or y-axis in the image frame. A displacement plot of the
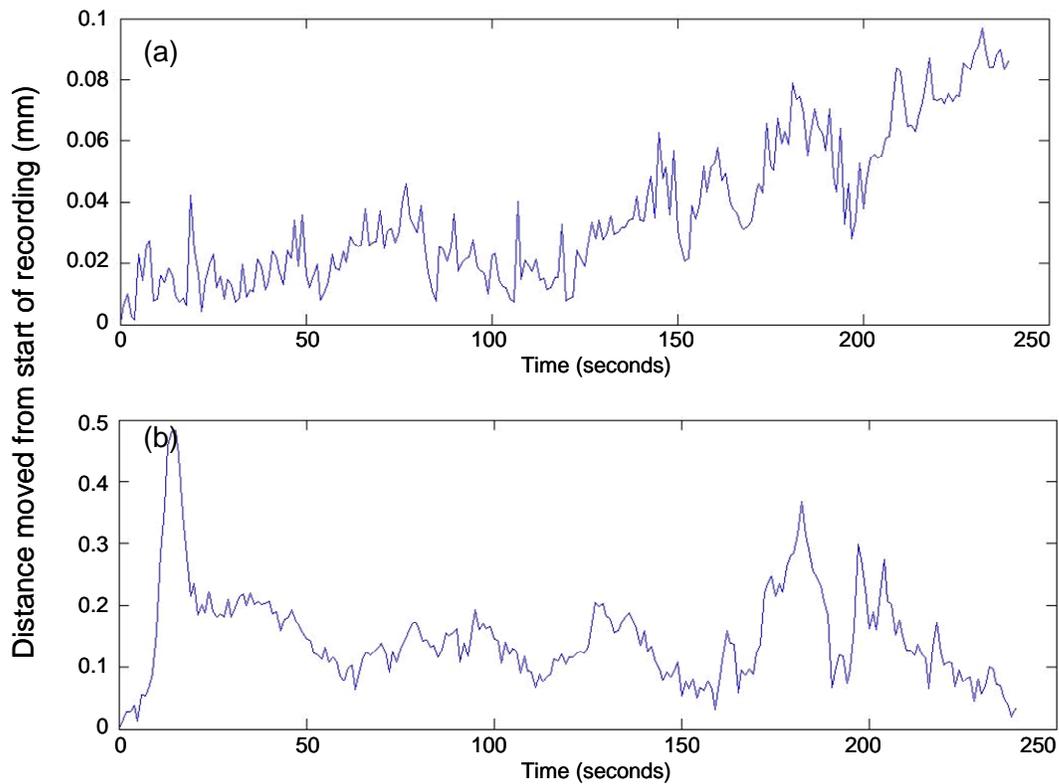
Fig. 2.3: Displacement of the eye with respect to initial frame (movement waveform), of recordings shown in Fig 2.1, over a four-min recording under (a) 1% isoflurane in air and (b) 2% isoflurane in air. y-axis scale is in mm.

eye with respect to the initial frame (from rat eyes in Fig. 2.1) under 1% and 2% isoflurane anesthesia is shown in Fig. 2.3.

Care was taken to minimize the movement of the eye relative to the camera, by mounting the camera on the same platform as the stereotaxic headset. The movement detected in Fig. 2.3 originated from the motion of the eye within the orbit, and was confirmed by the relative movement of the black ink spot with respect to extra-orbital landmarks, like the lacrimal gland and supra-orbital ridge.

Eye Movement Under Anesthesia
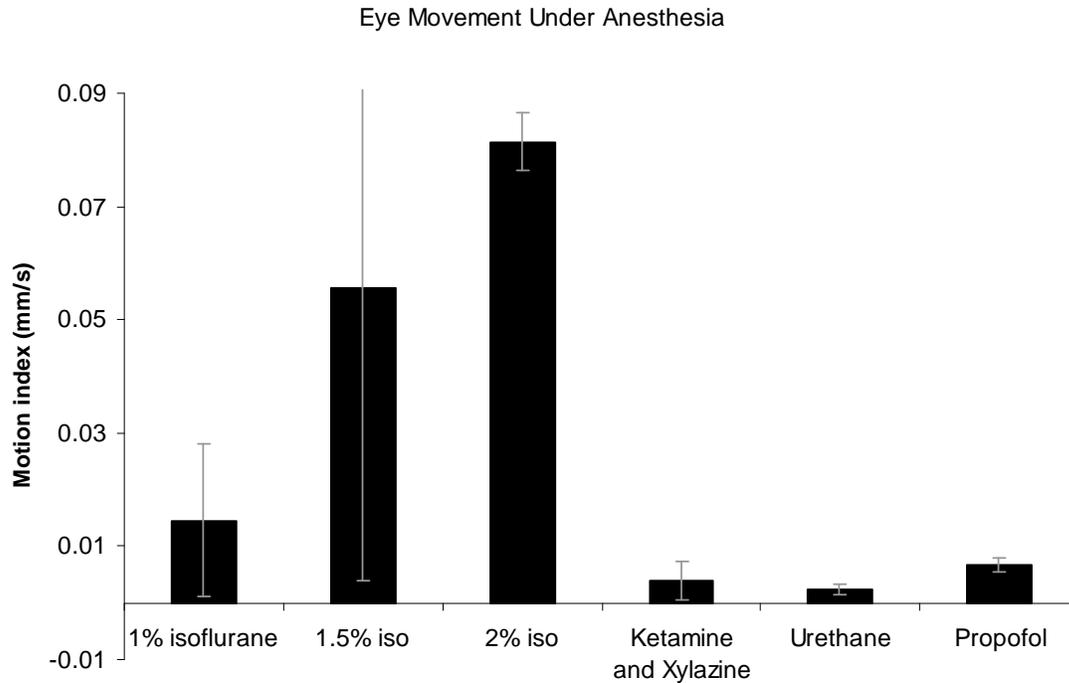
Fig. 2.4: Average distance moved (motion index, mm/frame or mm/s) by the eye under various anesthetics (n=6 in each group).

Fig. 2.4 shows the plot of motion index (or average displacement of the eye from frame to frame) under various anesthetics. Anesthetics other than isoflurane showed much lower motion index, but none of the anesthetics tested completely removed movement. Eye movement was the least under urethane and ketamine/xylazine anesthesia at motion indices of 0.0023 ± 0.0009 mm/s and 0.004 ± 0.030 mm/s, respectively, for four minutes. Eye movement under propofol and 1% isoflurane was significantly higher ($p<0.05$) with motion indices of 0.007 ± 0.001 and 0.014 ± 0.013 mm/s, respectively.

Careful study of the motion indices and the variability in movement patterns under the different anesthetics suggested that urethane was the only effective anesthetic for reliable high-resolution retinal MRI lasting few minutes. One reason for this could be that urethane achieved a much deeper level of anesthesia than the others tested.

To further explore the possibility of using light anesthetics, especially with fMRI, we examined the possibility of supplementing the anesthesia with a muscle relaxant like pancuronium bromide. Pancuronium bromide is a non-depolarizing, competitive
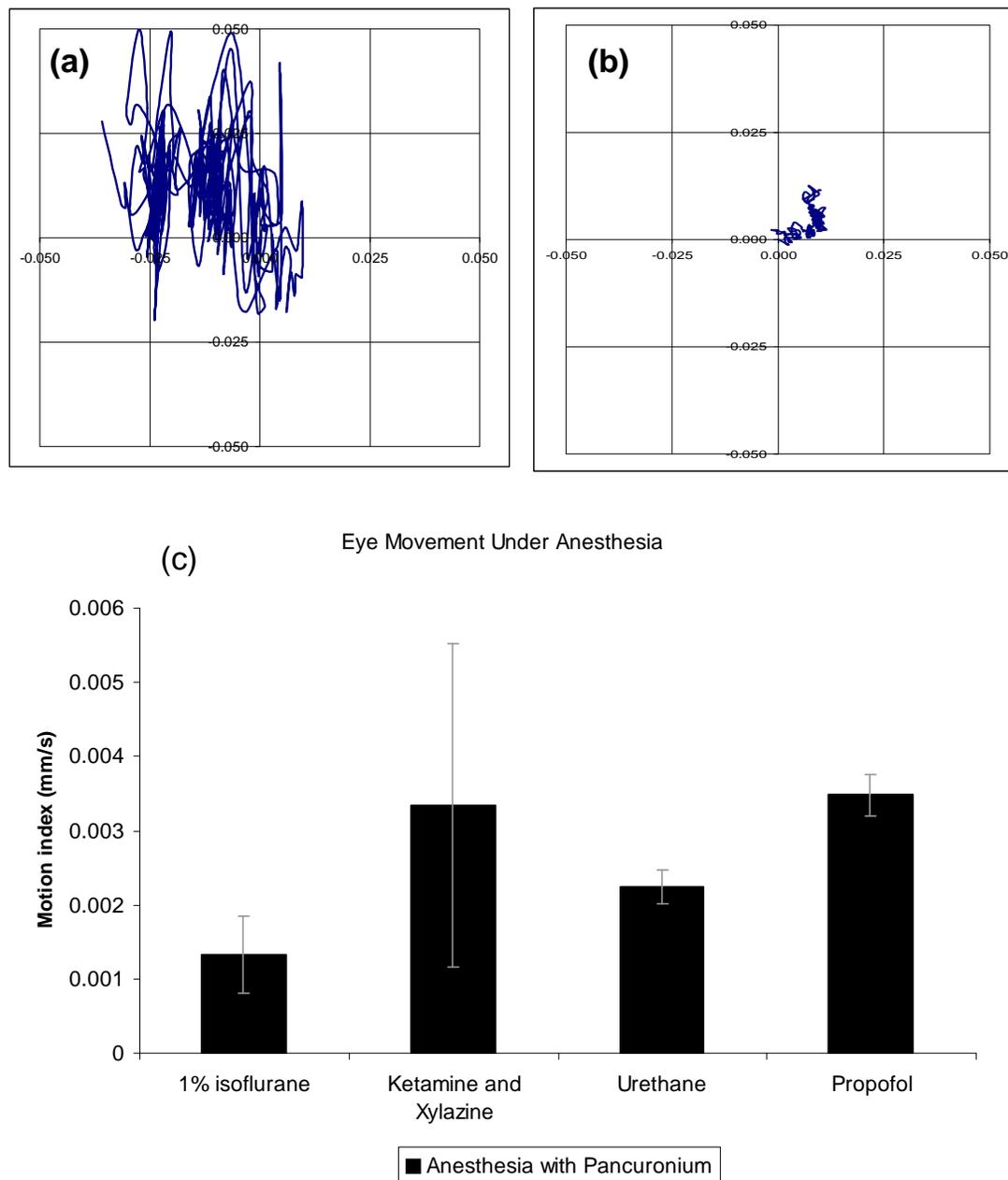
Fig. 2.5: Effect of pancuronium on the eye movement in rat. Comparison of eye movement patterns of rats anesthetized with (a) 1% isoflurane alone and (b) 1% isoflurane and supplemented with pancuronium. (c) Average distance moved (motion index, mm/frame or mm/s) by the eye under various anesthetics when supplemented with pancuronium bromide (n=5 in each group).

antagonist of acetylcholine receptor. This drug acts rapidly at neuro-muscular junctions preventing muscle contractions. Pancuronium has no hormonal activity, and its effects can be reversed by neostigmine, which is a cholinesterase inhibitor. Inhibition of cholinesterase by neostigmine prevents the breakdown of acetylcholine, increasing its concentration in the neuromuscular junction and causing it to compete with pancuronium. The blood pressure was continuously monitored to ensure the animal was not conscious or stressed during the examination.

Eye movements were significantly reduced ($p < 0.05$) when pancuronium bromide was used to supplement isoflurane, ketamine/xylazine or propofol anesthesia, as seen in Fig. 2.5. However, there was no significant change in motion index under urethane anesthesia supplemented with pancuronium. Rats anesthetized with 1% isoflurane and supplemented with pancuronium showed significantly lower eye movement than any other drug tested (although 1.5% and 2% isoflurane was not tested in this case). This was followed by the movement index from rats anesthetized with urethane with or without pancuronium. Ketamine/xylazine and propofol anesthesia supplemented with pancuronium also showed only minimal eye movement. The motion index under 1% isoflurane with pancuronium was 0.0013 ± 0.0005 mm/s for four minutes. Therefore, 1% isoflurane supplemented with pancuronium was determined to be the best choice of anesthesia among the protocols tested.

Administration of pancuronium significantly increased the heart rate in all groups of animals studied ($p < 0.01$). Under 1% isoflurane anesthesia, the heart rate increased ($p < 0.01$) from 380 ± 30 bpm to 428 ± 5 bpm (~10% increase). Correspondingly, the mean arterial blood pressure (MABP) dropped from 120 ± 9 mm Hg to 108 ± 5 mm Hg

(p<0.01, ~10% decrease). The drop in blood pressure was also statistically significant in the ketamine/xylazine group, but not in the urethane or propofol groups. However, both the heart rate and the MABP recorded were within the normal physiological range for an adult rat.

High frame-rate recordings

High frame-rate recording was done under various anesthetics to identify the source of the residual movement eye seen after the injection of pancuronium bromide. It was hypothesized that these small movements may be a result of respiration or cardiac pulsation. To test this hypothesis, the movement waveform of each HFR recording was
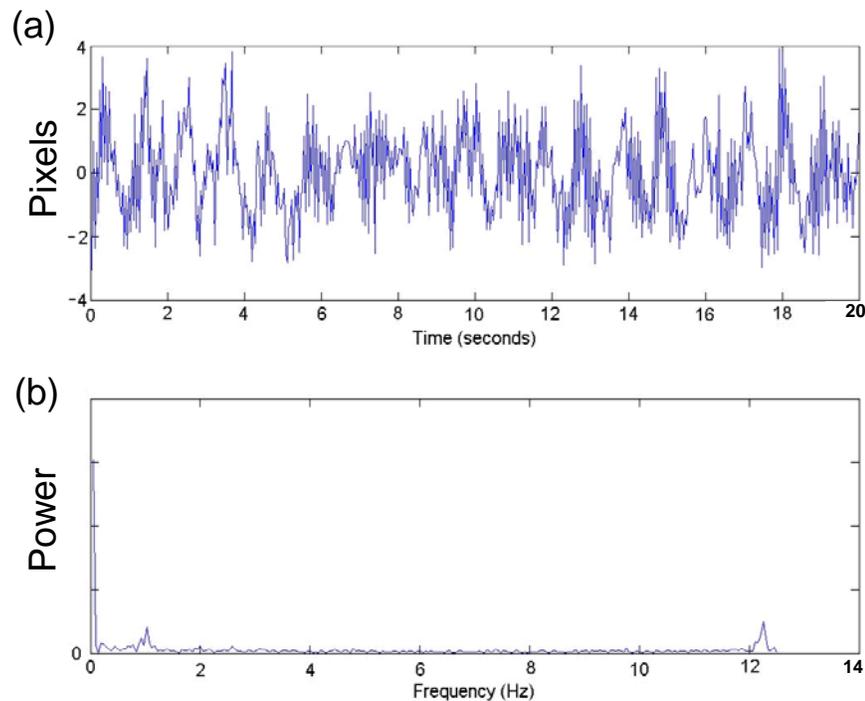
Fig. 2.6: (a) Displacement of the eye with respect to the initial frame and (b) frequency components in the movement waveform determined by Fourier transformation in a high frame-rate recording under 1% isoflurane and pancuronium bromide. Three peaks (at ~0 Hz, ~1 Hz and at 12.2 Hz are clearly seen. Y-axis (a) distance moved in number of pixels (b) power.

observed and its frequency components analyzed using Fourier transformation as shown in Fig. 2.6.

Plots of movement waveform, under 1% isoflurane, supplemented with pancuronium, clearly showed previously undetected high-frequency oscillations. Frequency decomposition of this movement waveform showed three peaks, at ~0Hz (low-frequency component), ~1Hz (mid-frequency component) and ~12.2 Hz (high-frequency component). The low-frequency component was ignored as it originated from the eye not oscillating about its position in the first frame. The mid-frequency component was clearly dominant in the motion plot and nicely corresponded to the respiration frequency of the animal. To verify this hypothesis, we varied the respiratory frequency and repeated the recording. The mid-frequency in the Fourier plot was found to linearly follow the respiratory frequency with an R^2 value of 0.99 as shown in Fig. 2.7.
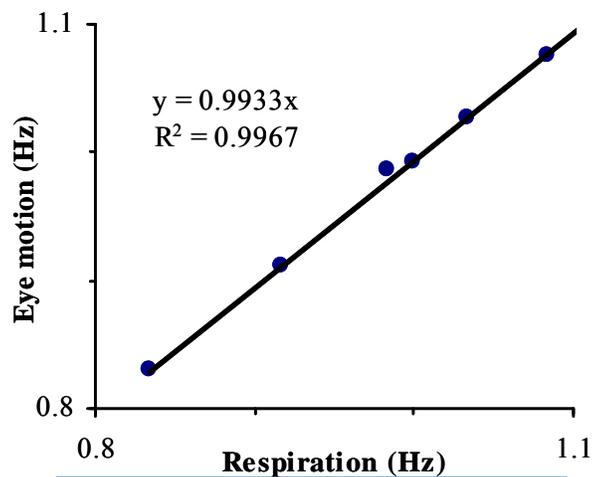
Fig. 2.7: Change in mid-frequency component of eye motion with change in respiration rate under 1% isoflurane with pancuronium bromide.

The source of the high frequency component in the data could not be easily determined as it did not vary with either the respiratory rate or the pulse rate (~7 Hz). It was consistently seen in the 12.2 Hz region, leading us to believe that it was systemic noise.

Urethane anesthesia, by itself, provided a stable eye for long periods. Urethane is the anesthetic choice of one other group doing retinal MRI [111, 112]. It provides a stable plane of anesthesia, with very little physiological changes, and minimal cardiovascular or respiratory depression. However, urethane is also known to produce a much deeper plane of anesthesia and analgesia than most anesthetics. The anesthesia produced by urethane is extremely long lasting and making it sometimes difficult for the small rodents to recover. Ketamine/Xylazine cocktails have long been used for ERG experiments in rats, with the rats recovering in about 2 h after the initial i.p. injection. However, most MRI experiments last over 2-3 h, and it may be difficult to monitor the plane of anesthesia of the rat inside the magnet and to maintain a stable anesthetic level. The situation is complicated by the fact that the rate of drug absorption for an i.p. injection may be variable from one setup to another, and potentially causing a variable anesthetic plane even if the drug is infused slowly over the imaging time.

Isoflurane and propofol can be delivered from outside the magnet room, where their dosage and thus the anesthetic level of the rat can be controlled easily. However, propofol is generally delivered i.v., and additional setup and surgery is required. Isoflurane, on the other hand, can be titrated to very low concentrations so as to maximize the functional response [106]. The rat can easily recover from both isoflurane and pancuronium as tested in our lab. Rats anesthetized with isoflurane and supplemented with pancuronium showed no movements other than that due to respiration, and the amplitude of eye movement was the least among the anesthetics tested. Due to these overall advantages, isoflurane supplemented with pancuronium bromide was used as an anesthetic for all retinal MRI.

ERG recordings

Finally, the electrophysiological response in rats anesthetized with 1% isoflurane was compared with and without pancuronium. The standard ERG consists of an a-wave from the initial hyper-polarization of the photoreceptor cells; a b-wave from the depolarization of the inner retinal neurons like ganglion cell; and oscillatory potential (OP) often seen in the rising portion of the b-wave which arises mainly from the bipolar
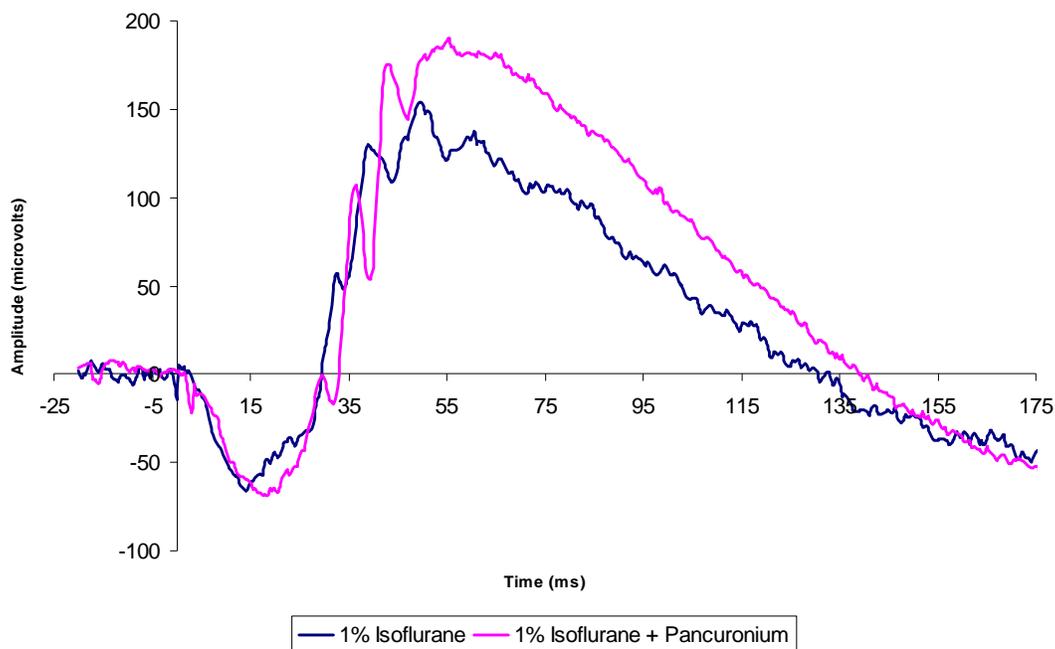
Fig. 2.8: Electroretinogram (ERG) recorded from a rat anesthetized under 1% isoflurane with and without the muscle relaxant pancuronium bromide. Group averaged amplitude and latency did not show any differences between the groups with and without pancuronium.

cells. Sample ERG responses to a single flash of light recorded from a rat is shown in figure 2.8. There were no differences seen in either the amplitude or the latency of the various waves due to pancuronium, indicating that pancuronium did not alter the electrophysiological response significantly. However, the ERG waveform by itself

looked much smoother in the animals supplemented with pancuronium. This is probably due to the lack of any electrical activity in the muscles (EMG) being superimposed on the ERG signal as well as the lack of any motion of the eye itself.

2.1.4 Conclusion

Pancuronium was critical in suppressing eye movements in rats under anesthesia. Among the anesthetics tested, eye movement was found to be the least for rats anesthetized with 1% isoflurane and supplemented by the muscle relaxant pancuronium bromide. The amplitude of eye movement in a rat anesthetized under these conditions was about 1.3 μm, far lower than the expected resolution in MRI. However, any of these anesthetics tested, supplemented with pancuronium, would be suitable for anatomical MRI of the retina.

Use of a muscle relaxant with isoflurane implies that the rats need to be artificially ventilated during the entire study. This enables a finer control of the animal's physiology as well as the dosage of the volatile anesthetic. HFR imaging of the eye under 1% isoflurane and pancuronium showed that most of the residual motion is due to respiration. This movement could potentially result in some blurring of the image, however, the amplitude of these movements were extremely small. Finally, ERG experiments demonstrated that using pancuronium to supplement isoflurane did not significantly change the latency or amplitude of the electrophysiological response to a flash stimulus. Therefore, 0.9-1.0% isoflurane was used in all retinal fMRI experiments and 1.5% isoflurane for all anatomical MRI experiments, always supplemented with

pancuronium bromide. Other anesthetics like urethane were not used for any of the MRI studies.

2.2 Radio-frequency coil design

MRI in the brain and other organs are routinely performed with an in-plane resolution (pixel size within the slice) of a few millimeters. However, MRI of the rat retina, which itself is only about 300 μm thick, requires at least a 20-50 fold increase in the in-plane resolution alone. The MRI signal from such high resolution pulse sequences are expected to be low in signal amplitude as (i) only a small portion of the sample is excited at a time (small field of view or FOV); and (ii) each voxel in the image represents a small volume of the sample and therefore a smaller number of protons gives rise to a weaker signal.

One way to improve the MRI signal is by optimizing the design of the RF coil. As discussed in the Introduction (Section 1.4), RF energy is used in MRI to tip the magnetization of the sample into the x-y plane, where it precesses around the z-axis. This precession induces an alternating current in an RF coil that is sensitive to magnetization in the x-y plane, which becomes the signal detected for image formation. The RF, similar to ultrasound, is absorbed by the tissues in the body, and thus is attenuated during both transmission and reception. The depth of penetration of the RF field and its uniformity of irradiation depends on the power of the RF, the RF coil dimensions and its geometry. Likewise, a receiver coil placed very near the sample can maximize the signal detected by the MRI. Therefore, efficient RF coil design is a significant factor for improving the final MR image quality.

Transmission of the RF and reception of the signal can be achieved through (i) a single coil switched between transmit and receive modes (transmit receive coil); or (ii) two separate coils for transmission and reception. Consideration for the choice and design of RF coil(s) includes (i) the final SNR of the image; (ii) the FOV or the size of the region being imaged; and (iii) the specific absorption rate (SAR) of the RF energy in the tissue.

2.2.1 Single-coil system

In a single-coil system, a small one- or two-loop surface coil is placed directly on or around the rat eye. The coil is switched internally (via the MRI-instrument hardware) between the RF power amplifier during the transmission phase of the pulse sequence to a pre-amplifier during the signal receiving phase, thus acting in a transmit/receive mode.

The transmit/receive coil has to be small enough to fit closely into the area being imaged for best signal reception but large enough to uniformly irradiate the entire retina. The first type of coil tested was a simple surface coil. The energy of RF transmitted by a surface coil varies with depth, and is
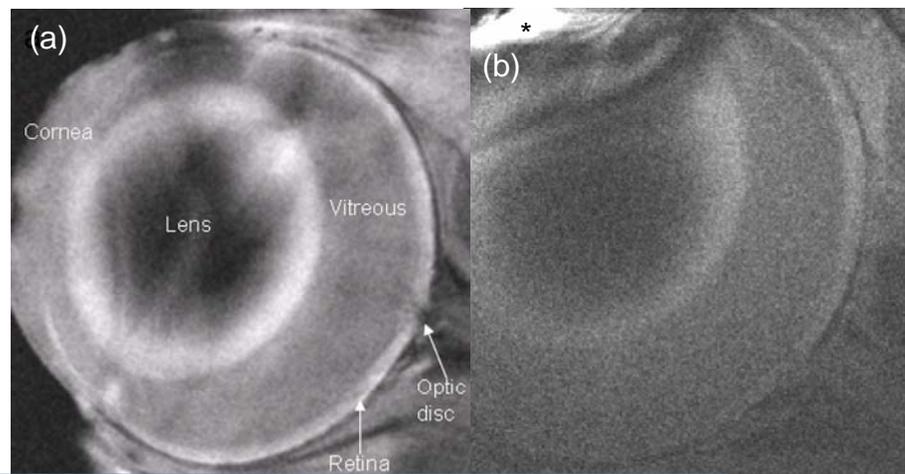
Fig. 2.9: MRI of the rat eye acquired with (a) 0.6-cm-radius RF coil and (b) 0.3-cm-radius RF coil acting in transmit/receive mode, all other imaging parameters being identical. The image acquired from the larger surface coil is clearly more uniform over the entire eye, while the image acquired with the smaller coil had a better SNR in a small region marked by *.

homogenous in concentric spheres of different radii. This surface coil design is therefore possible because the eye is a superficial organ and relatively small in size (diameter of ~0.6 cm).

High-resolution MRI of the eye was obtained using surface coils of radius 0.6 cm and 0.3 cm. The larger surface coil was placed around the eye while the smaller one was placed on the surface of the eye, near the junction of the superior lateral rectus muscle and the sclera. Figure 2.9 shows a comparison of the images acquired with both surface coils. The images acquired with the larger coil were very uniform throughout the eye and capable of easily identifying major anatomical structures of the eye as shown. Oversampling was used in the phase and frequency directions to remove wrap-around artifact at the cost of imaging time and TE. A small region in the images acquired with the small RF coil showed very high SNR indicating that this coil may be suitable for localized retinal imaging if placed directly behind the eyeball, right next to the retina. Changing the RF power to increase the penetration depth could potentially increase the excitation field from the small coil. But this is not always feasible as it leads to non-uniform flip angles and non-uniform images. Inhomogeneous B_1 field can be seen (in Fig. 2.9a and more obviously in Fig. 2.9b) as dark bands running across the image. Note that there are no obvious inhomogeneities seen across the retina. Furthermore, increased RF power deposition (increased SAR) on tissue closest to the coil can cause hotspots. An increased temperature in the eye can causes it to dry up (a painful condition), and even alter the optical properties and sensitivity of the eye during long scans.

Another possibility for retinal imaging was an even higher resolution scan of a small region by using the small coils. These coils could be physically placed behind the eye, right next to the retina. This was, however, far more difficult to achieve considering that the actual loop was connected to the (much larger) tuning and matching circuits as shown in the schematic diagram in Fig. 2.10. The coil itself and the leads connecting the coil to the tuning circuit can impinge in the eye, changing its physiological parameters like intraocular pressure and baseline blood flow. Furthermore, the leads connecting the coil to the tuning circuit will have its own associated signal loss.
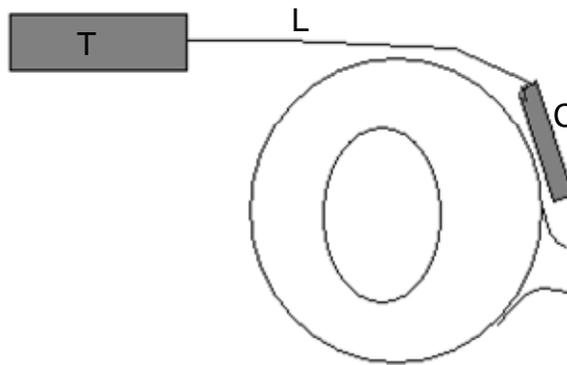
Fig 2.10: Schematic diagram of a small transmit/receive RF coil (C), placed at the back of the eyeball for high SNR imaging of the retina. A conventional coil would have to be connected to the RF tuning (T) circuit through leads (L), which could press on the eye, changing the intraocular pressure, and thus its physiological condition.

This issue however could be at least partially solved by using an inductively-coupled coil. An inductively-coupled coil uses two separate loops; one large loop in transmit-receive mode connected to the amplifiers, and a smaller loop placed close to the region being imaged; inductively coupled to the larger loop. The RF induced in one coil is picked up by the other coil in this arrangement and the greater the mutual inductance between the coils, the larger the signal induced.

In order to achieve good matching between the loops, each loop had to be individually tuned to the resonant frequency of the MRI, and placed parallel to each

other, so that their centers line up. Any gain in signal amplitude by placing a small loop right next to the retina could easily be lost by misaligning the two loops. Therefore, careful surgical placement of the small loop behind the eye would be required for successfully implementing this design. This was not a preferred setup, however, as it involved an additional interventional procedure.

We chose to explore the feasibility of inductively coupling a single-turn 3.5-mm- and a two-turn 2.5-mm-radius coil to a quadrature volume transmit/receive coil. The small loop was placed at the back of the eye, without a surgical procedure. Therefore, the tilt of the small loop could not be accurately determined. A quadrature coil is made up of two coils aligned perpendicular to each other to minimize coupling between them. Therefore, quadrature coil will pick up orthogonal components of the signal induced in the small loop, irrespective of its spatial orientation.

Figure 2.11 shows images acquired using a 2.5-mm-radius, two-turn coil, inductively coupled with a quadrature transmit/receive coil. The small coil can be seen clearly to impinge on the eye ball (arrow) and distort its shape. The FOV of this image was increased to show the extent of the region being imaged. The main drawback of using a surface coil in transmit/receive mode was the entire rat head becoming MRI visible, preventing the use of very small FOV for high resolution scans. Oversampling (of 6× to 8×) in
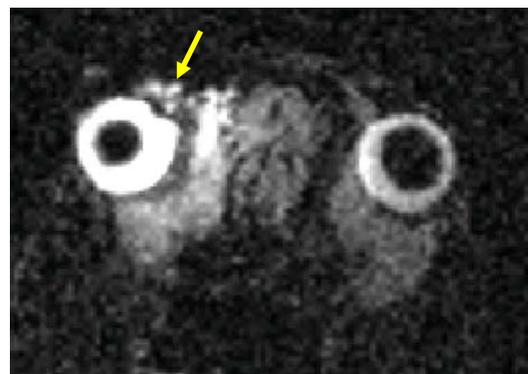
Fig. 2.11: Image of a rat eye acquired using a loop of radius 2.5 mm placed behind the eye (arrow) inductively coupled to a quadrature volume coil in transmit/receive mode.

frequency and/or phase directions was required to completely eliminate the aliasing artifact, increasing the scan/echo times. Furthermore, the gain in SNR from the small loop was only a factor of ~3 compared to the volume coil, due to poor coupling between the coils.

2.2.2 Dual-coil system

Typically, body coils have large uniform RF excitation field, imparting a uniform flip angle over a large region. However, the large distance between the tissue of interest and coil reduces its sensitivity to the received signal, thus compromising its SNR. Therefore, for high SNR and uniform images it is desirable to use a combination of large transmit coil and a small receive coil placed near the region to be imaged.

Figure 2.12 shows the image of the eye acquired with a large volume transmit coil and a single-turn, 0.6-mm-radius receive coil placed directly around the eye. This setup did not improve the retinal signal significantly. Furthermore, tissue outside the FOV is also excited by the large coil and the signal from these extraocular tissues is folded back into the image of the eye, giving rise to aliasing (wrap-around) artifacts, just as in the case of inductively coupled coil. 6 to 8× oversampling in the phase and/or frequency directions, at the cost of imaging time and TE, could be required to effectively remove these extraocular tissues from the imaging field due to the large excited region.
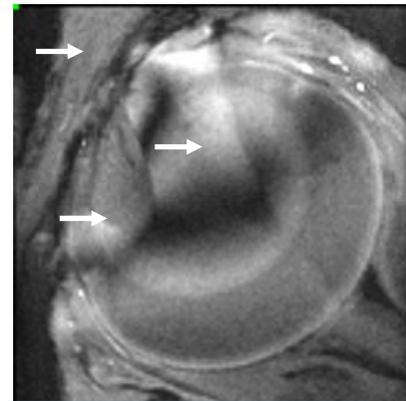
Fig. 2.12: Image acquired using a dual coil system showing aliasing (wrap-around) artifact (arrows) despite a 2× oversampling used during acquisition.

2.2.3 Conclusion

The best results for uniform retinal imaging with high SNR was achieved by using a single-loop surface coil of 0.6-cm radius placed directly on the rat head around the eye. Higher-resolution images could potentially be acquired by surgically placing an inductively-coupled small loop behind the eye, directly next to the retina, with another well-aligned surface coil acting as a pickup loop. However, this technique was too invasive for our requirements, and would not give a good overview of the entire retina.

The eye was kept moist for the duration of the scan by using a thin layer of hydroxypropyl methylcellulose eye drops. A 2× oversampling was used in both the frequency- and phase-encoding detections to remove wrap around artifacts from the high resolution scans at the cost of TE and scan time. The relatively small RF excitation field in the single-coil setup allowed the use of small FOV with minimal oversampling, compared to the large RF excitation field of the volume coil used in dual or inductively-coupled coils. This avoided complications in the setup of animals for MRI scans while minimizing any invasive procedures that may be required. Images acquired with this setup not only showed all anatomical landmarks of the entire eye, but also had good resolution to differentiate retinal layers as seen in the following sections.

2.3 Animal Setup

All MRI studies were performed on a Bruker 4.7T or 7T system, equipped with an 11.6 cm, 20G/cm gradient-coil set. The rats were anaesthetized with isoflurane and their

trachea intubated using a 14 gauge (or 16 gauge for smaller rats) catheter as shown in Fig. 2.13.

To perform the intubation, the rats were deeply anesthetized using 3-5% isoflurane for 2-3 min, and then placed on a vertical platform as shown. The head was tilted back using rubberband as shown. A laryngoscope was used to carefully insert the catheter
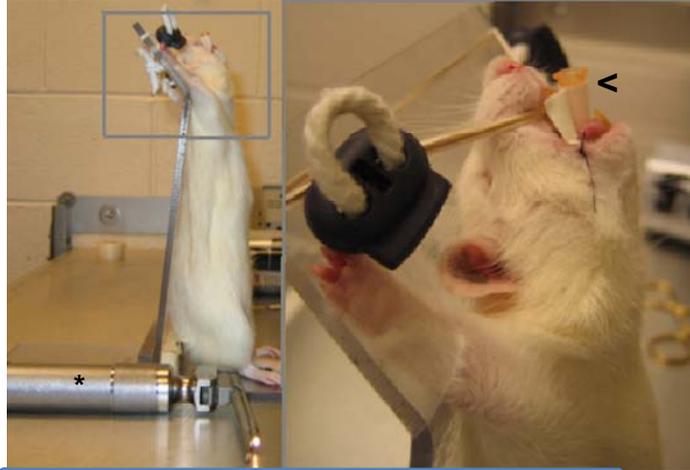
Fig 2.13: Animal setup. Tracheal intubation in rat was performed by using a 14 gauge catheter(<) and a laryngoscope (*). The rat head was tilted back slightly to make the procedure easier.

into the trachea. The entire procedure took approximately 30 seconds and was completed before the rat recovered from anesthesia. The rat was then taken down from the platform, and anesthesia resumed using 2% isoflurane. The white tape attached to the catheter was sutured securely to the corner of the mouth. The rats were artificially ventilated (Harvard apparatus, Holliston, MA) either in room air or under mildly hyperoxic conditions (30% O2) during the reminder of the setup procedure.

In some rats, the femoral vein was catheterized for remote delivery of drugs like pancuronium, Gd-DTPA or MION. If the femoral vein was not catheterized, then an intraperitoneal line was placed to remotely administer pancuronium. Similarly, blood pressure was monitored by catheterizing the femoral artery. A PE20 tube was inserted into the femoral artery and the other end connected to a pressure transducer (Harvard

Apparatus, Holliston, MA). The blood pressure, end tidal CO2, and rectal temperature (Kent Scientific, CT) were recorded using a Biopac system (AcqKnowledge, Harvard Apparatus, Holliston, MA).
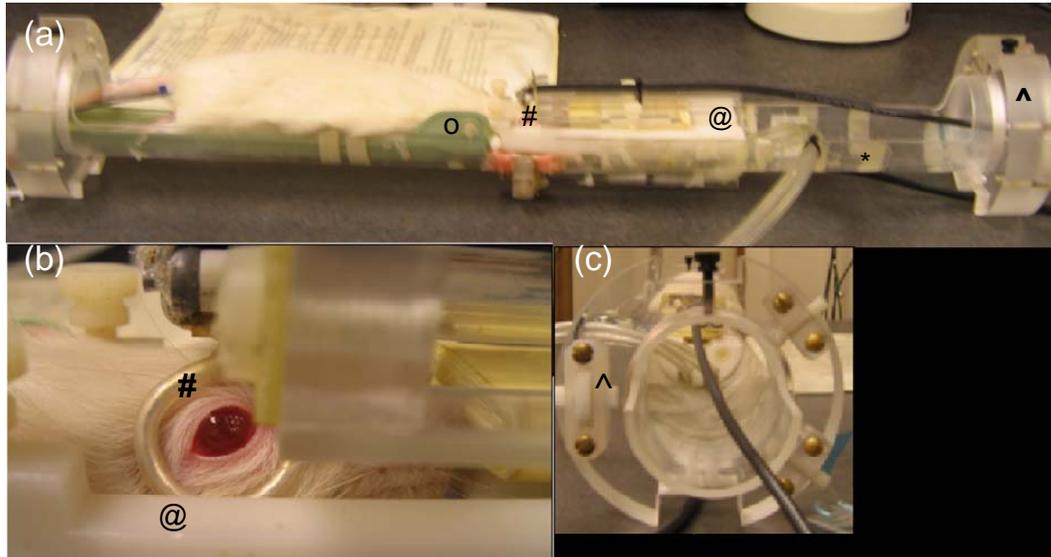
Fig. 2.14: Animal setup. Photograph of the animal-holding apparatus for the MRI. (a) The overall setup is seen with cradle (*), offcenter rings (^), RF coil (#), stereotaxic headset (@), and circulating warm water heating pad (o). A larger magnification of the (b) RF coil and the (c) offcenter cradle rings are also shown.

After surgery, the head was secured in a plastic stereotaxic head holder using ear and tooth bars. The rats were then secured onto an imaging cradle as shown in Fig. 2.14. The imaging cradle was designed with off-center supports or rings (Fig. 2.14c) so that the eye was always positioned in the center of the magnet. The center of the cradle could be swapped from left to right by rotating the rings through 180 degrees, depending upon the eye being imaged. The rats were then setup in the cradle with a circulating hot water pad to maintain its body temperature for the
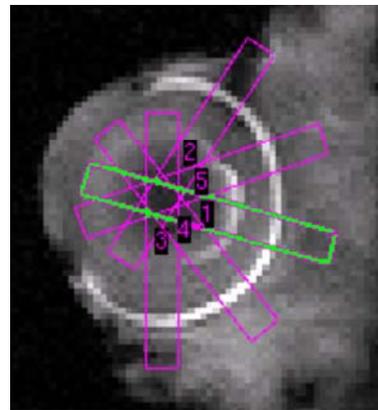
Fig. 2.15: Slice positioning. Radial plan of five 1mm thick slices covering the retina shown on a horizontal section of the eye. The slice marked with green is aligned along the visual-axis of the eye.

duration of the scan. The temperature of the water in the hot water pad was feedback-controlled by a rectal temperature probe.

Horizontal multislice images were first acquired as a localizer parallel to the base of the skull covering the entire eye. In an image that included the eye and optic nerve, imaging slices were placed along the visual axis as shown with the green box in Fig. 2.15. For a more complete coverage of the retina, 5 slices were positioned in a radial fashion (radial plan) as seen in the figure. The regions in which the slices cross had very poor SNR but, that region was placed on the lens as shown.

2.4 Data Analysis

2.4.1 Signal averaging

SNR and CNR are important imaging parameters that determine the quality of an MR image. While techniques like improving coil design and minimizing eye motion are first step, it was possible to further improve the SNR and CNR by reducing the detected noise. The noise in an MRI system is Johnson noise [113], which arises from Brownian motion of electrons within the tissue and coil. Taking multiple measurements of the sample under identical conditions decreases the effect of random noise in the image, while the contribution from the signal remains the same. Typically, the SNR of the image increases by a factor equal to the square root of the number of signal averages.

The down-side of signal averaging is an increase in scan time. In the high-resolution MRI of the retina, it was also imperative to avoid any movement artifacts, however small, during the scan. A longer scan time means more probability of eye motion. Optical measurements lasting for only 4 min revealed small oscillations of ~6-

μm amplitude. Even though the movements associated with respiration were minimized by controlling the ventilator volume, removal of all drift or movements over a scan lasting ~ 10-15 min could not be ruled out. Some drift on the order of 30 to 50 μm was sometimes observed over these scan times, which could be picked up by the high-resolution scans. It was therefore decided that the high-resolution images would be acquired by taking multiple short scans (a few seconds to 1 min per scan) and averaging them offline. This allowed for close observation of movement from one scan to the other, and the possibility that any drift or movement could be corrected before averaging. Also, images showing any motion artifacts could be dropped before averaging, thus preventing movement at a single time point from spoiling the entire scan.

As a first step, images were viewed with Stimulate (John Strupp, University of Minnesota). Any drift or movement in the images were then corrected using either ImageJ (NIH, Register ROI plugin: open software by Michael Abramoff, MD, PhD) or
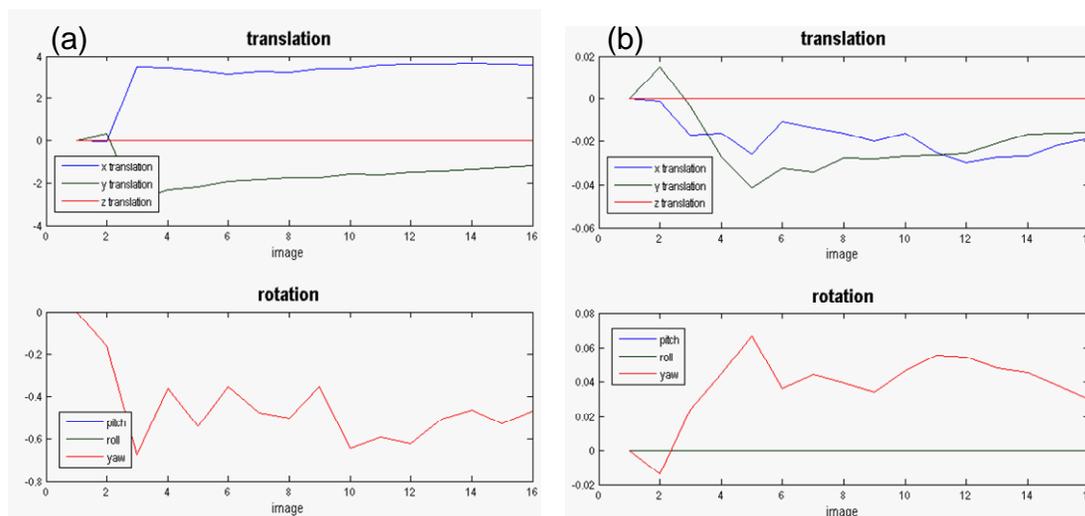
Fig. 2.16: Movement correction. (a) One of the worst cases of eye movement shows one significant movement between images 2 and 3 and (b) same set of images after correction with SPM. Scale: top row is number of pixels; bottom row is degrees. Note that the scale in (a) is 100 (top) and 8 (bottom) times that in (b).

Matlab-based spatial parametric mapping or SPM (The FIL methods group, London, UK) with six-parameter affine registration with a Mutual Information algorithm [114]. Eye movement calculated by SPM software for a typical scan taken with 16 repetitions over 13 min and 40 s is shown in Fig. 2.16a. SPM corrected any drift artifact as shown in Fig. 2.16. Sequences with residual drift artifacts after SPM corrections were discarded from analysis. Signal averaging was always done on these motion corrected images.

2.4.2 Quantitative analysis

The retina has a thin and elongated shape. Since the entire retina was to be imaged
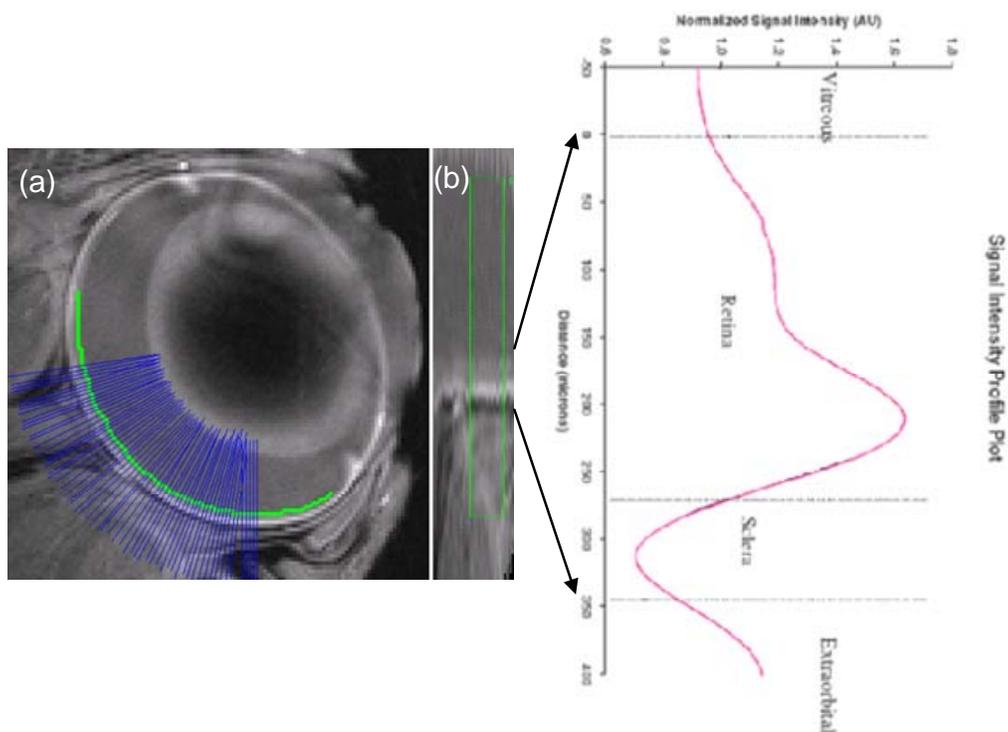
Fig. 2.17: Signal intensity profile plot across the retina. (a) The green line traces the inner edge of the retina, and blue lines are drawn perpendicular to the edge at each pixel. (b) Signal intensities along the blue line are then interpolated into another image, before the average signal intensities of a portion of the retina (box) is calculated and plotted.

at the same time, only a few pixels were expected to make up its thickness. Therefore, the quantitative analysis of the signal intensities within the retina required very careful

placement of the ROIs. Such ROI placements became more difficult for detecting finer structures within the retina as ROIs always run the risk of being contaminated by the signal intensities of their neighboring pixels. Therefore, an alternate method was devised for a more accurate calculation of the retinal signal intensities.

Programs were written in Matlab to generate signal intensity profile plots across the retina. Firstly, the 'edge' function in Matlab was used to detect all edges in the image by looking for local maxima of the gradient in the image calculated using the derivative of the Gaussian filter ('canny option'). This option was found to be most reliable for detecting the retinal edges. The pixels that traced the retinal edge were stored (Fig. 2.17a). Slope of the edge at each point (except for the first and last 8 points) was found by curve fitting 8 of its neighbors to a polynomial equation of 4th degree, and finding the first derivative at that point. Lines were then drawn perpendicular to the edge extending for a distance of 25 pixels on either side of the retina. The pixel intensities along these lines perpendicular to the retina were interpolated into another image, thereby flattening retina (Fig. 2.17b). The signal intensities along the direction parallel to the retina were averaged and plotted as a function of distance from the estimated vitreo-retinal boundary. This process of analysis was used throughout this thesis.

The signal-intensity-profile-plot method described here proved useful in quantifying the thickness and signal intensities in sub-retinal structures as seen in Chapters 3, 4, 5, 6 and 7. However, neither the thickness of these sub-retinal structures, nor their signal intensities can be accurately determined by this technique due to partial volume effect from neighboring pixels. A more complete discussion of these effects can be found in Section 4.4.3, and is referred to in relevant sections throughout this thesis.

Chapter 3: T_1, T_2, T_2* and Water Apparent Diffusion Coefficient of the Rat Retina

The knowledge of quantitative T_1, T_2, T_2* and water apparent diffusion coefficient (ADC) would help to systematically optimize structural, physiological and functional MRI contrast of the retina. Quantitative T_1, T_2, T_2* and average ADC maps of the retina were acquired at 50 μm in-plane resolution. The quantitative parameters were first calculated by carefully placed ROIs on the retina, vitreous and extraocular muscle. ROI analysis yielded an average retinal T_1 of 1500 ± 500 ms, T_2 of 59 ± 1 ms T_2* of 30 ± 10 ms and ADC of $1.0 \pm 0.7 \times 10^{-3}$ mm^2/s at 7T. Profile plots of pixel-by-pixel maps of T_1, T_2, T_2* and average water ADC were drawn across the retina to determine variations in these parameters within the retina. These quantitative measurements are expected to set the stage for future MRI studies of the retina.

3.1 Introduction

The retina consists of multiple well-defined layers which include, starting from the vitreous boundary, the ganglion cell layer, inner plexiform layer, inner nuclear layer, outer plexiform layer, the outer nuclear layer, and the photoreceptor segments. The plexiform layers are synaptic links between adjacent cell bodies. The retina is nourished by the *retinal* and *choroidal* vascular layers located on either side. The *retinal* vasculature exists within the ganglion cell layer and the inner nuclear layer. The *choroid* is located beneath the photoreceptor layer, sandwiched between the retinal pigment epithelium and sclera. The outer nuclear layer and the photoreceptor segments in the middle are avascular. The total retinal thickness including the choroid, is approximately 300 μm [115, 116]. Imaging techniques that are capable of visualizing different retinal layers are important for studying normal physiology, to diagnose many retinal diseases and longitudinally track their progression.

The retina has historically been imaged using optical techniques. The fundus camera provides surface anatomy. Intrinsic optical imaging yields information regarding relative oxygenation and blood volume [117]. Fluorescein angiography [118] and indocyanin-green angiography [119, 120] provide qualitative blood flow of large vessels [121] whereas laser-Doppler flowmetry measures blood flow changes from a small area [122, 123]. More recently, optical coherence tomography with adaptive optics offer exquisite depth-resolved anatomical information [124] and initial results of blood-flow imaging of the retina using optical coherence tomography has been demonstrated [62, 125]. While these optical imaging techniques have made remarkable contributions to our

understanding of retinal physiology, there are several limitations. First, these techniques require an unobstructed light pathway for signal detection. Diseases, such as cataract formation and vitreal hemorrhage, may preclude the use of optical imaging techniques. Second, due to tissue absorption of visible or near-visible light, these techniques (except optical coherence tomography) are limited to imaging the retinal surface [126, 127]. Finally, to-date, none of the above imaging techniques have the capability to study anatomy, physiology and function with layer-specificity in a single setting non-invasively.

Magnetic resonance imaging is a powerful diagnostic tool capable of providing anatomical, physiological (oxygenation, blood flow and blood volume) and functional information without depth limitation in a single setting. While MRI has lower spatial resolution and longer acquisition times compared to optical imaging techniques, MRI of retina has a large field of view and can be performed without depth limitation. Furthermore, MRI is not limited by media opacity and can measure blood volume in small vessel (as opposed to large vessels in fluorescein angiography). Advances in MRI technology contributed by numerous laboratories have made very high spatial resolution possible, with the capability of visualizing columnar and laminar structures *in vivo* [128] and single cells *in vitro* [129, 130]. Layer-specific anatomical [115, 131], manganese-enhanced [112], basal blood-flow and physiologically-induced blood-flow [132] MRI, visually-evoked [133] and layer-specific, physiologically-induced BOLD fMRI [115] have been reported.

In order to systemically optimize structural, physiological and functional MRI contrasts of the retina, knowledge of quantitative T_1, T_2, T_2^* and water apparent diffusion

coefficient (ADC) of the retina and its surrounding tissue are essential. Moreover, these MRI parameters will likely change in disease states and thus quantitative MRI measurements could be utilized to stage retinal disease progression and monitor therapeutic intervention. In return, the highly structured retina, with multiple well-defined layers and its layer thicknesses, provide an excellent model to test emerging high-resolution anatomical, physiological and functional MRI techniques. The goal of the present study was to measure quantitative T_1, T_2, T_2* and water ADC in the normal adult rat retina. These measurements are expected to set the stages for future MRI studies of the retina.

3.2 Theory

3.2.1 T_1 map

As seen in Section 1.4, an RF pulse rotates the tissue magnetization away from the B_0-field direction (z-axis), which then returns to its equilibrium following RF excitation according to the T_1 relaxation time constant. If a second RF pulse is applied before complete recovery, the magnetization in the x-y plane is proportional to the tissue-water T_1 relaxation time constant and the time interval between the RF pulses. For an image acquired immediately after a second 90º RF pulse, the signal intensity S is given as:

$$S = M_0 \left(1 - e^{-\frac{TR}{T_1}} \right), \tag{3.1}$$

where M_0 is the proton spin density and TR is the repetition time. A series of images acquired with different TR values can then be used to determine the T_1-relaxation-time constant using a curve-fitting algorithm.

However, excitation power from a surface coil varies with depth of tissue and different pixels along the retina may not experience a perfect 90º RF pulse. The T_1 relaxation equation therefore needs to be modified to include the efficiency of the excitation α (with $\alpha=1$ for a perfect 90º pulse) as

$$S = M_0\left(1-\alpha e^{-\frac{TR}{T_1}}\right),$$ (3.2)

where M(0) is the residual magnetization immediately following the RF pulse and

$$\alpha = \frac{M_0 - M(0)}{M_0}.$$

3.2.2 T_2 and T_2* map

After an RF pulse, the x-y component of magnetization decays with a time constant of T_2. The signal decay is caused by dephasing resulting from subtle changes to the resonant frequency of individual spins, depending upon their environment, as described Section 1.4. T_2 or transverse relaxation is an intrinsic property of the tissue but additional signal dephasing can occur due to local magnetic field inhomogeneities and tissue susceptibility, as discussed in Chapter 1. While the 180º RF pulse in a spin-echo sequence rephrases the magnetic field inhomogeneities and susceptibility effects, the gradient-echo pulse sequence does not. Therefore, images acquired at different echo-

times (TE) in a spin-echo sequence depends only on the T_2 relaxation rate, and that of a gradient-echo sequence depends on the T_2* relaxation rate.

The T_2 decay of signal in a spin-echo sequence is given as

$$S = S_0 \left(e^{-\frac{TE}{T_2}} \right), \tag{3.3}$$

where S_0 is the spin density and S is the signal intensity at the echo time TE. The T_2 map was generated using a Matlab fitting program based on the non-linear least squares method, as was the case for T_1 fit. The flip angle experienced by the tissue is less critical in measurement of transverse relaxation compared to longitudinal relaxation, and was ignored in the calculation.

The T_2* relaxation time was calculated in a similar manner. However, magnetic field inhomogeneities affect the calculation of T_2* relaxation as they add to the rate of signal dephasing. Consequently, uniform shimming of the entire imaging region was critical to minimize this contribution in the calculated T_2* map.

3.2.3 Water ADC map

Molecular diffusion during the process of echo generation (TE), results in reduced signal intensity through destructive phase interference between individual precessing isochromats. Routine MRI scans can be made particularly sensitive to diffusion by the application of two large gradient pulses of equal amplitude, but opposite sign or sense, within the TE period. These diffusion gradients act to encode and decode the spatial location of the spins in the tissue. A net displacement of spins, between the encoding and decoding periods, cause a loss of signal intensity in the final image.

Mathematically, the ADC (or D) of a molecule in the tissue of interest is given by equation $S = S_0(e^{-bD})$, where S_0 is the spin density and S is the signal intensity obtained with a diffusion gradient applied. The b-value (b) is the measure of the strength of the diffusion encoding, and depends on the strength and separation of the diffusion gradients. The water ADC maps were generated using a Matlab program from images acquired with and without diffusion encoding and according to the equation:

$$\frac{S}{S_0} = e^{-bD} \text{ or } \ln\left(\frac{S}{S_0}\right) = -bD \text{ ; rearranging gives } D = \frac{\ln\left(\frac{S_0}{S}\right)}{b}. \qquad (3.4a,b)$$

Therefore, the water ADC can be calculated from two diffusion-weighted images, one acquired with very low b-value and another with a large b-value. Just as in the case of the T_2 map, the water ADC map is not greatly affected by the flip angle. However, the diffusion gradient strength, duration and separation need to be carefully chosen for optimizing the ADC measurement.

3.3 Materials and methods

Animal preparations: Experiments were performed on normal adult male Sprague Dawley rats (300-350 g, n = 5) anesthetized with isoflurane, intubated using a 14 gauge catheter, paralyzed with pancuronium bromide (3 mg/kg first dose, 1 mg/kg/hr, i.p.) and mechanically ventilated as described previously. End-tidal CO_2 (Surgivet capnometer, Waukesha, WI), heart rate and arterial oxygen saturation (Nonin-8600, Plymouth, MN), and rectal temperature (Digisense, Cole Palmer, Vernon Hills, IL) were continuously monitored and maintained within normal physiological ranges.

MRI methods: MRI studies were performed on a Bruker 7-Tesla/30-cm magnet and a 40 G/cm B-GA12 gradient insert (Bruker, Billerica, MA). Rats were placed in a head holder consisting of ear and tooth bars. A small circular surface coil was placed on the eye for imaging. Magnetic field homogeneity was optimized using standard FASTMAP with an isotropic shimming voxel encompassing the entire eye. A single mid-axial imaging slice bisecting the center of the eye was imaged to minimize partial-volume effect.

Data to produce T_1 maps were acquired using progressive saturation recovery sequence with spin-echo acquisition and variable TRs of 100, 200, 400, 800, 1600, 3200, and 6400 ms, TE of 31.1 ms, flip angle = 90°, and number of averages = 4. The other parameters were slice thickness = 0.8 mm, FOV = 12.6 mm × 12.6 mm and data matrix = 256 × 256, giving an in-plane resolution of 50 μm.

Data to produce T_2 maps were acquired using conventional Hahn spin-echo acquisition with variable TEs of 31.1, 41.1, 51.1, 61.1, 81.1 and 101.1 ms, TR of 3200 ms, flip angle = 90°, and number of averages = 4. The other parameters were the same as in T_1 measurements.

Data to produce T_2* maps were acquired using gradient-echo acquisition with variable TE's of 6.5, 12 and 20 ms and TR of 400 ms, flip angle = 30°, and number of averages = 4. The other parameters were the same as in T_1 measurements.

Water ADC maps were measured using conventional spin-echo diffusion-weighted acquisition with variable b-values of 0 and 1000 s/mm^2, TR = 2000 ms, TE = 20.5 ms, diffusion-gradient separation Δ = 12 ms, gradient duration δ = 3.5 ms, slice thickness = 0.8 mm, FOV = 6.4 mm × 6.4 mm and acquisition matrix = 128 × 128, giving

an in-plane resolution of 50 μm. The water ADC was measured along the x-, y- and z-gradient directions separately.

The image acquired using a spin-echo sequence with TR = 6400 ms, TE = 31.1 ms, and an in-plane resolution of 50 μm was used as a reference image for the signal-intensity-profile plots. This image showed the best contrast between the vitreous, retina and scleral tissue, and could be easily used to identify the retinal boundaries. This image was aligned with the retinal maps.

Data analysis: Image analysis employed code written in Matlab (MathWorks Inc, Natick, MA) and STIMULATE software (University of Minnesota). First, time-series images were corrected for motion and drift as described previously. Quantitative MRI parameters were analyzed using region-of-interest (ROI) analysis and pixel-by-pixel calculation. ROI analyses were performed to obtain average water T_1, T_2, T_2* and ADC values for the vitreous, retina and extraocular tissue. Pixel-by-pixel T_1, T_2 and T_2* maps were calculated using a Matlab curve fitting routine with non-linear least-squares regression. To objectively quantify these MRI maps, automated profile analysis was performed [115]. Briefly, the retina was first detected using an edge-detection technique. Radial projections perpendicular to the vitreous boundary were then obtained with spatial interpolation (3×). Quantitative MRI parameters were plotted across the retinal thickness and averaged for the entire length of the retina. All values and error bars on graphs were reported as mean ± standard deviation (SD).

3.4 Results

Signal intensity from the vitreous, retina and extraocular muscle obtained at various TR and TE are plotted in Fig. 3.1. The signal intensities are normalized to the signal intensity from the vitreous at TR = 6400 ms in the T_1 plot, and at TE = 31.1 ms in the T_2 plots. The T_1 and T_2 relaxation times of the retina and extraocular muscle were
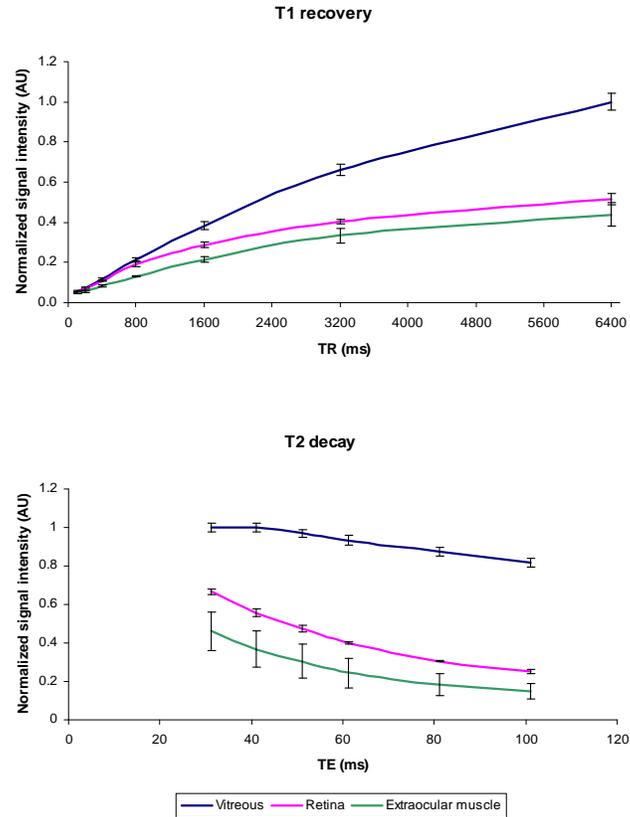
Fig. 3.1: Changes in normalized signal intensity with TR and TE. The signal from the vitreous, retina and extraocular muscle is normalized to the vitreous at longest TR and shortest TE. (a) The signal intensity from the tissue is seen to (a) increase with TR and (b) decrease with TE, as expected (n=5, mean ± SD)

	Vitreous	Retina	Extraocular muscle
T1	4.5 ± 0.3 s	1.5 ± 0.5 s	2.5 ± 0.4 s
T2	450 ± 80 ms	59 ± 1 ms	47 ± 7 ms
T2*	60 ± 20 ms	30 ± 10 ms	NA
Average ADC (x10^{-3} mm^2/s)	2.3 ± 0.3	1.0 ± 0.3	1.1 ± 0.3

Table 3.1: Quantitative T_1, T_2, T_2* and average water ADC of the retina derived from ROIs drawn on the vitreous, retina and extraocular muscle. The T_2* value from extraocular muscle was not available due to large susceptibility artifacts (n=5, mean ± SD)

seen to be shorter than that of the vitreous. The signal intensities from each tissue increased with TR and decreased with TE as expected. The signal intensity from the vitreous was seen to increase by 32% to 40% between the TR of 3200 ms and 6400 ms, while that from the retina and extraocular muscle increased only by 6.3% to 8% in the same TR period. Similarly, the signal intensities from the retina and extraocular muscle were seen to decrease by 40% to 52% between the TE values of 31.1 ms and 61.1 ms, while that from the
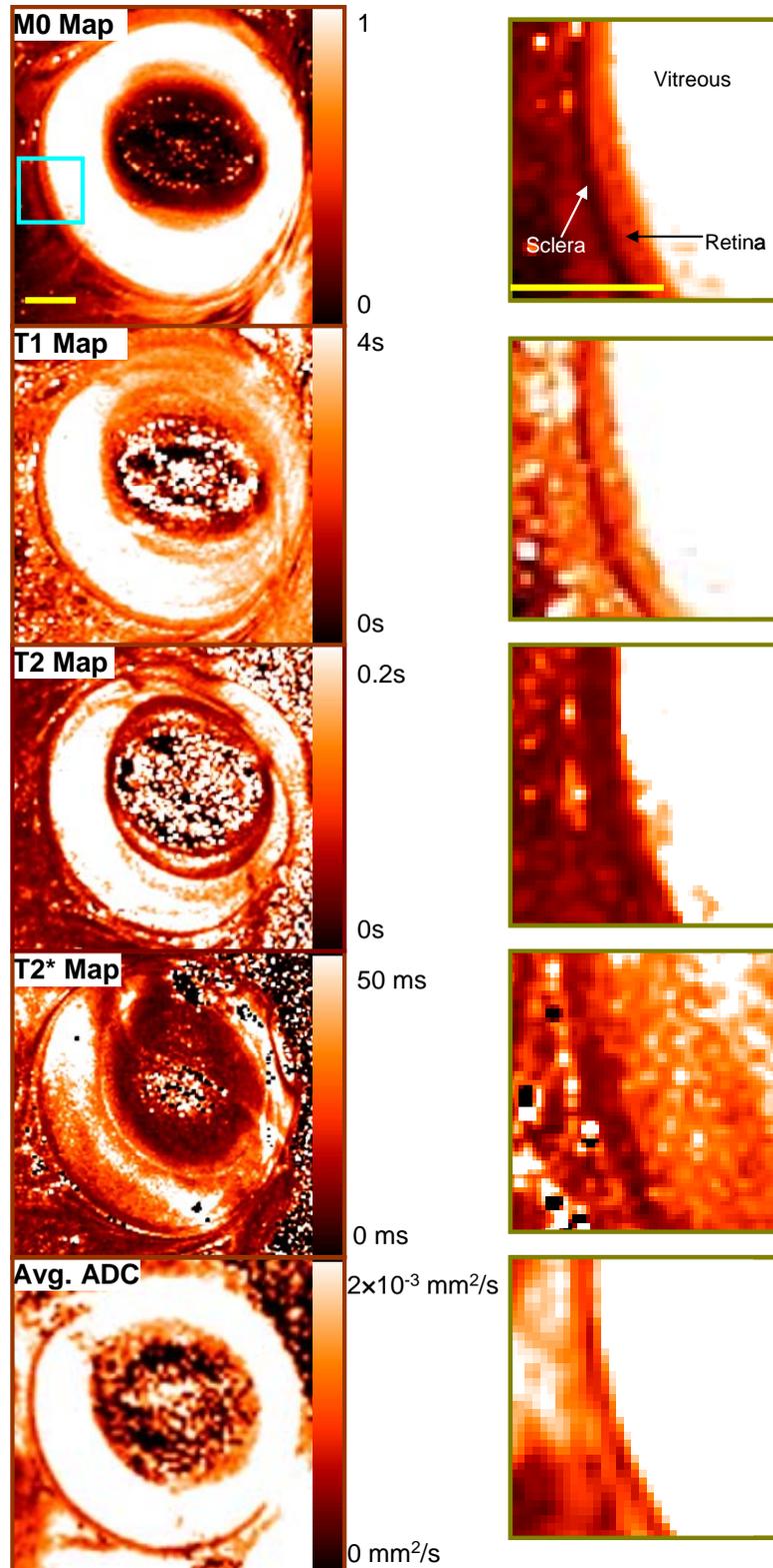
Fig. 3.2: Map of M_0 (blue inset is region being magnified), T_1, T_2, T_2^* and average water ADC of the rat eye. A region of the retinal map (blue box) is magnified on the right in each case. The display scales for individual maps are shown on the right side of each map. In general, vitreous showed much higher longitudinal, transverse relaxation times as well as water ADC as compared to the retina. Scale bar is 1 mm.

vitreous decayed only by 8% to 11% in the same TE interval.

Water T_1, T_2 and ADC values were larger in the vitreous compared to the retina as expected. The average T_1 values calculated from the vitreous, retina and the extraocular
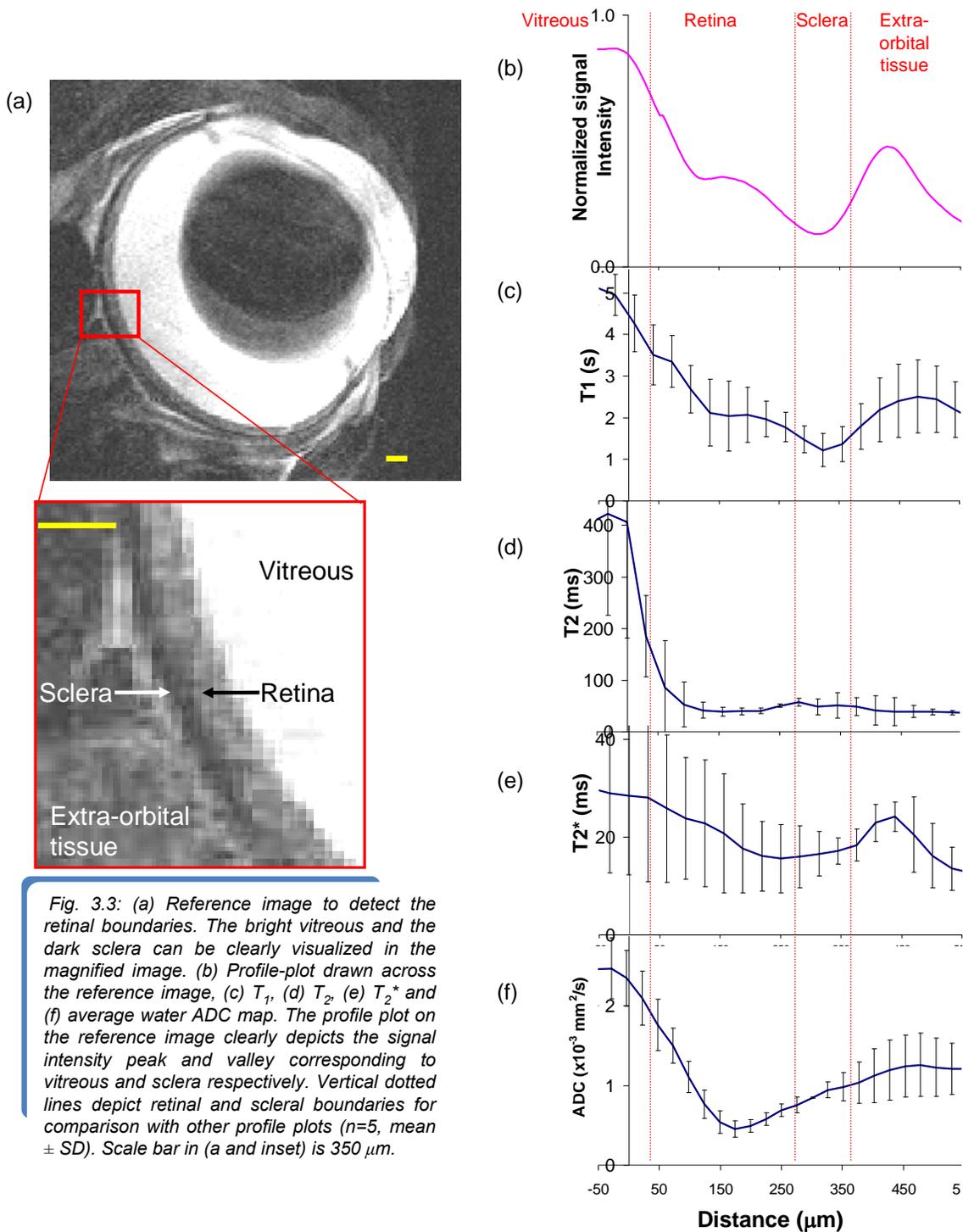
Fig. 3.3: (a) Reference image to detect the retinal boundaries. The bright vitreous and the dark sclera can be clearly visualized in the magnified image. (b) Profile-plot drawn across the reference image, (c) T_1, (d) T_2, (e) T_2* and (f) average water ADC map. The profile plot on the reference image clearly depicts the signal intensity peak and valley corresponding to vitreous and sclera respectively. Vertical dotted lines depict retinal and scleral boundaries for comparison with other profile plots (n=5, mean ± SD). Scale bar in (a and inset) is 350 μm.

muscle were 4500 ± 300 ms, 1500 ± 500 ms and 2500 ± 400 ms, respectively. Similarly, the average T_2 values for the vitreous, retina and extraocular muscles were 450 ± 80 ms, 59 ± 1 ms and 47 ± 7 ms, respectively. The average T_2^* values from the vitreous and retina were 60 ± 20 ms and 30 ± 10 ms, respectively, while the average water ADC values were $2.3 \pm 0.3 \times 10^{-3}$ mm^2/s and $1.0 \pm 0.3 \times 10^{-3}$ mm^2/s, respectively, as summarized in Table 3.1. The pixel-by-pixel map of M_0 (from T_1 data), T_1, T_2, T_2^* and ADC from the rat eye is shown in Fig. 3.2.

Figure 3.3a shows a reference image in which the hyper-intense vitreous and hypo-intense sclera can be easily distinguished from the retina. The profile plot of the reference image shows distinct boundaries between the retina and the vitreous as well as retina and the sclera (Fig. 3.3b). The tissue boundaries, estimated at the half-height of signal intensity changes at the structural boundaries in the reference profile plot (denoted by vertical dotted lines) helped in the analysis of water T_1, T_2, T_2^* and average ADC, as shown in Fig. 3.3. To provide some quantitative analysis, quantitative MRI parameters were averaged every 50 μm from -100 to 300 μm, where 0 is defined as the edge of the vitreous in the reference image. The average water T_1, T_2, T_2^* and ADC values are summarized in Table 3.2.

Water T_1, T_2 and ADC of the vitreous were high compared to the retina as expected due to its more fluid-like properties. Sclera and lens are more solid tissue with low water density and short T_2 and their measurements were less reliable, given the ranges of TE used. The quantitative MRI profiles are relatively uniform within the retina, with high and low values on either side due to partial-volume effects.

	-100 to -50 μm	-50 to 0 μm	0 to 50 μm	50 to 100 μm	100 to 150 μm	150 to 200 μm	200 to 250 μm	250 to 300 μm
T1 (s)	4.6 ± 0.5	4.9 ± 0.4	4.4 ± 0.8	3.7 ± 0.6	3.1 ± 0.7	2.5 ± 0.8	2.1 ± 0.5	2.0 ± 0.4
T2 (ms)	400 ± 200	420 ± 80	200 ± 100	70 ± 20	42 ± 7	40 ± 4	50 ± 10	50 ± 20
T2* (ms)	30 ± 20	30 ± 10	30 ± 20	30 ± 10	20 ± 10	20 ± 10	17 ± 6	16 ± 6
Avg. ADC ($\times 10^{-3}$ mm²/s)	2.3 ± 0.5	2.5 ± 0.4	2.4 ± 0.4	1.8 ± 0.4	1.2 ± 0.4	0.6 ± 0.2	0.5 ± 0.1	0.7 ± 0.1

Table 3.2: Quantitative T_1, T_2, T_2 and average water ADC of the retina, as a function of distance from the vitreo-retinal surface. (n=5 rats, mean ± SD)*

3.5 Discussion

This study reports the layer-specific measurements of water T_1, T_2, T_2* and ADC of the retina across the retinal thickness at 7T. Water T_1, T_2, T_2* and ADC of the retina are similar as those of the brain but differ markedly from those of the vitreous and sclera. These data are helpful for systemically optimizing structural, physiological and functional MRI contrasts in the retina. These MRI parameters can also be useful for optimizing parameters for anatomical and functional MRI studies, staging retinal disease progression and monitoring therapeutic intervention.

3.5.1 Interpolation and partial-volume errors in profile-plots

The resolution of the images used for the calculation of MRI parameters herein (50 μm) provided only 5 to 6 pixels across the retina. ROI analyses of the retinal-MRI-parameters were error-prone, due to partial volume contamination from neighboring pixels as well as due to any imperfections in drawing the ROI. Furthermore, ROI analyses provide a single value for the retina and cannot depict any variations in parameter within the retina.

On the other hand, signal-intensity-profile plots across the retina provide a practical way to detect subtle variations in signal-intensities within the retina. However, this technique is also prone to contamination from neighboring pixels during interpolation of the pixel-intensities. Interpolation was essential in the technique to smoothly fit the intensities of the pixels, which were otherwise relatively far apart within the retina. Interpolation performed with three points per pixel minimized the contamination from neighboring pixels and provided a smooth profile which was representative of the actual image. Matlab-based simulations (reported in Chapter 4, and discussed in Section 4.4.3) [115] showed that the intensity and thickness determined using signal-intensity-profile plots matched the actual intensity and thickness in the image for layers thicker than the pixel size. Since the thickness of the retina is larger than the image resolution, the parameter values obtained from the profile plots can be deemed accurate. Finally, the profile-plot technique was semi-automated to minimize errors and bias from the operator.

The MRI parameters calculated from the vitreous was consistently higher than that from the retina as expected, causing a large partial volume error in the vitreo-retinal boundary as seen in the profile plots. In order to more accurately determine the tissue boundaries, a reference image was chosen that had high contrast between the vitreous, retina and sclera, as seen in Fig. 3.3. A profile plot drawn on such an image showed retina at half the signal intensity of the vitreous and sclera at about 20% of the vitreal signal intensity. Vitreo-retinal and sclero-retinal boundaries were drawn at signal intensity halfway between the adjacent tissues, a technique modified from the well-established full-width at half-maximum technique of detecting layer thickness [115].

3.5.2 Accuracy of calculation

Optimization of the RF pulses and imaging parameters are essential for the accurate calculation of these relaxation parameters. As seen in the Section 1.4 of the Introduction chapter, a spin-echo acquisition for T_1 calculation assumes a 90º and 180º RF pulse for the acquisition of the signal. Any changes to the 90º or 180º RF pulses, due to the use of a surface coil, can change the shape of the T_1 curve and underestimate the T_1 of the tissue. This issue was mitigated by using a large enough surface coil that could provide a relatively uniform flip angle throughout the eye as discussed in Chapter 2.

The T_1 and T_2 values of the vitreous may be more susceptible to experimental errors because of the choice of parameters. Firstly, TR may not be sufficiently long for complete recovery. Ideally, the longest TR value chosen for the T_1 calculation needs to be comparable to the time required for complete recovery of M0, which is ~5 times the T_1 of the tissue. The signal intensities from the retina and the extraocular tissue did not significantly increase as the TR is increased from 3200 to 6400 ms (6.3% to 8%), indicating an almost complete recovery of M_0 in these two tissues. However, the signal from the vitreous was found to increase by 32% to 40% as the TR increased from 3200 to 6400 ms. The T_1 of the vitreous was therefore more likely to be underestimated. The reliability of the calculation was increased by using a larger number of sampled TR values and a non-linear least-squares algorithm for fitting the data. A simulation to determine the accuracy of fit revealed that the T_1 value could be estimated with an accuracy of 97 ± 2% for a tissue T_1 of 1000 ms and 92 ± 3% for a tissue T_1 of 5000 ms with the parameters chosen herein and 2.5% added noise (low end of the experimental noise in the MRI images, data not shown).

Secondly, TE may not be sufficient long for the vitreous signal to decay by a factor of 1/e (poor dynamic range). The longest TE for T_2 calculation should ideally show a signal attenuation of about 50-60% from the shortest TE. An approximately 50% decay in signal intensity is seen from both the retina and extraocular tissue between TE values of 31.1 and 61.1 ms. The signal intensity in the vitreous, on the other hand, was reduced only by ~11% between the same echo times, with a maximum attenuation of the vitreal signal of only about 20% at the longest TE value. The vitreal T_2 calculation was therefore likely to be more affected by noise due to its small dynamic range. However, the parameters used for imaging the retina provided adequate signal intensity changes for reliable calculation of the T_1 and T_2 relaxation times.

The calculation of T_2^* was more inaccurate as observed by the large standard deviations in the profile plot. T_2^* decay of signal depends not only on the intrinsic T_2 decay, but also local magnetic field inhomogeneities as well as tissue susceptibility. In most cases these artifacts resulted in regions of high T_2^*, as seen in the corresponding map in Fig. 3.3. Retinal T_2^* imaging was especially challenging due to the large susceptibility differences in various tissue in close proximity to the retina, like fat behind the eye, vitreous and lens, as well as air due to the relatively superficial location of the retina. Care was taken to position the eye in the center of the magnet with off-center legs on imaging cradle as discussed in Section 2.3 of Chapter 2, and this error was minimized through voxel shimming using the FASTMAP algorithm [134].

3.5.3 Comparison with brain data

Very few reports of brain T_1 measurements *in vivo* at 7T have appeared in the literature. The whole-brain T_1 was 1.8 ± 0.1 s in rats (unpublished data) and is in agreement with previously reported values in mice (*ca.* 1.6 s in the cortex and 1.7 s in hippocampus [135]) and rats (1.6 s in striatum and cortex [136]) at 7 T. The quantitative T_1 value measured from the thalamus of rats at 7T is reported to be 1780 ± 165 ms [137]. All these reported T_1 values are comparable to the T_1 measured for the retina herein. Similarly, T_2 values from the rat brain have been reported to be 47.8 ms [138] and 43 ± 1 ms for grey matter in the spine [139], which correspond well with the T_2 values measured from the retina herein.

The average water ADC measured from the normal brain cortex is 0.7×10^{-3} mm^2/s [140]. The average water ADC from the retina measured using an ROI method was $1.0 \pm 0.3 \times 10^{-3}$ mm^2/s (Table 1), while the minimum water ADC from the profile plot was determined to be $0.5 \pm 0.1 \times 10^{-3}$ mm^2/s (Fig. 3.3, Table 3.2). The discrepancy in the calculated water ADC measurements highlight the advantages of using the signal-intensity-profile-plot technique compared to the ROI technique. While a single average water ADC value could be determined with the ROI analyses, the signal-intensity-profile-plot technique showed variations in water ADC across the retina. The water ADC value was observed to be $2.4 \pm 0.4 \times 10^{-3}$ mm^2/s at the region of the vitreo-retinal boundary and reached a minimum of $0.5 \pm 0.1 \times 10^{-3}$ mm^2/s at ~150 μm from the boundary. While the high water ADC values near the vitreo-retinal boundary can be explained by the influenced by the high water ADC of the vitreous, as discussed in Section 3.5.1, one possible explanation for this decrease in water ADC within the retina

is the presence of the avascular layer in the retina. Free-flowing blood in tissues contributes to an increase in the observed water ADC of the tissue [141], with a 7% increase in ADC reported with an increase in perfusion of 4 mL/min in phantoms [142]. The unique architecture of the retina may prove useful in assessing the contribution of perfusion towards water ADC in tissue. Apart from the retina, the T_2 and ADC derived from the cerebrospinal fluid corresponded well with those of the vitreous, due to the similarity of the fluids.

3.5.4 Comparison with cat retina

The water T_2 and ADC values reported herein for the rat were also compared to the corresponding values reported in retina of cats at 4.7T [131]. Water T_2 and ADC maps in the cat retina revealed three distinct bands, with the inner band corresponding to the vascular inner retina, the middle band being the avascular photoreceptor cells and the outer band corresponding to the choroid and tapetum. While the inner and middle retinal bands are essentially similar in peripheral cat and rat retina, the rat retina lacks tapetum in the outer band. The T_2 value in the inner and middle bands was calculated as 67 ± 5 ms to 48 ± 5 ms, respectively, at 4.7T. The T_2 values obtained from the inner and middle bands in the cat retina were comparable to those in rat retina, accounting for the shortening of T_2 at 7T, albeit there were no obvious layers observed in the T_2 map of rat retina. Similarly, the average water ADC value in the inner and middle retina in cats was determined to be $\sim 0.85 \times 10^{-3}$ mm^2/s, while the smallest average water ADC value measured from the rat retina was $0.6 \pm 0.1 \times 10^{-3}$ mm^2/s.

3.5.5 Implications for retinal MRI

Contrast in an MR image depends on the differences in relaxation and diffusion properties of the tissue water. Quantitative evaluation of these relaxation and diffusion parameters helped design pulse sequences that provide optimal contrast between tissues of interest, for example, in the better visualization of the retina through suppression of vitreous. Since the T_1 value of the vitreous is more than twice that of the retina, an effective T_1-weighted pulse sequence was designed as discussed (Chapter 4) for anatomical scans of the retina [115]. Heavily T_1-weighted images yielded a hypo-intense vitreous, allowing better visualization of the retina. Another possibility for clearer retinal imaging would be to use an inversion pulse in front of the imaging sequence, allowing for higher T_1-weighting and better suppression of the vitreous (fluid-attenuated, inversion-recovery pulse sequence).

Knowledge of the T_2 and T_2* relaxation times of tissue is most commonly used in blood-oxygenation-level-dependent functional imaging. The MRI signal-intensity change due to a change in deoxy-hemoglobin concentration has been widely used to detect neuronal function [96]. It has also been established that the optimal TE for detection of these signal-intensity changes is in the vicinity of the T_2 or T_2* of the tissue, depending on the imaging sequence [143, 144]. Knowledge of the quantitative value of T_2 and T_2* can therefore be used to obtain the maximal functional response from the retina.

Knowledge of the average water ADC of the retina and vitreous is used in the next chapter to obtain functional images of the retina by suppressing the vitreal signal. The average water ADC from the vitreous was about 3.5 to 3.9 times that of the retina. By applying a small diffusion gradient (b=450 s/mm^2) [115], a significant signal

attenuation in the vitreous of ~70% was achieved, while the signal intensity from the retina was attenuated by only about 25%. This allowed not only a clearer visualization of the retina against a dark vitreous background but also improved detection of small signal intensity changes in the retina as a result of stimulus.

The quantitative relaxation rates in the brain have been shown to change in, for example, disease states like edema, ischemia, and demyelination. Average water ADC in the brain is a good indicator of water and ion equilibrium [145], and is routinely used in the detection of acute stroke. The retina is also affected by edema, ischemia and degeneration that results in changes in tissue microstructure which raises the possibility that changes in the relaxation and ADC parameters could help identify retinal diseases. Moreover, the highly organized microstructure within the retina could yield anisotropic diffusion in the various retinal layers. Diffusion anisotropy is a very sensitive tool for the detection of microscopic structural changes in the brain, and may prove to be a very useful tool to detect early retinal degeneration.

3.6 Conclusion

This study reports quantitative measurements of water T_1, T_2, T_2^* and ADC values of the retina across the retinal thickness at 7T. T_1, T_2 and T_2^* values of the retina are similar as those of the brain, but differ markedly from that vitreous, as expected. These measurements are expected to set the foundation for systemically optimizing structural, physiological and functional MRI contrasts in the retina. These MRI parameters may also be useful for staging retinal disease progression and monitoring therapeutic intervention.

Chapter 4: Structural and functional MRI reveals multiple retinal layers

[Adapted from Cheng et al, PNAS (2006)103:17525-17530]

MRI of the retina, performed at high spatial resolution, was able to resolve three bands within the rat retina which corresponded histologically to (i) the combined ganglion cell layer, inner nuclear layer and the embedded retinal vessels, (ii) the avascular outer nuclear layer and photoreceptor segments, and (iii) the choroidal vascular layer. Imaging with an intravascular contrast agent (gadolinium-diethylene- tri-amine-pentaacetic acid, or Gd-DTPA) enhanced the retinal and choroidal vascular layers on either side of the retina, but not the avascular outer nuclear layer or the vitreous. Similarly, blood-oxygen-level dependent (BOLD) functional MRI revealed layer-specific responses to hyperoxia and hypercapnia. Importantly, layer-specific BOLD responses in the two vascular layers were different, suggesting the two vasculatures are differentially regulated. This study demonstrated that MRI is a powerful investigative tool capable of resolving lamina-specific structures and functional responses in the retina as well as probing lamina-specific changes in retinal diseases.

4.1 Introduction

The diagnosis of retinal disease relies on the demonstration of structural or functional alterations in the retina or its vasculature, as described in the introductory chapter. Fundus photography and optical coherence tomography [146] have made critical contributions to the diagnosis of disease-induced structural changes, whereas blood-flow abnormality in the retina can be measured by using fluorescein angiography, indocyaningreen angiography, and laser Doppler flowmetry [123]. Functional imaging of the retina was recently reported using intrinsic optical imaging [147]. However, laminar resolution of deep retinal layers using these modalities is confounded by strong tissue absorption, optical scattering, and disease-induced opacity of the vitreous humor, cornea, and lens (such as vitreal hemorrhage and cataract).

In contrast, MRI has no depth limitation and is widely used to non-invasively study anatomy, physiology, and function in a single setting. Structural MRI provides detailed anatomical images *in vivo*. Concomitant use of an i.v. contrast agent (such as gadolinium-diethylene-tri-amine-pentaacetic acid or Gd-DTPA) selectively enhances vascular structures and reveals disease-induced vascular permeability changes. The development of functional MRI (fMRI), such as blood-oxygen-level-dependent (BOLD) fMRI, has revolutionized brain mapping by providing noninvasive, real-time visualization of brain function [96]. Although the spatial resolution of MRI is lower than optical and histologic techniques, recent advances have made fMRI of cortical columns [148-150] and laminar structures [151, 152] possible. However, even higher spatial resolution and contrast are required if fMRI is to be successfully applied to the retina.

As discussed in Chapter 1, the neural retina is organized into three major nuclear layers [153], containing: (i) the ganglion cell soma; (ii) the inner nuclear layer containing soma of bipolar, amacrine, and horizontal cells; and (iii) the outer nuclear layer containing soma of photoreceptor cells. These nuclear layers are separated by two plexiform layers, containing axons and dendrites from the neurons as described in earlier chapter. These cell layers are nourished by two separate blood supplies: the retinal and choroidal vasculatures [154], located on either side of the retina. The retinal vasculature, located closest to the vitreous, nourishes the ganglion cell and inner nuclear layers and is embedded primarily within the ganglion cell layer with some capillaries projecting deep into the inner nuclear layer. By contrast, the choroidal vasculature nourishes the avascular outer nuclear layer and is external to the neural retina, sandwiched between the retinal pigment epithelium and the sclera. Importantly, it has been suggested that blood flow in the two vascular beds is regulated differently. Choroidal blood flow exceeds local metabolic requirements and is many times higher than either retinal or cerebral blood flow [155]. The retinal and choroidal vessels also respond differently to hyperoxic and hypercapnic inhalation stimuli. Retinal vessels strongly vasoconstrict in response to pure oxygen inhalation and vasodilate in response to inhaled carbon dioxide, whereas the choroidal vessels only weakly vasoconstrict in response to pure oxygen and weakly vasodilate in response to carbon dioxide [155, 156].

This chapter reports layer specific structural and BOLD fMRI of rat retina *in vivo*. Structural MRI reveals three distinct bands that correlate histologically with known laminar structures. fMRI reveals layer-specific and differential BOLD responses to hyperoxia and hypercapnia.

4.2 Materials and method

Animal preparation: Anatomical and functional imaging was performed on wild type adult rats (Spague Dawley, n=24 for anatomy scan, subset of n=8 for BOLD, age 3-4 months). The rats were setup as described in Section 2.3 of Chapter 2, under 1% isoflurane with endo-tracheal intubation and artificial ventilation. The femoral vein was catheterized for the injection of Gd-DTPA (an MRI contrast agent). End-tidal CO2 (EtCO2) and rectal temperature was continuously monitored and maintained within normal physiological ranges. The rat eye was lubricated and centered in the magnet using position and localizer scans, and high resolution anatomical images were acquired along the superior-inferior direction of the eye through the visual axis.

MR imaging: MRI studies were performed on a Bruker 4.7-Tesla/30-cm magnet and a 40 G/cm B-GA12 gradient insert (Bruker, Billerica, MA). High-resolution anatomical imaging of the retina was performed using a gradient echo sequence; a short TR of 150 ms and TE of 3.6 ms were used to achieve T_1-weighted images. Images were acquired at 60 μm in-plane resolution with a slice thickness of 0.5 mm, with FOV from 7.7 mm × 7.7 mm and acquisition matrix of 128 × 128. Thirty-two signal averages were acquired as a time series over 10.2 mins and the images were averaged offline after correction of any movement artifacts.

BOLD fMRI images were acquired by using two-segment, spin-echo, diffusion-weighted, echo-planar imaging. Diffusion-weighted preparation was used to suppress the otherwise overwhelmingly strong, fast-diffusing water signal from the vitreous. The

fMRI parameters were: TR of 1 s per segment, TE of 51 ms, 1.0-mm slice thickness, diffusion-gradient-pulse separation (Δ) of 20 ms, diffusion-gradient-pulse duration (δ) of 3.5 ms, b value of 450 s/mm^2, 128 × 128 data matrix, and 11.5 mm × 11.5 mm field of view, yielding a 90 μm × 90 μm in-plane resolution. Acquisitions of each fMRI data block took 320 s. Hyperoxic (100% O_2) and hypercapnic (5% CO_2, 21% O_2, balance N_2) challenges were used to modulate tissue oxygenation and blood flow. Ambient air was used as a baseline. Images were acquired continuously in 320-s blocks (100 s during baseline and 220 s hyperoxia or hypercapnia) with at least 10-min intervals between blocks.

Histology: Standard histology was performed on the eye at the corresponding region after MRI. Eyes were enucleated and fixed overnight in 2% paraformaldehyde by directly injecting the solution into the eyes as well as by immersion. Eyes were then rinsed in 0.1M phosphate buffer and dissected to isolate the posterior eyecup, dehydrated in graded ethyl alcohol and finally embedded in epoxy-resin. The embedded eye cup was then sectioned at 0.5 μm, mounted on slides, stained with toluidine blue and digitally photographed. The thickness of different layers of the neural retina and choroidal vasculature were semiautomatically derived by using an image analysis program (Image Pro, Cybernetics, Silver Spring, MD). The various retinal layer thicknesses were measured from one edge to the other in a direction perpendicular to the retinal surface and RPE layer. Three such measurements were made in each slice and at least three slices were measured in each rat to obtain the average thickness in each rat.

Data analysis: The total retinal thickness and thickness of individual retinal layers observed in the MRI were measured using full width at half maximum height (FWHM) using profile plot method, described earlier. Thicknesses of individual MRI-derived layers were obtained on all 24 rats, and from histology on a subset of nine rats. BOLD data were derived from 8 of the 24 rats imaged using a cross-correlation method. The percentage-change in signal was calculated from ROIs carefully drawn on the corresponding retinal layer, before and after systemic stimulation.

Simulation: To estimate the accuracy of the thickness measurements, three simulation experiments were performed using Matlab-generated images. In the first simulation, an image was generated using Matlab with a single hyper-intense band, on a black background. The thickness of the band was varied with respect to the pixel size, which was assumed to be 60 μm, just as in the case for MRI. The thickness of the band was measured using profile plot method, and plotted against the actual thickness. In the second experiment three bands of alternating hyper- and hypo- intensities with thickness of 92, 83 and 79 μm were simulated with varying signal-to-noise ratio (SNR) from 1× to 8× the experimental SNR. The profile plots as well as FWHM thickness obtained at low and high SNR were compared. The measurements were repeated seven times. In the third simulation, the thickness of the third (outer) band was varied between 79 and 5 μm, and compared to the derived thickness in the profile plot.

4.3 Results

High-resolution anatomical MR imaging of the rat eye was done using T_1-weighted scans. The normal total thickness of the retina in rats from the vitreo-retinal surface to the sclera is known to be about 300 μm [116, 157]. Therefore, the MRI spatial resolution was adjusted to obtain multiple pixels within the retina, with the aim of delineating the different cellular and vascular layers. The lowest spatial resolution achievable, with sufficient contrast-to-noise ratio to be able to identify the individual retinal layers, was 60 μm for the anatomical MRI scans and 90 μm for the fMRI scans.

Fig. 4.1: Anatomical images at 60 μm × 60 μm resolution from a normal adult rat. Three distinct layers (solid arrows) of alternating bright, dark, and bright bands are evident. Sclera (dashed arrow) appears hypo intense. (Adapted from Chen et al PNAS (2006) 103:17525). Scale bar is 300 μm.
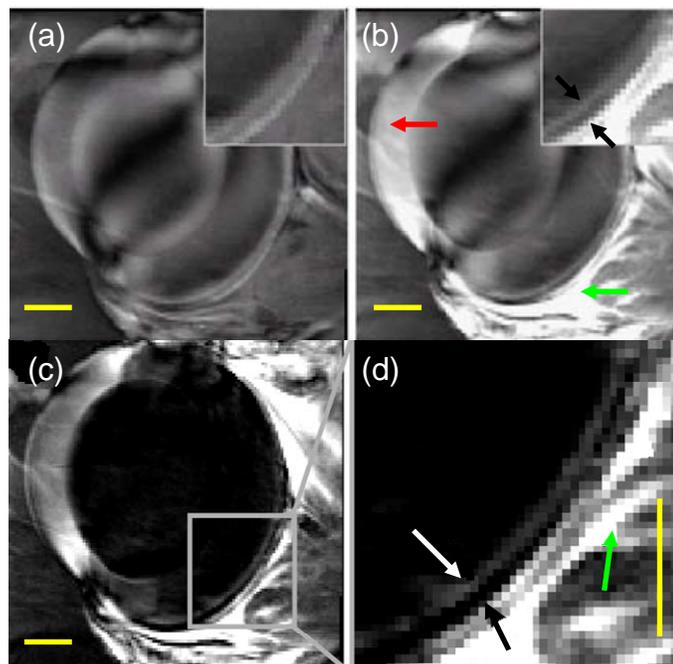
Fig. 4.2: Contrast-enhanced MRI delineating two vascular layers on either side of the retina. MRI of the retina at 60-μm in-plane resolution (a) before and (b) after Gd-DTPA administration. (c) The difference image. The green arrows depict extraocular enhancement and the black and white arrows in the expanded views indicate the inner and outer bands of the retina corresponding to the two vascular layers. (Adapted from PNAS (2006) 103 (46):17525). Scale bar is 1mm.

4.3.1 Layer-specific anatomical MRI

Figure 4.1 depicts an image of a normal rat retina, revealing three distinct bands as indicated by the alternating bright and dark signal intensities. The vitreous and the sclera appeared relatively hypointense because of the long T_1-relaxation-time constant of the vitreous water and the low water content of the sclera [131], as seen in Chapter 3. Administration of the i.v. contrast agent Gd-DTPA markedly enhanced retinal boundaries (Fig. 4.2), consistent with the localization of Gd-DTPA-impermeable vasculature on either side of the retina. The outer strip was thicker and more enhanced than the inner strip. In contrast, no enhancement was observed in the middle band, lens or vitreous. The Gd-DTPA-enhanced inner and outer strips correlated, respectively, with the inner and outer bands of the images without Gd-DTPA.
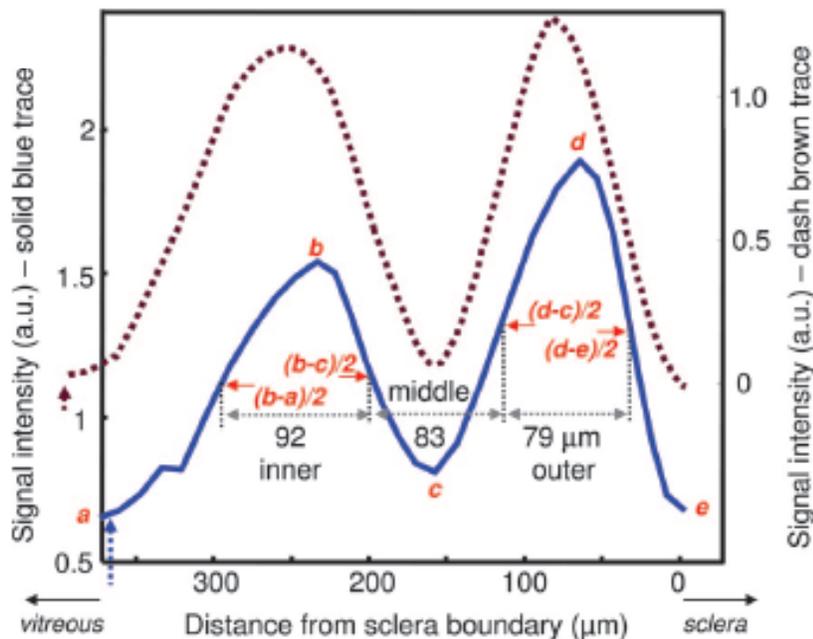
Fig. 4.3: Intensity profiles of the retina in two rats. The outer, middle, and inner bands are clearly delineated in the profile plots. Values in μm indicate the band thicknesses of the solid trace. (Adapted from PNAS (2006) 103 (46):17525).

Retinal images were virtually flattened and intensity profiles obtained to calculate laminar thicknesses (Fig. 4.3). To assign MRI-derived retinal layers, images were compared with standard histology. A histologic section depicting standard cell layers, the embedded retinal vascular layer, and a distinct choroidal vascular layer is shown in Fig. 4.4. Comparative analysis yielded the following layer assignments. The inner MRI band correlated with the combined ganglion cell layer, inner nuclear layer and the embedded retinal vessels. Consistent with the inclusion of a vascular component, Gd-DTPA enhanced this band. The middle band, which

Fig 4.4: Histological section of a normal adult Sprague–Dawley rat retina stained with toluidine blue. Three vertical bars on the left show the assignments of the three MRI-derived layers. GCL, ganglion cell layer; IPL, inner plexiform layer; INL, inner nuclear layer; OPL, outer plexiform layer; ONL, outer nuclear layer; IS+-OS, inner and outer photoreceptor segment; CH, choroidal vascular layer. (Adapted from PNAS (2006) 103 (46):17525).

appeared relatively hypointense on anatomical imaging, was not enhanced by Gd-DTPA and was thus assigned the avascular outer nuclear layer and the photoreceptor segments. Gd-DTPA enhanced the outer band, which was assigned the choroidal vascular layer. The thicknesses of inner, middle and outer bands were observed to be 92 ± 9, 77 ± 9, and $37 \pm$

8 μm respectively by histology and 100 ± 20, 80 ± 10, and 90 ± 10 μm respectively by MRI. The total retinal thickness was observed to be 210 ± 10 μm by histology and 270 ± 30 μm by MRI. MRI-derived thicknesses of the inner and middle bands were similar to histologic measurements, whereas the outer band was significantly thicker than the histology-derived thickness of the choroidal vascular layer.

4.3.2 Layer-specific BOLD fMRI

BOLD fMRI was used to probe the layer-specific responses to hyperoxia and hypercapnia. Robust layer-specific BOLD fMRI responses were detected in the retina of wild type rats. Importantly, the two vascular layers responded differently to inhalation stimuli. Hyperoxia induced a larger BOLD response in the outer band ($12 \pm 2\%$, n = 8) than the inner band ($7 \pm 2\%$, p < 0.01) (Fig. 4.5a). In contrast, hypercapnia induced a smaller BOLD response in the outer band
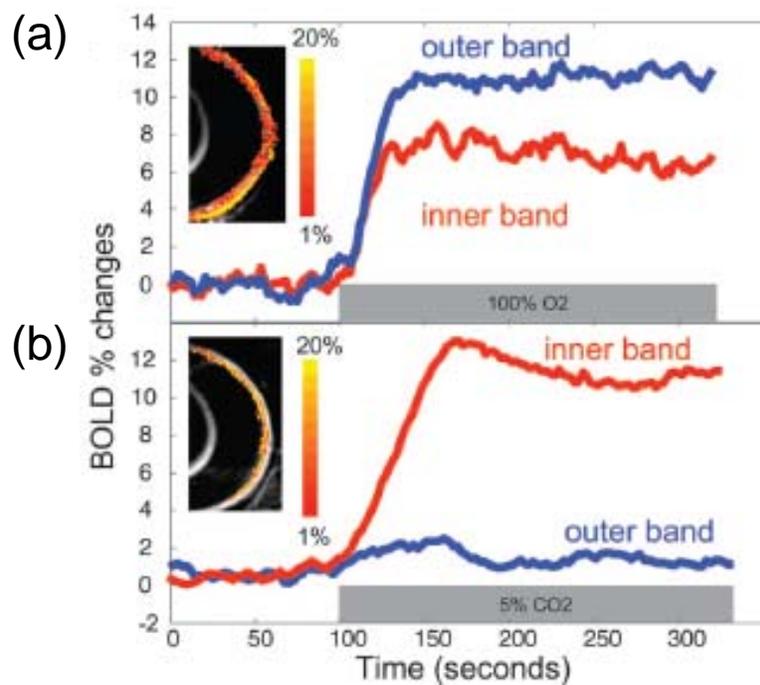
Fig. 4.5: Differential layer-specific BOLD fMRI of the retina. Layer-specific BOLD fMRI responses to hyperoxia (100% O_2) (a) and hypercapnia (5% CO_2 in air) (b) from a normal rat at 90 μm in-plane resolution. BOLD percent change maps are overlaid on echo-planar images. The color bar indicates 1–20% BOLD changes. (Adapted from PNAS (2006) 103 (46):17525).

(1.6 ± 1%, n = 8) than in the inner band (10 ± 2%, p < 0.01) (Fig. 4.5b). Small BOLD

responses detected in the middle band (hyperoxia: 1.5 ± 1% and hypercapnia: 1 ± 2%)

were likely due in large part to partial volume error from adjacent bands.
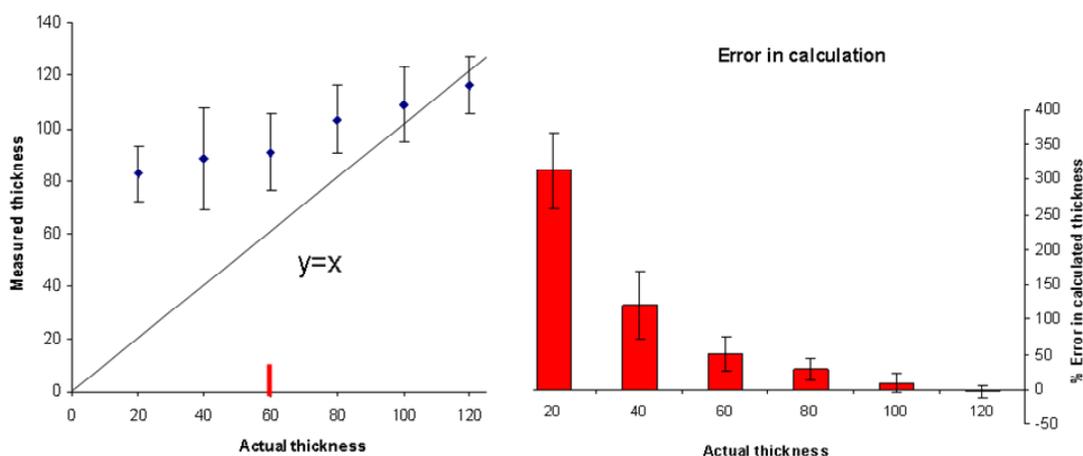
Fig. 4.6: Simulation of thickness calculation using a profile-plot method. (a) A plot of measured thickness vs. the input thickness (n=7 for each thickness), shows minimum thickness that can be measured with 60 μm spatial resolution. (b) Measure of the percentage error in calculated thickness shows that accurate measurements (within 1 SD) may be possible only if the actual thickness is at least 1.66 times the image resolution. Note that the point spread function and other system transfer functions were not considered in this simulation.

4.3.3 Simulations

To verify the robustness of the thickness determination, simulation studies were

performed on images generated in Matlab and the thickness calculated using a profile-

plot method. Calculated band thickness from multiple measurements (made with a

different and random partial volume) for various input band thicknesses is shown in Fig.

4.6. A clear overestimation is seen in the measured thickness (actual thickness is outside

2 standard deviations from measured thickness) when the pixel size is more than the input

thickness of the band. The actual line thickness lies within the measured value ± one

standard deviation when the line thickness was at least 1.66 times the pixel resolution

(under these simulation conditions with n=7). Furthermore, the percentage error in measured thickness maximized at 50% partial volume.

A second simulation was done with three bands in the input image and with 1× and 8× the SNR obtained in the MRI, to test its effects on the measured thickness. While the thickness of the trough was underestimated by 4%, the thicknesses of the peaks were overestimated by about 3%-7% compared to the input thickness (Fig. 4.7). Adding noise did not significantly alter the measured thickness, although it did increase the standard deviation of the measurements. The measured peak

	Inner band	Middle band	Outer band
Input intensity (a.u.)	1.5 (peak)	0.8 (trough)	1.9 (peak)
Input thickness (μm)	92	83	79
Measured thickness (noise=1x)	95 ± 2	80 ± 1	85 ± 2
Measured thickness (noise=8x)	97 ± 10	80 ± 4	88 ± 6
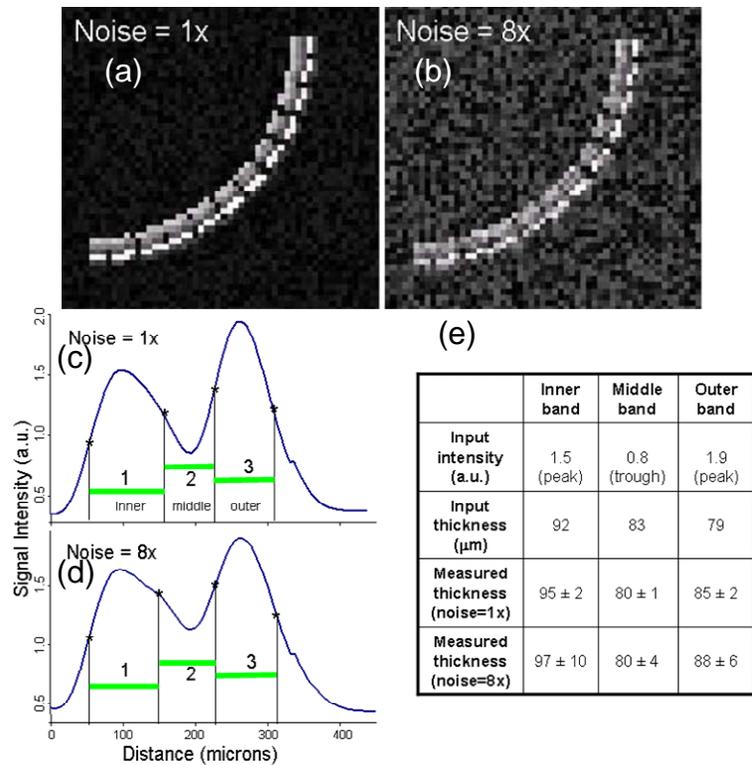
Fig. 4.7: An image of 3 curved lines of relative intensities 1.5, 0.8 and 1.9 and thickness 92, 83 and 79 μm generated at (a) 1x and (b) 8x noise. Profile plots of (a) and (b) are shown in (c) and (d) respectively. (e) Table shows a comparison of input and measured thicknesses with no significant increase in calculation-error with noise. (Adapted from PNAS (2006) 103 (46):17525).
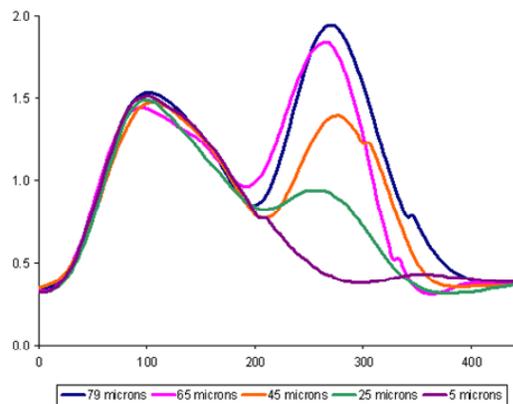
Actual Thickness of outer band	79	65	45	25	5
Calculated intensity	1.94	1.84	1.39	0.94	-
Calculated Outer band	85	77	87	79	-

Fig. 4.8: Comparison of profile plots obtained with various thickness of the outer band.

amplitudes were similar to the input amplitudes.

The thickness of the outer band calculated from the third simulation did not decrease with the input band thickness (input thickness less than $1.5 \times$ image resolution). However, the peak signal intensity of the outer band reduced by more than 50% as its thickness was reduced from 79 μm to 25 μm, as seen in Fig. 4.8.

4.4 Discussion

Anatomical MRI reveals three discernable layers in normal retina, designated here as the inner, middle and outer bands. Administration of Gd-DTPA enhanced the inner and outer retinal band, confirming the avascularity of the middle band, and assisting with layer assignment. BOLD fMRI shows layer specific and differential responses to physiologic challenges.

4.4.1 Laminar structures

The assignment of MRI bands is supported by both general histological assessment and Gd-DTPA-enhanced imaging. MRI-derived thicknesses of the neural retina, as reflected by the inner and middle bands, agree with histological measurements [116, 157]. In contrast, the outer band as measured by MRI was significantly thicker than the histological determination of the choroidal vascular layer herein and in Steinle *et al.* [158]. The discrepancy between the *in vivo* and histologic data could arise from collapse of choroidal vessels after removal of orbits from the systemic circulation, histological shrinkage, or partial volume error. These differences in thickness underscore the importance of *in vivo* measurements.

Subtraction of post- and pre-Gd-DTPA-contrast images showed marked signal enhancement on either side of the retina. Greater Gd-DTPA enhancement of the outer band compared with the inner band is consistent with the higher blood flow and volume in the choroidal versus the retinal vasculature [155]. High choroidal blood flow appears necessary to maintain a large oxygen gradient that facilitates oxygen delivery to the avascular outer nuclear layer [159] and dissipates the heat produced [160]. Taken together, the MRI layer assignments are consistent with known layer structures of the retina.

4.4.2 Vascular coupling and BOLD response

Coupling of blood flow, oxygenation, and metabolism in the brain has been well described. The vascular coupling in the retina is, however, not as well studied due to the limitations of imaging techniques described previously. However, the majority of the techniques used to describe the vascular changes in the retina cannot readily distinguish between the retinal and choroidal vasculature. Physiologic respiratory challenges with oxygen or carbogen modulate tissue oxygenation, as measured by oxygen polarographic electrodes [161]. Visual stimulation modulates optical absorption and scattering as detected by intrinsic optical imaging [147, 162]. Finally, visual-evoked BOLD fMRI of the retina [133] has been reported.

The BOLD fMRI data reported herein demonstrates layer-specific and differential responses to hyperoxia and hypercapnia in the retinal and choroidal vascular layers. These observations are consistent with Laser Doppler flow [123] and oxygen-electrode [161] measurements of blood flow and oxygenation. Inhalation of pure oxygen increases

capillary and venous oxygen saturation and thus increases the BOLD signal [96]. A strong hyperoxia-induced BOLD increase was detected, likely because of the high vascular density of the choroid. The anesthesia used herein could also increase arteriovenous oxygen difference, amplifying the hyperoxia-induced BOLD signal changes. More importantly, hyperoxia-induced BOLD signal showed a larger increase in the outer band (choroidal vascular layer) than in the inner band (retinal vascular layer). This is likely because hyperoxia is known to markedly decrease retinal blood flow by 60% [163, 164], which counteracts the BOLD-signal increase from elevated oxygen tension induced by hyperoxia. In contrast, hyperoxia did not significantly affect choroidal blood flow [163, 164]. The higher choroidal vascular density in the outer band compared with the retinal vascular density in the inner band could further amplify the differential BOLD responses between the two vasculatures.

On the other hand, hypercapnic stimulation causes vasodilation and increases blood flow in the brain, which leads to decreased fractional oxygen extraction and increased capillary and venous oxygen saturation [96]. Thus, hypercapnia is also expected to increase the MRI signal. In the retina, hypercapnia strongly dilates retinal vessels, whereas it has a much smaller dilatory effect on choroidal blood vessels [155, 163]. Consistent with the vasodilatory response, the BOLD signal increase in the inner band containing the retinal vessels was larger than in the outer band. Together, these results support the contention that the two vascular supplies to the retina are differentially regulated.

4.4.3 Sources of error

Possible errors in MRI measurements

There is an obvious lower limit to the thickness of a layer that can be measured using an image with a resolution of 60 μm. Discrepancies in the measured thickness and signal intensities of a band can arise from partial volume errors. A bright band on a dark background may occupy an integer number of pixels, depending on band thickness and image resolution. For example, a horizontal line of 60-μm thickness could be one pixel thick in an image with 60-μm in-plane resolution or could have its intensity distributed over two rows of pixels. When the thickness of the band is measured in the latter case, the apparent thickness of the band would be larger, and the maximum signal intensity calculated would be smaller due to partial-volume error. Furthermore, an increase in SNR could lead to a change in the measured thickness of the hyper-intense bands and a decrease in the thickness of the hypo-intense band due to the hyper-intense nature of noise. Simulations were done in Matlab to address these issues, which applies to all the thickness and intensity calculations in this thesis.

The layer thickness and signal intensity measured were relatively accurate when the thickness of the layer was >1.5 times the resolution or size of pixel. At smaller layer thickness, the measured thickness plateaus off at about 1.3 times the pixel size, as seen in the first simulation. It was also noted that the peak amplitude was also modulated by the thickness due to partial-volume effects, as seen in the third simulation. One way to accurately determine the thickness of the retinal bands would be to image them at two or more different resolutions. A decrease in the thickness of the individual layers with resolution can then be interpreted as the measured thickness being an overestimation of

the actual thickness. Furthermore, a measured thickness of more than 1.5 times the pixel resolution can be interpreted as a relatively accurate measurement.

On the other hand, noise levels in the range of actual MRI noise (1.5%) and even eight times the actual MRI noise (10%) did not significantly affect the average measured thickness. However, the uncertainty of the measurement increased with lower SNR as expected, and a higher number of measurements may be required with low SNR images for more reliable thickness calculations. These simulations provide an interesting insight into the variations of the measured thickness and pixel intensity values with variations in input layer thickness. It should be noted here that the overall transfer function of the MRI was not included in the simulation.

Possible errors in histology sections

Care was taken to ensure that the retinal histology was performed in roughly the same location as the MRI slice. MR images were acquired in a sagittal plane running along the superior-inferior aspect of the eye, and including the optic nerve head. After MRI, the superior aspect of the eye was marked with a pen to maintain the orientation for histological sections. The posterior eyecup was dissected after fixation and cut into two halves along the optic nerve head in a plane parallel to the MRI slice. The two halves were then embedded in paraffin and sectioned on a microtome. The first few slices in each half, that lie within the MRI slice thickness were analyzed using Image Pro software to determine the thickness of the layers.

Tissue shrinkage due to fixation, embedding and sectioning can be a major source of error in thickness measurement with histology. It has been shown that paraffin

embedded cervical tissue sections shrank by ~15% when fixed with 8% formaldehyde, compared to unfixed sections [165], whereas the use of 3.1% glutaraldehyde in Hanks' balanced salt produced negligible shrinkage [166]. We have used either 2% formalin or 2% glutaraldehyde in our experiments, to reduce the mount of shrinkage in retinal tissue without affecting the fixing process. A small amount of the fixative (~5 µL) was directly injected into the eye at the limbus for better access of the fixative to the retina. Histology using the technique described herein has been commonly used for fixing the retina while maintaining its structure, despite some reports of nuclear collapse. The thickness of the rat retina measured *in vivo* using high-resolution OCT corresponded well with the thickness measured on histological sections using techniques similar to that reported herein [157]. Finally, the thickness of the normal rat retina measured in our MRI and histology corresponded well with other observations made with histology and OCT, validating the histological method used herein [116, 156, 157, 167-169].

4.5 Conclusion

High-resolution MRI detection of lamina-specific structures and functional responses in the retina is reported here. These technologies have the potential to provide powerful insights into how retinal and choroidal oxygenation is regulated and how retinal diseases may affect the two vasculatures and the neural tissues they subserve. Given the remarkable progress in MRI technologies for imaging the brain, translating these technologies to longitudinally study the retina could critically impact retinal research.

Chapter 5: Contrast-Enhanced MRI of the Retinal Anatomy

High-resolution T_1-weighted MRI revealed three bands in the rat retina, corresponding to the retinal and choroidal vascular layers and the avascular layer. This chapter explores contrast-enhanced MRI of the retina, to obtain a more detailed picture of the retinal anatomy. Paramagnetic ions like gadolinium (Gd^{3+}) and manganese (Mn^{2+}) change the MRI signal by shortening the T_1- and T_2-relaxation times of the neighboring water molecules. Mn^{2+} is also a bioactive element, entering the neurons mainly through voltage-gated calcium channels. In this chapter, the bioactive properties of Mn^{2+} have been exploited for improving contrast between retinal layers.

Intra-peritoneal (i.p.) and intra-vitreal administration of $MnCl_2$ was explored. While i.p. injection resulted in increased signal intensity from the inner and outer retina, manganese-enhanced MRI (MEMRI) of the rat retina 24 h post intravitreal injection of 5 μL of 30 mM $MnCl_2$ revealed seven layers of alternating bright and dark signal intensities in the 4.7T scanner. At a higher magnetic field of 7T, the optimal dosage for imaging these seven layers was determined to be 5 μL of 12 mM $MnCl_2$. Following the intravenous administration of Gd-DTPA, which does not cross the blood-retinal barrier, the vascular and avascular layers could be identified in the retina, which assisted in the assignment of the observed MRI layers. Cross-validation with histology confirmed MRI layer assignments and laminar thicknesses. Finally, high-resolution emulsion autoradiography with trace amounts of Mn^{54} was used to corroborate the layer assignments. The autoradiography revealed a larger concentration of Mn^{54} in the plexiform and photoreceptor segment layers as compared to the nuclear layers.

MEMRI was shown in this study to be a powerful investigative tool to resolve layer-specific retinal structures and to probe layer-specific changes in retinal diseases.

5.1 Introduction

High-resolution MRI of the rat retina can identify only three different layers in the retina. These layers correlate with the two vascular and one avascular layer of the retina when imaged with an intravascular contrast agent. Retinal MRI cannot differentiate the various cellular layers of the retina, due to the obvious lack of intrinsic T_1 or T_2 contrast among the various retinal layers. One way to improve the contrast is to use targeted MRI contrast agents that enhance the signal intensity in specific retinal layers. In this chapter, the use of manganese (Mn^{2+}) is investigated as an MRI contrast agent to image retinal anatomy.

Mn^{2+} is both an MRI contrast agent and a calcium analog, entering the neurons primarily through voltage-gated calcium channels and being trapped intracellularly with a half-life on the order of weeks. However, Mn^{2+} does not readily cross the blood-brain barrier (BBB), making access to the neurons difficult. It has been shown that physiological uptake of Mn^{2+} in the brain takes place primarily across the BBB at low dosage [170], while at higher concentrations, Mn^{2+} ions enter the brain through the choroid plexus [171, 172]. The BBB-transport of Mn^{2+} is a transferrin-receptor-mediated process, which likely saturates at high concentrations. However, Mn^{2+} transport across the choroid plexus is many times faster and Mn^{2+} distribution in the brain reaches a steady state 24 h after systemic administration. Once in the neurons, Mn^{2+} has a very slow clearance rate of the order of a couple of weeks [173].

The blood-retinal barrier (BRB) is similar in many ways to the BBB, and the former has often been used as a model to study the flux of materials across the BBB

[174]. As seen in the Introductory chapter, the BRB is composed of retinal pigmented epithelium (RPE) cells and the endothelial cells. The RPE is an ion-transporting barrier which restricts the transport of polar solutes from the choroidal vasculature into the neural retina. The endothelium of the retinal vasculature is composed of tight junctions just as in the blood-brain barrier, with considerable resistance to Mn^{2+} transport. Delivery of MRI contrast agents to the retina after systemic administration, therefore, would likely require specific carrier-mediated processes.

The BRB, however, can be bypassed by the intravitreal injection of Mn^{2+}. Intravitreal injection has become a popular technique to deliver drugs into the neural retina [175]. This technique is relatively safe and easy to perform due to the superficial nature of the eye. Furthermore, delivering the contrast agent directly to the region of interest has the potential to reduce the dosage required by orders of magnitude, reducing the exposures to other organs.

In this chapter, the Mn^{2+} uptake dynamics in the retina were explored following a systemic administration of $MnCl_2$. The BRB was then bypassed by injecting Mn^{2+} directly into the vitreous. MEMRI was performed 24 h post intravitreal injection of isotonic $MnCl_2$. The Mn^{2+} concentration in the various retinal layers post intravitreal administration was then semi-quantified using Mn^{54} autoradiography.

5.2 Intraperitoneal injection of $MnCl_2$

5.2.1 Materials and methods

Animal preparation: Two studies were performed to analyze the dynamics of Mn^{2+} uptake in the retina post intraperitoneally (i.p.) injection. In the first study, rats (n=15, Sprague-Dawley, 350-450g) were anesthetized under 2% isoflurane and isotonic $MnCl_2$ (66 mg/kg body weight) solution was injected i.p. The rats were then allowed to recover normally in their cages. After a predetermined time of a few minutes, and then at 4, 12, 24 or 48 h (n=3 at each time point), rats were anesthetized under 1.5% isoflurane, intubated, mechanically ventilated, and setup on an imaging cradle with an eye coil as described in Chapter 2. A thin PE50 tube filled with saline was placed directly next to the eye to serve as a reference signal.

In a second study, retinal Mn^{2+}-uptake dynamics were studied longitudinally in a single session starting just before Mn^{2+} injection and continuing upto 6 h post injection. Rats (n=5, Sprague-Dawley, 350-450 g) were first setup in the imaging cradle with mechanical ventilation and i.p. line for remote administration of Mn^{2+}. Once inside the MRI magnet, the rats were dark-adapted for 30 min and a pre-Mn^{2+} MRI was performed. After the baseline scan, a 66 mg/kg iso-osmotic $MnCl_2$ was remotely administered through an i.p. line. MRI of the retina was then performed at 0, 15, 30, 45, 60, 90, 120, 180, 240, 300 and 360 min after i.p. injection.

MR Imaging: High resolution MRI was performed using a 7T/30-cm-bore MRI equipped with a 40 G/cm gradient set (Bruker, Billerica, MA). T_1-weighted, gradient echo images were acquired with a TR of 100 ms, TE of 6.5 ms, flip angle (FA) of 40 degrees, FOV of 7.5 mm x 7.5 mm, imaging matrix of 256 x 256, in-plane resolution of

30 μm and slice thickness of 0.8 mm. A time-series of 16 images were acquired and averaged offline to post correct any motion artifacts.

Data analysis: The images were analyzed using a signal-intensity-profile method as described in Section 2.4. The signal intensity at various time points in different imaging sessions were normalized using a saline phantom as a reference in the first study. The second study did not require a saline phantom for signal normalization as images at all time points were acquired in a single session with a 'user range' option, which allowed equal dynamic range of signal in all scans. Peak signal intensity from the various retinal layers seen on the MRI was plotted against time.

5.2.2 Results

In the first study, three distinct layers of alternating bright and dark signal intensities were visible within the retina between 0 to 24 h post Mn^{2+} administration, as seen in the images and profile plots in Fig. 5.1. Images acquired at 4 h after i.p. injection showed an approximately 60% increase in signal in the retinal margins, as compared to the pre-$MnCl_2$ baseline scan. The signal enhancement appeared to maximize in the 4-h scan and was stable between 12 and 24 h. All signal enhancement in the retina was eliminated by 48 h, and the signal intensity returned to approximately pre-injection levels. There was no signal enhancement seen in the vitreous, even at 48 h post i.p. injection.

(a)

Pre-Mn

4 hrs

24 hrs

48 hrs

Signal intensity profile plot

(b)

Normalized Signal Intensity (AU)

Distance μm

pre-Mn   4hrs   12 hrs   24 hrs   48 hrs
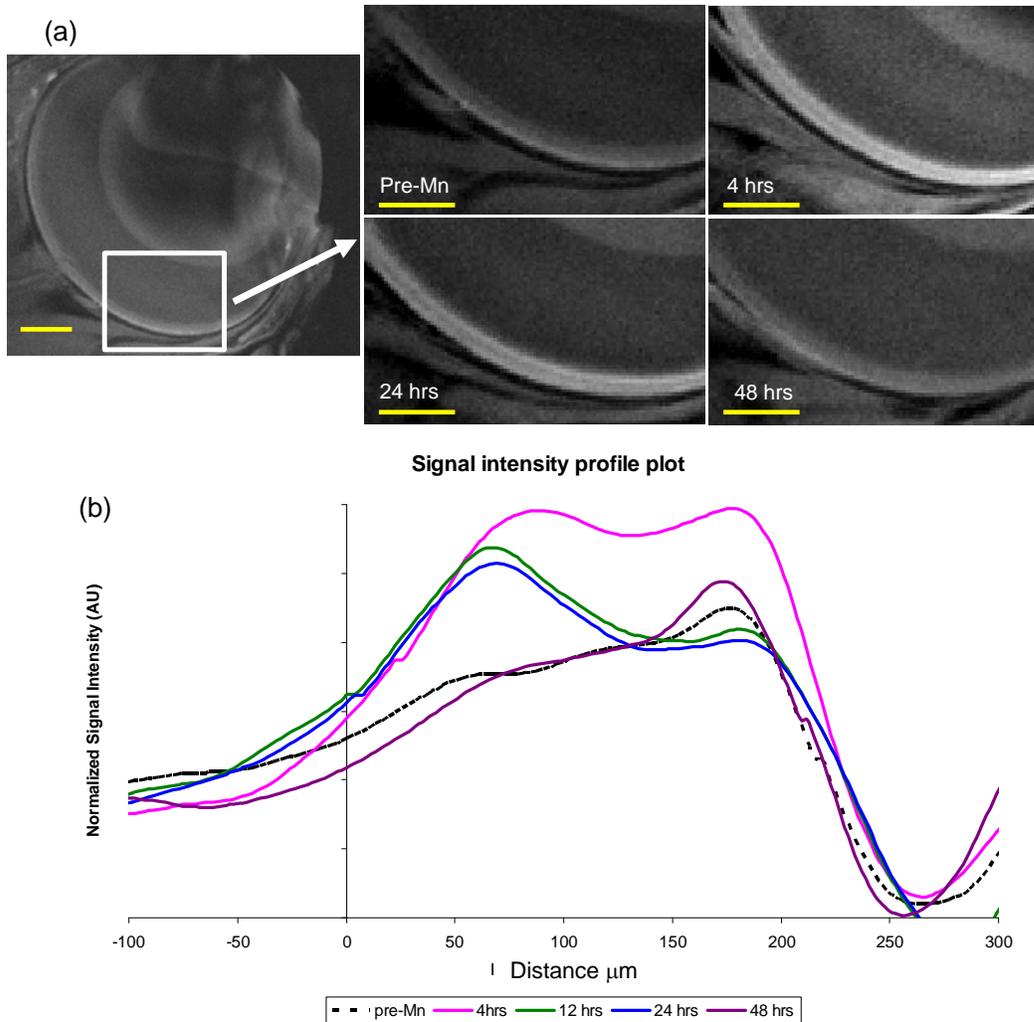
Fig. 5.1: Signal intensity changes following intraparitoneal injection of 66 mg/kg isoosmolar MnCl$_2$ in different rats. Two distinct layers of enhancement are seen to maximize at approximately 4 hours post injection. Scale bars in (a) is 1 mm.

In the second study, longitudinal changes to retinal signal intensity were explored between 0 and 6 h post-i.p.-Mn^{2+} administration. The signal intensity from the retina did not change significantly between 4 and 6 h post-Mn^{2+} administration, and these time points were omitted from the analysis. Selected profile plots of the retina, from 0 - 4 h post-Mn^{2+} administration are shown in Fig. 5.2. Distinct enhancement was seen in the inner and outer boundaries of the retina with a darker layer making up the middle of the

retina, similar to the first study. There was no significant enhancement seen in the vitreous over the time ranges studied.

Signal intensity profile plot
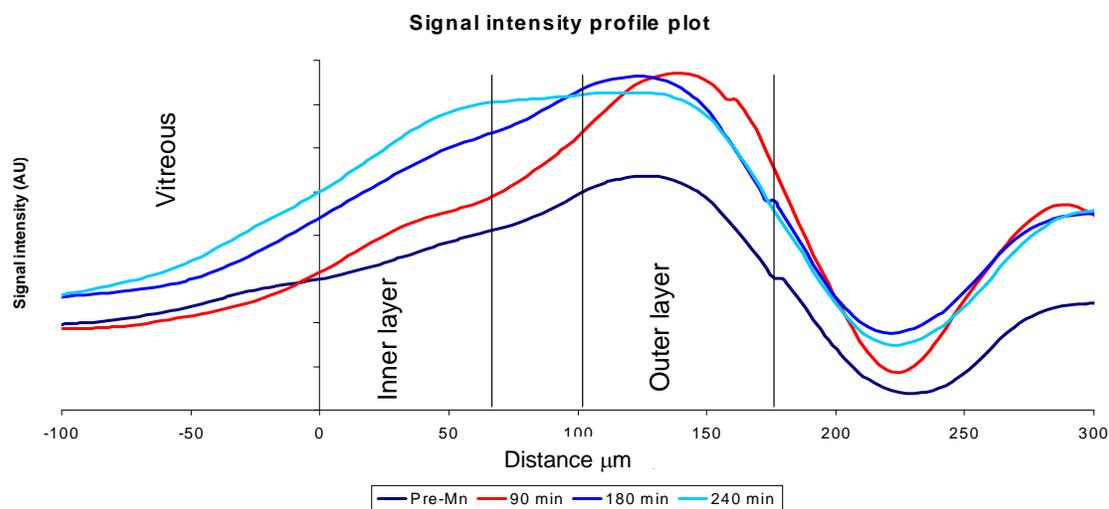
Fig. 5.2: Signal-intensity-profile plots across the dark-adapted retina pre- and post i.p. injection of 66mg/kg MnCl$_2$. A difference in the uptake dynamics is seen in the inner and outer retinal boundaries (marked by the vertical lines).

5.2.3 Discussion

MEMRI of the retina acquired after the i.p administration of MnCl$_2$ showed signal enhancement in the retina lasting up to 48 h. Group-averaged, signal-intensity increases from the inner and outer retinal layers, as well as the vitreous, showed a different time course of enhancement for the inner and outer bright layers of the retina. While the signal intensity of the inner retinal layer seemed to increase steadily over the 4-h period, the signal intensity from the outer retinal layer increased rapidly and reached a peak within 90 min after i.p. injection.

The amounts of Mn used for this study was less than half the LD$_{50}$ (lethal dose, 50%) suggested for i.p. injection in rats (MSDS), and far less than some of the highest dosage used in literature for MEMRI (175 mg/kg i.v.) [173]. The route of administration

of Mn in this study was intraperitoneal, allowing a slower absorption of $MnCl_2$ into the blood stream, compared to the direct intravenous routes in some MEMRI studies of the brain. Slower absorption from the peritoneum, with the well-adjusted osmolarity (isotonic solution) and pH of the $MnCl_2$ reduced the Mn^{2+} cardiac toxicity. Histology performed on the Mn^{2+}-injected rats showed an essentially intact retina.

Although the half-life of Mn^{2+} in the rat is of the order of 146 days [176], the elimination rate varies widely from one organ to another. Mn^{2+} is actively taken up from the blood by the liver and kidneys. In general, the half-life of Mn^{2+} in the brain is on the order of 50-75 days [177], while that in the blood is much shorter, on the order of hours after intravenous injection [178]. Comparing the data from the i.p. injection of Mn^{2+} and the half-life of Mn^{2+} in various tissues, it was concluded that the majority of the MRI signal change originated from the vasculature. Furthermore, group-averaged signal from the vitreous, normalized to the saline reference signal, did not show significant enhancement, suggesting little or no leakage of Mn^{2+} across the BRB. Another possibility is that the endothelial cells outlining the choroidal vessels strongly accumulated Mn^{2+} in a manner similar to the cerebral vasculatures [87, 179]. This could result in increased signal from the vasculature, which could vary as the concentration of Mn^{2+} in the blood varies.

These results also suggest that the dynamics of Mn^{2+} after systemic administration is different in the retina and the brain. The transport of Mn^{2+} into the brain and its subsequent clearance is slow and complete elimination takes months. The Mn^{2+} transport across the epithelial cells in the capillaries is thought to be saturable, and, at high doses, Mn^{2+} enters the brain primarily through the fenestrations in the capillaries of the choroid

plexus where the CSF is replenished. The vitreous, unlike the CSF, is not replenished and the fenestrations in the choroidal capillaries of the eye do not seem to leak Mn^{2+} into the neural retina. The RPE layer sandwiched between the neural retina and the choroids is responsible for maintaining the ionic balance in the retina, and may be actively excluding any transport of Mn^{2+} into the neural retina. Furthermore, our data show that the transport of Mn^{2+} across the endothelial cells in the retinal capillaries is not significant for differential accumulation and imaging the anatomy of the retina. Another possibility could be that any transport of Mn^{2+} across the endothelial cell is countered by its anterograde transport along the neurons. However, we failed to pick up any significant enhancement along the optic nerve, once again suggesting that the amount of Mn^{2+} in the neural retina is very small if not absent.

Analysis of short time points shows a progressive increase in signal between 0 - 4 h post-Mn^{2+} administration. Another study found similar increases in retinal signal intensity after i.p. administration of 44mg/kg $MnCl_2$ [167]. Inhibition of retinal function with ouabain caused a reduction in signal enhancement post-$MnCl_2$ administration in that study. This effect was attributed to the reduced ion demand in the retina due to inhibition of retinal function by ouabain. However, the effect of ouabain on non-manganese-enhanced retinal signal intensity was not studied. More importantly, the signal intensity of the retina between different rats was normalized using noise intensity. That strategy may generate erroneous signal enhancement depending on the tuning and matching of the RF coil on any given animal setup, as well as other conditions such as ghosting or movement artifacts. In our study, the signal intensity was normalized in different animals using a saline reference signal. Since the signal intensity of the saline reference phantom

is expected to be much more stable and a more effective strategy for signal normalization between animals.

In our study, there was no significant difference in the dynamics or final enhancement in the inner retina between groups imaged in the dark or those imaged with a flashing light (data not shown). However, the outer retinal signal enhancement in dark-adapted rats was significantly lower than those illuminated with flashing light in the first half hour. One explanation could be an increased choroidal blood flow or associated BOLD effects due to decreased deoxy-hemoglobin. However, this effect was limited to the choroidal vasculature indicating that it may be a transient event brought on by the increase blood flow due to photoreceptor activation. This signal enhancement was not explored further in the present study due to the absence of sustained neural enhancement as well as the transient nature of the differences between the two groups.

In summary, we did not find any evidence of Mn^{2+} crossing the BRB up to 48 h after i.p. injection. The concentration of Mn^{2+} in was too low to provide contrast among the various layers of the neural retina. Therefore, methods were sought to bypass the BRB and administer Mn^{2+} directly into the vitreous.

5.2.4 Conclusion

Retinal enhancement post-i.p. injection of Mn^{2+} was limited to the retinal and choroidal vasculature. Anatomical layers of the retina were not observed at any time point after the i.p. administration of Mn^{2+} either due to an insufficient dose or unfavorable kinetics of Mn^{2+} leakage from the vasculature to the neural retina.

Techniques to bypass the blood-retinal barrier could therefore be more efficient in Mn^{2+} delivery to neural retina and potentially provide an opportunity for retinal imaging.

5.3 Intravitreal injection of $MnCl_2$

5.3.1 Materials and methods

Animal Preparation: Two groups of rats were used in this study: (i) The optimal dosage was determined by intravitreal injection of 5 μL of isotonic $MnCl_2$ at varying concentrations (0.12 to 60 mM) in wild-type rats (Sprague-Dawley, n=20, 350-450g); and (ii) the optimal dose of $MnCl_2$ derived from the first group was used to obtain layer-specific MEMRI in wild-type rats (Sprague-Dawley, n=5, 350-450g).

Rats were anesthetized under 2% isoflurane and $MnCl_2$ was injected intravitreally at the region of the ora serrata, approximately 1 mm behind the limbus. The Mn^{2+} was administered slowly, over 2 min, *via* a 30½-gauge needle and a Hamiltonian syringe. The needle was left in place for additional 2 min before withdrawal.

After intravitreal $MnCl_2$ injection, animals were returned to their cages and allowed to recover normally. Twenty-four hours after $MnCl_2$ injection, the rats were anesthetized under 2% isoflurane and the femoral vein was catheterized for remote administration of drugs during MRI. The trachea was intubated and rats were mechanically ventilated, paralyzed (pancuronium bromide, 3 mg/kg first dose, followed by 1 mg/kg/hr, i.v.) and placed on imaging cradle as described in Chapter 2. MRI was performed under 1% isoflurane anesthesia with continuous monitoring of end-tidal CO_2

and rectal temperature. MRI was performed before and after i.v. administration of Gd-DTPA (0.4 mL/kg, 0.5 M, i.v.) while the Mn^{2+}-injected animals were in the magnet.

MR imaging: MRI experiments were performed on a Bruker 4.7T or 7T scanner (Billerica, MA). Separate experiments were done at different field strengths to determine Mn^{2+} dosage for optimal visualization of the various retinal layers (optimal dosage). Images were acquired on the 4.7T system using a conventional gradient-echo pulse sequence with TR = 100 ms, TE = 8.5 ms, FA=45 degrees, 0.8 mm slice thickness, 16 repetitions acquired as a time series, data matrix = 256 x 256, and FOV = 6.4 mm x 6.4 mm, yielding an in-plane resolution of 25 μm x 25 μm. Imaging parameters on the 7T system were essentially similar except that the FA was reduced to 40º to compensate for the longer T_1 relaxation time at higher field.

Data analysis: Data analysis was performed using the Stimulate software package [180] and profile-plot-analysis programs written in Matlab as described in Chapter 2. The thickness of each layer within the retina was calculated using signal-intensity profiles and full-width-at-half-maximum (FWHM) estimates. Automated determination of FWHM via multiple-Gaussian model was initially explored but found to be unreliable due to the many parameters required to fit the data in the presence of irregular baselines (data not shown). Manual FWHM determination was employed and found to be reliable although laborious.

Histology: Standard histology was obtained (with help of Dr. Pardue, Atlanta VA hospital) on the same animals approximately along the same imaging slices. Following anesthetic overdose, eyes were enucleated and fixed in 2% glutaraldehyde by directly injecting it into the eyes as well as by immersion. Eyes were rinsed in 0.1 M phosphate buffer, dissected to isolate the posterior eyecup, and divided into two halves along the optic nerve. The eyeball was embedded in epoxy-resin and sectioned at 5 μm for toluidine blue staining and retinal thickness measurements. The thickness of different layers of the neural retina and choroidal vasculature were semi-automatically derived using an image analysis program (Image Pro, Cybernetics).

5.3.2 Results

The dose-response of 5-μL intravitreal injections of $MnCl_2$ on a 7T system is shown in Fig. 5.3. Signal enhancement in the retina and vitreous was seen at all concentrations of $MnCl_2$. MRI performed 24 h after a 5-μL intravitreal injection of 12 mM $MnCl_2$ showed seven distinct layers of alternating bright and dark layers in the retina. This was deemed as the optimal dose for anatomical imaging of the retina on a 7T system. Higher concentrations of $MnCl_2$ resulted in increased thickness of the innermost dark layer as seen in Fig. 5.3d. The signal-intensity-profile plots across the retinal thickness are shown in Fig. 5.3e. Similarly, the optimal dose of $MnCl_2$ was determined to be 5 μL of 30 mM $MnCl_2$ solution at the 4.7T.

The retinal layers were numbered #1 through #7, starting with the inner retinal layer as shown in Fig. 5.4a. Signal intensity profiles projected perpendicular to the retinal surface showed a diffuse bright layer closest to the vitreous (#1) and three bright layers (#3, #5 and #7) interdispersed by three dark layers (#2, #4, and #6) as shown in Fig. 5.4b. The layers were tentatively assigned as #1: ganglion cell, #2: inner plexiform, #3: inner nuclear, #4: outer plexiform, #5: outer nuclear, #6: inner and outer segments and #7: choroid, as indicated in the accompanying histology.
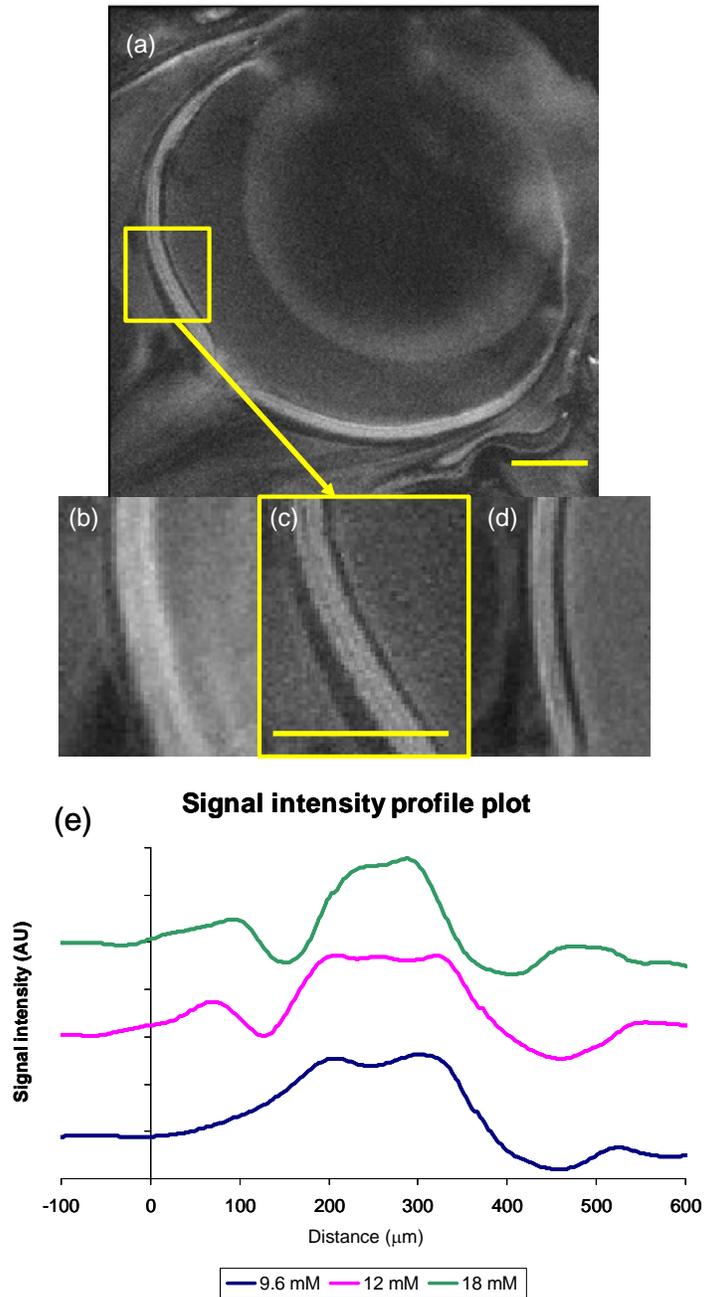
Fig. 5.3: Dose response MEMRI in eyes of different rats at 7T. (a) and (c) shows seven layers of alternating signal-intensity, 24 h post 5 μL intravitreal injection of 12 mM isotonic MnCl$_2$. The seven layers are not seen after either (b) 9.6 mM isotonic MnCl$_2$ or (d) 12 mM isotonic MnCl$_2$. (e) Stacked signal-intensity-profiles plots from these rats show the seven layers consistent with MRI images. Scale bars in (a) and (c) is 1mm.

Intravenous injection of Gd-DTPA enhanced the retinal and choroidal vasculature as shown in Fig. 5.5. Subtraction of pre- and post-Gd-DTPA images and comparison of their intensity profiles showed enhancement of layer #1-3 and 7. However, there were no
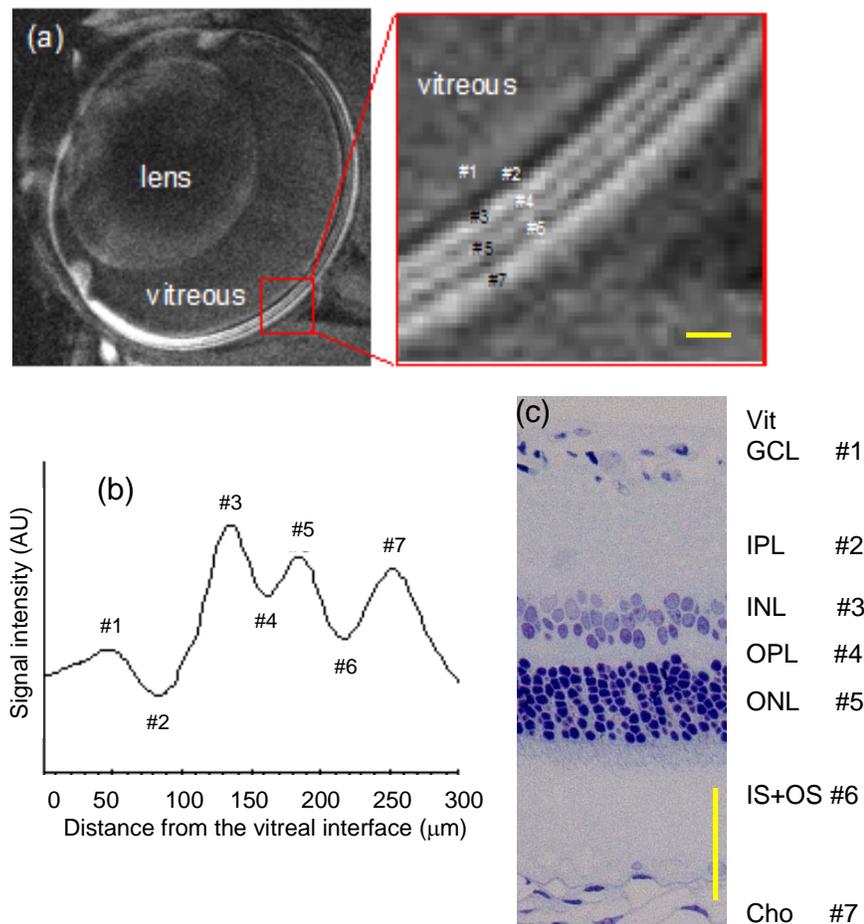
Fig. 5.4: (a) Mn^{2+}-enhanced anatomical MRI at 25 μm x 25 μm in-plane resolution, (b) signal-intensity-profile plot in the retina in (a). (c) Histology performed on the same rat, with tentative assignments of the MRI layers: 1. ganglion cell layer (GCL), 2. inner plexiform layer (IPL), 3. inner nuclear layer (INL), 4. outer plexiform layer (OPL), 5. outer nuclear layer (ONL), 6. Inner and outer photoreceptor segments (IS+OS), 7. choroidal vascular layer (Cho). Scale bars in (a, inset) is 100 μm and in (c) is 50 μm.

significant enhancements of the middle sections of the retina or the vitreous, confirming the tentative layer assignment. The outer retinal layer #7 was more enhanced than the inner layers #1-3, and the outer layer showed an apparent increase in size. The anterior

segment of the eye, on the other hand, was enhanced by Gd-DTPA due to the absence of a tight barrier (data not shown).

The thickness of individual layers observed in MRI was cross-validated with histology on the same rats. MRI and histological-layer assignments and laminar thicknesses were tabulated and are

Fig. 5.5: MEMRI of the rat retina (a) before, (b) after Gd-DTPA intravenous administration and (c) the difference image between (a) and (b). (D) Signal-intensity profiles obtained perpendicular to the retina before and after the intravenous administration of Gd-DTPA. Signal enhancement were observed in the outer layers on either side of the retina (as indicated by large arrows), most evident in the "difference" image. Scale bars in (a), (b) and (c) is 100 μm.

summarized in table 5.1. The total thickness of the normal retina including the choroidal vascular layer was 280 ± 30 μm by MRI and 250 ± 10 μm by histology. Histological examination did not show any obvious changes in the retina of the Mn^{2+} injected rats.

5.3.3 Discussion

Seven distinct layers of alternating bright and dark intensities could be seen in the retina, 24 h after the injection of 5 μL of 30 mM $MnCl_2$ at 4.7T and 12 mM $MnCl_2$ at 7T. These MRI-visible layers were assigned to be ganglion cell layer, inner plexiform layer, inner nuclear layer, outer plexiform layer, outer nuclear layer, inner and outer segment

layer and choroidal vascular layer. Gd-DTPA, an intravascular contrast agent, was used to confirm the layer assignment.

Layer	MRI Layer	MRI thickness (pre Gd-DTPA)	MRI thickness (post Gd-DTPA)	Histology thickness
Nerve fiber	1	70 ± 30	50 ± 10	-
Ganglion cell				31 ± 6
Inner plexiform	2	50 ± 3	51 ± 9	46 ± 4
Inner nuclear	3	38 ± 6	38 ± 5	39 ± 6
Outer plexiform	4	30 ± 7	33 ± 3	$14 \pm 3**$
Outer nuclear	5	25 ± 1	30 ± 10	44 ± 7
Photoreceptor segments	6	28 ± 3	30 ± 5	60 ± 20
RPE	-	-	-	5 ± 0.8
Choroids	7	$40 \pm 10^*$	$60 \pm 10^*$	$35 \pm 7**$
Total retinal thickness	**1-7**	**280 ± 30**	**280 ± 30**	**250 ± 10**

*Table 5.1: The laminar thickness (μm, mean $\pm$ SD) of the wild type Sprague-Dawley rat retina determined by MRI (n=7) and histology (n=5). The choroidal-vascular layer post-Gd-DTPA was significantly thicker (*p < 0.05) than pre-Gd-DTPA. Some retinal layer thickness were significantly different (** p<0.05) between MRI than histology*

Mn^{2+} dose response

The dose response of 5-μL intravitreal injections of $MnCl_2$ on a 7T system is shown in Fig. 5.3. At lower concentrations of $MnCl_2$, three retinal layers were faintly visible. As the concentration of $MnCl_2$ was increased from 0.17 to 9.6 mM, the brightness of the retina was also seen to increase (data not shown). However, the best contrast between the retinal layers were seen 24 h after administration of 5 μL of 12 mM $MnCl_2$. Higher concentrations of $MnCl_2$ resulted in increased thickness of the innermost dark layer as seen in Fig. 5.3d and e. This effect is consistent with increased T_2^* signal decay at high concentrations of $MnCl_2$, and the retinal layers closest to the vitreous, appeared to

be most susceptible to this increased T_2* signal decay. The increased T_2* from the pixels in the inner dark layer seemed to obscure one of the bright layers on the retina due to susceptibility or partial volume error (PVE), and only 5 or sometimes 6 layers were seen in the retina at this concentration.

The dose-response of $MnCl_2$ indicates that the retinal contrast arises due to increased transverse relaxation in regions of increased Mn^{2+} accumulation. Mn^{2+} enters the cell primarily through voltage-gated calcium channels and is transported in an anterograde manner. This would suggest that the high density of axon terminals and dendrites in the plexiform layers make an ideal region for Mn^{2+} influx into the retina. Also, the proximity of the inner plexiform layer to the vitreous may be responsible for the high concentration and sensitivity of the inner layer. The axons in the nerve-fiber layer have a different morphology than that in the plexiform layers, in that the synapses of these axons are not inside the eye. This could possibly explain the signal intensity from these axons being same as that of the cell body.

Images were acquired 24 h after $MnCl_2$ injection, which allowed substantial $MnCl_2$ to be absorbed by the retinal neurons, and sufficient contrast to develop between the various retinal layers. Images acquired at 7T shortly (4 h) after the injection of $MnCl_2$ showed only 6 layers in the retina just as in the case of a higher dose (Fig. 5.7c), due to the large vitreal concentration of Mn^{2+}. Images acquired at low dose and shorter injection-to-scan intervals, yielded insufficient or inconsistent contrast to reliably distinguish different layers in the retina. The long time required for even distribution of $MnCl_2$ precluded reliable functional studies in Mn^{2+}-injected rats exposed to light and dark as in the case of i.p. injection.

Layer assignment

The hydrophilic nature Gd-DTPA and its large size prevent it from crossing blood-brain or blood-retinal barriers. Therefore, intravascular Gd-DTPA can be used to identify the extent of the retinal and choroidal vasculature [115] that resides on either side of the retina. Gd-DTPA experiments, therefore, established the boundaries of the retina, set the upper limit of the retinal thickness and helped in layer assignment. Layer #1-#3 was assigned to the ganglion cell layer, inner plexiform layer and the inner nuclear layer because the layers were enhanced by Gd-DTPA, consistent with embedded retinal vessels within these layers. The avascular layers of the retina are most of the outer plexiform layer and the photoreceptor layers. These layers make up layers #4-#6 in the MRI, but a consistent lack of MRI signal enhancement was seen only in layer #5. This suggests that the layers #4 and #6 were affected by partial volume error or interpolation error during the plotting of the signal-intensity profile. Neither decreasing the interpolation factor nor reducing the area of the retina analyzed showed a decrease in signal enhancement from layers 4 and 6. This suggests that the error originates at the MRI data acquisition stage. This explanation is likely to be most valid for layer 4, as the outer plexiform layer is very thin and likely to be heavily contaminated by signal from the neighboring layers. Furthermore, the choroidal flow is very high, and likely to easily contaminate the neighboring pixels in the MRI.

The seven MRI-derived layers were interpreted to correspond to the seven layers delineated by histology. The choroidal vasculature was significantly thinner in the histological sections than in the MRI. This could be attributed to the collapse of the big choroidal vessels upon enucleation, which was apparent in the histology slides. The RPE layer could not be assigned in the MRI images as it is an extremely thin 5-μm layer in histology, and invisible in the MR images due to partial volume error (discussed in more detail in the simulation experiment in Chapter 4, Section 4.3.3 and Section 4.4.3). Lastly, the nerve-fiber layer was consistently absent in the histological slices. This layer is composed of dispersed axons emanating from the ganglion cell layer, which are often lost during the thin-sectioning procedure used for histology. In the MRI, however, this layer contributes to the diffuse inner layer (#1) in the retina, due to the nature and density of the ganglion cells. One of the best depictions of the nerve-fiber layer obtained by MEMRI can be seen in Fig. 5.6, where the optic nerve is seen continuous with the inner diffuse bright layer.
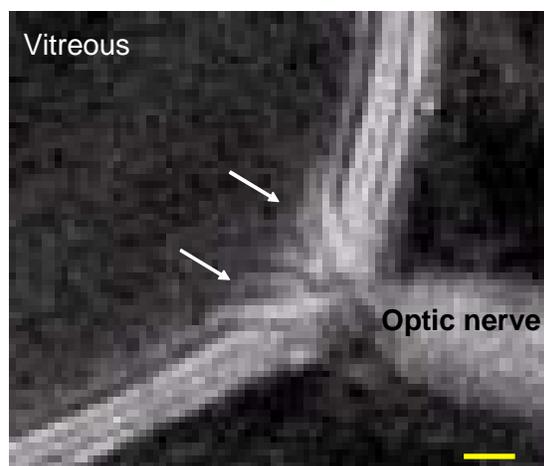
Fig. 5.6: One of the best depictions of the nerve fiber layer from our various MEMRI experiments. The ganglion cell axons (arrows) can be seen entering the optic nerve disc to form the optic nerve. Scale bar is 200 μm.

The above interpretations of retinal layers are consistent with the notion that the plexiform layers were more T_2- and T_2*-enhanced than the nuclear layers. One potential explanation is that the intracellular volume of the cell body is larger than that of the synaptic processes in the plexiform layer, diluting the effects of the intracellular Mn^{2+}.

There is also evidence that calcium channels for Mn^{2+} entry into the neuron are preferentially distributed in the axons and dendrites of the neurons [181]. While these assignments are believed to be valid, it may also be the case that the contrast of the nuclear layers and the plexiform layers are reversed, as well as the possibility that a bright or dark MRI layer includes multiple retinal layers. These alternative MRI laminar assignments, however, did not fit the data. Specifically, these alternative interpretations were inconsistent with the vascular boundaries established by Gd-DTPA enhancement, and thicknesses of the respective layers established by histology. Direct validation was performed by autoradiography experiments, as discussed in next section, to test the hypothesis of the above layer assignments.

Retinal thickness measurements

The MEMRI technique demonstrated higher resolution and higher contrast for delineating retinal layers. The retinal layer thicknesses determined by histology in this study are in good agreement with published histology [58, 182]. However, the thickness of the individual layers in the rat retina was not reported in that study. The total retina thickness in adult rats derived from the lower resolution MRI scans performed without Mn^{2+} was 270 ± 30 μm by MRI and 210 ± 10 μm by histology [115], which is comparable to the thickness observed herein. The choroidal thickness seen in the unenhanced lower-resolution scans [37] was 86 ± 10 μm and in the high-resolution, Gd-DTPA-enhanced images was 60 ± 10 μm. This difference can be attributed to better accuracy in the higher-resolution scans and the better contrast-to-noise ratio of the MEMRI scans. MRI-derived choroidal vascular thickness was consistently thicker than

that derived from histology. Possible explanations for the discrepancy between *ex vivo* and *in vivo* choroid thickness are: 1) histology is susceptible to fixation shrinkage, 2) vessels in the extracted choroid collapse in the absence of blood pressure, and 3) partial-volume error (PVE) could potentially overestimate choroid thickness in MRI scans.

Of note, there was an apparent thickness-increase in the choroidal vascular layer from 40 ± 10 μm pre-Gd-DTPA to 60 ± 10 μm post Gd-DTPA ($p<0.05$), likely due to the increased PVE associated with the increased signal intensity of the choroidal layer. Gd-DTPA could be making some of the larger choroidal vessels more visible, thereby increasing the thickness of the layer. We found one report on choroidal thickness of ~25 μm by histology [183], apart from our own studies reported in Chapter 4 [37]. The lack of literature on choroid thickness is likely due to the difficulty in extracting intact choroid and the obvious collapse of the non-perfused choroidal vessels, making it appear thinner in histology. *In vivo* imaging techniques based on optical imaging techniques are largely limited by the opacity of the retina and the RPE.

Partial volume error (PVE)

While the spatial resolution used here compared favorably to published literature, potential for partial volume error exists for imaging retinal layers. As suggested by the simulations to determine the accuracy of the thickness measurements (discussed in Section 4.4.3), the thickness of thin (thickness of layers comparable to image resolution) bright layers are generally overestimated and dark layers underestimated due to PVE. Given the resolution and imaging slice thickness employed in this study, PVE had negligible effect on the measurement of the entire retinal thickness and thus the total

retinal thickness was reliably determined. With respect to individual layers, however, this was more of an issue because each layer consisted of only 1-3 pixels. Nonetheless, seven layers in the MR images and intensity-profiles were clearly resolved. Therefore, although there is some PVE, the overall conclusions in regard to MEMRI layer assignments are likely to be valid.

One way to mitigate PVE is to increase the spatial resolution of the scans. However, experiments at 13-μm in-plane resolution with the same setup were too noisy for reliable layer-thickness calculations. Apart from the obviously lower signal from smaller voxels, the high resolution scans also suffer from signal loss due to diffusion of water out of the voxel during the TE interval. A quick calculation of the diffusion distance of water in retina (average retinal ADC = 0.64×10^{-3} mm^2/s) and vitreous (ADC = 2.5×10^{-3} mm^2/s) reveals that the mean-square displacement of water molecules is expected to be about 5 μm in the retina and 30 μm in the vitreous during the spin-echo generation (Chapter 3). Therefore, the diffusion of water is not negligible at in-plane resolutions on the order of 13 μm. Diffusion of water out of a pixel is an added cause for signal loss within a pixel, resulting in poor SNR and CNR at these resolutions.

Intravitreal injections

Intravitreal injections have been demonstrated to be a safe and efficient form of drug delivery, especially for a single dosage in rats, rabbits, primates and humans [184]. However, the large size of the rat lens and the small vitreal volume made intravitreal injections difficult to perform routinely. The best results were obtained using a 30½-gauge needle that was broken off and sharpened at a 2-mm length. Injections were done

at the ora serrata with the needle oriented at a steep downward angle to avoid damage to the lens. The best access was obtained by holding the eye still using a curved forceps. Furthermore, the injection volume and its osmolarity needed to be carefully controlled. To derive the appropriate injection volume, the approximate volume of the vitreous was estimated from the MR images to be 53 μL in a 3-month-old adult rat. This estimate was consistent with measurements using MRI and other techniques [185, 186], but significantly higher than that reported in Ref. [187]. Five-microliter injections were chosen as an effective dose for delivering $MnCl_2$ uniformly to the entire retina. A larger injection volume was avoided to prevent loss of $MnCl_2$ post-injection due to high intraocular pressure. Smaller volumes were found to distribute $MnCl_2$ non-uniformly in the retina [187]. Although the intraocular pressure (IOP) was not monitored, MRI and visual inspection did not reveal significant distortion of the eye shape due to intravitreal Mn^{2+} injection, suggesting that IOP was not significantly perturbed. Furthermore, the osmolarity of the injections was carefully controlled since hypertonic and hypotonic intravitreal injections cause neuronal death and retinal detachment [187]. The osmolarity of the vitreous was maintained after intravitreal injection by using a 330 mOsmol $MnCl_2$ solution at a pH of 7.2, similar to the vitreous [188, 189].

Mn^{2+} toxicity

Overdose of Mn^{2+} is associated with permanent neurological damage and a syndrome similar to Parkinson's disease [190-192]. Even though Mn^{2+}-based contrast agents have been approved for limited use in human liver, these contrast agents employ chelated Mn^{2+} and are generally targeted to specific tissues and easily excreted from the

body. In this study, the bioactive property of free Mn^{2+} was required to provide tissue contrast within the retina; therefore, chelated forms could not be used. Furthermore, the clearance of Mn^{2+} from the vitreous is likely to be by absorption and transport in the retinal neurons, due to the stagnant nature of the vitreous. This would potentially increase the Mn^{2+} concentration in specific sites in the brain and retina. Gross histology and behavioral assessment did not show any obvious signs of Mn^{2+} toxicity or changes in retinal thickness within 24 h after intravitreal Mn^{2+} injection. However, the acute and chronic Mn^{2+} toxicity in the retina remains to be rigorously demonstrated. It should be noted that the dosage used in this study is ~10 times lower than those of intravitreal Mn^{2+} injections employed in tract tracing of the optic nerve and the visual pathway (2 μL of 800 mM $MnCl_2$ [193, 194]).

5.3.4 Conclusion

High-resolution, MEMRI was developed for imaging lamina-specific structures in the rat retina *in vivo* without relying on optical transparency. High-resolution contrast-enhanced MRI of the retina can be used for anatomical images of rat retina. Intravitreal injection of Mn^{2+} allowed the blood-retinal barrier to be bypassed and permitted differential accumulation of Mn^{2+} in the different retinal layers. Gd-DTPA contrast-enhanced MRI studies confirmed the vascular boundaries of the retina and facilitated layer assignment. MRI layer thicknesses were quantified and compared to standard histology.

The contrast provided between the retinal layers in MEMRI was better than that in most other retinal imaging techniques. Imaging methods like OCT and

ultrasonogrpahy rely on reflection of waves from boundaries between tissue layers and therefore the layer boundaries are better visualized than the layer itself. Other techniques like laser speckle and ophthalmoscopy lack the ability to tomographically visualize retinal images. MRI provides excellent tissue contrast, with depth discrimination as well as a full overview of the retina and the eye, which is helpful for identifying small lesions.

5.4 Mn^{54} Autoradiography for layer assignment

Layer assignments in MEMRI were based on MRI signal changes in response to Mn^{2+} uptake and depiction of vascular layers using Gd-DTPA. MRI before and after injection of Gd-DTPA in rats injected intravitreally with $MnCl_2$ helped establish the boundaries of the retina as well as locate the choroidal vessels. The many retinal layers seen in the MEMRI however could not be definitely assigned without further corroboration. To this end, qualitative or semi-quantitative assessment of the distribution of Mn^{2+} in the retina was performed post-intravitreal injection. To determine the various layers observed on the MRI, MEMRI and Mn^{54} autoradiography was performed in separate group of rats 4 h after intravitreal injection of 18 mM $MnCl_2$. The MRI and autoradiography could not be performed on the same animal due to restrictions on the use of radioactive material in the MRI suite. Similar restrictions prevented animals being left overnight to replicate the optimal imaging dosage and the times derived in previous section (24 h post-intravitreal injection of $MnCl_2$). Therefore, the behavior of $MnCl_2$ in the various retinal layers was determined by using short scan times and slightly higher concentrations of $MnCl_2$, as well as MRI on a separate group of animals.

5.4.1 Materials and methods

Semi-quantification of Mn^{2+} accumulation in the various retinal layers was performed by emulsion autoradiography with Mn^{54} (technique described [195] and [196] performed under direct supervision of Prof. M. J. Kuhar, Emory University). Trace amounts of Mn^{54} in HCl (2 nM, 20 μCi, half-life of 312.7 days) were first evaporated in an Eppendorf tube before adding 5 μL of 18 mM $MnCl_2$. The solution was injected intravitreally into the rat eye (n=3) and the animal was allowed to recover normally. Four hours after Mn^{54} administration, the animal was deeply anesthetized and the eye enucleated. Autoradiography was also performed on one control animal where radioactive Mn^{54} was omitted from the intravitreal injection. The eyes were immediately frozen onto a cryostat chuck using tissue-tech OCT solution and dry ice, and left overnight in an -80º C. Sixteen-micrometer sections were obtained in a saggital plane similar in orientation to the MRI. The cryostat was kept at -25º to -30º C and the slices were loaded onto a slide.

Emulsion-coated coverslips were prepared in advance by dipping coverslips (25 mm × 75 mm) in emulsion (Kodak, NTB), melted on a 40º C water bath in a dark room. These emulsion-coated coverslips were allowed to dry for 4 h and stored in a black slide box at 4º C with ample amounts of Drierite capsules to absorb moisture. Care was taken that the slide box did not leak light and expose the coverslips. After a week, the emulsion-coated coverslips were carefully mounted on the slides with sections of the retina, and fixed in place with superglue and binder clips at one end of the slide. The assembly was then returned to the dark slide box with Drierite capsules, and stored in a 4ºC refrigerator for varying exposure times.

Slides were developed at specific time points (1, 2, 4, 8, and 12 weeks after mounting) in a dark room, to determine the optimal level of exposure. The developer (Kodak, DEKTOL) was prepared and diluted 1:1 in distilled water. Both the developer and fixer (Kodak, Rapid fix) were cooled to 16º C before use. The cover slips were bent away (without full separation) from the slide using a toothpick. Care was taken not to break the coverslip or to prevent it from detaching completely from the slide to ensure that the autoradiographic image was co-registered with the histological sections of the eye on the slide. The assembly was then dipped sequentially in the developer (2 min), water (10 s), fixer (3 min), and water (1 min). The developed slides were allowed to dry for 24 h.

Once dry, the slices were stained in 0.2% Pyronin Y (Nissil stain, Sigma) in 0.1M acetate buffer at a pH of 4.2. The stain was prepared by dissolving 5 mg of Pyronin Y in 250 mL of acetate buffer. The acetate buffer was prepared by mixing 150 mL of 0.2M acetic acid (made by adding 2.3 mL glacial acetic acid to 197.7 mL of distilled water) and 100 mL of 0.2M sodium acetate (made by adding 2.72 g of sodium acetate trihydrate to 100 mL distilled water) and adjusting the to pH 4.2 with acetic acid or sodium hydroxide. After rinsing in 50% ethyl alcohol for 40 s and once in water, the slide assembly was placed in Pyronin Y for 7 min for staining. After staining, the slides were washed in acetate buffer briefly, before being progressively dehydrated in graded ethyl alcohol and xylene. After staining, the coverslip was carefully mounted back on the slide with permount and allowed to dry for a few hours. After staining, both the stained retinal tissue and the autoradiographic image were viewed at the same time under a microscope. The slides were photographed under 5×, 10× and 20× magnification.

MRI was performed on a separate group of animals injected with 5 μL of 18 mM non-radioactive MnCl$_2$. The animals were allowed to recover after the injection in normal light conditions. Four hours post injection, animals were anesthetized, their trachea intubated for mechanical ventilation, and paralyzed with pancuronium bromide as described earlier. MRI was performed on a 7T Bruker system, using a gradient-echo sequence with TR = 100 ms, TE = 6.5 ms, FA=35º and an in-plane resolution of 25 μm. The relative signal intensity observed in each layer of the retina was compared to the density of the grains in each layer obtained from autoradiography.
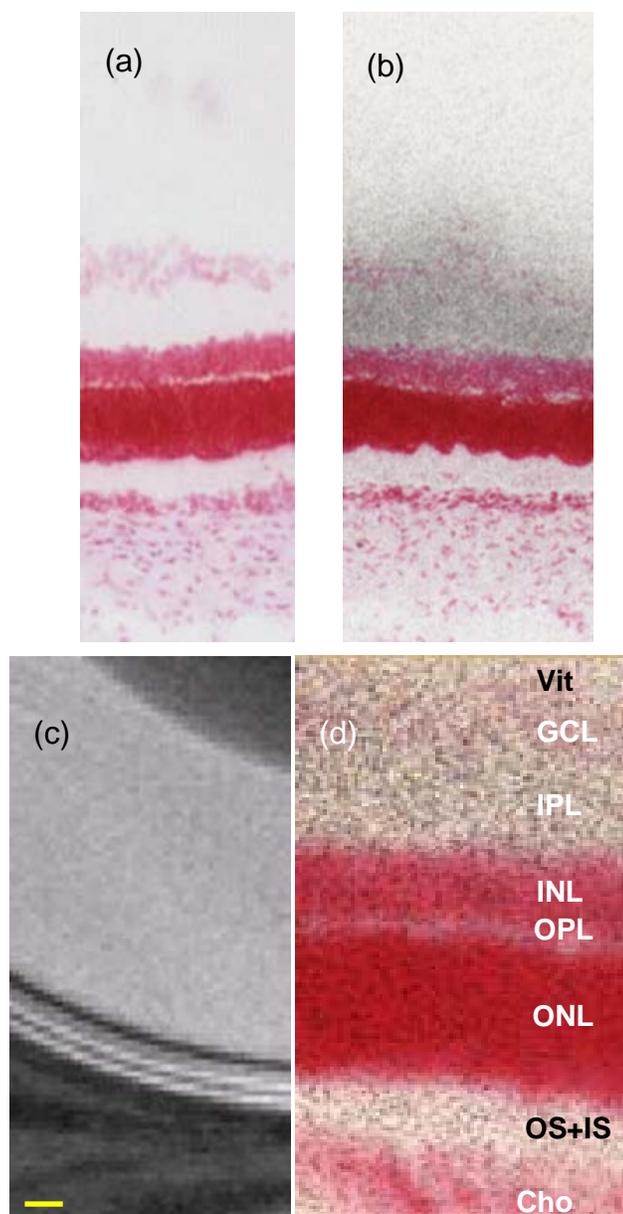
Fig. 5.7: Autoradiogram of the retina at 10x magnification from rats injected with (a) 18 mM MnCl$_2$ without Mn^{54} (control) and (b) 18 mM MnCl$_2$ with 2 nM Mn^{54}. (c) MRI of the rat retina acquired under similar conditions as (a). (d) Images taken at 20x magnification shows the distribution of the grains. The microscope has been focused on the grains on the cover-slip, making the image of the retina slightly out of focus. VI=vitreous; GCL=Ganglion cell; IPL=inner plexiform; INL=inner nuclear; OPL outer plexiform; ONL=outer nuclear; OS+IS=photoreceptor segments; Cho=choroidal vasculature. Scale bar in (c) is 200 μm.

5.4.2 Results and Discussion

Figure 5.7 shows the autoradiographic images from control and Mn[54]-injected rats in comparison with MRI. Both the control slides and Mn[54] slides showed very little background exposure away from the retinal tissue (data not shown). The ideal exposure time for Mn[54] slides was determined to be 6-8 weeks. Control rats, injected with 5 μL of 18 mM non-radioactive $MnCl_2$, did not show any patterns in the autoradiography grains, and the grain density in the retina was very low compared to the Mn[54] slides. The Mn[54] slides showed a high grain density in the regions of the vitreous, choroid and retinal tissue.

The number of grains in a unit area from a section of each retinal layer was counted and plotted against the MRI-derived signal intensity (Fig. 5.8). In general, the grain densities in the plexiform layers were greater than those in the nuclear layers. The highest grain density was observed in the inner plexiform layer (IPL) as shown in Fig. 5.7b and 5.8a. The grain density in the vitreous away from the retina was lower than that at in the IPL, indicating that Mn[54] was actively taken up by the neurons (Fig. 5.7b). The grain densities in the outer layers were comparatively lower than those in the inner layers, probably due to the proximity to the injection site as well as the relatively short time between injection and quantification. However, grains were visible in the choroid-vascular layer indicating that substantial amount of Mn[54] had crossed the blood-retinal barrier.

Comparison of autoradiography and MRI suggests that while some Mn^{2+}-dependent T_1 enhancement was seen throughout the retina, differential accumulation of Mn^{2+} within the retina caused signal loss due to T_2^* decay. The grain count is a direct measure of the contrast agent concentration which is directly proportional to the

relaxation rate. If one assumes similar initial M_0 and T_2 between the different retinal layers, the change in transverse relaxation rate in each layer depends on the concentration of Mn^{2+} in the the layer. The observed T_2 relaxation rate is given by the Eq. 1.34 (Chapter 1) as

$$\frac{1}{T_{2,observed}} = \frac{1}{T_{2,solvent}} + R_{2,Mn}[Mn^{2+}], \qquad (5.1)$$

where $[Mn^{2+}]$ is the concentration of the Mn^{2+} and $R_{2,Mn}$ (equal to $\frac{1}{T_{2,Mn}}$)is the relaxivity of Mn^{2+}. The MRI signal from the tissue can be rewritten from Eq. 1.30a and 1.30b (Chapter 1) and Eq. 3.3 (Chapter 3) as $S = S_0 e^{\frac{-TE}{T_2}}$. Substituting for $T_{2,observed}$ the equation can be written as

$$S = S_0 e^{-TE(R_{2,solvent}+R_{2,Mn}[Mn^{2+}])} = S_0 e^{-TER_{2,solvent}} e^{-TER_{2,Mn}[Mn^{2+}]} \qquad (5.2)$$

This equation is of the form $y = ae^{bx}$, where a and b are constants and y is the signal intensity in tissue with x mM Mn^{2+}. The plot of autoradiography grain-density to MRI signal-intensity was fit to this model and the correlation coefficient was determined to be 0.81 (Fig. 5.8b), suggesting a high probability that the contrast between the retinal layers was generated due to transverse relaxation. The vitreal signal intensity was omitted from the above plot due to its obviously higher T_2 values.

These results corroborated the results from the dose-response study, where the dark inner retinal layer grew darker and thicker when the Mn^{2+} concentration was increased from 9.6 mM to 12 mM and 18 mM. It should be noted that the signal intensity from the ganglion-cell and inner-nuclear layers were obtained from the interpolated plot of signal-intensity profiles, at their corresponding distances relative to other layers.

(a)

(b)

$$y = 1.6583e^{-1.2814x}$$
$$R^2 = 0.8071$$
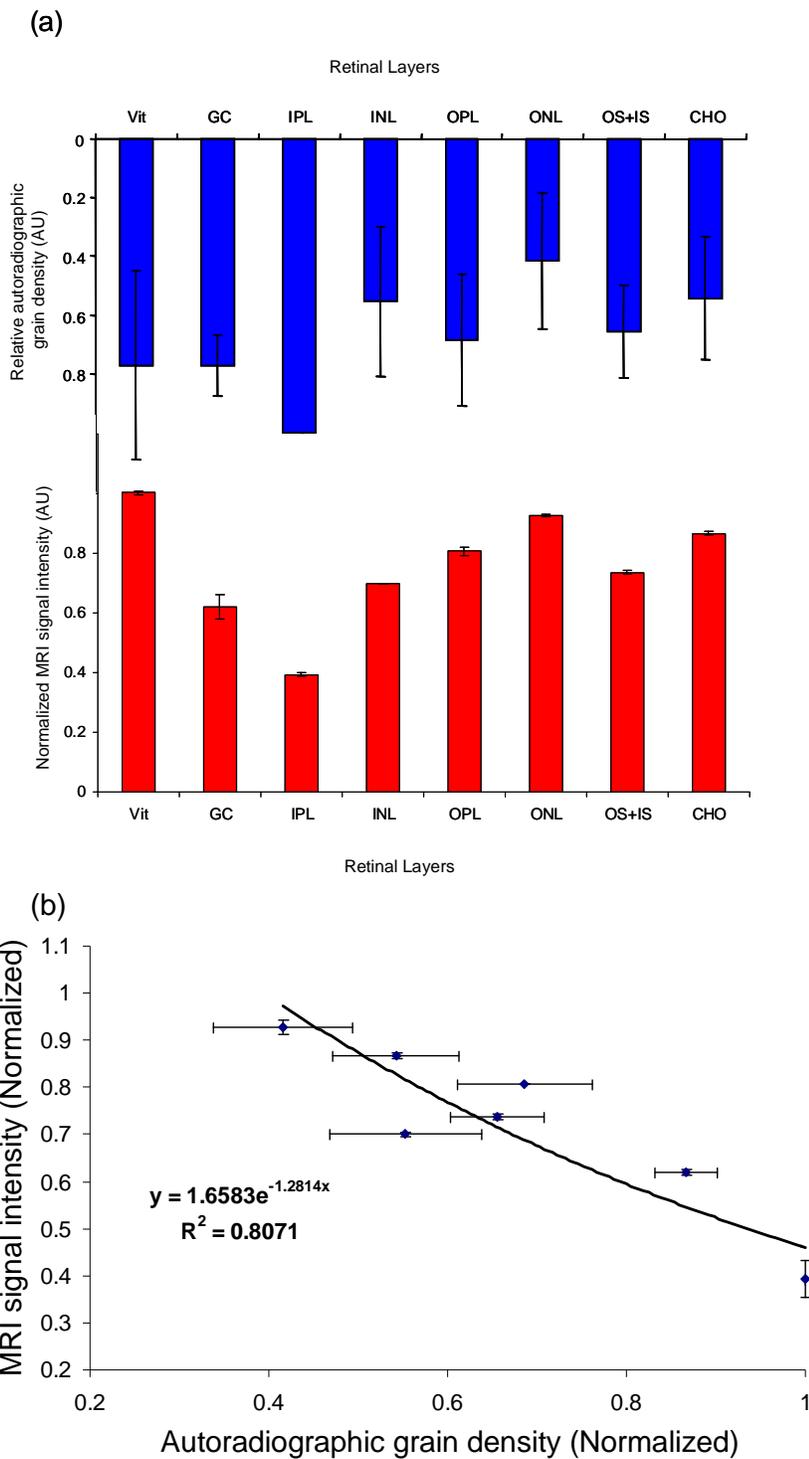
Fig. 5.8: (a) Comparison of relative autoradiographic grain-density (plotted in reverse) and MRI signal intensity from each layer of the retina (separate group of animals). (b) Plot of relative MRI signal-intensity and autoradiographic grain-density in the various retinal layers shows decreased MRI-signal intensity with increased autoradiographic grain-density. The MRI signal-intensity of the GC and INL were interpolated from the profile plot. Vit=vitreous; GCL=Ganglion cell; IPL=inner plexiform; INL=inner nuclear; OPL outer plexiform; ONL=outer nuclear; OS+IS=photoreceptor segments; CHO=choroidal vasculature.

Autoradiography showed that the plexiform layers accumulated more Mn[54] per

unit area than the nuclear layers. Studies on the dopaminergic retinal neurons suggest a higher concentration of voltage-gated calcium channels in the dendrites and axons than the perikaryon [181]. Since Mn^{2+} primarily enters the neuron through voltage-gated calcium channels it is likely to accumulate in the plexiform layers. However, Mn^{2+} is also transported anterograde and is even known to cross synapses. This suggests that the MRI contrast was generated when there was substantially more Mn^{2+} influx into the plexiform layers than the efflux or transport into the nuclear layers. This might explain the counter-intuitive nature of the dose response in Section 5.2, where 9.8 mM $MnCl_2$ failed to show any substructure, while 12 mM showed 7 retinal layers and 18 mM $MnCl_2$ showed only 5-6 layers.

T_1-contrast enhancement is theoretically easier to generate from MRI contrast agents than T_2-contrast. However, we failed to generate any T_1-contrast differences between the retinal layers, even at concentrations a 100 times lower than those used for structural imaging of the retina. This was probably due to the active accumulation of Mn^{2+} in the tissue as well as the anterograde transport along the neuron, resulting in more or less equal concentration of Mn^{2+} across the retina, despite differences in uptake.

It should be noted here that the outer plexiform layer in cryo-sections was visibly thinner than that in paraffin histology. Similar thinning of the OPL was seen in control rats as well as those not injected with Mn^{2+} (data not shown), suggesting that the effect was not from the injection. This can be attributed to the process of tissue fixation, and paraffin fixed tissue is routinely considered a better representation of the *in vivo* tissue morphology. However, cryosectioning and emulsion autoradiography techniques are well established, and have been used extensively to study receptor localization. Quick freezing

of the eye may help reduce the probability of Mn^{2+} leakage out of the cell after enucleation.

It should be noted that the GC and INL layers cound not be clearly identified in the MR images due to the short time between Mn^{2+} injection and imaging. The MRI signal intensity of the vitreous was high compared to that in Section 5.2, and was attributed to the small interval between the $MnCl_2$ administration and MR imaging. Therefore, layer #1 (GC layer) was not easily detected in the MRI performed at 4 h post-intravitreal injection, due to the hyperintense vitreous. Furthermore, a clear peak was not visible from the signal-intensity-profile plot for the INL, due to partial volume error from the IPL. The signal intensities for the GC and INL were therefore derived from the profile plot at the expected location, rather than from peak or valley estimates as was usually the case.

5.5 Summary

High-resolution MRI of the retina, 24 h after intravitreal injection of Mn^{2+}, revealed seven layers which were designated as ganglion cell layer, inner plexiform layer, inner nuclear layer, outer plexiform layer, outer nuclear layer, inner and outer segment layer and the choroidal vascular layer. The layer assignments were confirmed by using high-resolution emulsion autoradiography with trace amounts of Mn^{54}. The differences in contrast between various retinal layers originated from the differential uptake of Mn^{2+} and higher Mn^{2+} accumulation in the plexiform and photoreceptor segment layers. The technique developed here also has the potential to image functional aspects of the retina, as Mn^{2+} primarily enters the cell through voltage-gated calcium channels.

A potential improvement of this technique for animal studies could result from creating a chelated form of Mn^{2+}, or other MRI contrast agents, with markers of specific retinal cells or layers. High-resolution retinal imaging post-intravitreal administration of such a contrast agent would ensure reliable imaging of the labeled cell types in the retina in animal models, with ability to track any changes to specific retinal cells over time.

MEMRI has proved versatile as a minimally invasive technique to image retinal layers in rats. This technique may provide insights into diseases like retinal dystrophy by providing longitudinal assessments in disease models of rats. The sensitivity of layer specific MEMRI may also be promising for assessing focal lesions of the retina, like macular degenerations, and their response to therapy.

Chapter 6: Blood Volume Imaging of the Rat Retina

To complement the results of the BOLD fMRI, we developed retinal blood volume imaging techniques based on using monocrystaline iron oxide nano-colloid (MION) as a contrast agent. Relative baseline blood volume and fractional changes to blood volume due to stimulus were calculated in the retinal and choroidal vasculatures. Hypercapnia and hyperoxia were used to induce the systemic stimulation. In resting state, the choroidal vasculature had approximately 9 times the blood volume of retinal vasculature. The fractional change in retinal blood volume was 0.5 ± 0.1 for hypercapnic stimulus and -0.5 ± 0.2 for hyperoxic stimulus. However, the fractional blood volume changes in the choroidal vasculature were significantly lower at 0.1 ± 0.1 for hypercapnic stimulus and -0.3 ± 0.1 for hyperoxic stimulus. These results suggest a higher degree of regulation in the retinal vasculature compared to the choroidal vasculature.

6.1 Introduction

As in the brain, blood flow in the retina is tightly regulated to maintain oxygenation within its various layers [197, 198]. While the choroidal vasculature is generally dense and superfluous, the retinal vasculature is sparsely distributed within the retina itself, mainly to provide the photoreceptors with unhindered access to light. Moreover, there is a large avascular layer in the retina made up of densely-packed photoreceptor cells, which relies on passive diffusion of oxygen from neighboring vascular regions to meet its energy requirements. Adequate blood flow in the retina is essential for its proper functioning, not only due to the high metabolic demand in the retina, but also for delivering an adequate supply of oxygen and nutrients to the avascular layers.

Changes in retinal blood flow, volume, and oxygen extraction has been associated not only with functional activation [199] but also to changes in physiological condition and in retinal diseases. Blood flow to the retina can be affected by physiological stimuli such as hyper- or hypocapnia, and ocular perfusion pressure [200]. Diseases of the retina like glaucoma, ischemic neuropathy, diabetic retinopathy and retinal degeneration are known to influence the retinal perfusion either through functional or vascular deficits [201-203]. Therefore, determining the baseline retinal perfusion as well as perfusion changes during functional or systemic stimulation may help in early detection as well as the localization of some retinal diseases and thereby improve prognosis through early intervention.

In Chapter 4, BOLD fMRI was used to indirectly detect changes in the concentration of deoxy-hemoglobin. In those experiments, we had detected large changes in BOLD signal were detected from the retinal and choroidal vessels during hyperoxic stimulation while BOLD signal changes were observed only from the retinal vessels during hypercapnic stimulus. In this chapter we sought to supplement the BOLD fMRI data by developing techniques to detect layer-specific relative baseline blood volume and fractional changes in blood volume during systemic stimulation in the retinal and choroidal vessels of wild type rats using monocrystalline iron oxide nano-colloid (MION) contrast agent.

MION has an average size of 17 nm [98, 99], almost twice the size of high-density lipoproteins in blood plasma. MIONs contain a central Fe crystal of size 4-7 nm (super-paramagnetic iron oxide or SPIO class of contrast agents), surrounded by multiple dextran molecules, which thereby increases its size. This large size makes MION a blood-pool contrast agent, with a half-life in the order of hours. Intravenous administration of MION has been used in this chapter to image retinal blood volume in the rat retina.

The covering of dextran molecules prevents easy access of solvents to the Fe core, making MION an effective T_2 contrast agent, relying on the susceptibility effect to induce a large sphere of field fluctuations in the solute. These strong magnetic field fluctuations cause a decrease in the transverse relaxation time of the solvent surrounding the contrast agent, primarily due to time-dependent changes at or near the Larmor frequency. This change in transverse relaxivity is directly proportional to the concentration of the paramagnetic particles and has the units of s^{-1} mM^{-1}. Shortly after intravenous injection,

MION has been shown to distribute evenly in the blood plasma [204], reducing the signal intensity of the perfused tissue due to shortened transverse relaxation. The amount of signal reduction is proportional to the amount of MION in the tissue, and therefore the blood volume of the tissue. This technique also offers a minimally invasive way to calculate the relative baseline blood volumes from retinal and choroidal vessels by measuring the change in transverse relaxivity [205].

Blood-volume imaging using MION, can also be adapted to measure fractional changes in blood volume in response to a stimulus. Following a typical stimulus, the MRI signal intensity changes due to changes in local concentration of deoxy-hemoglobin (BOLD signal changes, Chapter 4). Upon injection of MION, the MRI signal intensity changes due to a change in concentration of MION as well as deoxy-hemoglobin. Therefore, relative blood volume changes can be estimated by eliminating the change in signal intensity due to deoxy-hemoglobin, from the signal intensity changes after MION injection. Fractional change in blood volumes during stimulation can directly be determined, as a ratio of relative blood volume changes to the relative basal blood volume [204, 205].

6.2 Materials and methods

Animal preparation: Wild-type Long-Evans rats (LE, n=7, 350-450g) were first anesthetized, intubated, mechanically ventilated and paralyzed as described in Chapter 2. The femoral vein was catheterized for the administration of MION (5mg/kg). The femoral artery was catheterized for monitoring the blood pressure. After surgery, the rats were setup on an imaging cradle with stereotaxic headset, eye coil and heating pad as

described in Chapter 2. Physioloical parameters were continuously monitored throughout the experiments. Once inside the magnet, the rats were allowed to rest for approximately 1 h while their physiology stabilized. Images were acquired before and after the administration of MION. MION was diluted in 1cc of PBS, as per manufacturer's instructions for injection, and the physiology of the rat monitored during injection for any temporal variations. The injection lasted about 1 min.

MR imaging: High-resolution anatomical MRI studies were performed on a Bruker 4.7T or 7T/30-cm magnet and a 40 G/cm B-GA12 gradient insert (Bruker, Billerica, MA). Images were acquired using a GE sequence with a TR of 200 ms, TE of 6.5 ms, FA of 20º, slice thickness of 0.8 mm, FOV of 7.5 mm × 7.5 mm, imaging matrix of 256 × 256 and in-plane resolution of 30 μm. T_2*-weighted images were acquired for ~14 min with 8 repetitions, 4 as a baseline and 4 during a gas challenge. Systemic stimulation was delivered through hypercapnia (5% CO_2, 21% O_2 balance air) and hyperoxia.

Data analysis: The images acquired before and after MION injection were carefully analyzed for motion artifacts and drift. Any drift was corrected using SPM as described in Chapter 2. The images acquired using various stimuli, before and after MION injection, were averaged and a pixel-by-pixel map of ΔR2* calculated. The relative blood volume in the retinal and choroidal vasculature was calculated from profile plots of ΔR2*. The fractional blood volume change due to stimulation was calculated from the baseline and stimulation images before and after injection of MION as per the equation

$$\Delta BV_f = \frac{\Delta R_2^*{}_{[\Delta dHb + \Delta BV]} - \Delta R_2^*{}_{[\Delta dHb]}}{\Delta R_2^*{}_{[MION]}}, \text{ or as percentage change as: } \Delta BV_f \times 100\%.$$

6.3 Results

6.3.1 Physiology

The animal physiology could be maintained over the course of the experiment lasting 3-5 hours. There were no significant changes in any of the baseline physiological parameters monitored before or after the injection of MION. The EtCO2 measured before the injection of MION (30 ± 2 mmHg) was not different from that measured after the injection (30 ± 2 mmHg, p>0.9). The mean arterial blood pressure before MION administration (MABP: 110 ± 20 mmHg) was not statistically different from after the
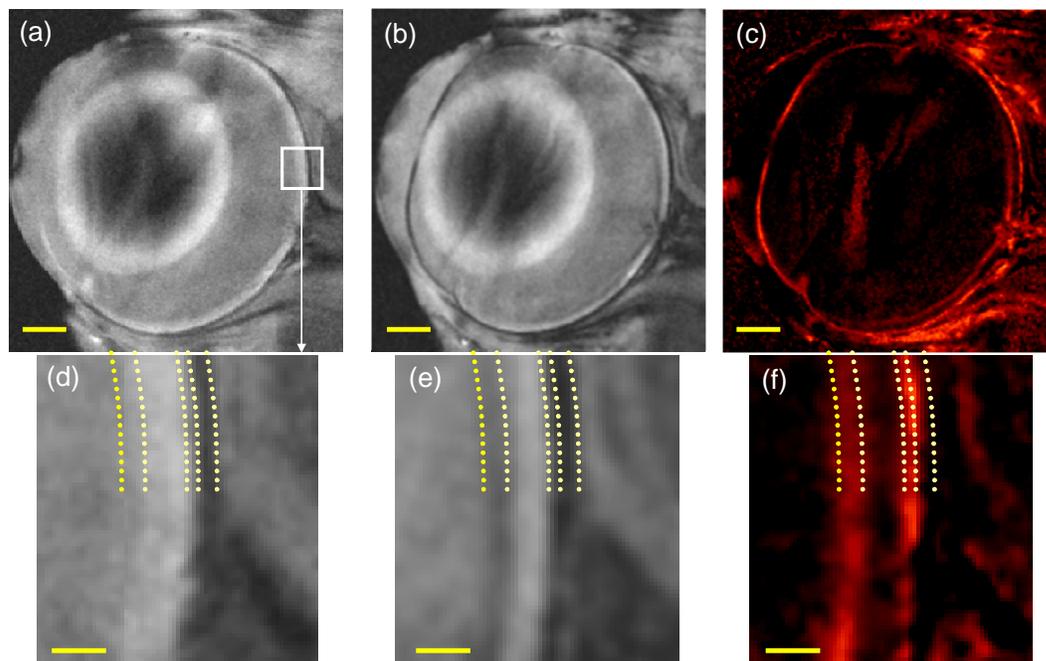
Fig. 6.1: Comparison of rat-eye MRI acquired using a gradient-echo sequence with an in-plane resolution of 30 μm × 30 μm, (a) before and (b) ~10 mins after i.v. administration of 5mg/kg MION. The retinal and choroidal vasculature can be seen distinctly in (c) pixel-by-pixel map of relative blood volume. Portions of the retina in (a), (b) and (c) are magnified in (d), (e) and (f) respectively. Approximate boundaries of the retina and sclera are traced with dotted lines for reference. Scale bars: top row is 1 mm and bottom row is 200 μm.

MION injection (120 ± 10 mmHg, p>0.8). Similarly, the heart rate before MION injection (400 ± 40 bpm) was not significantly different from after MION injection (410 ± 40, p>0.6). The EtCO2 significantly decreased by 10 ± 3% during hyperoxia and increased by 148 ± 2% during hypercapnic challenges (p<<0.01). There were no significant changes in any other physiological parameter measured during the systemic gas challenges.

6.3.2 Relative blood volume of retinal and choroidal vasculature

Figures 6.1a and b (portions of which are magnified in 6.1d and e) shows the baseline images acquired before and after the administration of MION, at 30-μm in-plane resolution. Dotted lines are drawn as guides along the apparent boundaries of the retina, choroid and sclera on the top half of the magnified images in 6.1d, e and f. A pixel-by-pixel map of ΔR2* was calculated from these two images as seen in Fig. 6.1c (magnified in 6.1f). Since ΔR2* quantifies the amount of MION per pixel, which in turn is proportional to the amount of
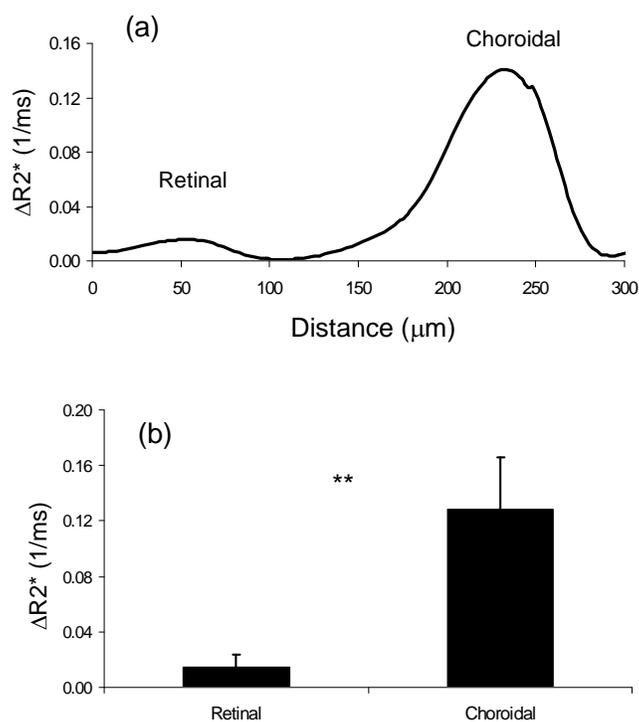
Fig. 6.2: Comparison of relative blood volumes in the retinal and choroidal vessels of Long Evans rats. (a) ΔR2* profiles across the retina in a representative wild-type Long Evans rat. (b) Group averaged ΔR2* from retinal and choroidal vessels shows significantly higher blood volume in choroidal compared to retinal vessels. (**: p<0.001, n=7).

blood in the pixel, the map of ΔR2* depicts the relative blood volume (rBV) in the retina. The relative blood volume in the choroid can be seen to be higher than that in the retinal vessels. The retinal and choroidal vessels are seen to be separated by an avascular layer, as expected.

In order to quantify the blood volume changes, signal-intensity-profile plots were drawn on the retina in the ΔR2* map as shown in Fig. 6.2a. Two distinct peaks of can be seen in the ΔR2* profile plot. The retinal ΔR2* calculated from wild-type LE rats was 0.015 ± 0.008 ms^{-1}, which was significantly lower ($p<0.001$) than that from the choroid which was 0.13 ± 0.04 ms^{-1}. The peak ΔR2* from the choroidal vessels were approximately 10 ± 3 times larger than the ΔR2* from the retinal vessels (Fig. 6.2b). The group averaged FWHM thickness of the choroidal layer was 80 ± 10 μm while that of the retinal vessels were 60 ± 20 μm, as shown in table 6.1. The two peaks in the ΔR2* profile plots were separated by 200 ± 30 μm. Blood volume index (FWHM thickness of vasculature × peak ΔR2* or rBV) of the retinal and choroidal vessels was 1 ± 3 μm/ms and 11 ± 4 μm/ms, respectively. The choroidal blood volume index was 20 ± 10 times that of the retinal blood volume index.

n=7	Retinal	Choroidal	Ratio (Choroidal / retina)
Relative blood-volume (Peak ΔR2* in ms^{-1})	0.015 ± 0.008	0.13 ± 0.04	10 ± 3
Layer thickness (μm)	60 ± 20	80 ± 10	1.5 ± 0.7

Table 6.1: Comparison of the retinal and choroidal thickness and blood volumes as detected by MRI in Long-Evans rats. A ratio of choroidal to retinal values is also shown.

The MRI signal-intensity changes, and therefore the ΔR2* calculated from the retinal vasculature, was maximal near the optic nerve head and tapers off near the peripheral retina, as can be seen in the map in Fig. 6.1c. The variations in ΔR2* in the retinal and choroidal vasculature of one representative rat, plotted from the superior to the inferior peripheral retina passing through the region of the optic nerve head, is shown in Fig. 6.3. The average ΔR2* in the peripheral retinal vasculature was 5 ± 5 ms^{-1}, was significantly smaller than that in the central retinal vasculature 28 ± 7 ms^{-1} (p<0.01). The choroidal blood volume on the other hand did not show variations between the central and peripheral retina. The average ΔR2* was 130 ± 20 ms^{-1} in the peripheral choroid and 100 ± 20 ms^{-1} in the central choroid (p>0.05). All ΔR2* measurements reported in this study are the peak ΔR2* values obtained from profile plots drawn approximately 1 mm from the optic nerve head. This region was chosen as it represented an average value of the retinal and choroidal blood volumes.

Similar experiments were performed in wild-type Sprague-Dawley rats for inter-
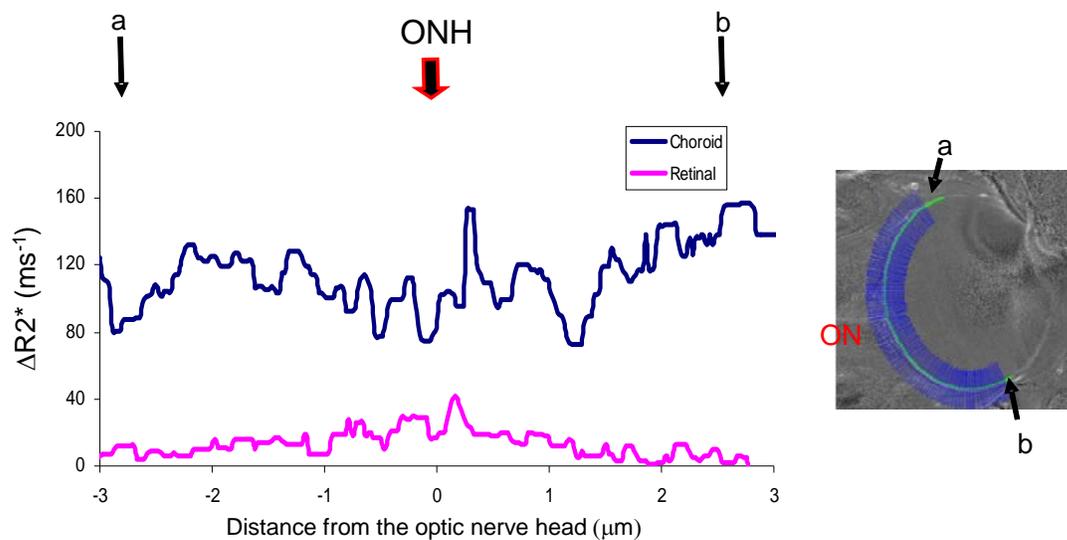
Fig. 6.3: Variation in retinal and choroidal blood volume with distance from the optic nerve head (ONH). The extent of the graph is from the superior to the inferior peripheral retina as shown in the inset.

strain comparisons. The relative retinal blood volume calculated from wild-type Sprague-Dawley rats was 0.02 ± 0.01, significantly lower than the relative blood volume in the choroid which was 0.12 ± 0.04. Neither peak $\Delta R2*$ values were significantly different from those of the corresponding vasculature in LE rats. The peak $\Delta R2*$ from the choroidal vessels were approximately 8 ± 3 times larger than the $\Delta R2*$ from the retinal vessels, which was not significantly different from those of the wild-type LE rats. Similarly, there were no apparent differences in the thickness of the retinal vasculature.

6.3.3 Changes to blood volume in response to gas challenge

The profile plot of $\Delta R2*$ in Fig. 6.4 shows the baseline $\Delta R2*$ (in blue), and the $\Delta R2*$ due to systemic hypercapnic (in pink) and hyperoxic (in green) stimulus. There was significant differences in the peak-$\Delta R2*$ in both the retinal and choroidal vasculature. However, significant changes were not seen in the width of the peak as determined using FWHM during the gas challenge. The peak-$\Delta R2*$ increased by $50 \pm 10\%$ in the retinal vasculature and $10 \pm 10\%$ in the choroidal vasculature during hypercapnic stimulus. The fractional increase seen in the retinal blood volume
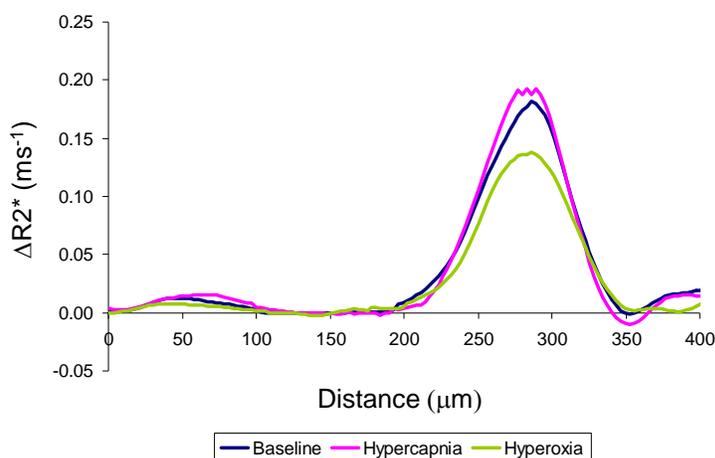
Fig. 6.4: Relative blood-volume at baseline, hypercapnia and hyperoxia stimulus in the same rat. The relative blood-volume of both the retinal and choroidal vasculature is seen to decrease in hyperoxia, and increase in hypercapnia. Although the magnitude of change is higher in the choroidal vessels, the fractional change is low due to high baseline blood volume.

was significantly higher than those observed from the choroidal vasculature (choroidal to retinal ratio of 0.3 ± 0.2; p<0.01). Similarly, the peak-$\Delta R2^*$ decreased by 50 ± 20% in the retinal vasculature and 30 ± 10% in the choroidal vasculature during hyperoxic stimulus. The fractional blood volume changes in the retinal vasculature were significantly higher than those from those in the choroid (choroidal to retinal ratio of 0.5 ± 0.4; p<0.05). These changes are graphed in Fig. 6.5. The retinal and choroidal blood volume changes derived from SD (data not shown) and LE wild-type rats were not significantly different during hyperoxic or hypercapnic stimulation.

6.4 Discussion

The relative baseline blood volume and fractional changes to blood volume during inhalation challenge in retinal and choroidal vasculature was reliably detected using MION. The ratio of choroidal to retinal blood volume was determined to be 10 ± 3 in wild-type LE rats. The fractional changes in blood volume in response to gas challenge were much
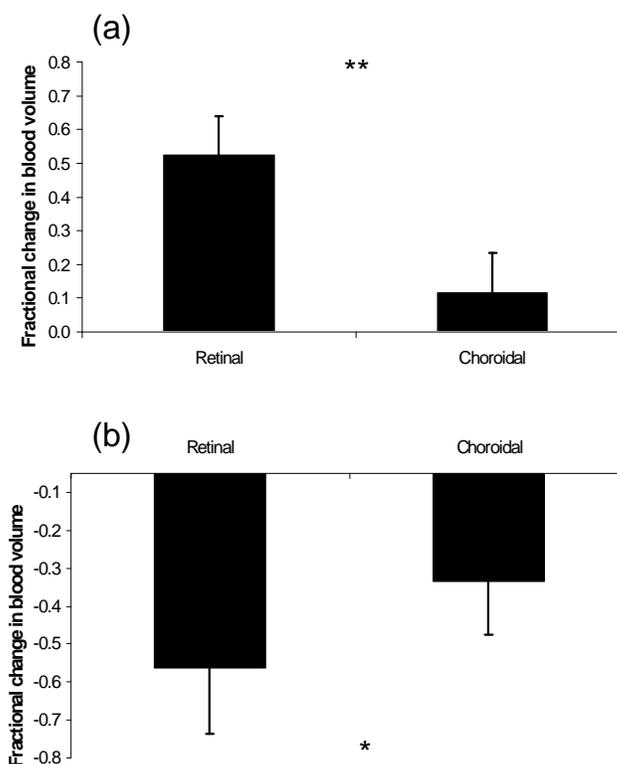
Fig. 6.5: Fractional blood volume change due to (a) hypercapnia and (b) hyperoxia in the retinal and choroidal vasculature (*: p<0.05; **: p<0.01, n=7).

higher in the retinal vasculature than the choroidal vasculature, indicating a higher degree of autoregulation in the retinal vasculature. The autoregulation in the retinal vasculature accounted for 64-79% of the fractional blood volume changes in the retina during gas challenge.

6.4.1 Animal physiology

Maintaining animal physiology throughout the experiment was important for the calculation of blood volume in the retina. The calculation of fractional blood-volume changes rely on removal of signal intensity changes due to deoxy-hemoglobin concentration changes during the stimulation [115, 205]. To remove this factor, gas challenge was performed before and after the injection of MION, and $\Delta R2^*$ due to changes in deoxy-hemoglobin alone ($\Delta R2^*$ before MION), was subtracted from the $\Delta R2^*$ after MION injection. However, any changes to physiological parameters like blood pressure in the duration of the experiment could alter the signal changes due to deoxy-hemoglobin before and after MION injection [107, 204, 206], thereby influencing the fractional blood-volume changes calculated. Therefore, the rat physiology was closely monitored for the duration of the experiment, and care was taken during the injection of MION by diluting the compound in PBS and the slowly administering the MION to the rat over one minute. Measurements before the start and towards the end of the experiment revealed no significant changes in blood pressure, heart rate or $EtCO_2$ in any of the animals imaged.

However, a significant increase of $EtCO_2$ was observed during the hypercapnic challenge as expected. Likewise, a small but significant decrease in $EtCO_2$ was observed

during hyperoxia, due to the relative lesser affinity of hemoglobin to CO_2 compared to O_2 [207]. These changes in physiological parameters were quickly reversed following the hyperoxic or hyper capnic challenges, and the physiological parameters returned to pre-stimulus values. At least a 10-min break was given between imaging sessions for animals to recover from the gas stimulus.

6.4.2 Choice of anesthesia

It should be noted that the anesthesic used in this study, isoflurane, is a potent vasodilator [208], and can bias the relative blood volume calculated herein. The ΔR2* measured using MION was likely to be overestimated in isoflurane anesthetized animals compared to the awake animals. Moreover, it is likely that vasodilation affects the two vasculatures differently, since they have very distinct characteristics and innervations as seen in Section 1.1. Therefore, the vasodilation due to isoflurane could influence the ratio of the retinal to choroidal blood volumes calculated. Finally, the ability of a vessel to respond to vasodilatory stimulus may be reduced by isoflurane, while it can have an increase in the vasoconstriction caused by hyperoxia.

Our choice of isoflurane anesthesia was based on detailed studies of eye movement as seen in Chapter 2. Involuntary movements seen in the eyes were minimal in animals anesthetized with isoflurane and paralyzed with pancuronium. We sought to minimize the dosage of isoflurane in combination with pancuronium, thereby maintaining a stable physiological state with maximal functional response.

6.4.3 Partial volume error in measurement of blood volume parameters

Measurements of blood volume as well as thickness of vasculature are subject to the partial-volume errors. A complete discussion on the smallest layer thickness that can be measured, as well as the effects of layer thickness on the peak signal intensity can be found in Section 4.4.3. The thicknesses of the vascular layers measured in this study are at least 2× the resolution of the MR image and, therefore, the measured layer thickness is expected to accurately reflect the actual *in vivo* layer thickness. Furthermore, the peak $\Delta R2*$ in the signal-intensity-profile plots reflect the relative maximum blood-volume in individual layers. The total blood-volume in the vascular layer is ideally proportional to the total area under the curve for each vascular layer in Fig. 6.2. However, the large standard deviation in the blood-volume-index (peak $\Delta R2*$ × area under curve) could be indicative of partial-volume error in the height measurement as well as that in the thickness measurement. While the blood volume analysis could be done either on peak height or the area under the curve, analysis of the peak height was preferred due to the lesser uncertainty in that measurement.

The fractional change in blood volume due to hypercapnic and hyperoxic stimulus was also calculated from the changes in peak height of $\Delta R2*$ in retinal and choroidal vasculatures. The relative blood volume in both the retinal and choroidal vasculature was seen to change in response to the systemic stimulus; however, there were no significant differences in the overall thickness of either the retinal or choroidal vasculature. The fractional change in blood volume was then derived by dividing the peak $\Delta R2*$ due to stimulus by the relative blood volume (or baseline peak-$\Delta R2*$).

6.4.4 Baseline retinal and choroidal blood volume

Comparison of the retina before (Fig. 6.1a) and after injection of MION (Fig. 6.1b) shows signal intensity changes in both the retinal and choroidal vasculature. While the choroidal signal changes could be seen all along the outer eyeball, the signal changes from the retinal vasculature were much more pronounced near the optical nerve. Indeed, the retinal blood volume determined near the optic nerve head was five times higher than that from the peripheral retina. The choroidal blood volumes from the peripheral and central retina were not significantly different. All the retinal vessels originate from the central retinal artery, which emerges into the inner retina through the optic nerve head. Therefore, the density of retinal capillaries reduces along the length of the retina from the optic nerve head to the periphery. This is reflected in the high blood volume of retinal vasculature near the optic nerve head. The choroidal vessels on the other hand, originate from the many medial and lateral posterior ciliary arteries, feeding into the choroid at various locations along the choroid [34]. This make up of the choroids may be responsible for the globally more uniform choroidal blood volume. Furthermore, some peaks and valleys seen in the choroidal blood volume plot could be explained by the presence of large vessels feeding the choroidal vasculature. The blood volume data reported herein are from a region of 10 pixels length of the retina (~0.3 mm) at a distance of 30 pixels (~1 mm) away from the optic nerve head in both the superior and inferior retina. This region of the retina was found to have values near the average value for the entire retinal vasculature. Furthermore, choosing the measurement from a small region away from the optic nerve head avoided contamination from the central retinal artery and vein.

Studies of the oxygen extraction and metabolic studies of the retinal vasculature suggest that the choroidal flow is high with low oxygen extraction compared to the retinal flow [209]. Studies with radioactively-labeled microspheres have shown that choroidal blood flow contributes up to 85% of the total blood flow to the retina of Rhesus monkeys [33]. The MION-based blood volume calculations of the retinal blood vessels are in general agreement with the relatively high blood flow in the choroidal vessels observed using other modalities. However, the microsphere technique detects the flow from the relative number of radioactive microspheres trapped within each vasculature [210]. The technique may underestimate the choroidal blood flow due to the significantly larger diameter of the choriocapillaris compared to the capillaries of the retinal vasculature. MION, on the other hand, is quickly distributed in the blood plasma and is distributed in the retinal and choroidal vasculature in proportion to their blood volume. Therefore, MION-based MRI is a more effective technique to measure relative blood volumes.

6.4.5 Vascular response to stimulus

Hypercapnia and hyperoxia are well-established and efficient models to study the vascular response to stimulus [211-213]. Increases in the fraction of inspired O_2 (FiO_2) or CO_2 cause robust and reproducible changes to MRI signal. These gasses also have small washout times in tissues allowing repeated measurements in short time. The relationship between cerebral blood flow and FiO_2 has been reported to be an exponential decay, with significant reduction in flow of 4% between FiO_2 of 0.2 and 0.6 in rats increasing to about 6% at FiO_2 of 1 [214]. Similarly, PET studies in human brain show an 11% increase in cerebral blood volume during inhalation of 7% CO_2 gas, with most of the

contributions arising from arteries [215]. The blood-volume changes in arteries alone were estimated at 66, in that study.

Autoregulation in the retinal vasculature is thought to be maintained through pH levels, endothelial vasoactive agents like nitric oxide and through O_2 and CO_2 tension [216]. Fundus photography in rats have revealed a 9% to 14% reduction in the diameter of major retinal vessels during hyperoxic challenge [217], which correspond to an 18% to 27% reduction in blood volume, compared to the 50% changes in blood volume observed herein. However, fundus photography cannot be used to measure the blood volume changes in the smaller retinal arterioles and capillaries, which are expected to have larger contributions to the total blood volume changes.

The choroidal vasculature, on the other hand, has a dense sympathetic innervations, while the posterior choroid is essentially devoid of parasympathetic innervations [35]. Stimulation of the cervical sympathetic trunk caused a 60% decrease in blood flow in the choroid as measured by Laser Doppler technique, and the blood flow was unaffected by parasympathetic stimulation [37]. The observations herein are consistent with the larger vasoconstriction than vasodilation seen in choriocapillaris [35, 36]. Furthermore, the relationship between changes to blood flow and volume is given by the Grubb relationship as $CBV = 0.8 * CBF^{0.38}$ (Grubb's formula), where CBV is the cerebral blood volume and CBF is the cerebral blood flow [218]. As per this model, a 60% decrease in blood flow observed during sympathetic nerve stimulation [37] results from a blood volume change of 31%. The magnitude of the blood volume change estimated is similar to the observed blood volume changes in the study herein, albeit with a different stimulus.

The fractional blood volume changes observed in the retina by MRI are consistently larger than those observed in the brain [214, 215]. One possible explanation for this difference could be the higher vascular density in the retina, compared to the brain. Discrepancies could also arise from factors such as differences in basic vascular makeup, differences in the anesthesia used during these studies, sensitivity differences between the modalities and even the location of the measurement of the hemodynamic properties. Furthermore, MRI signals are reduced by the increased presence of deoxy-hemoglobin in the veins, which could reduce the total signal contributions from the veins. Therefore, the fractional blood-volume changes derived herein could be weighted by the arterial blood more than the venous blood. This could result in its slight overestimation of the total blood volume changes since the arteries have a larger response to the stimulus as compared to veins.

The retinal vasculature is known to be more tightly autoregulated than the choroidal vasculature [219-222]. The choroidal and retinal blood flows are known to be separately regulated, as evidenced by the more acute increase in retinal blood flow as compared to choroidal blood flow post exercise in humans [200]. The choroidal vasculature consists of a mesh of capillaries and shunts with higher capillary-density and blood-flow compared to the retinal vasculature. This allows the capillaries to accommodate a much larger increase in blood flow without significantly changing the volume of its vessels. Indeed, the experiments herein show that the ratio of fractional blood-volume changes in the choroidal vasculature to the retinal vasculature was between 0.31 and 0.55, indicating larger fractional changes in the retinal vasculature with either stimulus. However, the overall magnitude of the $\Delta R2*$ changes were higher in the

choroidal vessels, compared to the retinal vessels, due to the much larger baseline blood volume in the choroids.

These observations agree with the layer-specific BOLD signal intensity changes observed in Chapter 4, where the BOLD-signal-intensity changes from the outer retina was negligible during hypercapnia, while significant in hyperoxia [115]. Furthermore, the BOLD changes observed in the inner retina were typically much higher than those observed in response to a similar stimulus presentation in the brain. These differences could be due to the differences in vascular reactivity of the retinal vessels as compared to the cerebral vessels, due to the unique architecture of the retina. This difference in choroidal response also help explain the lower BOLD-signal-intensity changes seen in the choroid during hypercapnic stimulus [115].

More recently, this laboratory has developed arterial spin-labeling techniques (ASL) for the estimation of blood flow in the retina [132]. In ASL, labeled protons are used as contrast agents, and differences in signal intensities between labeled and un-labeled images are used to estimate the flow rate of blood into the imaging slice. The quantitative blood flow in the retina was estimated at 6.3 ± 1 mL/g/min. The blood flow from the entire retina reduced by $25 \pm 6\%$ during hyperoxia and increased by $16 \pm 6\%$ during hypercapnia, which corresponds approximately to a fractional blood volume change of -0.57 and 0.48, respectively, as calculated using Grubb's formula. These results are similar to the blood volume changes observed from the retinal vessels alone using MION. It should be noted that the labeled water protons in ASL are considered as freely-diffusible tracers, crossing the BRB with ease and thus compromising layer

specificity. Furthermore, the resolution used for the ASL images were in the order of 60-90 μm in-plane, which may have reduced the ability to resolve individual vascular layers.

6.4.6 Leakage of MION

The steady-state blood-volume calculation by MRI assumes that there is no leakage of MION from either the retinal or choroidal vasculature. Leakage and/or accumulation of MION in the retinal layers could potentially result in an overestimation of the blood volume in the respective vasculature. The endothelial cells in the retinal vasculature form a tight blood-retinal barrier, preventing leakage. However, the choriocapillaris have fenestrations that are known to leak small molecules like vitamin A and sodium fluorescein, but not indocyanin-green dye. These differences in permeability are largely attributed to the differences in size of the dyes, and studies have shown that the particles of size of 11 nanometers [223] and 8 nanometers [224] do not leak out of the choriocapillaris.

MION particles are inert and have an average size of 17 nm, which is comparable to the size of large proteins and larger than high-density lipoproteins [225]. In general proteins and phospholipids of these size ranges do not leak out of the choroidal vasculature, unless in disease-state. Furthermore, leakage of MION out of the choroidal vasculature would cause a time-dependent increase in $\Delta R2^*$ of the choroid. However, no such changes were observed from the choroid over 2-3 h, indicating that there was no accumulation of contrast agent. Finally, signal-intensity changes can be seen in the ciliary bodies and in the iris in Fig. 6.1c, but not in the vitreous or aqueous humor, providing further evidence of the intravascular nature of MION.

6.5 Conclusion

The relative blood volume and fractional changes to blood volume during systemic stimulation were reliably detected using MION-based MRI. The retinal vasculature showed a lower baseline volume, but a higher degree of autoregulation on hypercapnic and hyperoxic stimulus. These techniques can also be adapted to study vascular changes during visual stimulation.

These results suggest MRI is a robust and reliable technique to measure both the baseline and fractional changes of blood volume simultaneously from the retinal and choroidal vasculature. These measurements were made possible due to the short total imaging time allowing maintenance of rat physiology, long half-life of the contrast agent in the blood, and the high in-plane resolution of the MRI scanner. The use of a non-diffusible contrast agent combined with higher resolution scans provided layer-specific blood volume information.

The fMRI techniques developed here offer unique and exciting possibilities for early detection of vascular and functional deficits in the retina before irreversible damage. The techniques developed herein can be adapted to measure the blood-volume changes during visual stimulation, and may help identify regions of functional deficit in disease models. Vascular changes in the retina are likely to be early indicators of various pathological conditions such as diabetic retinopathy and glaucoma. Early detection of these vascular changes, before the onset of anatomical deficits may help in improving the prognosis of some of these diseases. Furthermore, longitudinal evaluation of disease models can help better understand the etiology of complex diseases like diabetic retinopathy.

Chapter 7: Application of Retinal MRI Techniques to a Retinal Dystrophy Disease Model

Royal College of Surgeon (RCS) rats share a mutation with a majority of patients suffering from autosomal-recessive retinitis pigmentosa (RP). The mutation in these rats leads to progressive retinal dystrophy, with degeneration of the photoreceptor cells starting by postnatal day 20 (P20). A change in the retinal architecture is seen by P90, with loss of photoreceptor segment, outer nuclear and outer plexiform layers. These anatomical changes in the retina of RCS rats make it an ideal model to test the anatomical and functional retinal MRI techniques developed herein.

High-resolution MRI of the retinal structure revealed only one band in the adult RCS retina, compared to three bands in wild-type rats as well as P16 RCS rats that do not exhibit retinal dystrophy. Administration of the intravascular contrast agent Gd-DTPA, resulted in uniform enhancement of the entire retina in adult RCS rats, suggesting the loss of the avascular retinal layers. Manganese-enhanced MRI, 24 h after the intravitreal injection of $MnCl_2$ revealed a thinner retina and loss of outer plexiform, outer nuclear and photoreceptor segment layers in the adult RCS retina, consistent with histology. Blood-volume imaging with MION revealed increased baseline blood volume in adult RCS rats and decreased vasodilation in the retinal vessels in response to hypercapnia, as compared to normal wild-type rats. These experiments revealed the MRI of the retina has sufficient sensitivity and specificity to detect structural and functional changes in RCS rats.

7.1 Retinitis Pigmentosa

Retinitis pigmentosa (RP) is a group of genetic eye diseases that lead to slow and progressive retinal degeneration with considerable loss of visual acuity. A genetic mutation prevents the RPE from being able to recycle the photoreceptor segments. This leads to a collection of shed segments in the photoreceptor segment layer, and subsequent degeneration of photoreceptor cells [226]. Although the disease progression steps are variable depending upon the specific mutation, the cascade generally results in retinal degeneration due to the gradual loss of photoreceptor layer and partial or complete loss of visual acuity.

RP is prevalent in about 1 in 4,000 people in the USA [227], and is one of the best characterized of the retinal degenerative diseases. RP has been associated with mutations in more than 40 different genes or loci, leading to abnormalities in the photoreceptor cells or the retinal pigmented epithelium. Of these, more than 100 mutations have been identified in the gene that encodes retinal, but these account for only about 15% of all the genetic mutations identified as a cause of RP. The disease can be inherited as an autosomal recessive, autosomal dominant or X-linked. The X-linked version can be both recessive and dominant, although the dominant form is milder. Due to this variability, there is only a 50% likelihood of detection of RP using genetic testing [227, 228].

The progression of the disease is highly variable. Generally the earliest symptom is night blindness or large pigmented spots in the visual field. This is generally followed by loss of peripheral vision and in some cases complete loss of vision. While some patients may become totally blind, most others retain some sight throughout their life.

There is currently no treatment for RP, however, treatments that provide symptomatic relief, like carbonic anhydrase inhibition [229] and others that slow the progression like vitamin A supplements have been reported [230]. Gene therapy [231] and retinal prosthetics [232] have also been explored as forms treatments. It has been suggested that changing the metabolic environment can prevent some cells from going into apoptosis, and delay the dynamics of retinal degeneration. As in most cases, an early detection of these defects could result in better patient prognosis.

The Royal-College-of-Surgeons (RCS) rat [233] exhibit inherited retinal dystrophy and is a well-established animal model of autosomal recessive RP. At birth, the RCS rats exhibit essentially normal morphology of the retina. However, the RCS rat is homozygous for a null mutation in the *Mertk* gene, which encodes a receptor tyrosine kinase found in RPE cells. This results in impaired phagocytosis of the shed photoreceptor outer segment by the RPE [234, 235], which leads to the degeneration of the photoreceptor cells by postnatal day (P) 90 [226, 236, 237]. While the RCS rat retina has been well characterized, the lack of non-invasive physiological imaging techniques limits the investigation of the physiologic and functional changes of retinal degeneration and their temporal progression *in vivo*.

In this chapter, retinal MRI techniques developed in earlier chapters are used to detect anatomical and functional changes in RCS rats. As illustrated in previous chapters, MRI applied to the retina is a powerful technique that allows investigators to non-invasively obtain anatomical and functional data on the retina. As an example of potential disease applications, these MRI technologies were used to investigate adult RCS rat retina and compared it with the data from young RCS or wild-type rat retinas imaged

previously. High-resolution anatomical MRI, manganese-enhanced MRI, and blood-volume images of adult RCS rats are reported and compared.

7.2 Materials and methods

Animal preparation: Three sets of experiments were performed on separate groups of rats to analyze the anatomical and functional changes in retinal dystrophy:

1. The retinas of P16 (n=6, 20-30g) and P120 (n=4, 350-450g) RCS were compared rats by high-resolution anatomical MRI, representing stages before and after retinal degeneration.

2. Layer-specific, manganese-enhanced MRI was performed on P90 RCS rats (n=5, 350-400g) and the results were compared with age-matched wild-type Sprague-Dawley rats (n=5, 350-400g).

3. Blood-volume studies were performed on P90-120 RCS rats (n=7, 350-450g) and the results compared to age-matched, wild-type Long Evans rats (LE, n=7, 350-450g).

In each experiment, adult rats were anesthetized, intubated, mechanically-ventilated and paralyzed as described in Chapter 2. The femoral vein was catheterized for the injection of Gd-DTPA (0.4 mL/kg, 0.5 M) in Experiment 1 and 2, and for MION administration in Experiment 3. In Experiment 3, MION (5mg/kg) was diluted in 1mL of PBS to maintain the pH for injection. The physiology of the rat was monitored during injection for any temporal variations. The femoral artery was catheterized for monitoring the blood pressure in Experiment 3. After surgery, the rats were positioned on an imaging cradle with stereotaxic headset, eye coil and heating pad as described in Chapter 2.

Physiological parameters were continuously monitored throughout the experiments. Once inside the magnet, the rats were allowed to rest for approximately 1 h while their physiology stabilized, prior to data acquisition.

MR imaging: High-resolution anatomical MRI studies were performed on a Bruker 4.7T or 7T/30-cm magnet and a 40 G/cm B-GA12 gradient insert (Bruker, Billerica, MA).

In Experiment 1, a gradient-echo (GE) pulse sequence was used for anatomical imaging with a TR = 150 ms, TE = 3.5 ms, 0.5-mm slice thickness, 32 repetitions, 7.7mm × 7.7 mm FOV and 128 × 128 matrix yielding an in-plane resolution of 60 μm. Intravenous Gd-DTPA (0.4 mL/kg, 0.5 M) was administered, and imaging repeated, to detect the retinal and choroidal layers.

In Experiment 2, manganese-enhanced MR images (MEMRI) were acquired 24 h post-intravitreal injection of 5 μL of 30 mM $MnCl_2$ as described in Chapter 5. MRI was performed using a conventional GE pulse sequence with TR = 100 ms, TE = 8.5 ms, 0.8 mm slice thickness, 16 repetitions, data matrix = 256 × 256, and FOV = 6.4 mm × 6.4 mm, yielding an in-plane resolution of 25 μm.

In Experiment 3, MRI was performed before and after MION injection (i.v., 5mg/kg, diluted with 1mL of PBS) on using a GE pulse sequence with TR = 200 ms, TE = 6.5 ms, slice thickness of 0.8 mm, FOV = 7.5 mm × 7.5 mm, imaging matrix of 256 × 256 and in-plane resolution of 30 μm. T_2*-weighted images were acquired for ~14 minutes with 8 repetitions, 4 as baseline and 4 during a gas challenge. The imaging was performed before and after the injection of MION. Systemic stimulation was delivered using hypercapnia (5% CO_2, 21% O_2 balance air) and hyperoxia.

Data analysis: Images were analyzed using Stimulate software (John Strupp, University of Minnessota) or using codes written in Matlab as described in earlier chapters. In Experiments 1 and 2, the total retinal thickness and thickness of individual retinal layers observed in the MRI were measured at the full width at half maximum height (FWHM) using the profile-plot method as described in Chapter 2. Thicknesses of individual MRI-derived layers from RCS P16 and P120 were compared in Experiment 1, whereas those from RCS P90 and wild-type Sprague Dawley rats were compared in Experiment 2.

In Experiment 3, the images acquired before and after MION injection were carefully analyzed for motion artifacts and drifts. Any drift was corrected using SPM as described in Chapter 2. The images acquired with gas challenge, before and after MION injection, were averaged and a pixel-by-pixel map of ΔR2* calculated. The relative blood volume in the retinal and choroidal vasculature was calculated from profile plots of ΔR2*. The fractional blood-volume change due to stimulation was calculated from the baseline and stimulation images before and after injection of MION as per the equation

$$\Delta BV_f = \frac{\Delta R_2^*{}_{[\Delta dHb + \Delta BV]} - \Delta R_2^*{}_{[\Delta dHb]}}{\Delta R_2^*{}_{[MION]}}, \quad \text{or as percentage change as:} \quad \Delta BV_f \times 100\%, \quad \text{as}$$

described in Chapter 6.

Histology: Standard histology was obtained in most cases, on the same animals, approximately coinciding with the imaging slices. Following anesthetic overdose, eyes were enucleated and immersion fixed overnight in 2% glutaraldehyde for an hour. Eyes were rinsed in 0.1 M phosphate buffer, dissected to isolate the posterior eyecup, and

divided into two halves along the optic nerve. The eyeball was embedded in epoxy-resin and sectioned at 5 μm for toluidine-blue staining and thickness measurement. Thickness of different layers of the neural retina and choroidal vasculature were semi-automatically derived using an image analysis program (Image Pro, Cybernetics).

7.3 Results

7.3.1 High resolution anatomical imaging (Experiment 1)

Anatomical imaging of P16 RCS rat retina at 60-μm in-plane resolution reveled three distinct layers just as in wild-type rats, confirming normal retinal morphology (Fig. 7.1). Similar to the case of wild-type rats, i.v. administration of Gd-DTPA caused the
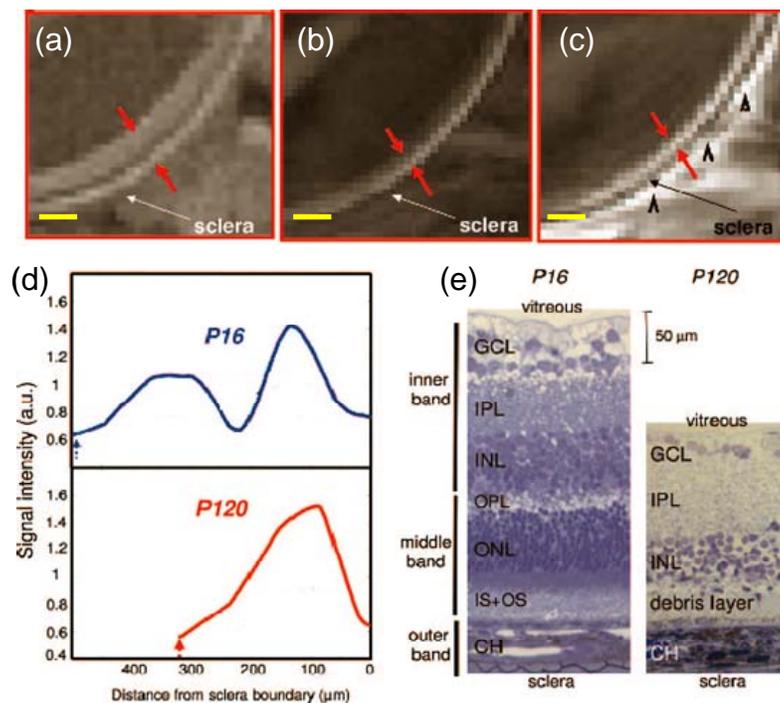
Fig. 7.1: High-resolution anatomical MRI of retina in (a) P16 and (b) P120 RCS rats at 60 μm in-plane resolution clearly shows loss of retinal layers with age. (c) Gd-DTPA enhanced MRI of the entire retina in a P120 RCS rat. (d) Signal-intensity-profile plots from P16 and P120 RCS rats clearly shows retinal thinning and loss of layers in MRI. (e) Comparison of retinal histology in P16 and P120 RCS rats. Scale bar in (a), (b) and (c) is 200 μm and (e) is 50 μm. (Adapted from PNAS (2006) 103 (46):17525).

enhancement of inner and outer retinal layers, with no enhancement seen in the middle layer.

MRI of the RCS retina at P120 revealed only a single band. Intravenous Gd-DTPA administration enhanced the entire retinal thickness in the P120 RCS rat, consistent with the loss of the avascular outer nuclear layer and the photoreceptor segments. Intensity profiles revealed an absent middle band and an overall thinning of the P120 RCS retina. The loss of the photoreceptor layer in P120 RCS retinas was confirmed by histological analysis. It should be noted that a debris layer is often seen in place of the photoreceptor cells in P120 RCS rats. This layer is likely avascular, although not picked up in MRI. This could be because the debris layer is too thin for the resolution of the MRI or the T_1-relaxation-time could be altered due to dystrophy.

RCS rat All Thickness in μm	RCS (P16)		RCS (P120)	
	MRI	Histology	MRI	Histology
Inner layer	157 ± 6	170 ± 30	-	100 ± 20
Middle layer	100 ± 20	110 ± 20	-	$29 \pm 8^*$
Outer Layer	100 ± 20	$34 \pm 4^*$	-	$35 \pm 1^*$
Total Thickness	$\mathbf{350 \pm 10^*}$	$\mathbf{310 \pm 40^*}$	$\mathbf{170 \pm 10^*}$	$\mathbf{170 \pm 20^*}$

Table 7.1: Retinal layer thickness calculated from histology and MRI at 60 μm in-plane resolution from P16 and P120 RCS rats. (* p<0.05).

The total thicknesses of the retina in P16 RCS rats was 350 ± 10 which is significantly higher than the thickness at P120 RCS rats of 170 ± 10 μm (p<0.01), as expected due to the loss of the photoreceptor cells. The P16 RCS retina was also slightly thicker than the P90-120 wild-type rats (270 ± 30 μm as discussed in the Chapter 4). This thinning of the retina with age is consistent with the observations that the nuclear layers in young rats contain at least 50% more nuclei and are considerably thicker than the adult

counterparts [238]. Histological estimation of the retinal thickness in P16 and P120 RCS rats revealed good correlation with MRI-derived layer thickness. These results suggest that MRI has sufficient sensitivity to detect the loss of the photoreceptor layer in P120 animals. The thickness data is summarized in Table 7.1.

Gd-DTPA experiments showed uniform enhancement of the entire retina in P120 RCS rats. This observation is in line with the histological observation of complete degeneration of avascular layer. Another possible reason for this observation could be leakage of Gd-DTPA through the blood-brain barrier. However, there was no evidence of Gd-DTPA leakage into the vitreous even after 1 h of Gd-DTPA injection in P120 RCS rats. The above experiments show that MRI has sufficient sensitivity and specificity to detect the loss of the photoreceptor layer in P120 RCS rats.

7.3.2 Manganese enhanced MRI (Experiment 2)

Figure 7.2 shows the comparison of MRI and histology from a wild-type and P90 RCS rat retina. While the wild-type rats showed seven retinal layers in MEMRI, only five layers of alternating hyper- and hypo-intensities were visible at P90. The overall retinal thickness was visibly reduced in the MEMRI of adult RCS P90 rats compared to those of the wild-type retina. Signal-intensity-profile plots confirmed the apparent decrease in overall retinal thickness of adult RCS rats.

Comparison of the MEMRI intensity profiles from wild-type and P90 RCS rats clearly revealed the disappearance of bands #4-6, diminished intensity of band #3, and the appearance of a debris layer. Histology in RCS P90 rats revealed that in place of the
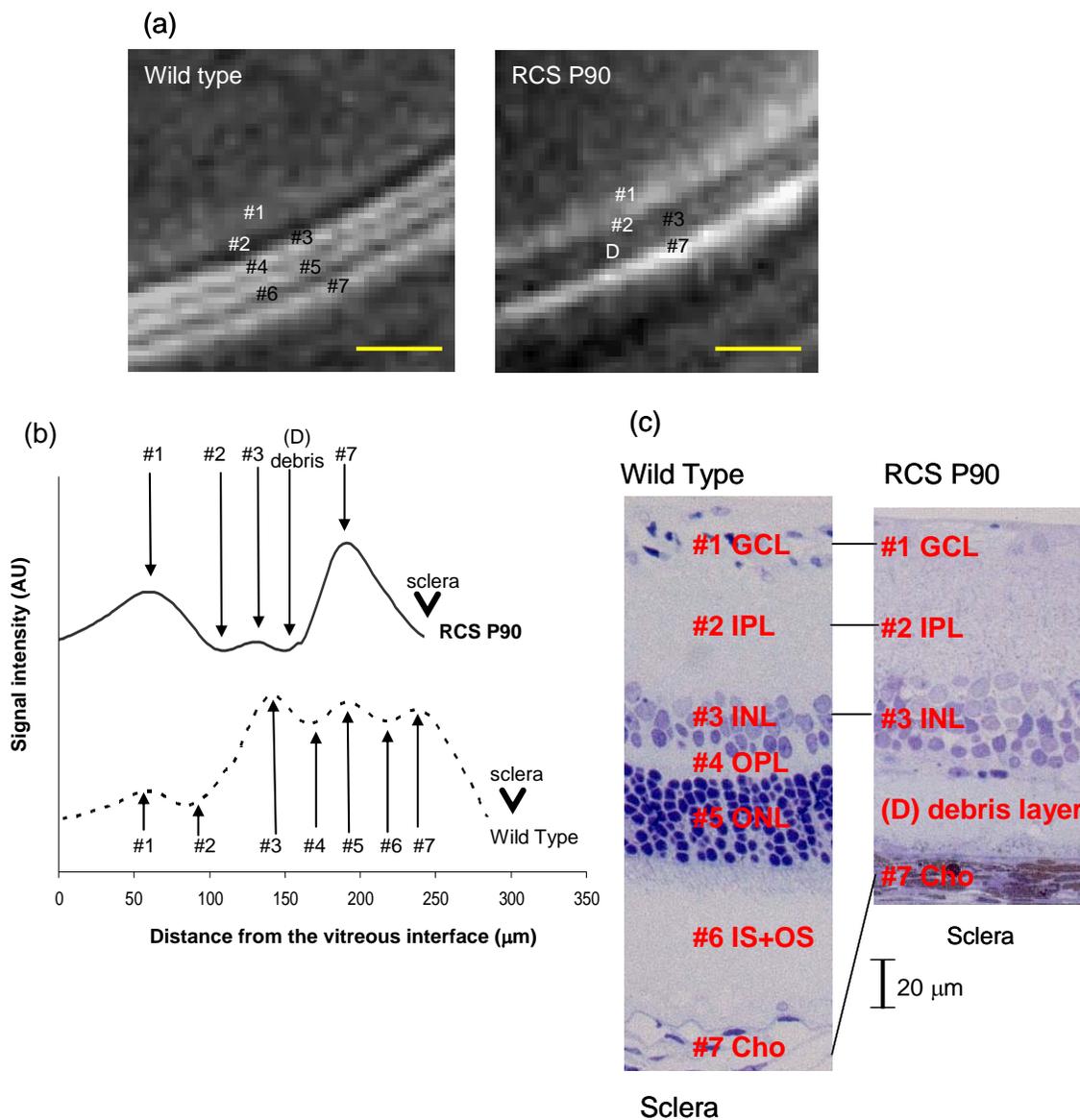
Fig. 7.2: High-resolution MEMRI of retina. (a) Mn-enhanced MRI, (b) intensity profiles, (c) histology of a wild-type and a P90 RCS rat retina. The layer assignments in the retina are: 1. ganglion cell layer (GCL), 2. inner plexiform layer (IPL), 3. inner nuclear layer (INL), 4. outer plexiform layer (OPL), 5. outer nuclear layer (ONL), 6. inner and outer photoreceptor segments (IS+OS), 7. choroidal vascular layer (Cho) and D indicates the debris layer in RCS rats. In the RCS rat at P90, layers #4, #5 and #6 appeared missing and the signal intensity in layer #3 was reduced whereas layer #1 was slightly more enhanced. The corresponding histological slides showed a debris layer in place of layers #4-6 in normal retina. The arrow head in (b) indicates the sclera. Scale bars in (a) is 200 μm and in (c) is 20 μm.

outer nuclear layer (corresponding to layer #5), inner and outer photoreceptor segments (#6) and the outer plexiform layer (#4), only a thin debris layer was visible and the total retinal thickness was markedly reduced. MRI- and histological-layer assignments and laminar thicknesses of the P90 RCS rat retina were tabulated and are summarized in Table 7.2. The total retinal thickness including the choroidal vascular layer of the P90 RCS retinas was 210 ± 20 μm by MRI and 210 ± 20 μm by histology, significantly thinner than the wild-type rat retina which was determined to be 280 ± 10 μm.

RCS rat (all thickness in μm)	MEMRI layer #	MRI thickness	Histology thickness
Nerve fiber	1	37 ± 3	-
Ganglion cell			30 ± 10
Inner plexiform	2	26 ± 5	61 ± 4**
Inner nuclear	3	20 ± 10	43 ± 9
Debris	D	25 ± 8	30 ± 10
RPE	-	-	5.0 ± 0.6
Choroid	7	32 ± 8	31 ± 2
Total retinal thickness	1-7	210 ± 20	170 ± 30

Table 7.2: The retinal layer thickness (μm, mean ± SD) in P90 RCS rat retina determined by manganese-enhanced MRI and histology (n=5). A debris is seen in the RCS rats in place of layers #4-#6. (** p<0.01).

7.3.3 Blood volume (Experiment 3)

Figure 7.3 a shows representative ΔR2* profile plots from a wild-type LE rat and a RCS rat with retinal dystrophy. The distance between the two vasculatures, as defined by the separation of their peaks was 130 ± 20 μm in RCS rats, which was significantly smaller than the peak-to-peak separation of 200 ± 30 μm in wild-type controls (p<<0.01,

n=7). As expected, the overall retinal thickness was reduced in RCS rats due to the complete loss of the photoreceptor layer in the retina.
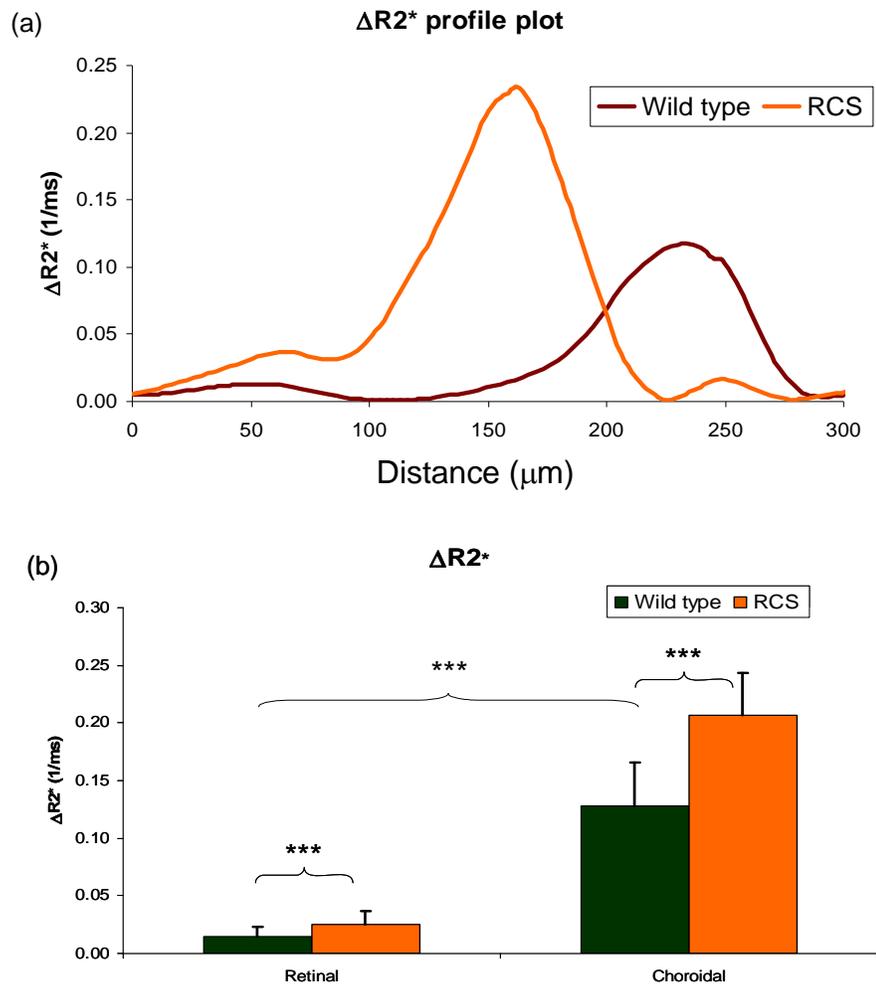
Fig. 7.3: Comparison of (a) ΔR2* profile plot in a representative P90 RCS and age-matched wild-type rat, (b) group-averaged peak ΔR2* from the retinal and choroidal vessels in dystrophic P90-120 RCS and age-matched wild-type LE rats. (* p<0.05; **p<0.01; and ***p<<0.01, n=7). Error bars are mean ± SD.

The average thickness of the retinal vasculature in RCS rats was 50 ± 10 μm and that of the choroidal vasculature was significantly higher than the retinal vasculature at 73 ± 7 μm. However, there were no differences in the thickness of the retinal or choroidal vessels between the wild-type and RCS groups. As in the case of the wild-type groups,

relative blood volume and fractional changes in blood volume during stimulation were calculated using the peak height.
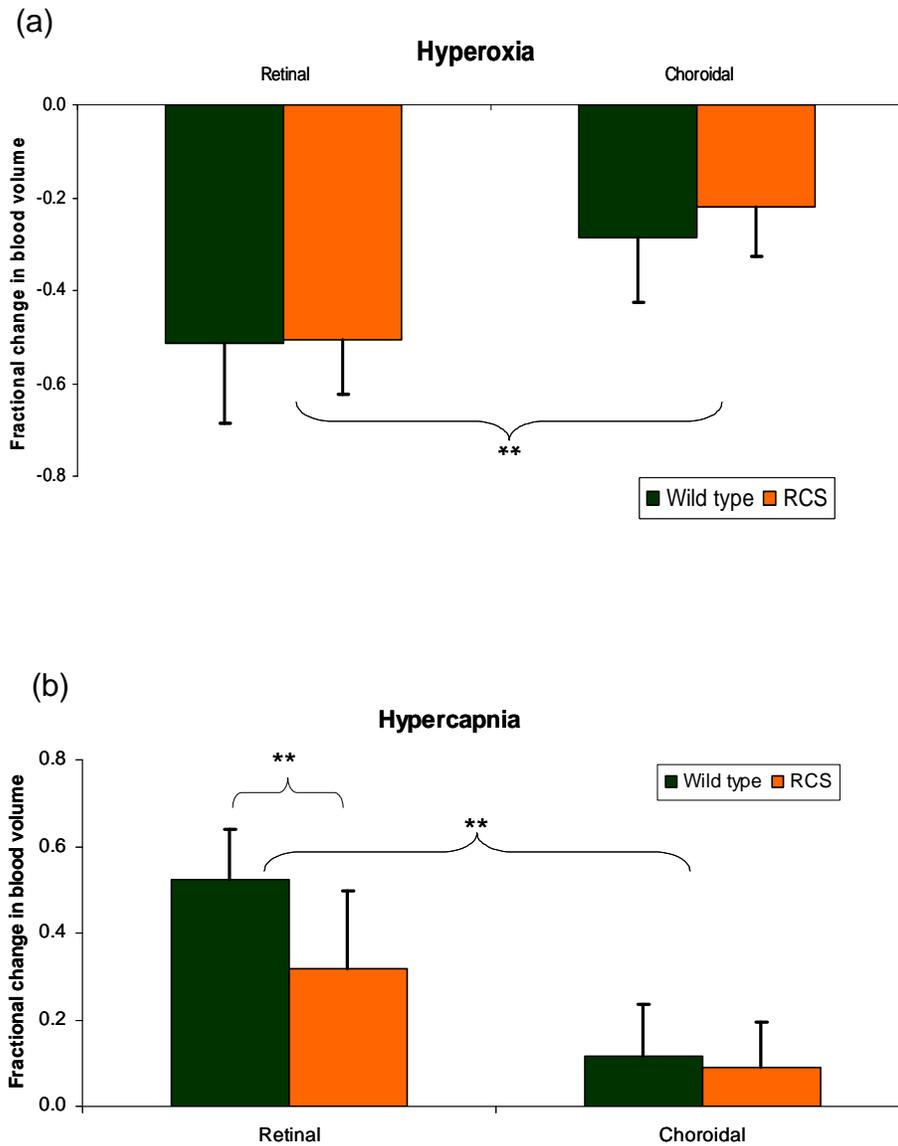
Fig. 7.4: Group-averaged fractional change in retinal and choroidal blood volume during (a) hyperoxic and (b) hypercapnic stimulation in dystrophic P90-120 RCS and age-matched wild-type LE and rats. (* p<0.05; **p<0.01 and ***p<<0.01, n=7). Error bars are mean ± SD.

$\Delta R2^*$ in retinal vasculature due to MION was 0.03 ± 0.1 ms^{-1} and that in the choroidal vasculature was significantly higher at 0.21 ± 0.04 ms^{-1} (p<<0.01). The

baseline $\Delta R2^*$ values calculated from the retinal and choroidal layers in RCS rats were significantly larger than those of the wild-type control rats, as shown in Fig. 7.3 ($p \ll 0.01$). However, the blood volume changes seemed to affect both the retinal and choroidal capillaries equally, and the ratio of blood volume between the retinal and choroidal vasculature in RCS rats was 9 ± 3. This was not significantly different from

RCS rats	Retinal vasculature	Choroidal vasculature	Ratio (choroidal/retinal)
Thickness (μm)	50 ± 10	70 ± 10	1.5 ± 0.2
$\Delta R2^*$ (ms^{-1})	0.03 ± 0.01	0.21 ± 0.04	9 ± 3
Fractional change – Hypercapnia	0.3 ± 0.2	0.1 ± 0.1	0.3 ± 0.4
Fractional change – Hyperoxia	-0.5 ± 0.1	-0.2 ± 0.1	0.5 ± 0.3

Table 7.3: Comparison of retinal and choroidal thickness and relative blood-volume in RCS rats. Units: Thickness in μm; Relative blood-volume in ms^{-1}.

that in wild-type LE (10 ± 3) or Sprague-Dawley (8 ± 3) groups.

Hyperoxic stimulation in RCS rats resulted in a fractional reduction of the retinal blood volume by 0.5 ± 0.1 while that in the choroidal volume was significantly lower at only 0.2 ± 0.1, as seen in Fig 7.4. These reductions were similar to the hyperoxic response seen in wild-type RCS rats ($p > 0.05$). However, the fractional increase the retinal blood volume of RCS rats on hypercapnia was 0.3 ± 0.2, which was significantly lower than that in wild-type LE rats ($p < 0.05$). The response from the choroidal vessels, on the other hand, was not significantly different. The thickness, baseline $\Delta R2^*$ and fractional change in blood-volume in response to stimuli from the retinal and choroidal vasculature of RCS rats is summarized in Table 7.3.

7.4 Discussion

Anatomical and functional changes in dystrophic adult RCS retina were detected by using the retinal MRI techniques developed herein. While high-resolution anatomical images revealed the loss of the avascular region in the adult RCS retina, manganese-enhanced MRI detected the loss of the inner nuclear and photoreceptor segment layers. The retinal thickness measured with MRI correlated well with toluidine-blue histology. Changes to basal blood volume and vascular compliance to hypercapnic stimulus was detected in adult RCS rats with steady-state blood-volume imaging.

7.4.1 Laminar structures and thicknesses

The RCS rats are born with essentially normal retinal morphology. However, a genetic defect results in the inability of the RPE to phagocytose shed-photoreceptor segments. The photoreceptor segments accumulate in a debris layer between the RPE and photoreceptor cells and is noticeable sometimes as early as P20 [239-241]. This debris layer, acting as a barrier to the efficient delivery of oxygen and metabolites to the photoreceptor cells, is thought to initiate photoreceptor degeneration [242, 243]. Indeed, high-resolution anatomical MRI revealed an essentially intact retina at P16 and a degenerated retina at P120 in RCS rats. This degeneration was visualized by a thinning and a reduction in the number of MRI-detected retinal layers. It is also possible, by using these non-invasive and versatile MRI techniques, to track the progression of the dystrophy and detect early anatomical and functional changes in the retina. Furthermore, evaluation of therapeutic techniques for slowing the anatomical or functional changes can be monitored in a longitudinal fashion in the same rat.

Manganese-enhanced MRI revealed a better resolution of retinal layer structure, with the capability of detecting individual layers of the neural retina and the choroid. This improved visualization of various neural retinal layers was essentially due to the differential accumulation of manganese. As seen in Chapter 5, there is increased Mn^{2+} accumulation in the plexiform and photoreceptor segment layers, which causes enhancement of T_2 contrast. Layer #3, designated as inner nuclear layer, adjacent to the debris layer in the P90 RCS rat retina was mildly hyper-intense, although the signal intensity was lower than that observed in the wild-type retina. This suggests perturbed Mn^{2+} accumulation in P90 RCS rats, likely due to functional and architectural changes in the outer plexiform layer and inner nuclear layer. Histology of layer #3 in the P90 RCS rat retina appeared relatively intact, consistent with published data, although subtle perturbations secondary to photoreceptor degeneration has been identified elsewhere [244].

MION experiments showed a similar thinning of the retina, as observed by the reduction in the peak-to-peak distance between the retinal and choroidal vasculature. There was a 40 ± 21% reduction in the peak-to-peak separation between the RCS and age-matched wild-type rats. However, there were no changes observed in the thickness of either the retinal or choroidal vasculature in RCS rats, when compared to the age-matched wild-type rats.

The thicknesses measured by MRI are subject to partial volume errors while the histology layer thicknesses will be affected by shrinkage, as discussed in Section 4.4.3. The errors are maximal in layers that have thickness comparable to or lower than the resolution of the MRI. Therefore, the individual layer thicknesses detected by the

MEMRI are at best an approximation as discussed in Chapter 5. However, total retinal thickness and blood-volumes calculated are more reliable due to the relatively high resolution of the images compared to the overall thickness.

7.4.2 Relative blood volume in the RCS retina

The $\Delta R2^*$ in RCS retinal and choroidal vessels show an increase of 46% to 80% when compared to age-matched wild-type rats. This change in $\Delta R2^*$ in RCS rats could be brought about by (i) change in baseline blood volume in RCS rats; (ii) changes in baseline retinal physiology like intraocular pressure and blood pressure; (iii) changes in total blood volume in RCS rats causing a change in dosage; or (iv) leakage of MION at the sites of the retinal vessels.

Both neovascularization as well as vascular drop-out have been reported in retinal vasculature of P120 RCS rats. The first changes are seen in the deep capillaries of the retinal vasculature young RCS rats, where there is a ~50% loss in capillary density with progression of retinal degeneration [244, 245]. This initial decrease in retinal blood volumes is however reversed through neovascularization as the deep retinal vessels come close to RPE cells in P120 RCS rats, resulting in an increase in the capillary bed volume [246-250]. Furthermore, there is an almost 50% increase in superficial retinal capillary density due to neovascularization in P120 RCS rats [251]. Consistent with all the above observations, fluorescein angiography studies in P70 RCS rats reveal hyper-fluorescent regions, suggesting regions of neovascularization and formation of coiled vascular tuffs as well as leakage in the retinal vasculature [252]. Consistent with these studies, we have

observed a 51%-80% increase in the retinal blood volume of RCS as compared to age-matched wild-type rats.

Corrosion-cast studies of the choroidal vasculature did not show any significant changes in P90 RCS rats as compared to congenic wild-types [253]. However, the choriocapillaris in the RCS retina progressively degenerates from 6 months of age, following loss of RPE cells. ICG angiography of P64 RCS rats have shown large regions of hyper-fluorescence and patchy dark regions in the choroid [254]. However, it was not immediately clear if the dark patches seen in the angiography originated due to atrophy in the choroids or in any of the superficial layers. One possibility is that changes in the RPE, retinal vasculature or the debris layer could interfere with the ICG signal. The cross-sectional images acquired in the MRI system circumvent the problem of interference of overlying tissue, providing more accurate measurements from the deep retinal layers. The choroidal blood volume was calculated to be 46% to 61% higher in the RCS retina than in the age-matched wild-type retina.

The baseline blood volume in retinal and choroidal vasculature increased by similar amounts in RCS rats as compared to wild-type rats, suggesting that it may also be caused by a change in physiology of RCS rats or error in the experimental setup. Although the intraocular pressures were not recorded in these rats, there is no evidence of altered intraocular pressure in RCS rats in the literature. The baseline blood pressure measured in RCS rats (MABP: 120 ± 20 mmHg) was not different from those in wild-type rats (MABP: 110 ± 20 mmHg, $p > 0.3$). Care was taken to maintain animal physiological parameters within normal range, before and after the injection of MION.

The dosage of MION was carefully adjusted to the body weight of the individual animal, with the assumption that the total blood volume is proportional to the body weight. Baseline blood volumes from wild-type Long-Evans, and wild-type Sprague-Dawley (n=6) strains were not statistically different, in either the retinal (LE: 0.015 ± 0.008 ms^{-1} and SD: 0.02 ± 0.01 ms^{-1}; p>0.5) or choroidal (LE: 0.13 ± 0.04 ms^{-1} and SD: 0.12 ± 0.04 ms^{-1}; p>0.5) vasculature, demonstrating the robustness of the method (data not shown). Any changes in total blood volume, either due to blood loss or dilution during surgery or due to the genetic defect in RCS rats could however alter the dilution of MION in the blood, thereby inducing errors in group comparisons. Additional care was taken during surgery so as not to affect the results of the experiment. Finally, measurements of changes in the plasma concentration of MION were attempted by low-rpm centrifugation of blood extracted from wild-type and RCS rats after MRI [255]. The MION concentrations measured by calculating the R2 in the MRI were, however, contaminated by lyses of erythrocytes. A better method for determination of MION concentration in plasma will help quantify the blood volume in the retinal vasculature.

Finally, the steady-state blood-volume calculation by MRI assumes that there is no leakage of MION from either the retinal or choroidal vasculature. Leakage and/or accumulation of MION in the retinal layers could potentially result in an overestimation of the blood volume in RCS rats. It has been shown in fluorescein angiography that the permeability of retinal vessels increases with age in RCS retina [254]. However, sodium fluorescein is a substantially smaller molecule than MION. Moreover, leakage of MION out of the retinal vasculature would cause a change of signal intensity in the vitreous, which was not observed in the MR images of RCS retina. MION particles are inert and

have an average size of 17 nm, which is comparable to the size of large proteins and high-density lipoproteins. Any leakage of MION-size particles would also cause protein extrusion in the retina, which has not been reported in RCS rats.

7.4.3 Stimulus-evoked changes to blood volume in RCS retina

The retinal blood flow is more tightly regulated than the choroidal, as seen by the smaller blood volume changes in the choroid relative to the retinal vasculature ($p < 0.01$) during stimulus in wild-type and RCS rats. Furthermore, the RCS and wild-type rats showed similar changes in blood volume to hyperoxic stimulus, while the response to hypercapnia was smaller in RCS rats compared to wild-type rats.

During hyperoxia the blood volume in the retinal and choroidal vasculature changed by $50 \pm 10\%$ and $20 \pm 10\%$, respectively, in RCS rats, which was not statistically different from the changes observed in wild-type rats. The BOLD signal changes during hyperoxia, in the choroidal and retinal vasculature, reduced slightly from 12 ± 2 and 7 ± 2, respectively, in wild-type rats to 9 ± 2 and 4 ± 3, respectively, in P120 RCS rats (n=4) [115]. Similarly, during hypercapnia, the blood volume in the retinal vasculature changed by $50 \pm 10\%$ in wild-type rats while the response reduced to $30 \pm 20\%$ in RCS rats ($p < 0.01$). The choroidal response to hypercapnic stimuli on the other hand was essentially absent in both RCS and wild-type rats. Similar studies on P120 RCS rats revealed a significant reduction in BOLD signal changes from 10 ± 2 to $0 \pm 6\%$ in the retinal vasculature and 1.6 ± 1 to $0 \pm 6\%$ in the choroidal vasculature [115].

It should be noted that the blood volume changes were not absent in the RCS retinal vasculature as was the case with the BOLD responses. It is possible that the

BOLD-signal-intensity changes due to vasodilation were negated by the decrease in blood oxygenation in BOLD fMRI, giving a net absence of BOLD. The interpretation of BOLD-signal-intensity changes is complex, and depends on many hemodynamic parameters like blood flow or volume changes, the rate of oxygen consumption and changes to the oxygen saturation level. A change in the observed BOLD-signal changes, is indicative of, but need not correlate directly with changes in hemodynamic parameters. $\Delta R2^*$ measured using MION is, however, a more direct measure of blood volume in the retina. Our understanding of the vascular response to hypercapnic and hyperoxic stimulus can be improved by direct inhibition or stimulation of the various vasomotor pathways.

Study of vascular response to flashing light or grids can help identify early functional changes in the retina. Significantly, the retinal evaluation techniques developed herein are minimally invasive, and can be used in longitudinal fashion to evaluate disease progression in a single animal. Furthermore, the retina is evaluated in a tomographic manner, without depth limitation or dependence on the clarity of the optic pathway. The techniques developed herein can help better the understanding of structural and functional changes in the retina, disease etiology, and even help evaluate various therapeutic options in a non-invasive and longitudinal manner.

7.5 Conclusion

Anatomical, baseline blood-volume and stimulus-evoked changes to blood volume in adult RCS rats were studied and compared to age-matched wild-type rats, using high-resolution anatomical imaging, manganese-enhanced MRI and MION-based blood volume studies. All these techniques reliably detected the retinal degeneration as a

loss of retinal layers and through thinning of the retina. Vascular changes were detected as an increase in baseline $\Delta R2^*$ in the RCS retina as well as a reduced stimulus-evoked change to the retinal blood volume.

Longitudinal experiments on RCS and age-matched wild-type rats are expected to yield insight not only into the different stages of disease progression but also help evaluate treatment strategies. Early, minimally-invasive detection of these anatomical and vascular changes in the retina in disease models may help in staging the diseases. Furthermore, longitudinal evaluation of other disease models in rats and monkeys can help better understand the etiology of complex diseases diabetic retinopathy and glaucoma. Further improvement in spatial resolution is expected. Given the remarkable progress in MRI technologies for on imaging the brain, translating these technologies to the longitudinal study of the human retina could critically impact retinal research.

Chapter 8: Conclusion

Retinal anatomy and function was reliably detected and evaluated in a rat model using the magnetic resonance imaging techniques developed in this thesis. Most of the current retinal imaging methods are based on optical techniques and rely on the clarity of the visual pathway. However, MRI of the retina can be performed even in conditions like cataract and retinal hemorrhages which hinder the direct visualization of the retina. MRI slices can be placed so as to cover the entire retina, and can image tissues without the limitation of depth and interference from overlying tissue. Furthermore, unlike other retinal imaging modalities, MRI offers the ability to detect the *in vivo* structural and functional abnormalities, in the same setup.

A minimum prerequisite for MRI is that the region being imaged does not move for the duration of the scan. This can be especially challenging for the eye as it is affected by voluntary and involuntary movements. Moreover, the imaging time on the MRI can vary from a few milliseconds to a few minutes. The experiments developed herein used a continuous dosage of a combination of muscle relaxant and anesthesia to remove motion-related artifacts in the experiments lasting a few hours. MRI is also an indirect method for measuring anatomical and physiological parameters, as MRI detects changes to relaxation properties of protons. However, these proton relaxation properties have been shown to directly correlate with physiological parameters of the tissue in most cases, and the use of MRI to detect tissue abnormalities is widely used in the field of medicine.

High-resolution MRI techniques were used to easily identify the major landmarks in the eye of a rat. Three retinal layers could be seen in high-resolution anatomical

images acquired without contrast agents. The three layers were identified, by the use of an intravascular contrast agent, as the vascular inner retina, avascular photoreceptor layers and the choroid. At even higher spatial resolutions, manganese-enhanced MRI revealed the different nuclear and plexiform layers in the retina. The various layers were confirmed by using Mn^{54} autoradiography. MION-based steady-state imaging was then performed to determine the relative blood volumes in the choroid and retinal vasculatures in the resting state. This technique also proved useful for reliably detecting the fractional changes in blood volume during various systemic stimulations.

The anatomical and functional imaging techniques developed herein were also applied in rat models of retinal disease. The RCS rat, a widely-studied model of retinal degeneration, has a mutation in the *Mertk* gene which is shared by some human retinitis pigmentosa patients. At birth, the RCS rat retina has essentially normal morphology, however, by the age of P90, most of the photoreceptors degenerate leaving only a debris layer in place of the outer plexiform layer, outer nuclear layer and the photoreceptor segment layers. The absence of the photoreceptor layer was evident from retinal thinning in anatomical and functional MRI of adult RCS rats. MEMRI of adult RCS rats revealed fewer layers in the retina, as expected. Significant differences were also seen between wild-type and age-matched RCS rats in the baseline blood volume and fractional blood volume changes in retinal vessels following hypercapnic stimulation. However, there were little differences in the fractional blood-volume changes during hyperoxic stimulation either from the retinal or choroidal vasculature. The study of continued progression of the retinal and choroidal vascular degeneration will be of interest to accurately characterize the dystrophy.

Future work

Retinal MRI has the potential to improve our understanding of retinal physiology, disease etiology, assist in earlier disease diagnosis, and even evaluate drug delivery. Retinal MRI has been shown here to be sufficiently sensitive to detect changes to retinal and choroidal blood volumes during systemic stimulation. Steady-state blood-volume imaging can help us understand better the hemodynamic changes due to visual stimulation. A preliminary study of visual stimulation has indicated that the response to diffuse-luminescence flicker light may be different from that seen between light and dark, with maximal response seen from different layers. MRI-based blood-volume studies have the potential to address this question in a non-invasive and layer-specific manner and experiments are being designed to explore these differences.

Application of the techniques developed in this thesis for the detection of anatomical and functional changes in other retinal disease models are also desired. Towards this end, long-term diabetic rats from collaborators at the Atlanta VA hospital will be procured for future studies. In general, retinopathic changes are not seen in diabetic rats due to the short life span of rats compared to time required for the development of lesions. It will therefore be interesting to identify functional or vascular deficits in long-term diabetic rats using the techniques developed herein. It is as planned to investigate the morphological and functional changes in disease models like glaucoma. Immuno-labeling of retina using intravitreal injection of layer-specific antibodies tagged with MRI contrast agents can be envisioned to improve anatomical imaging of the retinal dystrophies.

The *in vivo* nature of the MRI studies can help monitor the progression of the disease, in better understanding of its etiology, as well as evaluating treatment options. Recently, disease models like glaucoma, macular degeneration, retinal detachment, choroidal neovascularization as well as dystrophy and diabetic retinopathy have been developed in animals like rats, mice, rabbits, cats, and monkeys. The MRI techniques developed herein can be easily adapted to image any animal model. The feasibility for anatomical imaging of the retina on cats, rats and mice has already been demonstrated (unpublished data). The functional imaging techniques developed herein are easily adaptable to animal models having a reliable blood-retinal barrier. Therefore, these MRI offer a unique opportunity to further the understanding of these diseases, especially when combined with other histological and immunohistological techniques. MRI offers significant advantages compared to existing techniques of blood flow measurements like laser Doppler or microspheres, as repeated measurements can be made in the same animal, *in vivo*, with little perturbations of the physiology and without interference from overlying layers.

The MRI techniques developed herein, except for manganese-enhanced MRI, can also be implemented for the evaluation of human retina *in vivo* as long as the power of the MRI RF pulses do not exceed the maximum recommended specific-absorption rate. As more advanced MRI contrast agents get approval for human use, structural and functional MRI of the human retina may become more feasible. However, human MRI would require eye fixation to remove movement artifacts rather than the use of paralytic agents. The use of sub-Tenon's eye block, a local anesthetic routinely administered for surgical procedures of the eye, can also be considered for retinal MRI in humans, to

completely remove the involuntary movements. However, this would make the procedure far more invasive, and needs to be studied for its feasibility. This implies that the multiple short sequences may be needed for imaging human retina. This technique would also reduce the total RF energy deposited on the eye.

The retina, with its layered structure and its unique vascular makeup, also make it ideal to study the vascular-metabolic coupling as well as the effects of avascular neurons on the MRI signal. The retina is therefore a good model to improve understanding of the changes in MRI signal due to functional activation. Development of safer MRI contrast agent can potentially find application in human MRI while improving both the specificity and sensitivity of the scans.

Bibliography

1. S. Vannas, *Experimental examinations of the freezing of the anterior parts of the eye for the purpose of operation.* Acta Ophthalmol (Copenh), 1954. **32**(5): p. 631-2.

2. L.E. Lipetz, *A mechanism of light adaptation.* Science, 1961. **133**: p. 639-40.

3. J. Rohen, *[Studies on angle of anterior chamber; functional structure of ciliary body of some experimental animals and of humans.].* Albrecht Von Graefes Arch Ophthalmol, 1957. **158**(4): p. 310-25.

4. W. Schwarz, *[Electron-microscopical studies on the scleral and corneal structure in man.].* Z Zellforsch Mikrosk Anat, 1953. **38**(1): p. 26-49.

5. A. Kanai, T.C. Wood, F.M. Polack, and H.E. Kaufman, *The fine structure of sclerocornea.* Invest Ophthalmol, 1971. **10**(9): p. 687-94.

6. A. Ames, 3rd and D.A. Pollen, *Neurotransmission in central nervous tissue: a study of isolated rabbit retina.* J Neurophysiol, 1969. **32**(3): p. 424-42.

7. F.A. Chaudhry, R.J. Reimer, D. Krizaj, D. Barber, J. Storm-Mathisen, D.R. Copenhagen, and R.H. Edwards, *Molecular analysis of system N suggests novel physiological roles in nitrogen metabolism and synaptic transmission.* Cell, 1999. **99**(7): p. 769-80.

8. H. Varoqui, H. Zhu, D. Yao, H. Ming, and J.D. Erickson, *Cloning and functional identification of a neuronal glutamine transporter.* J Biol Chem, 2000. **275**(6): p. 4049-54.

9. A. Van Harreveld and E. Fifkova, *Effects of glutamate and other amino acids on the retina.* J Neurochem, 1971. **18**(11): p. 2145-54.

10. M.J. Neal and L.L. Iversen, *Autoradiographic localization of 3 H-GABA in rat retina.* Nat New Biol, 1972. **235**(59): p. 217-8.

11. P. Rosenberg, W.D. Dettbarn, and M. Brzin, *Acetylcholine and choline acetylase in squid giant axon, ganglia and retina.* Nature, 1966. **210**(5038): p. 858-9.

12. J. Haeggendal and T. Malmfors, *Evidence of Dopamine-Containing Neurons in the Retina of Rabbits.* Acta Physiol Scand, 1963. **59**: p. 295-6.

13. G. Thin and J.C. Ewart, *On the Structure of the Retina.* J Anat Physiol, 1876. **11**(Pt 1): p. 96-108.

14. A.W. Spira and M.J. Hollenberg, *Human retinal development: ultrastructure of the inner retinal layers.* Dev Biol, 1973. **31**(1): p. 1-21.

15. K. Naka and T. Otsuka, *Morphological and functional identifications of catfish retinal neurons. II. Morphological identification.* J Neurophysiol, 1975. **38**(1): p. 72-91.

16. S. Haverkamp and H. Wassle, *Immunocytochemical analysis of the mouse retina.* J Comp Neurol, 2000. **424**(1): p. 1-23.

17. O. Castro Gde and H. Martins-Ferreira, *Deformations and thickness variations accompanying spreading depression in the retina.* J Neurophysiol, 1970. **33**(6): p. 891-900.

18. A. Chan, J.S. Duker, T.H. Ko, J.G. Fujimoto, and J.S. Schuman, *Normal macular thickness measurements in healthy eyes using Stratus optical coherence tomography.* Arch Ophthalmol, 2006. **124**(2): p. 193-8.

19.   P. Gouras, *Opponent-colour cells in different layers of foveal striate cortex.* J Physiol, 1974. **238**(3): p. 583-602.

20.   A.E. Hendrickson and C. Yuodelis, *The morphological development of the human fovea.* Ophthalmology, 1984. **91**(6): p. 603-12.

21.   P.K. Brown and G. Wald, *Visual Pigments in Single Rods and Cones of the Human Retina. Direct Measurements Reveal Mechanisms of Human Night and Color Vision.* Science, 1964. **144**: p. 45-52.

22.   J.L. Schnapf, T.W. Kraft, B.J. Nunn, and D.A. Baylor, *Spectral sensitivity of primate photoreceptors.* Vis Neurosci, 1988. **1**(3): p. 255-61.

23.   J. Verweij, E.P. Hornstein, and J.L. Schnapf, *Surround antagonism in macaque cone photoreceptors.* J Neurosci, 2003. **23**(32): p. 10249-57.

24.   J.E. Dowling and B.B. Boycott, *Neural connections of the retina: fine structure of the inner plexiform layer.* Cold Spring Harb Symp Quant Biol, 1965. **30**: p. 393-402.

25.   J.E. Dowling and F.S. Werblin, *Organization of retina of the mudpuppy, Necturus maculosus. I. Synaptic structure.* J Neurophysiol, 1969. **32**(3): p. 315-38.

26.   S. Haverkamp, U. Grunert, and H. Wassle, *The synaptic architecture of AMPA receptors at the cone pedicle of the primate retina.* J Neurosci, 2001. **21**(7): p. 2488-500.

27.   S. Haverkamp, U. Grunert, and H. Wassle, *Localization of kainate receptors at the cone pedicles of the primate retina.* J Comp Neurol, 2001. **436**(4): p. 471-86.

28.   H. Wassle, U. Grunert, P.R. Martin, and B.B. Boycott, *Immunocytochemical characterization and spatial distribution of midget bipolar cells in the macaque monkey retina.* Vision Res, 1994. **34**(5): p. 561-79.

29.   A.G. Leventhal, R.W. Rodieck, and B. Dreher, *Retinal ganglion cell classes in the Old World monkey: morphology and central projections.* Science, 1981. **213**(4512): p. 1139-42.

30.   R.W. Rodieck and R.K. Brening, *Retinal ganglion cells: properties, types, genera, pathways and trans-species comparisons.* Brain Behav Evol, 1983. **23**(3-4): p. 121-64.

31.   P.R. Martin, *Colour processing in the primate retina: recent progress.* J Physiol, 1998. **513 (Pt 3**): p. 631-8.

32.   M. Iwasaki and H. Inomata, *Relation between superficial capillaries and foveal structures in the human retina.* Invest Ophthalmol Vis Sci, 1986. **27**(12): p. 1698-705.

33.   A. Alm and A. Bill, *Ocular and optic nerve blood flow at normal and increased intraocular pressures in monkeys (Macaca irus): a study with radioactively labelled microspheres including flow determinations in brain and some other tissues.* Exp Eye Res, 1973. **15**(1): p. 15-29.

34.   S.S. Hayreh, *Submacular choroidal vascular pattern. Experimental fluorescein fundus angiographic studies.* Albrecht Von Graefes Arch Klin Exp Ophthalmol, 1974. **192**(3): p. 181-96.

35.   A.M. Laties and D. Jacobowitz, *A comparative study of the autonomic innervation of the eye in monkey, cat, and rabbit.* Anat Rec, 1966. **156**(4): p. 383-95.

36.   M.C. Koss and T. Gherezghiher, *Adrenoceptor subtypes involved in neurally evoked sympathetic vasoconstriction in the anterior choroid of cats.* Exp Eye Res, 1993. **57**(4): p. 441-7.

37.   J.J. Steinle, D. Krizsan-Agbas, and P.G. Smith, *Regional regulation of choroidal blood flow by autonomic innervation in the rat.* Am J Physiol Regul Integr Comp Physiol, 2000. **279**(1): p. R202-9.

38.   I.C. Michaelson, *Retinal circulation in man and animals.* Thomas, Springfield IL, 1954.

39.   H. Fujisawa, H. Morioka, K. Watanabe, and H. Nakamura, *A decay of gap junctions in association with cell differentiation of neural retina in chick embryonic development.* J Cell Sci, 1976. **22**(3): p. 585-96.

40.   A.H. Bunt-Milam, J.C. Saari, I.B. Klock, and G.G. Garwin, *Zonulae adherentes pore size in the external limiting membrane of the rabbit retina.* Invest Ophthalmol Vis Sci, 1985. **26**(10): p. 1377-80.

41.   P.H. Glow and S. Rose, *Effects of Light and Dark on the Acetylcholinesterase Activity of the Retina.* Nature, 1964. **202**: p. 422-3.

42.   G. Falk and P. Fatt, *Mechanism of conductance changes produced by the photolysis of rhodopsin.* Exp Eye Res, 1969. **8**(2): p. 248-9.

43.   N. Ben-Tovim, *A new indirect ophthalmoscope.* Ophthalmologica, 1975. **170**(1): p. 56-63.

44.   F.C. Delori, E.S. Gragoudas, R. Francisco, and R.C. Pruett, *Monochromatic ophthalmoscopy and fundus photography. The normal fundus.* Arch Ophthalmol, 1977. **95**(5): p. 861-8.

45.   N.M. Ducrey, F.C. Delori, and E.S. Gragoudas, *Monochromatic ophthalmoscopy and fundus photography. II. The pathological fundus.* Arch Ophthalmol, 1979. **97**(2): p. 288-93.

46.   O. Kaefer, *Degenerative changes in retinal vessels. Photodocumentation with monochromatic filters.* Arch Ophthalmol, 1980. **98**(2): p. 303-6.

47.   R.V. Abadi and C.M. Dickinson, *Monochromatic fundus photography of human albinos.* Arch Ophthalmol, 1983. **101**(11): p. 1706-11.

48.   R.F. Spaide, *Fundus autofluorescence and age-related macular degeneration.* Ophthalmology, 2003. **110**(2): p. 392-9.

49.   U. Solbach, C. Keilhauer, H. Knabben, and S. Wolf, *Imaging of retinal autofluorescence in patients with age-related macular degeneration.* Retina, 1997. **17**(5): p. 385-9.

50.   P. Bischoff, H. Helbig, H. Niederberger, and B. Torok, *[Simultaneous ICG- and fluorescein-angiography for fundus examination].* Klin Monatsbl Augenheilkd, 2000. **216**(2): p. 120-5.

51.   R.C. Benson and H.A. Kues, *Fluorescence properties of indocyanine green as related to angiography.* Phys Med Biol, 1978. **23**(1): p. 159-63.

52.   S. Yoneya, T. Saito, Y. Komatsu, I. Koyama, K. Takahashi, and J. Duvoll-Young, *Binding properties of indocyanine green in human blood.* Invest Ophthalmol Vis Sci, 1998. **39**(7): p. 1286-90.

53.   S.S. Hayreh and J.A. Baines, *Occlusion of the posterior ciliary artery. I. Effects on choroidal circulation.* Br J Ophthalmol, 1972. **56**(10): p. 719-35.

54. D. Archer, A.E. Krill, and F.W. Newell, *Fluorescein studies of normal choroidal circulation.* Am J Ophthalmol, 1970. **69**(4): p. 543-54.

55. R.H. Webb and G.W. Hughes, *Scanning laser ophthalmoscope.* IEEE Trans Biomed Eng, 1981. **28**(7): p. 488-92.

56. D.J. Coleman, *Reliability of ocular and orbital diagnosis with B-scan ultrasound. 1. Ocular diagnosis.* Am J Ophthalmol, 1972. **73**(4): p. 501-16.

57. R.C. Gentile, D.M. Berinstein, J. Liebmann, R. Rosen, Z. Stegman, C. Tello, J.B. Walsh, and R. Ritch, *High-resolution ultrasound biomicroscopy of the pars plana and peripheral retina.* Ophthalmology, 1998. **105**(3): p. 478-84.

58. C. Jolly, J.C. Jeanny, F. Behar-Cohen, P. Laugier, and A. Saied, *High-resolution ultrasonography of subretinal structure and assessment of retina degeneration in rat.* Exp Eye Res, 2005. **81**(5): p. 592-601.

59. M.H. Chaudhari, F. Forsberg, A. Voodarla, F.N. Saikali, S. Goonewardene, L. Needleman, G.C. Finkel, and B.B. Goldberg, *Breast tumor vascularity identified by contrast enhanced ultrasound and pathology: initial results.* Ultrasonics, 2000. **38**(1-8): p. 105-9.

60. S. Huber, T. Helbich, J. Kettenbach, W. Dock, I. Zuna, and S. Delorme, *Effects of a microbubble contrast agent on breast tumors: computer-assisted quantitative assessment with color Doppler US--early experience.* Radiology, 1998. **208**(2): p. 485-9.

61. G. Bhagavatheeshwaran, W.T. Shi, F. Forsberg, and P.M. Shankar, *Subharmonic signal generation from contrast agents in simulated neovessels.* Ultrasound Med Biol, 2004. **30**(2): p. 199-203.

62. D. Huang, E.A. Swanson, C.P. Lin, J.S. Schuman, W.G. Stinson, W. Chang, M.R. Hee, T. Flotte, K. Gregory, C.A. Puliafito, and et al., *Optical coherence tomography.* Science, 1991. **254**(5035): p. 1178-81.

63. C.A. Puliafito, M.R. Hee, C.P. Lin, E. Reichel, J.S. Schuman, J.S. Duker, J.A. Izatt, E.A. Swanson, and J.G. Fujimoto, *Imaging of macular diseases with optical coherence tomography.* Ophthalmology, 1995. **102**(2): p. 217-29.

64. M.F. Marmor and E. Zrenner, *Standard for clinical electroretinography (1999 update). International Society for Clinical Electrophysiology of Vision.* Doc Ophthalmol, 1998. **97**(2): p. 143-56.

65. E. Marg, *Development of electro-oculography; standing potential of the eye in registration of eye movement.* AMA Arch Ophthalmol, 1951. **45**(2): p. 169-85.

66. G.B. Arden and J.H. Kelsey, *Changes produced by light in the standing potential of the human eye.* J Physiol, 1962. **161**: p. 189-204.

67. G.S. Brindley, *The passive electrical properties of the frog's retina, choroid and sclera for radial fields and currents.* J Physiol, 1956. **134**(2): p. 339-52.

68. K.T. Brown and T.N. Wiesel, *Intraretinal recording in the unopened cat eye.* Am J Ophthalmol, 1958. **46**(3 Part 2): p. 91-6; discussion 6-8.

69. F. Bloch, W.W. Hansen, and M. Packard, *Nuclear Induction.* Phys. Rev., 1946. **69**(1): p. 127.

70. F. Bloch, *The Principle of Nuclear Induction.* Science, 1953. **118**(3068): p. 425-30.

71. J.H. Gardner and E.M. Purcell, *A Precise Determination of the Proton Magnetic Moment in Bohr Magnetons.* Phys. Rev., 1949. **76**(8): p. 1262.

72.   R. Damadian, *Tumor detection by nuclear magnetic resonance.* Science, 1971. **171**(976): p. 1151-3.

73.   P.C. Lauterbur, *Image formation by induced local interactions. Examples employing nuclear magnetic resonance. 1973.* Clin Orthop Relat Res, 1989(244): p. 3-6.

74.   P. Mansfield, *Multi-planar image formation using NMR spin echoes.* J. Phys. C: Solid State Phys, 1977. **10**: p. L55-8.

75.   E.L. Hahn, *Spin Echoes.* Phys. Rev., 1950(77): p. 746.

76.   W. Krause, *Contrast agents. Magnetic resonance imaging.* 2002: Berlin : Springer. pp 19.

77.   C. Tanford, *Physical Chemistry of Macromolecules*. 1963: Wiley, New York, NY. 317–456.

78.   E. Lauffer, *Paramagnetic metal complexes for NMR imaging* Chemical reviews 1987. **87**(5): p. 900.

79.   S.H. Koenig and K.E. Kellar, *Theory of 1/T1 and 1/T2 NMRD profiles of solutions of magnetic nanoparticles.* Magn Reson Med, 1995. **34**(2): p. 227-33.

80.   C. Chambon, O. Clement, A. Le Blanche, E. Schouman-Claeys, and G. Frija, *Superparamagnetic iron oxides as positive MR contrast agents: in vitro and in vivo evidence.* Magn Reson Imaging, 1993. **11**(4): p. 509-19.

81.   C. Corot, P. Robert, J.M. Idee, and M. Port, *Recent advances in iron oxide nanocrystal technology for medical imaging.* Adv Drug Deliv Rev, 2006. **58**(14): p. 1471-504.

82.   M. Botta, *Second Coordination Sphere Water Molecules and Relaxivity of Gadolinium(III) Complexes: Implications for MRI Contrast Agents.* European journal of inorganic chemistry 2000. **2000**(3): p. 399 – 407.

83.   S. Koenig and R. Brown, *Magnetic resonance annual* ed. K. HY. 1987: Raven, new york.

84.   K.E. Kellar, P.M. Henrichs, M. Spiller, and S.H. Koenig, *Relaxation of solvent protons by solute Gd3+-chelates revisited.* Magn Reson Med, 1997. **37**(5): p. 730-5.

85.   R.E. London, G. Toney, S.A. Gabel, and A. Funk, *Magnetic resonance imaging studies of the brains of anesthetized rats treated with manganese chloride.* Brain Res Bull, 1989. **23**(3): p. 229-35.

86.   R. Lucchini, E. Albini, D. Placidi, R. Gasparotti, M.G. Pigozzi, G. Montani, and L. Alessio, *Brain magnetic resonance imaging and manganese exposure.* Neurotoxicology, 2000. **21**(5): p. 769-75.

87.   Y.J. Lin and A.P. Koretsky, *Manganese ion enhances T1-weighted MRI during brain activation: an approach to direct imaging of brain function.* Magn Reson Med, 1997. **38**(3): p. 378-88.

88.   P.B. Simpson, R.A. Challiss, and S.R. Nahorski, *Divalent cation entry in cultured rat cerebellar granule cells measured using Mn2+ quench of fura 2 fluorescence.* Eur J Neurosci, 1995. **7**(5): p. 831-40.

89.   K. Narita, F. Kawasaki, and H. Kita, *Mn and Mg influxes through Ca channels of motor nerve terminals are prevented by verapamil in frogs.* Brain Res, 1990. **510**(2): p. 289-95.

90. W.N. Sloot and J.B. Gramsbergen, *Axonal transport of manganese and its relevance to selective neurotoxicity in the rat basal ganglia.* Brain Res, 1994. **657**(1-2): p. 124-32.

91. S.H. Koenig and R.D. Brown, 3rd, *Relaxation of solvent protons by paramagnetic ions and its dependence on magnetic field and chemical environment: implications for NMR imaging.* Magn Reson Med, 1984. **1**(4): p. 478-95.

92. J. Donaldson, D. McGregor, and F. LaBella, *Manganese neurotoxicity: a model for free radical mediated neurodegeneration?* Can J Physiol Pharmacol, 1982. **60**(11): p. 1398-405.

93. D.G. Graham, *Catecholamine toxicity: a proposal for the molecular pathogenesis of manganese neurotoxicity and Parkinson's disease.* Neurotoxicology, 1984. **5**(1): p. 83-95.

94. A.S. Hazell and M.D. Norenberg, *Manganese decreases glutamate uptake in cultured astrocytes.* Neurochem Res, 1997. **22**(12): p. 1443-7.

95. J.B. Wittenberg, B.A. Wittenberg, J. Peisach, and W.E. Blumberg, *On the state of the iron and the nature of the ligand in oxyhemoglobin.* Proc Natl Acad Sci U S A, 1970. **67**(4): p. 1846-53.

96. S. Ogawa, T.M. Lee, A.R. Kay, and D.W. Tank, *Brain magnetic resonance imaging with contrast dependent on blood oxygenation.* Proc Natl Acad Sci U S A, 1990. **87**(24): p. 9868-72.

97. S. Ogawa, R.S. Menon, D.W. Tank, S.G. Kim, H. Merkle, J.M. Ellermann, and K. Ugurbil, *Functional brain mapping by blood oxygenation level-dependent contrast magnetic resonance imaging. A comparison of signal characteristics with a biophysical model.* Biophys J, 1993. **64**(3): p. 803-12.

98. A. Bogdanov, M. Papisov, R. Weissleder, T. Shen, and T. Brady, *Opsonization of dextran stabilized iron oxides with plasma proteins.* Proc 11th Annual Scientific Meeting SMRM, 1991.

99. T. Shen, R. Weissleder, M. Papisov, A. Bogdanov, Jr., and T.J. Brady, *Monocrystalline iron oxide nanocompounds (MION): physicochemical properties.* Magn Reson Med, 1993. **29**(5): p. 599-604.

100. F. Hennel and J.F. Nedelec, *Interleaved asymmetric echo-planar imaging.* Magn Reson Med, 1995. **34**(4): p. 520-4.

101. R.L. Ehman and J.P. Felmlee, *Adaptive technique for high-definition MR imaging of moving structures.* Radiology, 1989. **173**(1): p. 255-63.

102. X. Hu and S.G. Kim, *Reduction of signal fluctuation in functional MRI using navigator echoes.* Magn Reson Med, 1994. **31**(5): p. 495-503.

103. R.K. Meier and N. Dieringer, *The role of compensatory eye and head movements in the rat for image stabilization and gaze orientation.* Exp Brain Res, 1993. **96**(1): p. 54-64.

104. G. Laborit, R. Angiboust, and J.P. Papin, *A study of eye movement for assessing recovery from anaesthesia.* Br J Anaesth, 1977. **49**(8): p. 805-10.

105. C. Power, C. Crowe, P. Higgins, and D.C. Moriarty, *Anaesthetic depth at induction. An evaluation using clinical eye signs and EEG polysomnography.* Anaesthesia, 1998. **53**(8): p. 736-43.

106. G. Nair and T.Q. Duong, *Echo-planar BOLD fMRI of mice on a narrow-bore 9.4 T magnet.* Magn Reson Med, 2004. **52**(2): p. 430-4.

107. K.M. Sicard and T.Q. Duong, *Effects of hypoxia, hyperoxia, and hypercapnia on baseline and stimulus-evoked BOLD, CBF, and CMRO2 in spontaneously breathing animals.* Neuroimage, 2005. **25**(3): p. 850-8.

108. C. Prys-Roberts, *Anaesthesia: a practical or impractical construct?* Br J Anaesth, 1987. **59**(11): p. 1341-5.

109. R.G. Shulman, D.L. Rothman, and F. Hyder, *Stimulated changes in localized cerebral energy consumption under anesthesia.* Proc Natl Acad Sci U S A, 1999. **96**(6): p. 3245-50.

110. A. Grinvald, D. Shoham, A. Shmuel, D. Glaser, I. Vanzetta, E. Shtoyerman, H. Slovin, A. Sterkin, C. Wijnbergen, R. Hildesheim, and A. Arieli, *In-vivo optical imaging of cortical architecture and dynamics.* Technical Report GC-AG/99-6, 2001.

111. B.A. Berkowitz, Y. Sato, C.A. Wilson, and E. de Juan, *Blood-retinal barrier breakdown investigated by real-time magnetic resonance imaging after gadolinium-diethylenetriaminepentaacetic acid injection.* Invest Ophthalmol Vis Sci, 1991. **32**(11): p. 2854-60.

112. B.A. Berkowitz, R. Roberts, D.J. Goebel, and H. Luan, *Noninvasive and simultaneous imaging of layer-specific retinal functional adaptation by manganese-enhanced MRI.* Invest Ophthalmol Vis Sci, 2006. **47**(6): p. 2668-74.

113. T.W. Redpath, *Signal-to-noise ratio in MRI.* Br J Radiol, 1998. **71**(847): p. 704-7.

114. K.J. Friston, S. Williams, R. Howard, R.S. Frackowiak, and R. Turner, *Movement-related effects in fMRI time-series.* Magn Reson Med, 1996. **35**(3): p. 346-55.

115. H. Cheng, G. Nair, T.A. Walker, M.K. Kim, M.T. Pardue, P.M. Thule, D.E. Olson, and T.Q. Duong, *Structural and functional MRI reveals multiple retinal layers.* Proc Natl Acad Sci U S A, 2006. **103**(46): p. 17525-30.

116. R.G. Buttery, C.F. Hinrichsen, W.L. Weller, and J.R. Haight, *How thick should a retina be? A comparative study of mammalian species with and without intraretinal vasculature.* Vision Res, 1991. **31**(2): p. 169-87.

117. D.A. Nelson, S. Krupsky, A. Pollack, E. Aloni, M. Belkin, I. Vanzetta, M. Rosner, and A. Grinvald, *Special report: Noninvasive multi-parameter functional optical imaging of the eye.* Ophthalmic Surg Lasers Imaging, 2005. **36**(1): p. 57-66.

118. P.R. Preussner, G. Richard, O. Darrelmann, J. Weber, and I. Kreissig, *Quantitative measurement of retinal blood flow in human beings by application of digital image-processing methods to television fluorescein angiograms.* Graefes Arch Clin Exp Ophthalmol, 1983. **221**(3): p. 110-2.

119. D.R. Guyer, L.A. Yannuzzi, J.S. Slakter, J.A. Sorenson, and S. Orlock, *The status of indocyanine-green videoangiography.* Curr Opin Ophthalmol, 1993. **4**(3): p. 3-6.

120. U. Schmidt-Erfurth, *Indocyanine green angiography and retinal sensitivity after photodynamic therapy of subfoveal choroidal neovascularization.* Semin Ophthalmol, 1999. **14**(1): p. 35-44.

121. N.P. Blair, G.T. Feke, J. Morales-Stoppello, C.E. Riva, D.G. Goger, G. Collas, and J.W. McMeel, *Prolongation of the retinal mean circulation time in diabetes.* Arch Ophthalmol, 1982. **100**(5): p. 764-8.

122. F. Formaz, C.E. Riva, and M. Geiser, *Diffuse luminance flicker increases retinal vessel diameter in humans.* Curr Eye Res, 1997. **16**(12): p. 1252-7.

123. C.E. Riva, S.D. Cranstoun, R.M. Mann, and G.E. Barnes, *Local choroidal blood flow in the cat by laser Doppler flowmetry.* Invest Ophthalmol Vis Sci, 1994. **35**(2): p. 608-18.

124. J. Liang, D.R. Williams, and D.T. Miller, *Supernormal vision and high-resolution retinal imaging through adaptive optics.* J Opt Soc Am A Opt Image Sci Vis, 1997. **14**(11): p. 2884-92.

125. J. Alper, *OCT: images of coherence.* Science, 1993. **261**(5121): p. 555.

126. J. Koelle, C. Riva, B. Petrig, and S. Cranstoun, *Depth of tissue sampling in the optic nerve head using laser Doppler flowmetry.* Lasers Med Sci 1993. **8**: p. 49-54.

127. B.R. Masters and M. Bohnke, *Three-dimensional confocal microscopy of the living human eye.* Annu Rev Biomed Eng, 2002. **4**: p. 69-91.

128. D.S. Kim, T.Q. Duong, and S.G. Kim, *High-resolution mapping of iso-orientation columns by fMRI.* Nat Neurosci, 2000. **3**(2): p. 164-9.

129. E.M. Shapiro, S. Skrtic, K. Sharer, J.M. Hill, C.E. Dunbar, and A.P. Koretsky, *MRI detection of single particles for cellular imaging.* Proc Natl Acad Sci U S A, 2004. **101**(30): p. 10901-6.

130. L. Ciobanu and C.H. Pennington, *3D micron-scale MRI of single biological cells.* Solid State Nucl Magn Reson, 2004. **25**(1-3): p. 138-41.

131. Q. Shen, H. Cheng, M.T. Pardue, T.F. Chang, G. Nair, V.T. Vo, R.D. Shonat, and T.Q. Duong, *Magnetic resonance imaging of tissue and vascular layers in the cat retina.* J Magn Reson Imaging, 2006. **23**(4): p. 465-72.

132. Y. Li, H. Cheng, and T.Q. Duong, *Blood-flow magnetic resonance imaging of the retina.* Neuroimage, 2008. **39**(4): p. 1744-51.

133. T.Q. Duong, S.C. Ngan, K. Ugurbil, and S.G. Kim, *Functional magnetic resonance imaging of the retina.* Invest Ophthalmol Vis Sci, 2002. **43**(4): p. 1176-81.

134. R. Gruetter, *Automatic, localized in vivo adjustment of all first- and second-order shim coils.* Magn Reson Med, 1993. **29**(6): p. 804-11.

135. D.N. Guilfoyle, V.V. Dyakin, J. O'Shea, G.S. Pell, and J.A. Helpern, *Quantitative measurements of proton spin-lattice (T1) and spin-spin (T2) relaxation times in the mouse brain at 7.0 T.* Magn Reson Med, 2003. **49**(3): p. 576-80.

136. E.L. Barbier, L. Liu, E. Grillon, J.F. Payen, J.F. Lebas, C. Segebarth, and C. Remy, *Focal brain ischemia in rat: acute changes in brain tissue T1 reflect acute increase in brain tissue water content.* NMR Biomed, 2005. **18**(8): p. 499-506.

137. M. El-Sayed, *Assessment of Myelination and Demyelination of Nerve Tissue using MRI.* 1996.

138. Y. Cremillieux, S. Ding, and J.F. Dunn, *High-resolution in vivo measurements of transverse relaxation times in rats at 7 Tesla.* Magn Reson Med, 1998. **39**(2): p. 285-90.

139. F. Franconi, L. Lemaire, L. Marescaux, P. Jallet, and J.J. Le Jeune, *In vivo quantitative microimaging of rat spinal cord at 7T.* Magn Reson Med, 2000. **44**(6): p. 893-8.

140. Y. Hasegawa, L.L. Latour, C.H. Sotak, B.J. Dardzinski, and M. Fisher, *Temperature dependent change of apparent diffusion coefficient of water in normal and ischemic brain of rats.* J Cereb Blood Flow Metab, 1994. **14**(3): p. 383-90.

141. J. Zhong, O.A. Petroff, J.W. Prichard, and J.C. Gore, *Changes in water diffusion and relaxation properties of rat cerebrum during status epilepticus.* Magn Reson Med, 1993. **30**(2): p. 241-6.

142. D. Le Bihan, E. Breton, D. Lallemand, M.L. Aubin, J. Vignaud, and M. Laval-Jeantet, *Separation of diffusion and perfusion in intravoxel incoherent motion MR imaging.* Radiology, 1988. **168**(2): p. 497-505.

143. T.Q. Duong, E. Yacoub, G. Adriany, X. Hu, K. Ugurbil, and S.G. Kim, *Microvascular BOLD contribution at 4 and 7 T in the human brain: gradient-echo and spin-echo fMRI with suppression of blood effects.* Magn Reson Med, 2003. **49**(6): p. 1019-27.

144. C.T.W. Moonen, *Functional MRI.* Functional MRI, ed. P.A. Bandettini. 1999: Springer. 160-5.

145. M. Fischer, K. Bockhorst, M. Hoehn-Berlage, B. Schmitz, and K.A. Hossmann, *Imaging of the apparent diffusion coefficient for the evaluation of cerebral metabolic recovery after cardiac arrest.* Magn Reson Imaging, 1995. **13**(6): p. 781-90.

146. J.G. Fujimoto, C. Pitris, S.A. Boppart, and M.E. Brezinski, *Optical coherence tomography: an emerging technology for biomedical imaging and optical biopsy.* Neoplasia, 2000. **2**(1-2): p. 9-25.

147. A. Grinvald, T. Bonhoeffer, I. Vanzetta, A. Pollack, E. Aloni, R. Ofri, and D. Nelson, *High-resolution functional optical imaging: from the neocortex to the eye.* Ophthalmol Clin North Am, 2004. **17**(1): p. 53-67.

148. D.S. Kim, T.Q. Duong, and S.G. Kim, *Reply to "Can current fMRI techniques reveal the micro-architecture of cortex?"* Nat Neurosci, 2000. **3**(5): p. 414.

149. T.Q. Duong, D.S. Kim, K. Ugurbil, and S.G. Kim, *Localized cerebral blood flow response at submillimeter columnar resolution.* Proc Natl Acad Sci U S A, 2001. **98**(19): p. 10904-9.

150. K. Cheng, R.A. Waggoner, and K. Tanaka, *Human ocular dominance columns as revealed by high-field functional magnetic resonance imaging.* Neuron, 2001. **32**(2): p. 359-74.

151. A.C. Silva and A.P. Koretsky, *Laminar specificity of functional MRI onset times during somatosensory stimulation in rat.* Proc Natl Acad Sci U S A, 2002. **99**(23): p. 15182-7.

152. J.B. Goense and N.K. Logothetis, *Laminar specificity in monkey V1 using high-resolution SE-fMRI.* Magn Reson Imaging, 2006. **24**(4): p. 381-92.

153. H. Wassle and B.B. Boycott, *Functional architecture of the mammalian retina.* Physiol Rev, 1991. **71**(2): p. 447-80.

154. A. Harris, L. Kagemann, and G.A. Cioffi, *Assessment of human ocular hemodynamics.* Surv Ophthalmol, 1998. **42**(6): p. 509-33.

155. A. Bill, *Handbook of Physiology.* Bill A (1984) in Handbook of Physiology Part 2 in Microcirculation, eds Renkin EM, Michel CC (Am Physiol Soc, Bethesda,

MD), pp 1001–1035 ed. Microcirculation, ed. E. Renkin and C. Michel. Vol. Part 2. 1984, Bethesda, MD. 1001–35.

156. R. Sharma and B. Ehinger, *Alder's Physiology of the Eye*, ed. P. Kaufman and A. Alm. 1992, Mosby, St. Louis, MO. 319–48.

157. B.B. Thomas, S. Arai, Y. Ikai, G. Qiu, Z. Chen, R.B. Aramant, S.R. Sadda, and M.J. Seiler, *Retinal transplants evaluated by optical coherence tomography in photoreceptor degenerate rats.* J Neurosci Methods, 2006. **151**(2): p. 186-93.

158. J.J. Steinle and P.G. Smith, *Role of adrenergic receptors in vascular remodelling of the rat choroid.* Br J Pharmacol, 2002. **136**(5): p. 730-4.

159. R.A. Linsenmeier and L. Padnick-Silver, *Metabolic dependence of photoreceptors on the choroid in the normal and detached retina.* Invest Ophthalmol Vis Sci, 2000. **41**(10): p. 3117-23.

160. L.M. Parver, C. Auker, and D.O. Carpenter, *Choroidal blood flow as a heat dissipating mechanism in the macula.* Am J Ophthalmol, 1980. **89**(5): p. 641-6.

161. D.Y. Yu, S.J. Cringle, E.N. Su, and P.K. Yu, *Intraretinal oxygen levels before and after photoreceptor loss in the RCS rat.* Invest Ophthalmol Vis Sci, 2000. **41**(12): p. 3999-4006.

162. K. Tsunoda, Y. Oguchi, G. Hanazono, and M. Tanifuji, *Mapping cone- and rod-induced retinal responsiveness in macaque retina by optical imaging.* Invest Ophthalmol Vis Sci, 2004. **45**(10): p. 3820-6.

163. S. Trokel, *Effect of Respiratory Gases Upon Choroidal Hemodynamics.* Arch Ophthalmol, 1965. **73**: p. 838-42.

164. C.E. Riva, J.E. Grunwald, S.H. Sinclair, and B.L. Petrig, *Blood velocity and volumetric flow rate in human retinal vessels.* Invest Ophthalmol Vis Sci, 1985. **26**(8): p. 1124-32.

165. H. Boonstra, J.W. Oosterhuis, A.M. Oosterhuis, and G.J. Fleuren, *Cervical tissue shrinkage by formaldehyde fixation, paraffin wax embedding, section cutting and mounting.* Virchows Arch A Pathol Anat Histopathol, 1983. **402**(2): p. 195-201.

166. A.S. Brunschwig and A.N. Salt, *Fixation-induced shrinkage of Reissner's membrane and its potential influence on the assessment of endolymph volume.* Hear Res, 1997. **114**(1-2): p. 62-8.

167. B.A. Berkowitz, R. Roberts, H. Luan, D. Bissig, B.V. Bui, M. Gradianu, D.J. Calkins, and A.J. Vingrys, *Manganese-enhanced MRI studies of alterations of intraretinal ion demand in models of ocular injury.* Invest Ophthalmol Vis Sci, 2007. **48**(8): p. 3796-804.

168. B.A. Berkowitz, R. Roberts, A. Stemmler, H. Luan, and M. Gradianu, *Impaired apparent ion demand in experimental diabetic retinopathy: correction by lipoic Acid.* Invest Ophthalmol Vis Sci, 2007. **48**(10): p. 4753-8.

169. Y. Izumi, S.B. Hammerman, A.M. Benz, J. Labruyere, C.F. Zorumski, and J.W. Olney, *Comparison of rat retinal fixation techniques: chemical fixation and microwave irradiation.* Exp Eye Res, 2000. **70**(2): p. 191-8.

170. V.A. Murphy, K.C. Wadhwani, Q.R. Smith, and S.I. Rapoport, *Saturable transport of manganese(II) across the rat blood-brain barrier.* J Neurochem, 1991. **57**(3): p. 948-54.

171. A. Takeda, T. Akiyama, J. Sawashita, and S. Okada, *Brain uptake of trace metals, zinc and manganese, in rats.* Brain Res, 1994. **640**(1-2): p. 341-4.

172. A. Takeda, S. Ishiwatari, and S. Okada, *Influence of transferrin on manganese uptake in rat brain.* J Neurosci Res, 2000. **59**(4): p. 542-52.

173. I. Aoki, Y.J. Wu, A.C. Silva, R.M. Lynch, and A.P. Koretsky, *In vivo detection of neuroarchitecture in the rodent brain using manganese-enhanced MRI.* Neuroimage, 2004. **22**(3): p. 1046-59.

174. J.R. Burdo, D.A. Antonetti, E.B. Wolpert, and J.R. Connor, *Mechanisms and regulation of transferrin and iron transport in a model blood-brain barrier system.* Neuroscience, 2003. **121**(4): p. 883-90.

175. G.A. Peyman, *Antibiotic administration in the treatment of bacterial endophthalmitis. II. Intravitreal injections.* Surv Ophthalmol, 1977. **21**(4): p. 332, 9-46.

176. J.E. Furchner, C.R. Richmond, and G.A. Drake, *Comparative metabolism of radionuclides in mammals. 3. retention of manganese-54 in the mouse, rat, monkey and dog.* Health Phys, 1966. **12**(10): p. 1415-23.

177. D.Y. Lee and P.E. Johnson, *Factors affecting absorption and excretion of 54Mn in rats.* J Nutr, 1988. **118**(12): p. 1509-16.

178. W. Zheng, H. Kim, and Q. Zhao, *Comparative toxicokinetics of manganese chloride and methylcyclopentadienyl manganese tricarbonyl (MMT) in Sprague-Dawley rats.* Toxicol Sci, 2000. **54**(2): p. 295-301.

179. T.Q. Duong, A.C. Silva, S.P. Lee, and S.G. Kim, *Functional MRI of calcium-dependent synaptic activity: cross correlation with CBF and BOLD measurements.* Magn Reson Med, 2000. **43**(3): p. 383-92.

180. J.P. Strupp, *Stimulate: A GUI based fMRI analysis software package.* NeuroImage, 1996. **3**: p. S607.

181. P. Witkovsky, C. Shen, and J. McRory, *Differential distribution of voltage-gated calcium channels in dopaminergic neurons of the rat retina.* J Comp Neurol, 2006. **497**(3): p. 384-96.

182. K. Sho, K. Takahashi, T. Fukuchi, and M. Matsumura, *Quantitative evaluation of ischemia-reperfusion injury by optical coherence tomography in the rat retina.* Jpn J Ophthalmol, 2005. **49**(2): p. 109-13.

183. J.J. Steinle, D. Krizsan-Agbas, and P.G. Smith, *Regional regulation of choroidal blood flow by autonomic innervation in the rat.* Am J Physiol Regul Integr Comp Physiol, 2000. **279**: p. 202-9.

184. T.W. Lee and J.R. Robinson, *Drug delivery to the posterior segment of the eye: some insights on the penetration pathways after subconjunctival injection.* J Ocul Pharmacol Ther, 2001. **17**(6): p. 565-72.

185. B.A. Berkowitz, R.A. Lukaszew, C.M. Mullins, and J.S. Penn, *Impaired hyaloidal circulation function and uncoordinated ocular growth patterns in experimental retinopathy of prematurity.* Invest Ophthalmol Vis Sci, 1998. **39**(2): p. 391-6.

186. M.T. Block, *A note on the refraction and image formation of the rat's eye.* Vision Res, 1969. **9**(6): p. 705-11.

187. P. Dureau, S. Bonnel, M. Menasche, J.L. Dufier, and M. Abitbol, *Quantitative analysis of intravitreal injections in the rat.* Curr Eye Res, 2001. **22**(1): p. 74-7.

188. A. Marguerite, *Constant Distribution of 5,5 dimethyl-2,4-oxazolidinedione (DMO) in intraocular and cerebrospinal fluids of rabbits. III. Effect of ammonium chloride and probenecid.* Investigative Ophthalmology 1967. **6**(5).

189. A. Guyton, *Textbook of Medical Physiology*, ed. M. Wonsiewicz. 1991, Philadelphia, PA: WB Saunders. 1-1014.

190. A. Barbeau, *Manganese and extrapyramidal disorders (a critical review and tribute to Dr. George C. Cotzias)*. Neurotoxicology, 1984. **5**(1): p. 13-35.

191. I. Mena, O. Marin, S. Fuenzalida, and G.C. Cotzias, *Chronic manganese poisoning. Clinical picture and manganese turnover.* Neurology, 1967. **17**(2): p. 128-36.

192. Inoue N and M. Y, *Toxicology of Metals: (Neurological aspects in human exposures to manganese)*, ed. C. LW. 1996, Boca Raton, FL: CRC Press. 415-21.

193. G.P. Lin, W.Y.I. Tseng, H.C. Cheng, and J.H. Cheng, *Validation of diffusion tensor magnetic resonance axonal fiber imaging with registered manganese-enhanced optic tracts.* NeuroImage, 2001. **14**: p. 1035-47.

194. R. Pautler, A. Silva, and A. Koretsky, *In vivo neuronal tract tracing using manganese-enhanced magnetic resonance imaging.* Magn Reson Med, 1998. **40**: p. 740-8.

195. M. Kuhar and H.I. Yamamura, *Localization of cholinergic muscarinic receptors in rat brain by light microscopic radioautography.* Brain Res, 1976. **110**(2): p. 229-43.

196. B. Faulkner-Jones, *In-Situ Hybridisation to mRNA using radiolabelled cRNA probes*, University of Melbourne.

197. R.D. Hoge, J. Atkinson, B. Gill, G.R. Crelier, S. Marrett, and G.B. Pike, *Linear coupling between cerebral blood flow and oxygen consumption in activated human cortex.* Proc Natl Acad Sci U S A, 1999. **96**(16): p. 9403-8.

198. K.W. Small, E. Stefansson, and D.L. Hatchell, *Retinal blood flow in normal and diabetic dogs.* Invest Ophthalmol Vis Sci, 1987. **28**(4): p. 672-5.

199. C. Riva and D. Buerk, *Dynamic coupling of blood flow to function and metabolism in the optic nerve head.* Neuro-ophthalmology, 1998. **20**: p. 45-54.

200. T. Okuno, T. Sugiyama, M. Kohyama, S. Kojima, H. Oku, and T. Ikeda, *Ocular blood flow changes after dynamic exercise in humans.* Eye, 2006. **20**(7): p. 796-800.

201. L.E. Pillunat, R. Stodtmeister, R. Marquardt, and A. Mattern, *Ocular perfusion pressures in different types of glaucoma.* Int Ophthalmol, 1989. **13**(1-2): p. 37-42.

202. T.A. Ciulla, A. Harris, P. Latkany, H.C. Piper, O. Arend, H. Garzozi, and B. Martin, *Ocular perfusion abnormalities in diabetes.* Acta Ophthalmol Scand, 2002. **80**(5): p. 468-77.

203. E. Friedman, *A hemodynamic model of the pathogenesis of age-related macular degeneration.* Am J Ophthalmol, 1997. **124**(5): p. 677-82.

204. T. Nagaoka, F. Zhao, P. Wang, N. Harel, R.P. Kennan, S. Ogawa, and S.G. Kim, *Increases in oxygen consumption without cerebral blood volume change during visual stimulation under hypotension condition.* J Cereb Blood Flow Metab, 2006. **26**(8): p. 1043-51.

205. J.B. Mandeville, J.J. Marota, B.E. Kosofsky, J.R. Keltner, R. Weissleder, B.R. Rosen, and R.M. Weisskoff, *Dynamic functional imaging of relative cerebral blood volume during rat forepaw stimulation.* Magn Reson Med, 1998. **39**(4): p. 615-24.

206. R. Kalisch, G.K. Elbel, C. Gossl, M. Czisch, and D.P. Auer, *Blood pressure changes induced by arterial blood withdrawal influence bold signal in anesthesized rats at 7 Tesla: implications for pharmacologic mri.* Neuroimage, 2001. **14**(4): p. 891-8.

207. J. Nunn, *Nunns applied respiratory physiology.* 4 ed, ed. Butterworth-Heinemann. 1993, UK: Oxford

208. B.F. Matta, K.J. Heath, K. Tipping, and A.C. Summors, *Direct cerebral vasodilatory effects of sevoflurane and isoflurane.* Anesthesiology, 1999. **91**(3): p. 677-80.

209. P. Tornquist and A. Alm, *Retinal and choroidal contribution to retinal metabolism in vivo. A study in pigs.* Acta Physiol Scand, 1979. **106**(3): p. 351-7.

210. J.R. Mernagh, E.W. Spiers, and M. Adiseshiah, *The measurement of radioactive microspheres in biological samples.* Phys Med Biol, 1976. **21**(4): p. 646-50.

211. T. Omae, S. Ibayashi, K. Kusuda, H. Nakamura, H. Yagi, and M. Fujishima, *Effects of high atmospheric pressure and oxygen on middle cerebral blood flow velocity in humans measured by transcranial Doppler.* Stroke, 1998. **29**(1): p. 94-7.

212. A.A. Artru and J.D. Michenfelder, *Effects of hypercarbia on canine cerebral metabolism and blood flow with simultaneous direct and indirect measurement of blood flow.* Anesthesiology, 1980. **52**(6): p. 466-9.

213. S.S. Kety and C.F. Schmidt, *The Effects of Altered Arterial Tensions of Carbon Dioxide and Oxygen on Cerebral Blood Flow and Cerebral Oxygen Consumption of Normal Young Men.* J Clin Invest, 1948. **27**(4): p. 484-92.

214. D.P. Bulte, P.A. Chiarelli, R.G. Wise, and P. Jezzard, *Cerebral perfusion response to hyperoxia.* J Cereb Blood Flow Metab, 2007. **27**(1): p. 69-75.

215. H. Ito, M. Ibaraki, I. Kanno, H. Fukuda, and S. Miura, *Changes in the arterial fraction of human cerebral blood volume during hypercapnia and hypocapnia measured by positron emission tomography.* J Cereb Blood Flow Metab, 2005. **25**(7): p. 852-7.

216. A. Bill and G.O. Sperber, *Control of retinal and choroidal blood flow.* Eye, 1990. **4 (Pt 2)**: p. 319-25.

217. S. Jean-Louis, J.V. Lovasik, and H. Kergoat, *Systemic hyperoxia and retinal vasomotor responses.* Invest Ophthalmol Vis Sci, 2005. **46**(5): p. 1714-20.

218. R.L. Grubb, Jr., M.E. Raichle, J.O. Eichling, and M.M. Ter-Pogossian, *The effects of changes in PaCO2 on cerebral blood volume, blood flow, and vascular mean transit time.* Stroke, 1974. **5**(5): p. 630-9.

219. C.E. Riva, S.H. Sinclair, and J.E. Grunwald, *Autoregulation of retinal circulation in response to decrease of perfusion pressure.* Invest Ophthalmol Vis Sci, 1981. **21**(1 Pt 1): p. 34-8.

220. J.E. Grunwald, S.H. Sinclair, and C.E. Riva, *Autoregulation of the retinal circulation in response to decrease of intraocular pressure below normal.* Invest Ophthalmol Vis Sci, 1982. **23**(1): p. 124-7.

221. C. Delaey and J. Van De Voorde, *Regulatory mechanisms in the retinal and choroidal circulation.* Ophthalmic Res, 2000. **32**(6): p. 249-56.

222. C.E. Riva, P. Titze, M. Hero, and B.L. Petrig, *Effect of acute decreases of perfusion pressure on choroidal blood flow in humans.* Invest Ophthalmol Vis Sci, 1997. **38**(9): p. 1752-60.

223. O.O. Pedersen, *An electron microscopic study of the permeability of intraocular blood vessels using lanthanum as a tracer in vivo.* Exp Eye Res, 1979. **29**(1): p. 61-9.

224. T. Desmettre, J.M. Devoisselle, and S. Mordon, *Fluorescence properties and metabolic features of indocyanine green (ICG) as related to angiography.* Surv Ophthalmol, 2000. **45**(1): p. 15-27.

225. P.T. Williams, R.M. Krauss, A.V. Nichols, K.M. Vranizan, and P.D. Wood, *Identifying the predominant peak diameter of high-density and low-density lipoproteins by electrophoresis.* J Lipid Res, 1990. **31**(6): p. 1131-9.

226. E.M. Burden, H.W. Reading, and C.M. Yates, *An investigation into the structural integrity of lysosomes and its effect in the normal and dystrophic rat retina.* Exp Eye Res, 1971. **11**(1): p. 140.

227. C.H. Bunker, E.L. Berson, W.C. Bromley, R.P. Hayes, and T.H. Roderick, *Prevalence of retinitis pigmentosa in Maine.* Am J Ophthalmol, 1984. **97**(3): p. 357-65.

228. Stephen P. Daiger, Lori S. Sullivan, and Sara J. Bowne (2008) *Genes and Mapped Loci Causing Retinal Diseases.* **Volume**,

229. S.N. Cox, E. Hay, and A.C. Bird, *Treatment of chronic macular edema with acetazolamide.* Arch Ophthalmol, 1988. **106**(9): p. 1190-5.

230. E.L. Berson, B. Rosner, M.A. Sandberg, K.C. Hayes, B.W. Nicholson, C. Weigel-DiFranco, and W. Willett, *A randomized trial of vitamin A and vitamin E supplementation for retinitis pigmentosa.* Arch Ophthalmol, 1993. **111**(6): p. 761-72.

231. G.M. Acland, G.D. Aguirre, J. Ray, Q. Zhang, T.S. Aleman, A.V. Cideciyan, S.E. Pearce-Kelling, V. Anand, Y. Zeng, A.M. Maguire, S.G. Jacobson, W.W. Hauswirth, and J. Bennett, *Gene therapy restores vision in a canine model of childhood blindness.* Nat Genet, 2001. **28**(1): p. 92-5.

232. J.F. Rizzo, 3rd, J. Wyatt, M. Humayun, E. de Juan, W. Liu, A. Chow, R. Eckmiller, E. Zrenner, T. Yagi, and G. Abrams, *Retinal prosthesis: an encouraging first decade with major challenges ahead.* Ophthalmology, 2001. **108**(1): p. 13-4.

233. A. Gal, Y. Li, D.A. Thompson, J. Weir, U. Orth, S.G. Jacobson, E. Apfelstedt-Sylla, and D. Vollrath, *Mutations in MERTK, the human orthologue of the RCS rat retinal dystrophy gene, cause retinitis pigmentosa.* Nat Genet, 2000. **26**(3): p. 270-1.

234. R.J. Mullen and M.M. LaVail, *Inherited retinal dystrophy: primary defect in pigment epithelium determined with experimental rat chimeras.* Science, 1976. **192**(4241): p. 799-801.

235. P.M. D'Cruz, D. Yasumura, J. Weir, M.T. Matthes, H. Abderrahim, M.M. LaVail, and D. Vollrath, *Mutation of the receptor tyrosine kinase gene Mertk in the retinal dystrophic RCS rat.* Hum Mol Genet, 2000. **9**(4): p. 645-51.

236. J.E. Dowling and R.L. Sidman, *Inherited retinal dystrophy in the rat.* J Cell Biol, 1962. **14**: p. 73-109.

237. W.L. Herron, Jr., B.W. Riegel, and M.L. Rubin, *Outer segment production and removal in the degenerating retina of the dystrophic rat.* Invest Ophthalmol, 1971. **10**(1): p. 54-63.
238. D.Y. Yu, S.J. Cringle, V.A. Alder, and E.N. Su, *Intraretinal oxygen distribution in rats as a function of systemic blood pressure.* Am J Physiol, 1994. **267**(6 Pt 2): p. H2498-507.
239. D. Bok and M.O. Hall, *The role of the pigment epithelium in the etiology of inherited retinal dystrophy in the rat.* J Cell Biol, 1971. **49**(3): p. 664-82.
240. M.H. Chaitin and M.O. Hall, *Defective ingestion of rod outer segments by cultured dystrophic rat pigment epithelial cells.* Invest Ophthalmol Vis Sci, 1983. **24**(7): p. 812-20.
241. M. Tamai and G.J. Chader, *The early appearance of disc shedding in the rat retina.* Invest Ophthalmol Vis Sci, 1979. **18**(9): p. 913-7.
242. W.L. Herron, B.W. Riegel, O.E. Myers, and M.L. Rubin, *Retinal dystrophy in the rat--a pigment epithelial disease.* Invest Ophthalmol, 1969. **8**(6): p. 595-604.
243. K. Valter, J. Maslim, F. Bowers, and J. Stone, *Photoreceptor dystrophy in the RCS rat: roles of oxygen, debris, and bFGF.* Invest Ophthalmol Vis Sci, 1998. **39**(12): p. 2427-42.
244. S. Wang, M.P. Villegas-Perez, T. Holmes, J.M. Lawrence, M. Vidal-Sanz, N. Hurtado-Montalban, and R.D. Lund, *Evolving neurovascular relationships in the RCS rat with age.* Curr Eye Res, 2003. **27**(3): p. 183-96.
245. M.M. Lavail, L. Li, J.E. Turner, and D. Yasumura, *Retinal pigment epithelial cell transplantation in RCS rats: normal metabolism in rescued photoreceptors.* Exp Eye Res, 1992. **55**(4): p. 555-62.
246. R.B. Caldwell, R.S. Roque, and S.W. Solomon, *Increased vascular density and vitreo-retinal membranes accompany vascularization of the pigment epithelium in the dystrophic rat retina.* Curr Eye Res, 1989. **8**(9): p. 923-37.
247. M.M. LaVail, R.L. Sidman, and D. O'Neil, *Photoreceptor-pigment epithelial cell relationships in rats with inherited retinal degeneration. Radioautographic and electron microscope evidence for a dual source of extra lamellar material.* J Cell Biol, 1972. **53**(1): p. 185-209.
248. E.-H. E, *Research in Retinitis Pigmentosa.* Pathomorphology of the retina and its vasculature in hereditary retinal dystrophy in RCS rats, ed. Zrenner E, Krastel H, and G. HH. 1987, Cambridge, U.K.: Harvard University Press. 417.
249. M.M. LaVail, *Retinal Pigment Epithelium* The retinal pigment epithelium in mice and rats with inherited retinal degeneration ed. K.M. Zinn and M.F. Marmor. 1979, Cambridge, U.K.: Harvard University Press. 357-80.
250. E. El-Hifnawi, *Research in Retinitis Pigmentosa.* Pathomorphology of the retina and its vasculature in hereditary retinal dystrophy in RCS rats, ed. E. Zrenner, H. Krastel, and H. Goebel. 1987, London, UK: Pergamon Journals, Ltd. 417.
251. A.D. Seaton and J.E. Turner, *RPE transplants stabilize retinal vasculature and prevent neovascularization in the RCS rat.* Invest Ophthalmol Vis Sci, 1992. **33**(1): p. 83-91.
252. H.J. Zambarakji, D.J. Keegan, T.M. Holmes, A.S. Halfyard, M.P. Villegas-Perez, D.G. Charteris, F.W. Fitzke, J. Greenwood, and R.D. Lund, *High resolution*

imaging of fluorescein patterns in RCS rat retinae and their direct correlation with histology. Exp Eye Res, 2006. **82**(1): p. 164-71.

253. C.A. May, M. Horneber, and E. Lutjen-Drecoll, *Quantitative and morphological changes of the choroid vasculature in RCS rats and their congenic controls.* Exp Eye Res, 1996. **63**(1): p. 75-84.

254. T. Satoh and K. Yamaguchi, *Ocular fundus abnormalities detected by fluorescein and indocyanine green angiography in the Royal College of Surgeons dystrophic rat.* Exp Anim, 2000. **49**(4): p. 275-80.

255. H. Lu, C. Clingman, X. Golay, and P.C. van Zijl, *Determining the longitudinal relaxation time (T1) of blood at 3.0 Tesla.* Magn Reson Med, 2004. **52**(3): p. 679-82.